Design of Counter-current Tangential Chromatography to Improve Resin Lifetime and Operational Simplicity

A thesis submitted in fulfilment for the

degree of Doctor of Philosophy

by

Jose Mauricio Martin Bufajer

December 2020

Department of Biochemical Engineering

University College London

Torrington Place

London WC1 E7JE

Declaration of Authorship

I, Jose Mauricio Martin Bufajer, declare that this thesis titled “Design of counter-current tangential chromatography to improve resin lifetime and operational simplicity” and the work presented in it are my own. I confirm that:

- This work was done wholly while in candidature for a research degree at the Department of Biochemical Engineering in University College London.
- Where any part of this thesis has previously been submitted for a degree or any other qualification at this University or any other institution, this has been clearly stated.
- Where I have consulted the published work of others, this is always clearly attributed.
- Where I have quoted from the work of others, the source is always given. With the exception of such quotations, this thesis is entirely my own work.
- I have acknowledged all main sources of help.
- Where the thesis is based on work done by myself jointly with others, I have made clear exactly what was done by others and what I have contributed myself.

Signed: Jose Mauricio Martin Bufajer

Date: 11/12/2020

“No amount of experimentation can ever prove me right; a single experiment can prove me wrong.”

-Albert Einstein

Acknowledgements

I would like to thank for the assistance and direction imparted by my supervisors Yuhong Zhou and Daniel Bracewell.

I am certainly grateful to many people who have helped throughout my PhD degree.

Especially those who I have had the pleasure to interact beyond working constraints and become more than teammates or acquaintances.

I have said it a thousand times but I will say it again. Thanks to my parents, Soraya and Juan; my siblings, Soraya and Juan; and my grandmother, Lucia for the unconditional support, lessons, time, patience and love that have moulded me into the person you can see today. I have no words to express my gratitude.

This project would have never been possible without the financial support of the Department of Biochemical Engineering at University College London and the Consejo Nacional de Ciencia y Tecnologia.

“Don’t forget to smile in any situation. As long as you are alive, there will be better things later, and there will be many”

-Eiichiro Oda

Abstract

This thesis aims to understand current counter-current tangential chromatography (CCTC) design in bioprocessing. It assesses the structural and performance changes that occur in agarose- and synthetic-based chromatography resins as they are exposed to different equipment designs in order to improve resin lifetime and operational simplicity. The mixing and tangential flow filtration modules were characterized to provide a minimum residence time of 120 seconds and an operational flux of 70 LMH.

The chromatography resin was used in different equipment designs for 36 hours to assess the performance and structural properties. The results indicate that the shear caused by peristaltic pumps and hollow fibres caused an average size reduction of 5% in both synthetic and agarose resins. However, the agarose-based resin had significantly deformed. Both resins exhibited a deviation of 5% from their original dynamic binding capacity. The system's separation performance was tested using a two-component separation (BSA and myoglobin) and a salt step-gradient separation of ovalbumin variants. The two-component separation was a success with a purity and a yield of 99.9% and 93.2%, respectively. In contrast when attempting the more challenging separation of closely related ovalbumin variants using a step-gradient separation the inline mixing in the CCTC system prevented successfully separation.

Different coiled flow inverter reactor (CFIR) designs were explored as viable mixing modules for their operational flexibility, system simplification and cost-effectiveness. The best performing CFIR (λ 13.8) showed inferior results to the set of static mixers showing a normalised batch binding capacity of 0.9 and 1.0, respectively. However, this CFIR showed to be a more cost-effective reactor by being 17x cheaper while operating at 90% binding capacity efficiency.

The project established critical considerations for adsorbent use and CFIRs as a simplified and cost-effective mixing option, which aids the adoption of this technology for biopharmaceutical manufacturing.

Impact Statement

Downstream processing has been relatively neglected in recent years in comparison to upstream processing technologies. Large scale chromatography is the downstream processing workhorse for the capture and purification of therapeutic proteins. This research in the area of continuous counter-current tangential chromatography has delivered:

1. A wider understanding on this continuous non-packed bed chromatographic technique which will enable the technology mature and penetrate the downstream processing pharmaceutical market. This chromatography method could potentially decrease the production costs for mAbs and any other affinity based separation molecules due to its high throughput, lower chromatography resin volumes and 10x capacity. This technique will open the conversation to consider looking for alternatives to traditional batch chromatography, which can be expensive, long and dated compared to the current trends.
2. An exploration of the potential and limitations of continuous counter-current tangential chromatography, like high throughput and extremely short cycle times, will allow easier process development and higher product quality. This novel approach to chromatography allows a quick implementation and straightforward scalability without worrying about column dimensions and peak profile.
3. A simplification and redesign of the current chromatography system by the replacement of the static mixer modules for continuous flow inverter reactors will lead to better cost of goods and flexibility for the industry by significantly reducing the volume of resin used and the ability to easily modify the bind and elution residence time.
4. A revised and new design that is capable of being a viable single use chromatography technology. This feature will reduce the risk of cross-contamination, reduce the direct labour and validation/regulation costs, as well as being a more environmentally friendly option by reducing the use of water for cleaning procedures.
5. An assessment of the performance and physical structure of current commercial available chromatography resin under different shear stresses and mixing configurations. This will reduce the cost of goods as research for new media would not be necessary for the implementation of any non-packed bed chromatographic technique. Instead, the research can be focused on the optimisation of the technique itself.

Table of Contents

List of Figures

List of Tables

Nomenclature

Symbols

a	Particle Radius (Critical Flux)	m
AC	Affinity Chromatography	-
ADM	Axial Dispersion Model	-
a_i	Protein Concentration Determination Slope	-
AIDS	Acquired Immune Deficiency Syndrome	-
BBC	Batch Binding Capacity	g/L
b_i	Protein Concentration Determination Constant	-
BSA	Bovine Serum Albumin	
C	Particle Concentration (CFIR)	g/L
C_0	Initial BSA concentration	g/L
CAC	Continuous Annular Chromatography	-
CARE	Continuous Affinity-recycle Extraction	-
$C_{b,in}$	Static Mixer Inlet Bound BSA Concentration	g/L
$C_{b,out}$	Static Mixer Outlet Bound BSA Concentration	g/L
$C_{b,r}$	Retentate Outlet Bound BSA Concentration	g/L
CCF	Cell-clarified Fluid	-
CCSC	Continuous Counter-current Spiral Chromatography	-
CCTC	Continuous Counter-current Tangential Chromatography	-
C_f	Feed Free BSA Concentration	g/L
$C_{f,in}$	Static Mixer Inlet Free BSA Concentration	g/L
$C_{f,out}$	Static Mixer Outlet Free BSA Concentration	g/L
$C_{f,r}$	Retentate Outlet Free BSA Concentration	g/L
CFIR	Coiled Flow Inverter Reactor	-
C_i	Concentration in Sample	g/L

CIP	Clean-in-Place	-
COG	Cost of goods	-
C_p	Permeate Outlet BSA Concentration	-
CQA	Critical Quality Attributes	-
CV	Column Volume	CV
C_w	Fresh Buffer BSA Concentration	g/L
d	Fraction Volume Determination Slope	-
D/uL	Dimensionless Dispersion Number	-
Da	Daltons	Da
D_{ax}	Axial Dispersion Coefficient	m^2/s
DBC	Dynamic Binding Capacity	g/L
D_c	CFIR External Coil Diameter	m
De	Dean Number	-
D_{HCR}	HCR External Coil Diameter	m
D_m	Molecular Diffusion Coefficient	m^2/s
DNA	Deoxyribonucleic Acid	-
D_s	Effective Particle Diffusion	m^2/s
DSP	Downstream Process	-
d_{te}	External Coiled Tube Diameter	m
d_{ti}	Internal Coiled Tube Diameter	m
E	Experimental Dimensionless Residence Time Distribution Curve	-
e	Fraction Volume Determination Constant	L
E_{ADM}	Theoretical Dimensionless Residence Time Distribution Curve	-
EMA	European Medicines Agency	-
FDA	Food and Drug Administration	-
g	Gram	g
h	Hour	h
HCP	Host Cell Proteins	-

HCR	Helical Coil Reactor	-
HIC	Hydrophobic Interaction Chromatography	-
HIV	Human Immunodeficiency Virus	-
HPLC	High Performance Liquid Chromatography	-
IEC	Ion Exchange Chromatography	-
J_{CRIT}	Critical Flux	LMH
K	Correction Factor for Solid Content	-
K	Mass Transfer Coefficient (Critical Flux)	LMH
k_1	Binding Rate Constant Before 50%	-
k_2	Binding Rate Constant After 50%	-
L	Length of Hollow Fibre (Critical Flux)	m
L	Liter	L
L	Coiled Tube Length	m
LMH	-	$Lm^{-2}h^{-1}$
m	Meter	m
mAb	Monoclonal Antibody	-
m_{BSA}	Total Mass of BSA in Elution Step	kg
$m_{BSA.load}$	Mass of BSA in Load Step	kg
m_{myo}	Total Mass of Myoglobin	kg
MW	Molecular Weight	kg/mol
N	Disc Speed (USD disc rotary device)	rpm
N	Number of Stages (CCTC)	-
n	Number of Turns for Coiled Tubing	-
n_b	Total number of bends	-
n_{bends}	Number of Bends	-
NIR	Near Infrared Region	-
$n_{o,t}$	Optimum Number of Turns for the Coiled Tubing	-
N_{Pe}	Peclet Number	-

N_{Re}	Reynolds Number	-
n_{turns}	Number of Turns	-
OA	Optical Absorbance	-
p	Pitch Distance	m
PCC	Periodic Counter-Current Chromatography	-
PFR	Plug Flow Reactor	-
pH	Potential /Power of Hydrogen	-
pI	Isoelectric Point	-
P_{in}	Inlet Feed Pressure	Pa
P_{out}	Retentate Outlet Pressure	Pa
$P_{permeate}$	Permeate Outlet Pressure	Pa
PSD	Particle Size Distribution	-
Q_i	Binding Capacity	g/L
QbD	Quality by Design	-
Q_{max}	Maximum Binding Capacity	g/L
q_p	Permeate Flow Rate	L/s
q_r	Retentate Flow Rate	L/s
$q_{s,in}$	Static Mixer Inlet Fresh Slurry Flow Rate	L/s
$q_{s,out}$	Static Mixer Outlet Flow rate	L/s
q_w	Static Mixer Inlet Permeate Flow Rate	L/s
r_0	Fibre Radius	m
R^2	Coefficient Determination	-
R_i	Fractional Impurity Removal	-
RT	Residence Time	s
R_T	Total Fractional Impurity Removal	-
RTD	Residence Time Distribution	-
R_w	Relative Width	-
S	Average Sieving Coefficient	-

s	Second	s
SEM	Scanning Electron Microscopy	-
SMB	Simulated Moving Bed	-
SMR	Static Mixer Reactor	-
t_{ave}	Average Residence Time	s
t_f	Dimensionless Final Time Point	-
TFF	Tangential Flow Filtration	-
t_i	Residence Time at Moment i	-
TMB	True Moving Bed	-
TMP	Transmembrane Pressure	Pa
u	Mean Axial Velocity	m/s
USD	Ultra-scale Down	-
USP	Upstream Process	-
UV	Ultra-violet	-
v	Average Suspension Velocity	m/s
V	Total Batch Volume	L
V_b	Breakthrough Volume	L
V_R	Resin Slurry Volume	L
V_s	Resin Slurry Volume	L
V_s	Total Volume	L
vs	Versus	L
Y	Overall Yield	%
Y_e	Elution Step Yield	%
Y_s	Strip Step Yield	%

Greek Symbols

γ_0	Wall Shear Rate	1/s
τ_w	Wall Shear Stress	Pa
ϕ_b	Volume Fraction in the Suspension	%
ϕ_w	Volume Fraction at the Membrane Surface	%
α	Equation Simplification Variable	-
γ_{flow}	Retentate and Permeate Flow Rate Ratio	-
ε	Maximum Energy Dissipation Rate	W/kg
ε	Residual Error	-
θ	Binding Capacity over Maximum Binding Capacity	-
θ_i	Dimensionless Residence Time	-
λ	Curvature Ratio	-
σ	Residence Time Variance	s^2
σ_θ	Dimensionless Residence Time	-
φ	Resin Slurry Concentration	%
φ_{ave}	Average Slurry Fraction in Hollow Fibre	%
φ_{in}	Inlet Resin Slurry Fraction	%
φ_{out}	Outlet Resin Slurry Fraction	%
φ_r	Retentate Resin Slurry Fraction	%
ω	Liquid Fraction in Resin	%
μ	Viscosity	m^2/s

Thesis Layout

Succeeding this section, this thesis reviews literature to understand the core role of chromatography fundamentals, chromatography resin and chromatography in industry. The different chromatographic techniques are discussed and the reasoning to move forward into continuous processing. Afterwards, the materials and methods used in this research are outlined.

Chapter 3, the first of 4 results chapters, discusses the characterization of protein adsorption and desorption kinetics of the agarose- and methacrylate-based chromatography resin in batch and column formats; as well as the characterization of the operational parameters of the static mixer (batch binding capacity (BBC) studies) and the hollow fibre modules (critical flux studies). The parameters for the CCTC system, such as resin slurry, residence time, flow rate and flux; were decided for further separations. The end of the chapter introduces the concept of hindrance of resin performance and lifetime in the CCTC technique by measuring the resin bead particle size distribution (PSD).

Chapter 4 discusses the performance and structural characterization of both chromatography resin types that have been exposed to different CCTC equipment system components for different periods of time. The equipment designs focus mainly on the resin reservoir mixer, the peristaltic pump and the hollow fibre module. The characterization used DBC experiments, PSD studies, scanning electron microscopy (SEM) imaging (quantitative and qualitative analysis) to determine whether a deviation from the original state happened, quantify it and identify the component causing such deviation.

Chapter 5 applies all aforementioned characterization and operational parameters to build a custom 2-stage CCTC step rig. The CCTC rig performance was tested by doing a two-component separation of bovine serum albumin (BSA) (product) and myoglobin (contaminant), and a salt step-gradient separation of ovalbumin variants. The objectives of this chapter are to reproduce the CCTC performance reported in literature, identify the advantages and draw backs of the technique, and investigate whether the technique is capable of separating different molecules with closely related

elution behaviours. This section explores the areas of opportunity where the system can be improved or simplified upon.

Chapter 6 focuses on the proof of concept of coiled flow inverter reactors (CFIR) as viable mixing modules for simplification of the current CCTC system design. Different CFIRs were built along with their helical coil reactors (HCR) counterparts. CFIRs, HCRs and static mixer reactors (SMRs) will be characterized in terms of residence time (RT), relative width (R_w), axial dispersion reduction (N_{Pe}) and BBC. The objectives of this chapter are to introduce, test and establish the potential of CFIRs for protein adsorption in a continuous chromatography purification step and simplify the current CCTC system design (mixing modules) for added flexibility and cost reduction. This section uncovers an area of opportunity for CFIRs to be further explored and, ultimately, optimized.

Chapter 7 discusses whether the initial aim and objectives were met with a final conclusion. Chapter 8 explores the potential future work and developmental activities on the subjects previously discussed. Additionally, it examines the possible alternatives and simplifications the CCTC design which can be improved in order to aid the adoption of this emergent technology for biopharmaceutical manufacturing.

Chapter 1: Literature Review

1.1 Introduction and theoretical background

This literature review is structured to address the fundamental principles enclosed in this research. The understanding of continuous chromatography and CCTC requires comprehension of packed-bed batch chromatography, the foundation concepts, its components and factors that affect its purification and performance.

In this literature review the history and role of chromatography in bioprocessing in the current era is briefly addressed. The components that constitute a column and the role of the chromatography resins are emphasized. Description on basic structural properties of the resins used in this study and the various forces or conditions that can impact their structural damage and lifetime is presented. The section on chromatographic operation is designed to give a foundation on the stages of purification. Furthermore, it contrasts the differences between the stages of purification for column-based chromatography and CCTC. Also, it includes a thorough description of the system design and mode of operation of CCTC. Then, the description and role of the mixing and hollow fibre modules is presented. This section concludes with a variety of commercially available continuous chromatographic techniques, as well as a discussion on failed attempts on non-column chromatographic techniques as means of establishing a framework among all technique and demonstrating the reported advantages and disadvantages of CCTC.

The review moves on to highlight the need of characterization of the mixing and solid-liquid separation modules of the CCTC technique, as well as to explore different design options, to meet modern manufacturing economic and regulatory standards.

1.2 Research Motivation

The favouritism of biological-related products in the current biopharmaceutical market and advances in biochemical engineering and molecular biology have inevitably led to an increase in research and manufacture of cell line related products. Process control, bioreactor design and host cell engineering have been crucial for the optimization of upstream processing (USP). USP improvement has relatively neglected any important optimization at large-scale on downstream processes (DSP). This preference in innovation has created a production bottleneck that is shifting time constraints and costs of production to DSP. This bottleneck has started to be addressed by implementing continuous, single-use materials and flexible downstream operations (Gronemeyer, Ditz, and Strube 2014).

Batch processing has been the standard paradigm for commercial-scale manufacture of high value biological products. This non-continuous sequence facilitates the design and optimization of the manufacturing operations and accommodates offline measurements (Zydney 2016; Warikoo et al. 2012; Mollan and Lodaya 2004). Nevertheless, there has been a growing interest in the implementation of specific biotechnological steps in a continuous mode, with an end goal of making a complete transition into a full continuous manufacturing process. This transition intends to create a breakthrough in biotechnology as it was for chemical and pharmaceutical industries (Mascia et al. 2013). Successful efforts in bioethanol and microalgae industries have demonstrated that regulated continuous manufacturing is possible on biological systems, especially in DSP (Bangrak, Limtong, and Phisalaphong 2011; Qiu, Zhao, and Weatherley 2010; Unrean and Srienc 2010).

Chromatography has experienced a relatively poor translation from batch to continuous manufacturing. Despite the active push for continuous processing, some pharmaceutical companies still continue to use a traditional packed-bed column format for high purity requirements of therapeutic molecules, such as monoclonal antibodies (mAb) due to the lack of experience, unfamiliarity or lack of data supporting these continuous techniques. An innovation in continuous chromatography is needed to satisfy both, current and future demand (Challener 2018; Gottschalk 2013). Non-column-based chromatography seems to satisfy the economic and technological need

in industry due to its truly continuous mode and simple design for scalability and operation. Nevertheless, the technology is relatively new and improvements are required to make this a reliable process.

1.3 Biopharmaceutical Market

Biopharmaceutical products are among the most modern and noteworthy achievements in human history. The trend for the research and production of biopharmaceuticals, such as recombinant therapeutic proteins, mAbs and nucleic acids, has fared well in recent years. There is an active interest of converting pure knowledge into tangible curative products. The branch of science known as biotechnology has produced more than 200 therapies and vaccines against numerous diseases; for example: HIV/AIDS, cancer, diabetes, Alzheimer´s disease, heart diseases and arthritis (Huang and Mucke 2012; Kayser and Warzecha 2012; Tran et al. 2013).

In 2018, biopharmaceutical market revenue reported numbers of $237 billion and this is estimated to increase up to $388 billion by 2024. This trend is due to the few drawbacks and the growing acceptance for biopharmaceuticals treating what were considered previously untreatable diseases (as the ones mentioned earlier). The upward number of research projects done with mAbs and recombinant digestive enzymes reinforces this behaviour. These two biopharmaceutical products have a prevalent use in developed countries such as United Kingdom and United States of America (MordorIntelligence 2018).

Leading companies in this sector, with little or no experience at all, recognized this trend and have been acquiring small biotechnological start-ups or companies for the technological relevance in the current market; e.g. pioneering companies like Genentech, Chiron, Cetus and Bioge Idec have already been acquired by larger ones (Ho and Gibaldi 2013).

1.4 Downstream Processing

Any biopharmaceutical process starts with an USP, using microbial or mammalian cells to produce a desired molecule, continued by DSP that is the extraction and separation of the product from the biological bulk and afterwards purified. DSP can be properly defined as a series of operations that take the output from USP and generate a stable and pure product under certain standards and regulations. As the host microorganism is no longer needed (unless the microorganism is the product), DSP is mainly regulated by biochemical and physical factors, while USP is dependent on biological parameters (Kayser and Warzecha 2012). A conventional diagram depicting the separation between USP and DSP, as well as its main subdivisions, is shown in Figure 1.1.

The majority of the feed materials are in a complex mixture of products; they have contaminants and by-products, which makes the purification extremely challenging. Depending on the host platform the protein of interest represents 0.5% to 5% of the total protein in the cell medium broth. For this reason, DSP is divided into 4 stages: harvesting, clarification, purification and polishing. Harvesting involves the bulk separation of any biological material containing the desired product from any remainder of the USP, being cells or spend medium. Clarification is the removal of larger particulates and other major contaminants, such as lipid droplets and bigger debris. Harvesting and clarification can be done together when the product is expressed as an extracellular product by traditional means. The next steps depend on the specific characteristics of the molecules and contaminants to capture them. Finally, the polishing step can be defined as the inverse of the purification stage; that is, the capture of remaining contaminants (i.e. trace amounts of host cell proteins (HCP), leachables and deoxyribonucleic acid (DNA) fragments) while the product is released before all of them (Kayser and Warzecha 2012). The innate characteristics of the product protein, such as molecular weight/size, binding affinity, reactive groups, charge and hydrophobicity have been used as the basis for the creation of different DSP capture and polishing strategies (Ersson, Rydén, and Janson 2011). Chromatography falls under the last two steps, making it a crucial step, which is responsible for reaching purity regulatory standards while avoiding any product loss in the process line.

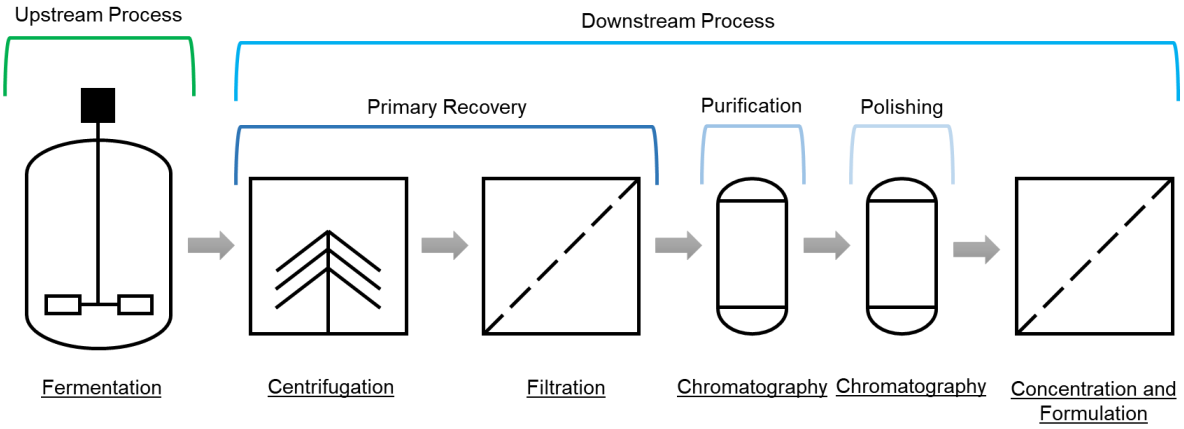

Figure 1.1. Conventional biopharmaceutical manufacturing line. The processing is divided into two main areas: USP and DSP. DSP is conventionally divided in: primary recovery, purification, polishing and formulation steps.

1.4.1 Downstream Processing Challenges

The market growth and the high dose required for patients has forced manufacturers to generate more product than ever before at lower costs and higher quality. As a consequence, there is an active push by the same industries to increase the manufacturing capacity. Unfortunately, the increase in manufacturing capacity is not always economically feasible on the short- and medium-run as costs are already under a rigorous budget and it would take a minimum of $200 to $400 million and 5 years to design, test and validate the same product (Farid 2007; Przybycien, Pujar, and Steele 2004). It is also possible to derive benchmark investment costs according to their size of $660 to $1,580 per ft^2 ($7,130 to $17,000 per m2). For example, Genentech expansion in Vacaville, United States, cost $600 million for 380,000,000 ft^2 with a total processing capacity of 200,000 L (Farid 2007; Bender 1996).

In order to solve these limitations, biotechnological industries have recently invested millions in new infrastructure, mainly USP equipment. This USP improvement has cost the companies around $20 billion due to the underutilized production capacity, which is around 60%. Even after USP capacity increased, DSP is physically incapable of handling those volumes of material because of time or process constraints related to high titres or volumes of product. This results in a product loss due to unfinished processing. An example of this USP intensification is the overall mammalian cell culture production capacity increased from 700,000 L to 2,550,000 L in 2010

(McGlaughlin 2012). In addition, the high production of USP volumes in combination with the pertinent optimizations on the operational parameters definitely shifted the bottleneck towards DSP.

This shifting of the bottleneck from USP to DSP can be attributed to different factors and it is a natural effect or consequence of the field maturing from smaller scales to larger ones due to the demand increase from the acceptance and approval of many therapeutic techniques. As a rule of thumb, upstream capacity can be increased without significantly raising the costs or not changing them at all whereas downstream capacity costs scale linearly or non-linearly due to its physical principles of separation. The cost distribution between the both of them vary depending on the scale; USP is highly expensive at lower scales while DSP becomes the major cost component for large scales. A facility can produce 5 to 10 kg of mAb per batch and optimise the process to produce 15 to 100 kg of mAb per batch in the exact same 20,000 L bioreactor. DSP that was not designed to process that amount of product material would struggle to purify it on the same processing time or with the same resources, material consumption or techniques, increasing the COGs for the whole process. For example, Sommerfeld and Strube calculated that increasing the overall fermentation titre from 0.1 to 1 g/L (10X increase) causes the ratio of USP to DSP from 55:45 to 30:70. This reflects the aforementioned statement about the COGs for different scales/titres, creating this infamous DSP bottleneck. This increase in titre would probably requires additional chromatographic columns or investment on chromatography techniques, as well as any costs related to subsequent filtration steps requiring larger areas or filtration times (Farid 2009; Yang, Qadan, and Ierapetritou 2019; Gronemeyer, Ditz, and Strube 2014; Sommerfeld and Strube 2005). In some cases, DSP mAb production can make of 50% to 70% of all the total COGs of production (Straathof 2011). However, the COGs/g can still fall if the increase in overall productivity outweighs this cost increases.

The DSP bottleneck can be addressed in different manners. One of the solutions is by removing number of steps or scaling up, increasing the overall yield per step. This approach has given us a typical overall process yield increase from 40% to 75%, with higher throughput. Even though the COGs are increasing, the overall productivity cost increase will overcome the increased COGs (Werner 2004; F. Li et al. 2006). A second option would be material reuse. This approach is usually seen in chromatography as

a large bioreactor of 10,000 L with a yield of 1 g/L can results in Protein resin costs of $4 million. This reuse can decrease all the costs dramatically as the overall cost would be distributed by the number of cycles it is been used (Lewis-Sandy 2001; Anurag S. Rathore et al. 2004) Buffer and water injections costs can even be larger than resin costs. For example, a fermentation of 20,000 L would require 140,000 L of buffer at a costs of $0,2 per L for pure water and $2 to $12 per L of buffer (Aldington and Bonnerjea 2007; J. X. Zhou and Tressel 2006; Warner and Nochumson 2003). In terms of chromatography, a trade-off can be made by addressing higher DBCs, higher flow rates and reuse limits by using a better chromatography media. All of these options have been addressed and have been implemented in manufacturing processes since the process was designed. Another alternative is to find different purification steps (platform or niche applications) to substitute the over-reliance on chromatography and its expensive chromatography media, such as separation methods based on monoliths or precipitation techniques (Farid 2009).

1.4.2 Continuous Downstream Processing

Continuous manufacturing has been used for a number of years by a huge variety of industries in the market; i.e. steel, pharmaceutical chemical and food (Godawat et al. 2015; N. G. Anderson 2001; T. H. Anderson and Brune 1982; Krohn et al. 2011). However, biotechnology is late to fully implement this type of operation, as a batch-mode process mode of operation is still the way to go for the therapeutic biomolecules. Efforts in the areas of bioethanol and microalgae have proved it is an achievable goal (Unrean and Srienc 2010; T. H. Anderson and Brune 1982; Krohn et al. 2011).

The expensive production of recombinant proteins, which sometimes cost more than noble metals or rare earth elements, can be listed as one reason for the reluctance to implement these technologies in DSP. A large-scale continuous process in biotechnology does not have the annual market demand to justify the investment (Jungbauer 2013). However, stratified medicine is starting to pressure companies to shift from batch-mode into continuous-mode manufacturing. A trend of decreasing blockbuster candidates justifying metric tons per year of product is forcing a paradigm

shift towards continuous operations of smaller scale, disregarding disposable technologies (Strube et al. 2011).

Continuous production has been demonstrated to be an efficient and robust way to increase product quality (A. S. Rathore 2015). The definition of manufacturing batches according to the Food and Drug Administration (FDA) and the European Medicines Agency (EMA) is: a batch is a specific quantity of a drug or other material that is intended to have uniform character and quality within specified limits, and is produced according to a single manufacturing order during the same cycle to manufacture (Jungbauer 2013). This definition does not specify mode of manufacture, so from the regulatory stand point there is no obstacle to avoid this type of operation. Even though there is no reason to dodge continuous manufacturing technologies, companies avoid this route as the process of interest must be relicensed and revalidated with bioequivalence studies. Continuous validation is still immature and has issues in terms of quality assurance/control and ambiguity between the regulators and companies for the definition of batch based on quantity (Lupis and Langer 2015; Walthe et al. 2015).

A strong investment is required to totally replace a traditional batch-wise purification process into a fully continuous manufacturing process. The cost of adapting the facilities and validation workload are the “real” costs involved in whether to do the technological shift or not. The use of a smaller unit operation volume in a continuous process would mean an annual capital cost of at least 10-fold lower (Hernandez 2015).

1.5 Chromatography

Chromatography is the name given to the group of separation methods based on the difference in rates of migration when sample components are passed through a stationary phase via a mobile phase. In traditional or packed bed liquid chromatographic techniques, the stationary phase is a solid phase packed into a tube and the mobile phase is a liquid containing the product of interest. Both phases enter in contact inside the tube, more commonly referred as a column, and if the stationary phase is able to retard in any way the product of interest or contaminant, it will migrate at a slower rate than the rest of the mobile phase and the components contained in it.

The product or contaminants can be recovered in different fraction pools based on time or volume injected to the column (Hansen, Pedersen-Bjergaard, and Rasmussen 2011). Specialized equipment/technology, such as a packing motor or system and a dedicated clean-in-place (CIP) system, is needed to run a chromatography purification run at an industrial scale as depicted in the diagram shown in Figure 1.2.

The composition of a mobile phase is changed during the separation run to alter the strength of interactions between the compounds of interest and the stationary phase, also known as resin or media. The consequence to this change in strength of interaction is elution of contaminants and target molecules at different time in particular order. The detection can be simple or sophisticated like using UV-based assays or Bradford assay (Hahn et al. 2016; Hammond and Kruger 1988). A chromatogram is generated from the run as absorbance against time or column columns (CV), protein concentration can be obtained by converting the absorbance at each given time. Table 1.1 presents the steps and a brief description of each of them that most typical chromatographic runs follow: equilibration, loading, washing, elution, strip and regeneration.

Table 1.1. Description of the conventional chromatography steps for a column separation for most chromatographic separations for analytical, preparative and industrial scale operations.

Step	Description
Equilibration	Compatible buffer with the resin and compound of interest is passed over the column. For 5 – 10 CVs.
Loading	Sample is loaded into the column usually with the same equilibration buffer.
Washing	The target molecule has been immobilized, all other components are washed with equilibration buffer or buffer containing components that disrupt any weak or unspecific interaction.
Elution	By changing the composition (ionic strength, pH, solubility or competing ligand) of the buffer the target molecule is eluted. The elution can be done as a gradient or a single step.
Strip	Any remaining proteins bound to the matrix are removed by increasing the strength of the elution buffer. This step does not revert the resin to its former capacity.
Regeneration	The resin is regenerated using a washing solution (compatible with the resin matrix) followed by equilibration buffer for further use. More than 2 CVs are recommended.

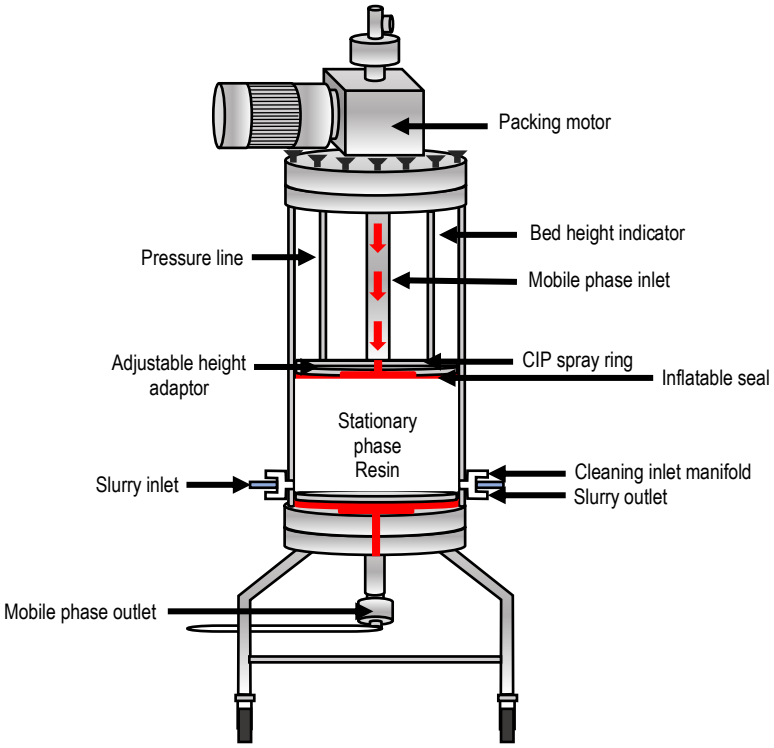

Figure 1.2. Schematic of common inlets, outlets and relevant parts of a conventional industrial chromatography column. Industrial columns cannot be easily packed and operated as analytical chromatography columns due to the size but the fundamental concepts still hold true. The column requires dedicated components and ports to achieve a high standard of cleaning and sterilisation.

1.5.1 Types of Chromatography

Chromatography has been classified by type of interaction between the stationary phase and the target molecule. There are several types depending on the mode of interaction between the matrix, ligand and target molecule, as seen in Table 1.2. Not all of the types are used regularly in industry, due to the intrinsic process limitations or cost of goods (COG) (Ersson, Rydén, and Janson 2011). There are two types of chromatography that have acquired relevance on the biopharmaceutical industry, especially in mAb production, in recent: ion exchange chromatography (IEC) and affinity chromatography (AC) (Bahadir 2013).

Table 1.2. Different types of liquid protein chromatography and the basis of its separation principle.

Separation Principle	Type of liquid protein chromatography
Antigenicity	Immunoadsorption
Biological Function	Affinity Chromatography
Carbohydrate Content	Lectin affinity chromatography
Charge	Ion exchange chromatography
Content of free –SH	Chemisorption
Hydrophobicity	Hydrophobic interaction chromatography Reversed phase chromatography
Isoelectric Point	Chromatofocusing
Metal Binding	Immobilized metal ion affinity chromatography
Size and Shape	Gel filtration/size exclusion chromatography
Others	Hydroxyapatite chromatography

1.5.2 Chromatography Resin

Chromatography resins (stationary phase) are also called matrix, gel, support or media. Resins are functionalized micro-particles used for separation in chromatographic techniques. The resin beads (sizes ranging from 30 to 200 µm) are properly packed into a column (diameters of up to 2 m) in order to achieve the separation, as depicted in Figure 1.3. The micro-particles, or beads, are created from different materials and can be functionalized for the desired purposes. Each resin possesses unique properties that can be exploited or taken into consideration when defining the separation methods. Table 1.3 has general information about the most common chromatography resins in the biochemical manufacturing and by no means it comprises all the different variations currently available in the market.

The properties of the resin will directly influence on the method used for the purification or the intended application and vice versa, changing any variable would impact the final purity and yield of the target molecule. Mechanical properties will affect the throughput and potential scale of manufacturing, as the resin needs to withstand relative high velocities and operating conditions in order to be a viable process. The resistance and rigidity are highly related to the maximum operating velocity as shear and pressure may damage the functionalized groups embedded on the surface of the beads and the physical structure of the bead. For example, rigid resins are able to withstand linear velocities of 2,000 cm/h while fragile resins only operate around 200

cm/h. Ligand type, density and distribution on the surface of the bead are related to binding capacity, selectivity and recovery (Pakiman et al. 2012; Hardin et al. 2009). Pore size and pore size distribution impact on binding capacity, as convective flow does not play a major role for the molecules to diffuse inside the bead. However, there is not an ideal pore size or ligand distribution as each product will require differential spatial arrangement (Wang et al. 2007). The resolution, product purity, removal of impurities and DBC can be influenced by bead size and ligand distribution. The bead size plays a major role as it determines the contact time between the bead and mobile phase in order to achieve total diffusion, void volume between beads increase as bead size and effective surface area increase, which in turn affects the number of ligands on it (Wu, Abraham, and Carta 2015). The smaller the beads, the better resolution and purification as total diffusion time decreases and effective contact area is increased. Chemical stability grants the resin resistance to certain compounds for operation, cleaning/storage and determines the lifespan of the material (Jiang et al. 2009). Finally, hydrophilicity and hydrophobicity properties might facilitate the recovery of the product and/or create an interaction with cleaning materials; as such agents can damage the resin backbone. Also, hydrophobicity can denature labile proteins with hydrophobic sections and makes the cleaning harder (Biosciences, 2001; Hagel, Jagschies and Sofer, 2008). The process scale, chosen throughput and target molecule will determine the type of chromatography media; however, extensive studies at different scales are required to reach the outcomes.

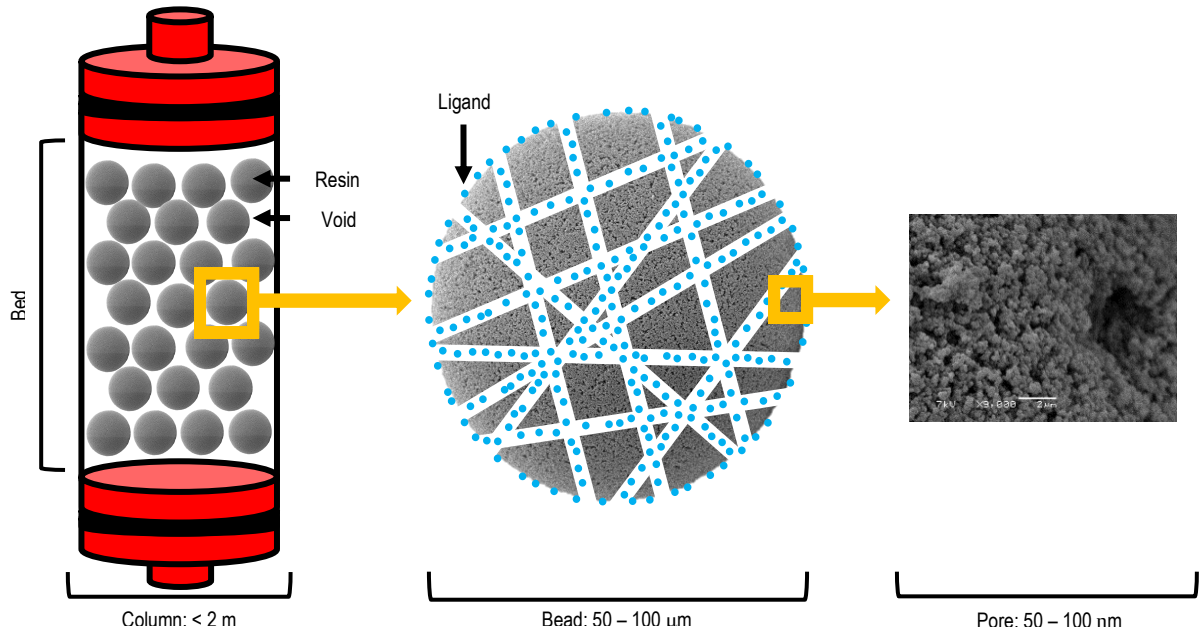

Figure 1.3. Diagram showing the comparison of scale between a large-scale column, resin bead and a SEM image of the surface of a Macro-Prep High Q ion exchange resin bead.

Table 1.3. Properties of different solid supports for chromatography protein separation (Lerche and Richter 1995; Gallagher 1987; *Downstream Column* 2020; Ioannidis 2009; Gustavsson and Son 2003; Elwinger 2017; *Purolite Life Sciences* 2021; Pakiman et al. 2012; Stone and Carta 2007; Boschetti 1994; Leonard 1997; Beneš, Horák, and Svec 2005; *Separation Science* 2021; Suda et al. 2009)**.**

Resin	Material	Properties
Agarose	D-galactose and 3,6-anhydro-Lgalactose repeating units extracted from red seaweed	High binding capacity due to the high porosity
		Non-fitted for heat sterilization
		Unstable on organic solvents and oxidizing conditions
		Nucleic acids and proteins may be adsorbed at high salt concentrations
		Swelling independent of pH
		Extensive hydrogen-bonding between the chains.
		Pore size depends on agarose content, frequently used from 2% (pore sizes of 70 and 150 nm) to 6% (pore sizes of 30 nm). Non-fitted for heat sterilization as the material turns into a gel-like substance at high temperatures.
		Average particle sizes range approximately from 20 to 100 µm. Some matrices can be bigger, depends on the application.
		Very stable under alkaline conditions.
		Soft material gives it flexibility but limitations under high pressures.
		Extremely hydrophilic, low unspecific binding.
Dextran	Cross-linked dextran chains	Dextran-grafted agarose or polyacrilamide chromatography matrices are usually used to improve flow properties and binding capacities.
		High flexibility.
		Poor flow properties due to the softness.
		High degree of hydrophilicity.
		Decreased exclusion limit, small pore sizes.
		Suitable at a wide range of pH (3 -13).
Methacrylate	Polymerizate from hydroxymethylmethacrylate and ethylendimethacrylate - among other variations	Internal porosity is much lower than agarose-based matrices, allowing access to biomolecules below 100 kDa.
		Suitable for smaller biomolecule purification such as peptides, small proteins and enzymes.
		Sizes from 30 to 200 µm.
		Compatible with most common CIP procedures used for agarose (1 M NaOH). Rigid nature capable of withstanding higher flow rates/higher pressures.
Silica	Silanol groups	Surface coating is required before using this media.
		Extremely rigid, perfect for high pressure processes/
		Porosity can vary similarly as agarose.
		Can resist biological solvents.
		Do not tolerate typical
		Very stable below pH 7 but not ideal for conditions above pH 7.

1.5.2.1 Agarose-based and Polymer-based Resins

Agarose-based resins are a common material used for biopharmaceutical manufacturing. Agarose is composed from a chain of repeating units of 1-3 linked β-D galactose and 1,4-linked 3,6-anhydro-α-L-galactose (Aoyagi 2001). The agar is extracted from red seaweed and processed into a dry powder form. The dry powder is solubilized above 85° C causing the chains to degrade. The viscous solution is cooled down and poured into a non-polar solvent with an emulsifier at specific stirring rates. The stirring rate is critical for determining the particle size (20 to 300 μm) and pore size distribution (Jungbauer 2005; Mu, Lyddiatt, and Pacek 2005). The beads are subsequently washed and cross-linked, affecting the overall pore size, rigidity and compressibility. Finally, the resin is functionalised with the desired ligand (proteins, aromatic groups, polar or non-polar groups) for its specific chromatographic separation (Ioannidis 2009; Keller, Friedmann, and Boxman 2001; Q. Z. Zhou et al. 2008).

Polymer beads are made from a variety of monomers polymerised in specific ratios, such as ethylene glycol dimethacrylate, hydroxyethylmethacrylate, poly(2-hydroxyethyl methacrylate, ethylene glycol dimethacrylate, styrene, glycidyl methacrylate, phenyl methacrylate, and 2,4,6-tribromo, 4-acetylphenyl acrylates, among others (Dowding and Vincent 2000). The manufacturing of the beads takes place in a bulk reactor with the monomer (organic phase) and the dispersant (aqueous phase). Monomer droplets are formed as the polymerization initiator and the aqueous phase are mixed (William 1951). The porosity and properties of the bead can be modified by modifying the stirring rates, UV stabilizers (aromatic ketones and esters), heat stabilizers (ethylene oxide derivatives), moulding lubricants and foaming agents (porogens) (Dowding and Vincent 2000).

The two main resin matrices that are used throughout the lifetime of this project were structurally made from agarose (Q Sepharose FF and Q Sepharose HP) and methacrylate (Macro-Prep High Q), due to their contrasting rigidity and literature concerning their use in CCTC.

1.5.2.2 Protein Adsorption

It is important to understand how the protein of interest gets transported onto and into the stationary phase in order to comprehend the behaviour and modelling of the binding kinetics. In chromatography, convective flow is what transports the mobile phase around the stationary phase, while diffusive flow dictates the rate in which the molecules transport through the film of liquid surrounding the bead, onto the surface of the matrix and finally into the absorbent pores (Ioannidis 2009). This means that there are mainly two phases during protein adsorption: mass transfer and diffusion driven kinetics. The mass transfer phase is the first and fastest of the two as the molecule of interest gets adsorbed on the superficial area of the bead. Diffusion is the second phase and happens at a slower rate as the diffusion rate of the molecule is independent from the mobile phase flow velocity. A full saturation of the chromatography media takes longer in larger beads. Smaller beads are more productive due to this but their use causes high pressures in the system. For this reason, a trade-off between size and pressure has to be made while designing any process.

Adsorption refers to the reversible adhesion dictated by the thermodynamics that occur between the target molecules and the ligand in the stationary phase. There are 4 main ways of interaction between the resin bead and the target molecule: external mass transfer through the film layer around the surface of the bead, diffusion through the surface, diffusion through the pore and reaction rate at the binding site of a ligand (A. Rathore and Kumar 2017), all of those interactions are shown the diagram in Figure 1.4. Protein adsorption has been studied and defined as a set of models known as the Equilibrium Models, with Langmuir being the most commonly reported of all (Mollerup 2008). The Langmuir isotherm model assumes the surface of the adsorbent is uniform, adsorbed molecules do not interact permanently, all adsorptions happen through the same mechanism and only one layer of adsorbent can occur on the surface (Poole 1995). However, protein adsorption modelling is still an evolving area due to difficult factors to take into account; i.e. protein denaturation, multiple interactions, protein asymmetry, cooperative effects, changing protein tertiary structure during adsorption, aggregation, etc. (Rabe, Verdes, and Seeger 2011). The model has been used to explore individual or single features during a chromatographic operation but a

multicomponent analysis has been done before (Guélat et al. 2012; Müller-Späth et al. 2011).

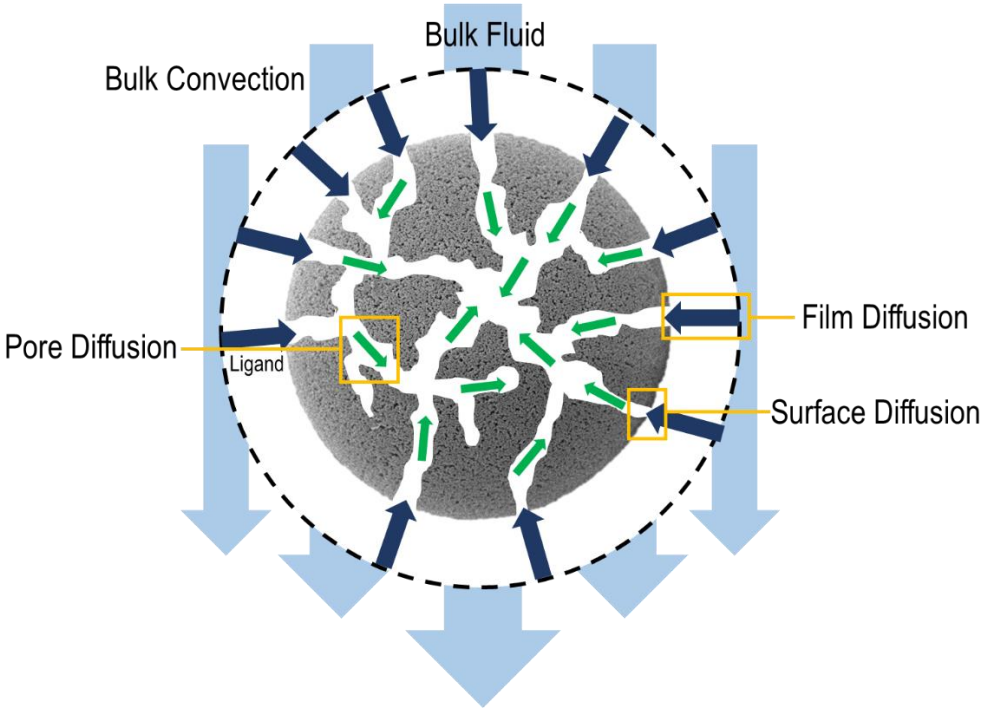

Figure 1.4. Schematic showing the different diffusion paths the target molecule needs to go through in order to interact with the ligands on and inside the matrix. Film, surface and pore diffusion dictate the reaction rate (adsorption and desorption kinetics) between the ligand on the surface and the target molecule.

1.5.3 Chromatography Process Economics

Up-to-date and undisclosed DSP manufacturing costs for therapeutic products are not detailed, incomplete or specific for any significant information. This accentuates the DSP bottleneck problem as there is no reliable comparison between unit operations and whole manufacturing lines. Nevertheless, the company Intelligen Inc. has created simulation using SuperPro Designer software. The calculations for the modelling included one batch of 10,000 L containing 50 kg of mAb (5 g/L), a predicted titre from trends in USP. For DSP, three chromatographic columns of 20 cm of MabSelect Sure (protein A), Capto S (cation exchange) and Capto Q (anion exchange) were considered. It is calculated that for any of the columns that the cost for buffers is $2 per litre and the labour cost is at $69 per hour with two shifts per day. For optimized

and modern facilities, a number of 4 operators are needed per shift. A total cost of $12,138 per kg is required only for operating the DSP manufacturing line for a total of 2 days (4 shifts or 26 hours) per batch with a yield of 79% (39 kg out of 50 kg in cell culture). The cost includes primary recovery, virus inactivation, formulation and the three chromatography steps already mentioned (Petrides et al. 2014), without including USP and further down the line costs such as transport and storage.

The matrix used for chromatographic techniques usually represents around 30% to 60% of the total DSP costs. In this simulation, Protein A chromatography contribute with 68% in the past and 43% (while combining different resins in different columns) of the total DSP cost (Petrides et al. 2014). Resin costs can be distributed by the number of cycles a packed bed can be used which makes the use of more expensive and sophisticated resins a viable option; i.e. if the process requires 4 processing cycles and the lifetime is assumed to be 200 cycles, the batch cost for the resin would be adjusted to 1/50 of the total purchase. AC has appropriated the majority of the costs while at the same time reducing them from $37,442 to $10,964 and decreasing the DSP process time by 300% (110 to 35 hours) (Farid, 2007; Hagel, Jagschies and Sofer, 2008). However, the time/cost reductions can be attributed to improved matrices and ligands rather than an improvement to the chromatography technique itself, as resins are still being underutilized by the intrinsic characteristics of the batch-column configuration.

Chromatography costs are inversely proportional to the increase of product titre, unlike USP costs. The issue does not disappear by having better resin materials, it only mitigates one aspect of the core problem and in the end, forces companies to search for alternative separation methods when it is too late or expensive to do so. The chromatography method used in industry is where the problem resides and feasible solution can always be found. For this reason, there has been a continuous push towards a cheaper chromatography technology or an alternative for industrial application.

1.6 Continuous Chromatography

The concept of continuous chromatography was developed to replace the dominance of traditional batch chromatography in primary capture and polishing steps. It represents a partial solution regarding the DSP bottleneck. Generally speaking, continuous chromatography offers several advantages: better quality control, lower capital cost, lower equipment footprint, enhanced flexibility in manufacturing (Dutta, Tan, Napadensky, Zydney, et al. 2016a). Even though a different number of approaches have been created only a few methods have reached large-scale commercial protein purification.

Continuous chromatography follows the basic principles (stationary and mobile phase, as well as all chromatography steps) explained for traditional batch column chromatography. The difference between these two general groups is the configuration/design of the column or columns. However, not all continuous chromatography processes are actually truly continuous, most of them work as a semi-continuous process.

1.6.1 Continuous Chromatography Potential

It has been noted that preparative chromatography is the single largest cost centred in DSP, around 60% to 80% of total production cost (about 50% only on chromatography media for all chromatography steps) due to rigorous regulations and expensive materials (as discussed before), making the process optimization a priority for the whole production (Crommelin, Sindelar, and Meibohm 2016). Even though chromatography processes are one of the most powerful and more reliable methods for biopharmaceutical analysis and purification, traditional methods start showing significant constraints on productivity, cost and performance when translated into production setting (Godawat et al. 2012). These new trends and optimisations are relatively new to the industry but there are some examples on Section 1.7 that justifies the switch between traditional to continuous methods.

The “DSP bottleneck” is not only caused by the high titres from USP, it is also attributed to inability of DSP equipment to cope with other continuous unit operations (Amit K. Dutta *et al.*, 2016). Despite the limitations of batch chromatography, this mode of operation will remain strong compared to continuous techniques like Simulated Moving Bed (SMB) and Periodic Counter-Current Chromatography (PCC) because they are not economically and technologically mature for the integration in most of the current biopharmaceutical processes (Langer 2014). Nevertheless, PCC chromatography has been successfully coupled for mAb capture with a perfusion bioreactor. The continuous system is able to couple with volumes 5X larger than batch mode techniques, while obtaining same critical quality attributes (CQA), purities and yields. In addition, this format allowed a resin utilization of almost 300% compared to traditional packed-bed methods; hence, reducing buffer usage while achieving an improved productivity (Godawat et al. 2012).

Batch chromatography, as any other batch process, suffers from equipment costs, low productivity, low flexibility and unsteady product quality (Zydney 2016). Productivity for chromatographic operations is defined as the product per volume of total resin and total cycle time, such definition raises the importance of decreasing the cycle time and increase resin utilization. In engineering and economic terms, the final objective is maintaining or improving the productivity by minimizing the amount of resin and time taken for production.

The primary capture systems typically work in batch-mode in large stainless-steel columns with each phase occurring one after another. The process has proven to be optimized on terms of scalability and practicality rather than efficiency and productivity. Hence, the resin is under-used (loss of capacity) due to incomplete loading that is brought by the fear of early product breakthrough. This avoids yield loss but directly affects the resin usage and time invested in the loading stage. As mentioned before Protein A and ion exchange resins are the most expensive aspect in the purification, as a consequence a total use of binding capacity is mandatory for these methods (Amit K. Dutta *et al.*, 2016).; i.e. a single column volume (CV) of Protein A resin can cost $15 million, without counting buffers or facilities (Shukla et al. 2007; Hober, Nord, and Linhult 2007; Kelley 2007). Also, the innate mechanism of loading, washing, eluting and cleaning steps leave a part of the column in an idle state (Longer 2010). This

brings poor productivities in batch-mode of 5 to 15 g/L/h if compared with productivities of 73 g/Lh (96% yield) when using CCTC (Amit K. Dutta *et al.*, 2016).

In addition to cost, the replacement of batch chromatography has the potential of increasing the quality through enhanced online control and uniformity on the microenvironment within the columns, as well as eliminating long holding times before and during the processes. Some processes have a long holding time before subsequent DSP, while others are processed instantly. There is evidence of variability in glycosylation profiles, deamination and degradation due to these long holding times (Pacis et al. 2011; Jiang et al. 2009). Also, protein aggregation and denaturation can occur if the peptide is adsorbed for long periods of time to the resin. This is a problem for batch systems as the column environment is heterogeneous; the proteins at the top remain attached for more than 30 min while the ones at the bottom are bound for a less amount of time. While in continuous systems, proteins remain bound to the resin for less amount of time due to the smaller processing volumes and reduced idle times. For example, Continuous Annular Chromatography (CAC) only keeps the necessary contact time between resin and protein before continuing to the next step (Guo and Carta 2015).

Continuous chromatography is an area relatively new to the industry but it is indeed an emergent technique that sooner or later will replace the traditional way of biomolecule purification due to its obvious process and economic advantages. Further research will make these types of technology rise above established techniques and gain trust from the research and also manufacturing companies.

1.7 Continuous Chromatography vs. Batch Chromatography

The increase in demand requires a larger production of the target molecule in the USP and DSP capabilities with their own unique problems (Gronemeyer, Ditz, and Strube 2014). Until 2014, 47 mAbs had already been approved in United States of America and Europe, with no signs of decreasing the rate of approvals. From 2004 to 2013, the global sales for mAbs from $39 to $ 75 billion which was significant compared to other recombinant protein therapeutics. It is estimated under this growth increase rate that

by 2024 that number will reach $140 billion. (James 2016; Ecker, Jones, and Levine 2015). It is only logical that the industry will strive to replace old technologies with newer ones that would satisfy this relatively new boom in demand. Chromatography is not an exception, as mentioned before, it is a sensible and crucial process step in terms of quality and also COGs.

Batch chromatography has been the staple of excellence for the purification of molecules in the biopharmaceutical market. However, continuous production of mAbs becomes an increasingly attractive alternative as the demand is still growing (Yang, Qadan, and Ierapetritou 2019). Process intensification has always been a recurring drive for innovation in any processing step. Continuous chromatography offers the ability to respond to a variable market demand (Arnold 2018). CCTC is not commercially available so it is hard to convey an idea of its impact in the market but there are instances where continuous chromatography techniques have been used for biopharmaceutical processes. A multicolumn chromatography approach has been used for mAb purification. Figure 1.5 shows some multicolumn techniques which are being used in industry at the moment. This multicolumn technique uses less than 60% to 70% of total chromatography media. Batch chromatography usually underutilises resin inside the column as the liquid is injected from the top while the bottom part of the column remains idle for long times in every step. A multicolumn step would minimise this idle zones by keeping the column length relatively short compared to a batch process. CCTC eliminates this completely as all resin beads are in contact with the buffer or solvent at all times, having no idle times. On top of that, a continuous chromatography would reduce the product loss as the breakthrough is fed into a second or third column (increased yields).

An analysis with different columns was done in order to demonstrate the cost savings potential of the using a continuous purification step. A 2,000 L batch with a product titer of 5 g/L of mAb was processed in batch mode using a column with 20 cm height and 60 cm diameter and in continuous mode using either four columns with a height of 10 cm and a 30 cm diameter or 3 columns with a 10 cm height and a 20 cm diameter. For the batch, 57 L of sorbent and six cycles requiring 6,100 L of buffer gave a productivity of 20 g/L of sorbent/h. The continuous process with the larger columns processed everything in 8 cycles while using 28 L of sorbent, 4,000 L of buffer with productivities of 60 g/L of sorbent/h. The smaller continuous columns would process

everything with only 9 L of media and 4,200 L of buffer. Assuming a cost of $12,000 per L of solvent, the batch process would cost $650,000 compared to $340,000 and $100,000 for the continuous counterparts (2X to 6X times cheaper). This first example shows the tremendous potential of continuous processes, resin utilisation is maximised and resin volume is minimised. A second example, a batch of 15,000 L with a mAb titre of 5 g/L was purified using a column 20 cm high and 1.8 m in diameter, while the continuous process purified the same lot with 4 columns 10 cm high and 30 cm in diameter. The buffer consumption was reduced from 509 to 28 L. Even if the processing time doubled from 24 to 40 h, the productivity increased from 5 to 56 g/L of media/h and the costs got reduced 20X ($6 billion to $300,000). It seems that even if there are larger cycle times, the productivity and cost decreases with a continuous system. Final example, a bioprocess fluid with a mAb titre of 4.3 g/L was purified in batch and continuous mode. The batch mode was done using a column 20 cm high and a 14 cm diameter requiring 3.1 of Protein A chromatography media ($37,000) and 200 L of buffer, while the continuous technique used 4 columns with a 5 cm height and 4.4 cm diameter, requiring 300 mL of Protein A chromatography media ($3,600) and 100 L of buffer. The batch process completed everything in 6 h with a final productivity of 12 g/L of media/h and the continuous process managed to purify everything in 11 h and a final productivity of 60 g/L of media/h (Arnold 2018). As seen from the examples, the productivity is significantly increased while the chromatography media and buffer costs decrease substantially due to the smaller nature of the continuous techniques (CCTC has the same characteristics as the continuous processes mentioned but the buffer consumption one). The only drawback was the increased higher cycle times but this can be mitigated by using chromatography media that could withstand optimum conditions at smaller column diameters/heights.

Chromatography is an expensive process step as the quality of the product in the DSP line heavily relies on its properly execution. Batch chromatography has proven to be the ruler for a long time; nevertheless, it does not mean batch processing is the future. Technological advancements and creative techniques (CCTC) are coming to the public eye with high potential.

1.8 Types of Column-based Continuous Chromatography

The simplest way of performing continuous chromatography is usually by loading, eluting and regenerating different columns in sequence or parallel (Jungbauer 2013; 1993). However, the diverse combination of columns and unusual ways of operation allows several continuous or pseudo-continuous modes to be developed. In general terms, almost all continuous chromatography techniques bring relatively the same advantages but each of them has a different purpose or context of use in mind.

1.8.1 Flow-Through Chromatography

Flow-through chromatography parallel column system is done in batch mode. The operation is simple; one column remains idle while the other is being used upon near saturation, at which point the columns are then switched. This is usually done with a single use monolithic and membrane columns (Etzel and Riordan 2009; Weaver et al. 2013).

1.8.2 Periodic Counter-current Chromatography

Created by GE, PCC utilizes multiple packed columns to create a semi-continuous (periodic) operation. PCC yields a periodic product concentration, starting with a high concentration to a really diluted stream at the end of the cycle. This is a problem for quality control and subsequent concentration steps, as well as a possible loss of product because of long binding time (Zydney 2016).

The system consists of multiple columns, traditionally 3, that switch between load, wash, elution and regeneration steps cyclically (Figure 1.5A). In the first stage, Column 1 is loaded with cell-clarified fluid (CCF) while the other two columns remain idle. During the second stage, Column 1 reaches saturation and the breakthrough is loaded into Column 2. For the third, stage, Column 1 is washed and the solution is loaded to

Column 3 to capture any unbound material, while Column 2 Is loaded with fresh CCF. Finally, Column 1 is eluted and regenerated, Column 2 reaches saturation point and the breakthrough is loaded to Column 3 (Zydney 2016). The cycle repeats indefinitely. This unit operation can be done using more than 3 columns to relax time constraints. The limitation or requirement is that the loading step has to take greater or equal amount of time than all the other steps combined.

1.8.3 Simulated Moving Bed Chromatography

SMB is a multicolumn cyclic separation of a binary mixture (product variants or oligomers). This technique is derived from the true moving bed (TMB) technique, where both, the mobile and stationary phase, are flowing through the system (Aniceto and Silva 2014). The biggest drawback is the complexity of the pumps and valves to make the whole system work. For example, this technique has been implemented at large-scale manufacturing for the separation of enantiomers and fructo-oligosaccharides (Vaňková et al. 2008; Rajendran, Paredes, and Mazzotti 2009).

A traditional 4-column configuration is used (Figure 1.5C) where only the mobile phase flows through the columns. First, feed material is loaded into Column 1 and both components migrate through the column. The weakest molecule bound is recovered at the end of Column 1. Then, between Column 2 and 3 additional buffers are added. Finally, most of the product is recovered in Column 3 and the rest is loaded to column 1. This simulated bed is only possible if the loading time is greater than all the other steps (Aniceto and Silva 2014; Zydney 2016).

1.8.4 Continuous Annular Chromatography

CAC is the only established method that gives truly continuous separation using a rotating column. It takes place in between the annular space of two rotating concentric cylinders. The design and column packing are more complicated because of its unique shape. The configuration of the column has been used for the purification of Factor

VIII coupled with a perfusion reactor while using an anion exchange resin (Vogel et al. 2002). However, this type of chromatography has not reached the large-scale purification process (Zydney 2016; Jungbauer 2013).

The operation mode does not vary from regular chromatography, but the rotation introduces a second principle of separation (Figure 1.5B). The feed is continuously introduced at a fixed point at the top while the products and contaminants are also collected at a fixed point at the bottom. The separation works under isocratic operation parameters. The column is rotated, while all inlets and outlets are kept stationary. In essence, the system works as a carousel of infinite number of columns moving in a circular manner while each chromatographic step happens at a determined point of the way.

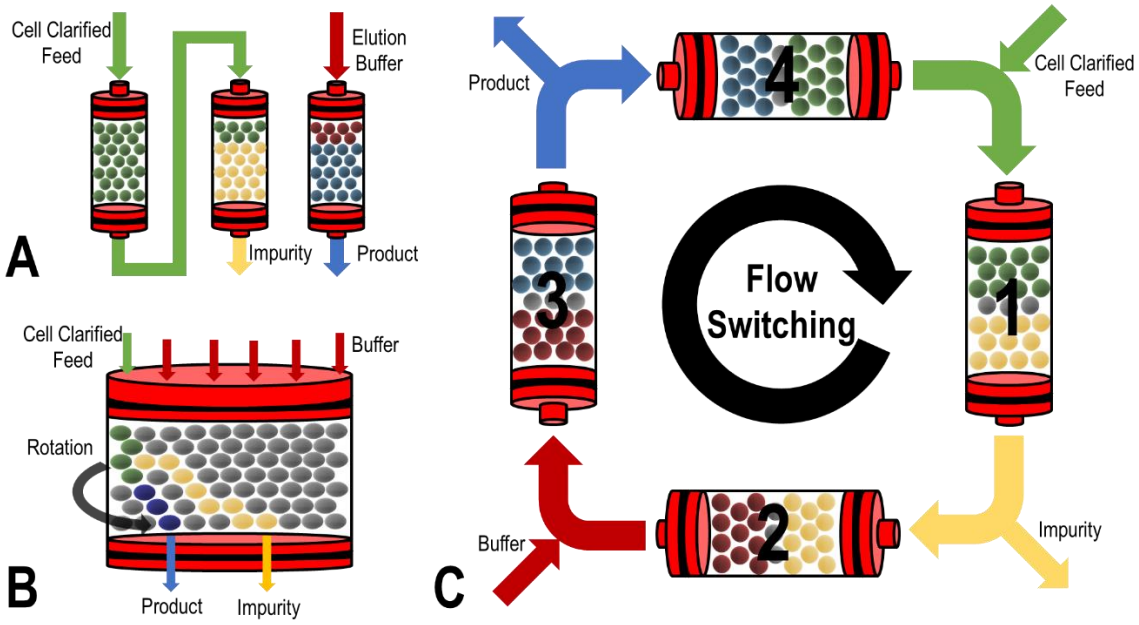

Figure 1.5. Operational schematics indicating buffer and feed inlets and outlets for different continuous chromatography techniques. A) 3-column PCC system; a set of interconnected columns operating in parallel. B) CAC column; a rotating column with fixed buffer inlets and harvesting outlets. C) 4-column SMB system; a set of synchronised and interconnected columns with a complex valve system switching in charge of switching inlets and outlet streams.

1.9 Non-column Chromatography

There is a current interest on using chromatographic resin in non-column techniques, usually in combination with membrane filters to separate the mobile phase. There have

been some efforts for creating a solid and pragmatic technique for manufacturing. However, there has not been a method that has remained as the staple for preparative or analytic techniques due to the lack of understanding, technology and dominance of traditional chromatography.

1.9.1 Continuous Counter-current Tangential Chromatography

Chromatan Corp. developed a new technology for protein purification termed CCTC. This system consists of static mixers and hollow fibre modules instead of a single or a set of columns. The system works by making the stationary phase flow as slurry through all chromatography steps (binds, wash, elute, strip and regeneration/clean). The micro-porous membrane filter inside the hollow fibre functions as a type of “column” that separates the resin and large particles in the system and allow the extraction of target proteins and contaminants through it. The steps can be performed in 1, 2 or 3 stages. These stages determine the total process yield of 85%, 95% and 98%, respectively. The whole system allows a truly steady state, continuous operation with continuous and stable product concentration. This technique has been proven to work with Macro Prep 25Q (ion exchange resin) and POROS MabCapture Protein A (affinity resin) with a slurry concentration of 10% (inside the static mixer) and 40% (end of hollow fibre) at flow rates of 100 and 25 mL/min, respectively (Shinkazh *et al.*, 2011; Napadensky *et al.*, 2013a; Amit K. Dutta *et al.*, 2015, 2016; Dutta *et al.*, 2017).

This technique has several advantages over column packing and batch processes. The static mixers and hollow fibres are much less expensive than stainless steel columns and have the possibility to be designed as a fully disposable flow path, reducing the validation stages, risk of contamination or equipment damage. It is plausible to couple this system with perfusion reactors or similar in its kind due to the truly continuous nature of CCTC. The use of static mixers gives uniform and low pressure drops without any energy input compared to stirred tanks that may have inefficient mixing dynamics, with considerable energy requirements. There is no evidence of protein degradation or aggregation in the fluid flowing through the system but this needs to be monitored thoroughly utilizing different parameters and target

molecules. The product obtained is eluted at a constant concentration due to the uniform residence time (RT). This multistage step process allows for high recovery and purity, while maximizing resin utilization and allowing buffer recycling in some steps such as cleaning, wash and strip steps. The productivity of the whole process increases as the resin is in non-stop use at every single point in the system. The average reported productivity is about 42 g/Lh while conventional column-based chromatograph has 5 to 8 g/Lh. There is still space for improvement by different type resin beads and size of the static mixers and membrane configurations, as well as piping design. It is believed that the productivity can reach up to 100 to 190 g/Lh for mAb purification with the adequate resin type and bead size (Napadensky et al. 2013a; Dutta et al. 2015a; Dutta, Tan, Napadensky, and Zydney 2016).

CCTC does not occur inside a column, it needs multiple sets of static mixers and hollow fibres working at the same flow rate in order to achieve a successful separation. Figure 1.6 depicts a simplified diagram of a CCTC system, it shows the inputs and outputs of each step; as well as the connection among the chromatographic steps. Figure 1.7 shows the same diagram but expanding upon it by adding the mixing modules (static mixers) and solid/liquid separation modules (hollow fibres) for each of the steps. In both diagrams, the resin slurry is recirculated from the last step (equilibration) into the first one (binding).

The operation of the whole system (Figure 1.6 and 1.7) can be exemplified with one step and its 3 stages (Figure 1.8). The stationary phase starts flowing from a hold up tank if operated in batch-mode or previous step to the first stage if operated as a complete CCTC system. First, the resin is diluted with the mobile phase (permeate) of the next stage and enter the static mixer that is designed to give enough RT for a successful bind, wash or elution. Then, the diluted slurry travels to the hollow fibre where it is concentrated and contaminants or products are separated and harvested. The concentrated slurry flows from the hollow fibre into the second stage where everything starts again with the exception that the mobile phase (permeate) is not harvested but recirculated into the previous stage. The product or waste collection is always made in the first stage, while the fresh feed and buffers are introduced in the last stage. The stationary phase flows from stage-1 to stage-3 while the mobile phase flows from stage-3 to stage-1, giving the system its counter-current nature.

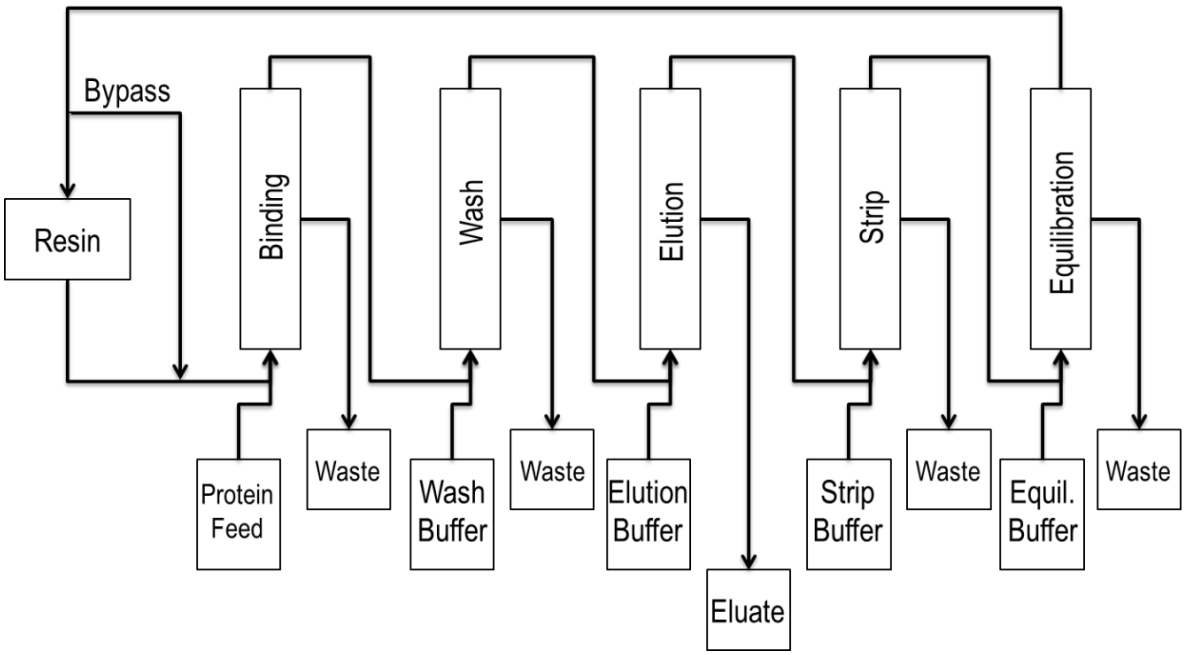

Figure 1.6. Diagram of a simplified CCTC system including all chromatography steps. The system is in total recirculation through a bypass valve before the resin reservoir. The diagram shows the individual steps with their respective feed, buffer and waste inlets and outlets. Each of the steps includes a set of mixing and solid/liquid separation modules (not shown).

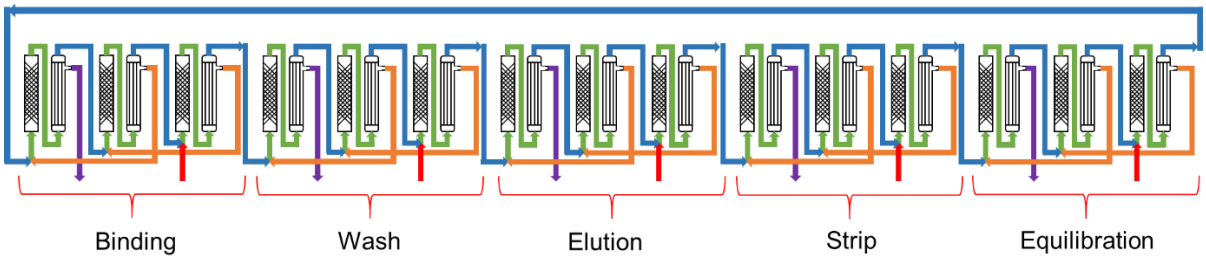

Figure 1.7. Diagram of complete 3-stage CCTC system. The system is in total recirculation through a bypass valve before the resin reservoir (not shown). The diagram shows each individual step with its three sets of mixing modules and solid/liquid separation modules. Each step has its independent inlet and outlet streams. The streams are depicted in different colours: concentrated resin slurry (blue), diluted resin slurry (green), counter-current permeate (orange), outlet stream (purple) and inlet stream (red).

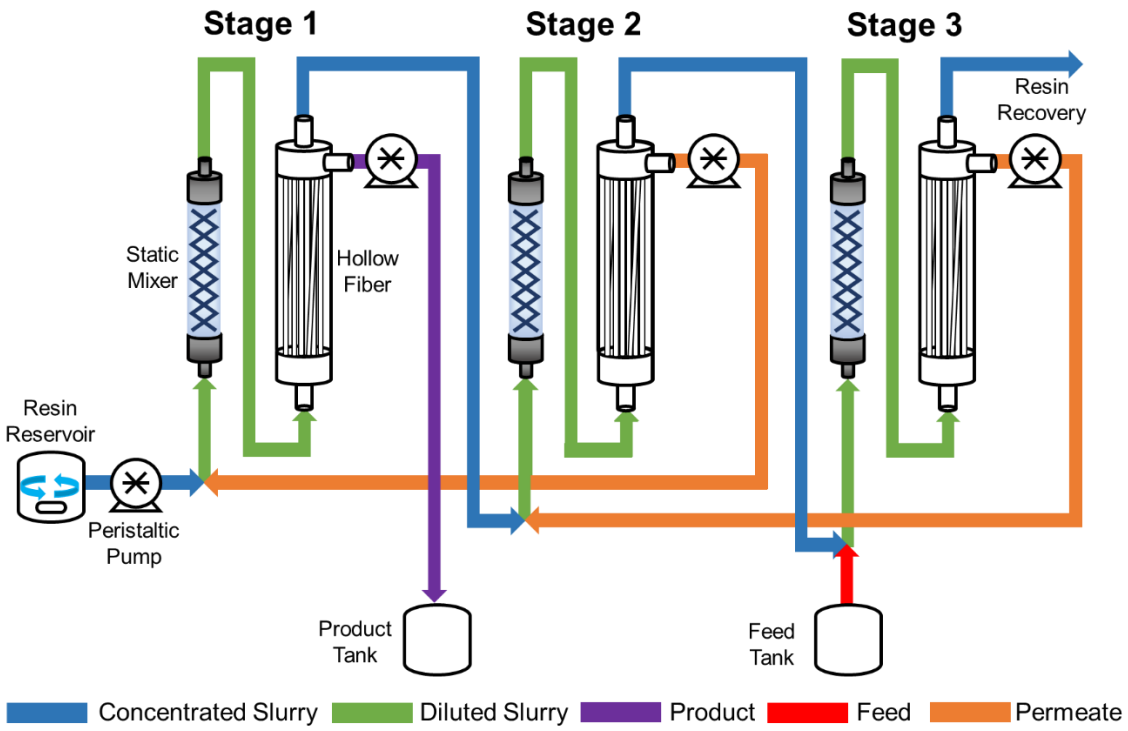

Figure 1.8. Flow map of a typical 3-stage CCTC system. The diagram is made from a set of mixing modules (static mixers) and solid/liquid separation modules (hollow fibres) in a counter-current manner. The resin slurry enters in stage-1 and is recovered in stage-3, while the feed/buffer is fed in stage-3 and subsequently, removed in stage-1. The resin slurry gets diluted and concentrated throughout the whole run. The static mixers provide the necessary residence time for any necessary reaction to occur, whilst the hollow fibre concentrate the resin slurry for the next stage and separate the free molecules in the slurry in order to be fed into the previous stage or collected out of the system.

1.9.1.1 Mixing Module

The current CCTC design utilizes a series of PVC static mixers. It is currently the only reported mode of in-line mixing. Though, a second option known as CFIR was explored in Chapter 6 as a viable replacement.

1.9.1.2 Static Mixer

A static mixer is a device used for continuous mixing, without any moving materials or energy consumption. It consists of a cylindrical or square housing filled with non-mobile mixing elements, as shown in Figure 1.9 (Paul, Atiemo-Obeng, and Kresta

2004). The number and design of elements vary from liquid and manufacturer. Static mixers are often utilized when the liquid is extremely viscous or when excessive/aggressive mixing is prohibited, especially for shear sensitive biological material. The main mixing effect comes from the introduction of chaotic mixing with repetitive non-mobile mixing elements that fold, stretch and create vortices in the liquid while it is flowing. The ultimate goal of the static mixer is to create axial and radial homogeneity at low costs and higher efficiency (Bertsch et al. 2001). The inclusion of a large series of static mixers into the flow path may cause a significant pressure drop in the entire system (Mathys, Schaetti, and Mandic 2004). However, no significant pressure drops have been reported in CCTC.

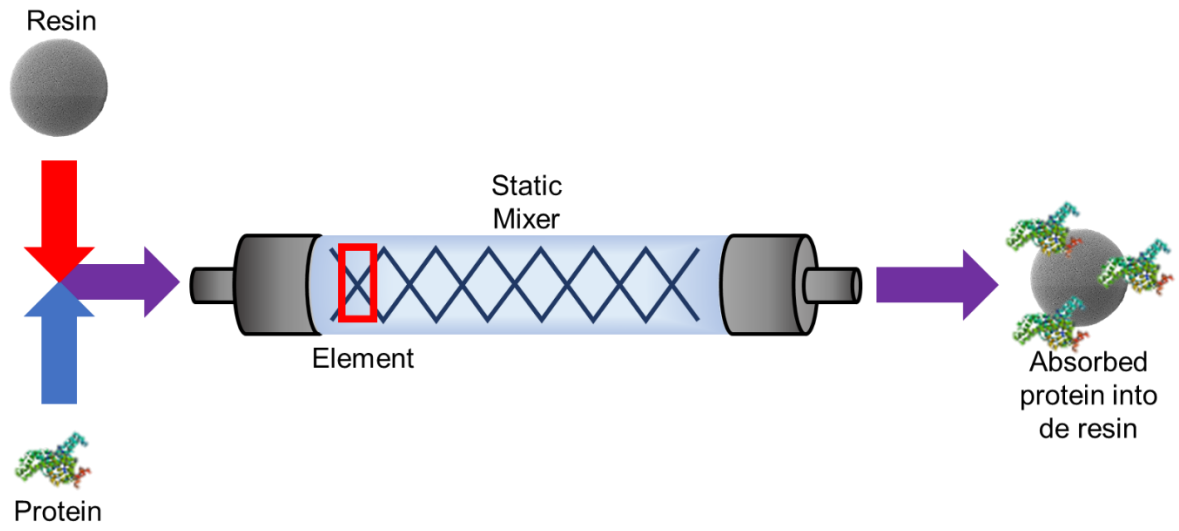

Figure 1.9. Diagram of the static mixer and its function in the binding step for CCTC. The resin slurry and protein feed are pumped into the inlet of the mixer. The elements inside and the dimensions (length and diameter) of the tube provide enough convective mixing to enhance the axial and radial homogeneity. Depending of the static mixer, it may cause a significant pressure drop.

1.9.1.3 Coiled Flow Inverter Reactor

A typical CFIR is a mixing reactor made mainly by helical coils that are bent at equidistant 90° angles, as shown in Figure 1.10 (Saxena and Nigam 1984). The helical/coiled structure of the tubes induces a secondary flow pattern known as Dean vortices. These Dean vortices are the main driving force of the mixing inside the CFIR

and are dependent on the flow velocity or the Reynolds number (N_{Re}), which is dependent on itself on the geometry of the tube, the flow rate and the liquid itself. At low Dean numbers (De), the secondary flows are weak and diffusion is mainly controlling the lateral mixing inside the tube. On the other hand, as the De increases the convective forces start to take control of the mixing, substantial when diffusion is the limiting factor mainly (Mridha and Nigam 2008). Mixing can be further enhanced by introducing some chaos in the fluid through a finite number of inversions to the helical coil (Saxena and Nigam 1984). Axial dispersion in helical coil reactor (HCR) with inversions was registered to be at least 20% less compared to simple HCRs. The chaotic mixing also helped to achieve close plug-flow regimes, as it decreases the acceleration in the central part and increases it near the wall at N_{Re} as low as 30 to 270 (Mridha and Nigam 2008).

CFIR are typically used to decrease the residence time distribution (RTD) in laminar flow regimes; hence, reducing the use of resources and enhancing the efficiency of the whole production line. Since most of the biochemical manufacturing unit operations are ran in laminar flow regime, such as precipitation of impurities or viral inactivation, CFIR is an ideal candidate as an alternate mixing process (Kateja *et al.*, 2016; David *et al.*, 2019). However, it has never been used for any adsorption or desorption chromatographic process in the past as non-column chromatography is still an emergent term for research and biomanufacturing.

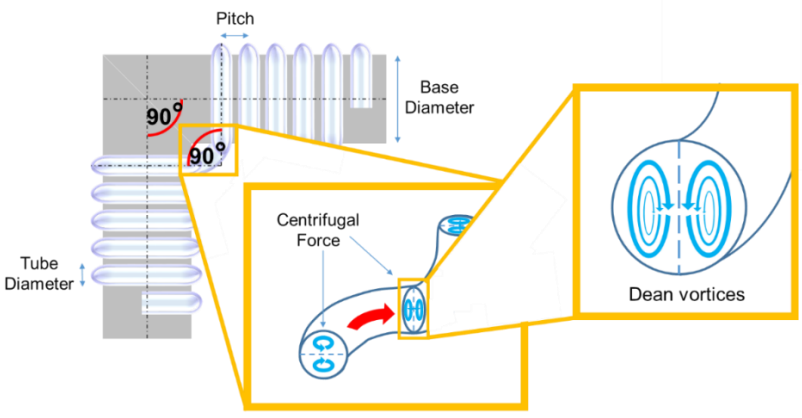

Figure 1.10. Diagram of the different parts of the CFIR. A) CFIR coil (grey) surrounded by helical coils (light blue), the helical coil has an inversion of 90° which causes an interchange between the streamlines participating in Dean vortex flow. B) Zoom in showing the two parallel Dean vortices between themselves and perpendicular to the wall of the tube inside the helical coil through the inversion. C) Dean vortices and its direction inside the helical coil caused by the centrifugal forces and flow inversion.

1.9.1.4 Solid/Liquid Separation Module: Hollow Fibre

A membrane is defined as a semi-permeable selective barrier that only allows the transport of one or more species while retaining or hindering the transport of others. The hindering/impediment of these species cause an accumulation at the upstream of the membrane surface known as concentration polarization (Chen, Li, and Elimelech 2004). The concentration polarization generates a diffusive transport down the concentration gradient and back into the bulk solution. At steady state this concentration-driven transport matches the transport associated with the pressure-driven filtration. If the latter is significantly greater, it will lead to the formation of a deposit (cake) that will provide an additional resistance to flow. Figure 1.11 displays the schematic of a hollow fibre focusing on the hollow fibre, the fibres themselves and the separation of protein and resin through the fibre.

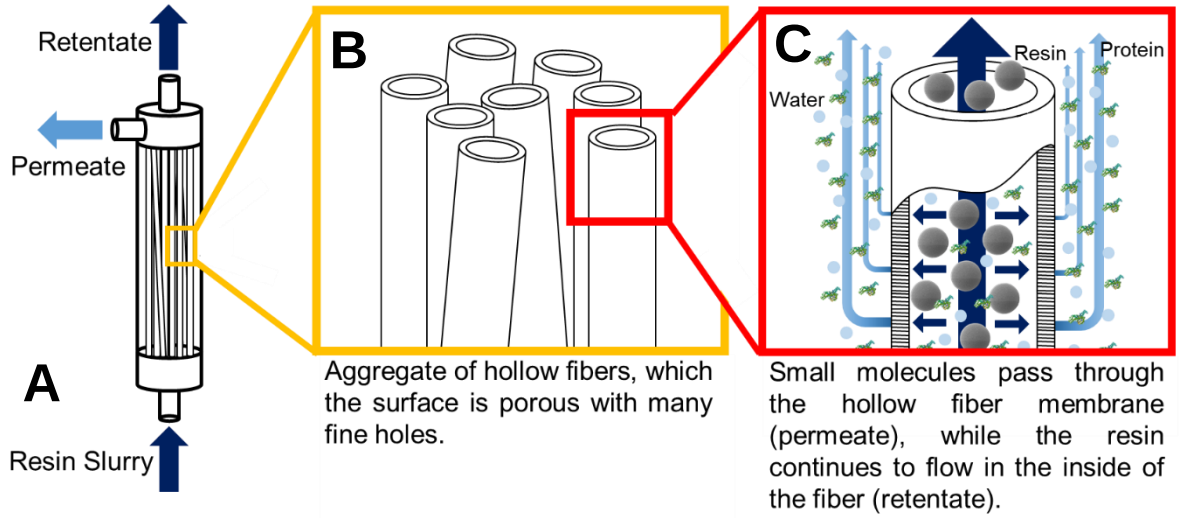

Figure 1.11. Schematic of A) hollow fibre inlets and outlets, B) individual fibres inside the cylinder and C) diagram of the crossflow filtration of resin slurry and the target molecule during the elution step. The resin beads are retained in the inside of the fibre and exit through the retentate (dark blue) while the target and buffer molecules are capable of crossing the selective membrane into the lumen of the hollow fibre and subsequently into the permeate (light blue). This recovery of the resin slurry allows the CCTC system to be a truly continuous chromatography process operation.

1.9.1.5 Membrane Fouling

The term membrane fouling refers to the alteration in membrane properties through the course of time and it can be caused by adsorption, pore blockage, pore constriction, deposit formation and gel formation (Bacchin, Aimar, and Field 2006). Figure 1.12 shows a diagram with all the possible fouling scenarios: adsorption, blocking and deposit formation.

Adsorptive fouling refers to the attractive forces between the membrane material and the particle species, causing the particles to block or reduce the pore diameter. It is relevant for protein and surfactants with hydrophobic membrane materials but insignificant for large particles as shear forces usually overcome this type of fouling. Pore blockage is when a particle physically blocks the entrance or pathway within the pore. It is problematic when dealing with small particles with similar sizes to the ones of the pore. Deposit formation is described as the accumulation of several layers of particles on the external surface of the membrane. The deposit will hinder effective lumen size, increasing the pressure gradient required for the filtration. Finally, gel formation is the formation of a gel layer on the surface of the membrane. This fouling mechanism is common with macromolecules like proteins at very high concentrations, exceeding their solubility limit (Bacchin, Aimar, and Field 2006; Belfort, Davis, and Zydney 1994).

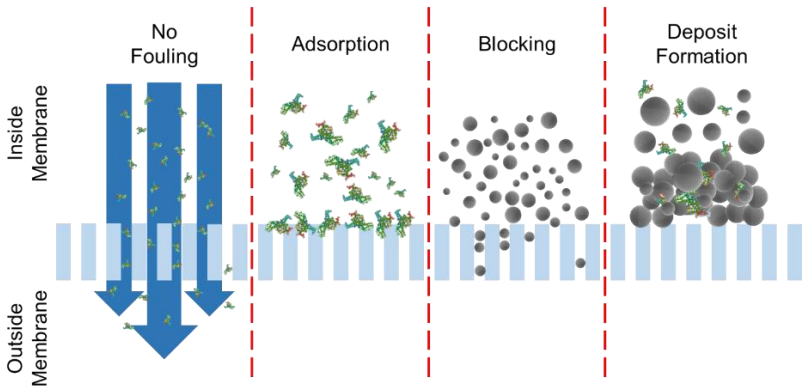

Figure 1.12. Schematic of the different types of fouling on a membrane: adsorption, blocking and deposit formation. Adsorption is the normal flow of particles without any obstruction or fouling. Adsorption is the interaction and adsorption between the membrane material molecules and any molecule partially or completely obstructing the pores. Blocking is the partial or completely physical impediment of flow through the pores. Deposit formation refers to the accumulation of material (cake) on top of the membrane pores.

1.9.1.6 Critical Flux

Critical flux is defined as the permeate flux under which no fouling with time is observed. An increase in flux will cause an irreversible deposit (fouling) to the system, typically seen by a continuous increase in transmembrane pressure (TMP) during constant flux. There are a variety of models to predict the critical flux for particle suspensions in membrane processes. For this project, the shear-induced diffusion model was used for the characterization of the hollow fibre module, however it is important to notice that other models exist such as: Brownian diffusion, surface interaction, and lateral migration.

1.9.1.7 Brownian Diffusion Model

The Brownian diffusion model assumes that the hindering of the filtrate flux is due to the formation of an accumulated layer of highly concentrated particles on the surface of the membrane. The thickness of the accumulated layer depends by the balance between convection towards the membrane and back-diffusion into the bulk solution. If the balance is disturbed (excess flux), the particles will accumulate on the surface; hence, increasing the TMP and leading to an inevitable fouling (Belfort, Davis, and Zydney 1994).

1.9.1.8 Shear-induced Diffusion Model

The shear-induced diffusion has the same assumptions as the diffusion model but the back-diffusion flux is assumedly controlled by shear-induced hydrodynamic diffusion instead of Brownian diffusion. Shear-diffusion arises from the random displacement of particles in the shear flow of the concentrated particles. The shear-induced diffusion effect is negligible for particles smaller than 10 nm but becomes significant for particles larger than 100 nm (Belfort, Davis, and Zydney 1994). This model is more appropriate

for calculating the critical flux due to the size of the resin beads, as they play the major role in the filtration process.

1.9.1.9 Surface Interaction Model

The surface interaction model assumes that a first-order physicochemical reaction within the concentration boundary layer at the membrane is the cause of fouling. The foulant starts to accumulate in the form of a deposit in a slow-linearly with time (Renaud and Probstein 1991).

1.9.1.10 Lateral Migration Model

The lateral migration model assumes that the back transport of particles in the surface of the membrane is due to hydrodynamic interactions with the flow boundary giving a lateral migration of particles. This lateral migration or inertial lift is a non-linear interaction between the particle and the surrounding flow field where particle size is non-negligible (Belfort, Davis, and Zydney 1994).

1.9.1.11 Continuous Counter-current Tangential Chromatography vs Traditonal Batch Chromatography

As previously stated, CCTC has been invented as an alternative to traditional batch chromatography techniques currently used in the biopharmaceutical industry. This alternative opens the door for a faster, hence cheaper, and highly productive purification process. CCTC has been developed for a relative short amount of time and it is not commercially available, making the comparison with other techniques a little limited. However, there is data that can back up the claims about the superiority on productivity and reduction on resources.

CCTC has been used and compared against column chromatography to separate mAb molecules from CCF and post-capture chromatography steps, as seen in Table 1.4. The steady state productivity of the CCTC were 67 and 101 g of mAb/L of resin/h for the chromatography media Capto Adhere and Capto Adhere ImpRes, respectively. A packed Capto Adhere chromatography column used to purify the same material giving 9.7 g of mAb/L of resin/h. The CCTC showed a productivity 6x to 10x higher than the one measured in the column format. Another way of analysing productivity is to compare difference in cycle times. In CCTC the cycle time is defined as the time a single bead travels from the binding step down to the equilibration step. As the CCTC does not have limitations on chromatography resin size, it allows a high flow/operation through the system. For the same process, it is calculated that the CCTC can achieve 5 and 8 cycles per hour, respectively; compared to the 0.3 cycles per hour in column format. It is important to notice that the column format could not run at the same flow rates as the CCTC due to the pressure drop it would experience by the small bead size, a 2x reduction in size would increase the pressure 4x. The column format yielded 90% of the total product while CCTC yielded 95%. This could be attributed to the homogeneous elution step. HCP, leached protein A and DNA were comparable between techniques(Dutta et al. 2017; 2015b).

The CCTC is capable of operating at 70 kPa (10psi), which is significantly less than in columns with pressures ranging around 300 kPa. This allows the CCTC flow path to be completely made out of plastic (tubing, connections, static mixer and hollow fibre). It is estimated that using the same Capto Adhere ImpRes media would result in a pressure of 1,200 kPa, making this process risky for the equipment and operators(Napadensky *et al.*, 2013; Amit K. Dutta *et al.*, 2016; Dutta *et al.*, 2017).

Table 1.5 shows the scale up comparison for processing 500 and 2,000 L between a CCTC system and a column. Because of the high productivity in CCTC, which is related to the continuous nature and the smaller particle size, the resin usage is decreased 8.3X; translated into 19 L of Capto ImpRes in CCTC and 156 L in column chromatography. This resin utilisation decrease would bring down the COGs for chromatography, as the resin is the most expensive material in the purification even taking into account the single-use materials (static mixers and hollow fibres) and increased buffer usage. It is estimated that CCTC would bring an estimated 65% cost reduction for clinical capture chromatography. However, the column chromatography

has an edge on buffer utilisation with 0.9 L of buffer/g of mAb versus the 3.4 L of buffer/g of mAb in CCTC. Concentrated buffer solutions can be easily implemented in CCTC due to its diluting operating nature and, in theory they can also be utilised for column chromatography but are not that popular in the manufacturing environment due to their challenging system controls and non-steady operations. The buffer usage can be optimised and reduced 40% if the wash output stream is reused for the bind step and the equilibration output stream for the strip step (Dutta et al. 2017). Further reductions in buffer can be made by the use of significantly reduced particle sizes by enabling faster kinetics and higher binding capacities (Fedorenko et al. 2020).

CCTC shows definitely a potential to overcome its traditional batch chromatography counterpart in the affinity separations department. It is not only attractive in terms of total amount of product but also on the high throughput it has shown in the most recent publications. Traditional batch chromatography can achieve amazing yileds and purities under optimised conditions but CCTC offers the same results at a better cost. Another advantage is the straightforward scalability, increase the static mixer volume to provide enough residence time and increase the membrane area in proportion to the scale; i.e. 2X scale would require twice the area. However, the technology has not been launched in the market and it seems it caters to a really specific niche (affinity separations) at the moment, making this claims only assumptions.

Table 1.4. Yield, productivity and product quantity comparison between CCTC and traditional column-based chromatography (Dutta et al. 2017)**.**

Performance	CCTC Capto Adhere	CCTC Capto Adhere ImpRes	Column
Yield (%)	95	95	90
Steady state productivity (g/L/hr)	67	101	-
Final elution pool productivity (g/L/hr)	55	81	9.7
HCP (ppm)	3	5	5
Leached protein A (ppm)	0.6	0.7	0.2
Monomer in load (%)	99.2	99.2	99.5
Monomer in elution pool (%)	98.7	99.0	99.6
Resin/process cycle per hour	5	8	0.3

Table 1.5. Scale up comparison between CCTC and traditional column-based chromatography on a scale of 500 and 2000 L operating for 9 h (Dutta et al. 2017)**.**

	CCTC (500 L)	CCTC (2000 L)	Column (500 L)	Column (2000 L)
Capto Adhere volume (K)	6.9	27.6	38.9	155.8
Capto Adhere ImpRes volume (L)	4.7	18.8	-	-
Average stage membrane area (m^2)	0.7-0.9	2.8-3.6	-	-
Total buffer volume (L) (10X Buffer concentrates in CCTC)	1083	4332	2926	11704
WFI volume (L) (CCTC in-line mixing)	9750	39000	-	-
Total buffer volume with recycle (L) (10X Buffer concentrates in CCTC)	691	2764	-	-
WFI volume with recycle (L) (CCTC in-line mixing)	6219	24876	-	-
Average buffer tank volumes (L)	150-250	600-1000	500-600	2000-2500

1.9.2 Other Non-column Chromatography Techniques

There have been other efforts reported in past years to achieve a non-column chromatography but the techniques did not manage to pass the research stage. In 1983, an affinity ultrafiltration for protein purification was developed using ultrafiltration units for each chromatography step (similar to CCTC but lacking static mixers). This process can achieve purities and yields of 70% (Kaul and Mattiasson 1993). Another example developed was a multistage affinity ultrafiltration process in which a series of tanks filled with resin slurry are connected while the mobile phase is being pumped through filters into the tanks. The process was batch like and similar to PCC or SMB (Wang et al. 2007). Finally, a technique called continuous affinity-recycle extraction (CARE) was developed and it worked with one binding tank and one desorbing tank in which the stationary phase is being pumped in between them. The product and contaminants are collected through a membrane module (Pungor et al. 1987).

These techniques were unsuccessful and not popularized for the same reason, as the processes did not excel in surpassing traditional packed-bed chromatography yields purities and productivities; nonetheless, it is important to recall their strong points and weaknesses for future research.

1.10 Research Aims and Objectives

This research aims to understand and simplify the current CCTC design and assess the structural and performance changes that occur in agarose- and synthetic-based chromatography resins as they are exposed to different equipment designs in order to improve resin lifetime and operational simplicity. This will potentially aide the adoption of the CCTC technique as a viable and competent option for purification technologies for biopharmaceutical manufacturing in the short- to medium-time term. This technique was selected as it has recently appeared as an emergent technology and a genuine alternative to the traditional packed-bed batch chromatography. The expected output is a mechanistic understanding of the deterioration of the chromatography resin in a CCTC system and the simplification of the CCTC design by studying a range of research objectives.

1.10.1 Objectives

Characterisation of protein sorption in the current CCTC design

- Characterization of protein adsorption and desorption kinetics of agarose- and methacrylate-based chromatography resins in batch and column format
- Characterization and exploration of operational parameters for the mixing module (static mixer) and solid/liquid separation module (hollow fibre)

In order to fulfil the first objective, the use of batch binding capacity (BBC) and dynamic binding studies (DBC) will be used to measure the binding adsorption and desorption kinetics of the Macro-Prep High Q (methacrylate) and Q Sepharose FF (agarose) chromatography resin in slurry and column formats. The resin characterization will be focused on their adsorption and desorption kinetics (BBC, DBC and their respective RT) in batch and column format. The second objective requires the use of the characterized resin slurry for the adsorption of BSA in a static mixer – where the impact of the engineering environment on the adsorbent will be studied. Also, the hollow fibre critical parameters need to be explored under different fluxes using resin slurry as

feed. The critical flux, TMP and flux will be employed for the future CCTC operating parameters.

Characterisation of the impact of the CCTC system on adsorbent materials

- Ultrastructural visualisation, qualification and quantification of agarose- and methacrylate-based chromatography media exposed to different CCTC equipment components
- Quantification of the performance of the aforementioned chromatography media
- Identification of CCTC component affecting the ultrastructural properties of the chromatography media

Different CCTC equipment configurations will be used to investigate how chromatography resin performance, bead size and surface properties vary after short (4 h) and long (up to 36 h) periods of time in continuous operation for Macro-Prep High Q and Q Sepharose HP. The system configurations/components that will be tested are the CCTC system as a whole, an isolated peristaltic pump with the resin reservoir mixer and the resin reservoir mixer by itself. The resin reservoir will be used with two types of mixers, a magnetic stirrer and an overhead impeller. In addition to these experiments, high shear studies using an Ultra-Scale Down (USD) disc rotary device will be employed to determine the mechanical robustness under high shears of 20% (v/v) Macro-Prep High Q and Q Sepharose FF resin slurries. In order to compare the configurations, SEM will be employed as a high visualization technique to observe and, quantify surface properties such as average pore size, average pore count and apparent porosity. Images from the SEM will be analysed using ImageJ for the image analysis. PSD studies are required to determine deformation and/fragmentation of the chromatography bead. DBC studies in an XK 16 column at 2 cm bed height is used to quantify the performance. These experiments will allow to identify the component with the most negative impact and assess the mechanical and performance robustness between both resin matrices.

Characterisation of CCTC separation performance in 2 component systems

- Anion exchange separation of BSA (product) and myoglobin (contaminant) in a batch 2-stage CCTC system

- Salt step-gradient separation of ovalbumin variants with closely related elution behaviour in a batch 2-stage CCTC system
- Identification of system short comings before, during and after operation

The separation of BSA and myoglobin in the custom 2-stage CCTC rig will be used to test the system and assess/identify the system short comings that are related to its preparation, operation, shut down and, also, not necessarily related to publishable results or data. The separation will be taking place in 5 steps: bind, wash-1, wash-2, elution and strip. Samples from the resin slurry retentate and product/waste permeate outlet streams will be taken at the beginning of each step until 20 min of operation to ensure steady state in all results. The protein concentration in the samples will be analysed to obtain experimental and theoretical yield and purity results. Before the CCTC separation is performed, a packed-bed chromatography separation will be performed to set operational parameters. The methacrylate-based resin, Macro-Prep High Q, will be used for comparison with reported results.

After the system has been tested and features assessed, a salt step-gradient separation of ovalbumin into its major variants was designed. The separation used the same mixing and solid/liquid separation modules that were used for the BSA and myoglobin separation. The separation will be taking place in 5 steps: bind, wash, elution-1, elution-2 and strip. Samples from the resin slurry retentate and product/waste permeate outlet streams will be taken at the beginning of each step until 20 min of operation to ensure steady state in all results. This separation will be used to assess the limitations of the CCTC technique to achieve a step-gradient separation of two species with closely related elution behaviour. Before the CCTC separation is performed, a packed-bed chromatography separation will be performed to set elution-1 and elution-2 salt-gradient concentrations, as well as to identify the elution point for the major variants. High performance liquid chromatography (HPLC) will be used to estimate such elution points with precision. The agarose-based resin, Q Sepharose FF, will be used as its BBC is significantly higher.

Design and characterisation of alternative CCTC formats

- Characterization of residence time distribution in different CFIR, HCR and static mixer reactor (SMR)

- Proof of concept of CFIR and HCR used as mixing modules for protein adsorption for chromatography resin

To simplify the CCTC design and proof of concept, a set of CFIR will be constructed with 6 different curvature ratios (λ), from 0 to 3 inversions and used under 3 different flow rates with the methacrylate-based chromatography resin, Macro-Prep High Q. HCR with equal internal tube diameter and equivalent length will also be used under the same conditions. Also, the SMR used in the original 2-stage CCTC rig will be used under the same conditions. Sodium chloride will be used as a tracer molecule to characterize the cross-mixing or axial dispersion reduction for all CFIRs, HCRs and SMRs. After being characterised, BBC studies will be used to assess the performance of each type of reactor in terms of total binding and productivity. An analysis using the characterisation values (length, RT, axial dispersion reduction, footprint and cost) will be employed to determine the significance of these residence time distribution (RTD) and BBC results and to ascertain whether CFIRs can be used as feasible mixing modules in a CCTC system.

Chapter 2: Materials and Methods

2.1 General Information

This chapter outlines the materials, experimental equipment and methods, as well as all the analytical techniques used for this research.

Unless otherwise stated, all chemicals were of analytical grade and purchased from Sigma-Aldrich (Poole, UK). Ultrapure water was used for all of the solutions filtered from a Milli-Q Reference Water Purification System (Merck, Germany).

2.2 Materials

The proteins used for this study were BSA (isoelectric point (pI) at 25° C: 5.3, molecular weight (MW): 66 kDa, Optimum Optical Absorbance (OA): 278 nm) and Myoglobin (pI at 25° C: 6.8 to 7.3, MW: 17 kDa, optimum OA: 280 nm). The proteins were dissolved in 20 mM phosphate buffer pH 7. Four resins available unpacked and pre-packed were employed for the experiments: Macro-Prep High Q (Bio-Rad Laboratories, USA), Q Sepharose Fast Flow, Q Sepharose HP (General Electric, United Kingdom) and Praesto Q anion exchange resin (Purolite, United Kingdom). When used unpacked, both resins were diafiltered into the desired buffer using a Stericup Filter unit fitted with a 0.22 µm polyethersulfone membrane (Merck, Germany) using at least 8 to 10 diavolumes of water to remove any ethanol and then, the same procedure was repeated with phosphate buffer.

The static mixer used for all experiments was made of clear PVC pipe with a 1 cm diameter and 12 elements (Cole-Palmer, UK). The hollow fibres were made of modified polyethersulfone with a pore size of 0.65 µm, a tube length of 45 cm and a total membrane area of 175 cm^2 (Repligen, USA). A single head peristaltic pump Masterflex and a double-head Masterflex peristaltic pump (Watson-Marlow, UK).

2.3 Determination of Fraction Analyte Concentration

The absorbance measurements from the samples and blanks were determined by a volume determination, followed by wavelength scan and finally, the concentration procedure. These are detailed in the next two sections.

2.3.1 Fraction Volume Determination

Fraction volume determination is relevant for mitigating volume-dispensing errors caused by human handling or inaccurate pipettes, giving more reliable protein concentrations. The fraction volume determination is based on the absorbance measurements at near infrared regions (NIR) of the wavelength spectrum as suggested by McGrown et al. (McGown & Hafeman, 1998). The results of this method gives a calibration method was performed using the Infinite 200 PRO microplate reader (Tecan, Switzerland) and 96-well full area plates (Corning, USA) with 20 mM phosphate buffer pH 7. Absorbance at 900 and 990 nm were measured for a series of known volumes. The measurements start at 30 and end at 250 µL, with 20 µL between each point. Equation 1 was fitted to the experimental data using the linear regression method to estimate the slope (d) and the intercept (e).

$$Volume\ (\mu L) = d(OA_{990} - OA_{900}) + e \quad (1)$$

2.3.2 Protein Wavelength Spectrum Scan

A complete wavelength spectrum scan was performed on each protein to determine optimum wavelength absorbance for concentration determination. Known amounts of BSA and myoglobin (0 to 8 mg/mL, 0.4 mg/ml between each sample) were dissolved separately in 20 mM phosphate buffer pH 7. The wavelength spectrum scan was done in the Infinite 200 PRO microplate reader with 96-well full area plates. The absorbance

measurements were normalised over their path length, determined from the volume calibration curve.

2.3.3 Protein Concentration Determination

Individual concentration calibration curves were built at 280 and 500 nm for BSA and myoglobin, respectively. For this purpose, known amounts of the proteins (0 to 8 mg/mL, 0.4 mg/mL between each step) were dissolved in 20 mM phosphate buffer pH 7. The absorbance was measured in the Infinite 200 PRO microplate reader with 96-well full area plates at the previously mentioned wavelengths, along with wavelengths at 900 and 990 nm. The absorbance measurements were normalised over their path length. Finally, the calibration curve was constructed using the linear regression method and the determination was defined on the form of Equation 2 and 3.

$$[BSA]\,(mg) = a_1\left(\frac{OA_{280}}{l}\right) + b_1 \quad (2)$$

$$[Myo]\,(mg) = a_2\left(\frac{OA_{500}}{l}\right) + b_2 \quad (3)$$

2.4 Protein Binding Kinetics

Traditional pre-packed column chromatography and CCTC techniques rely on different mechanisms of measuring the binding capacity. Hence, appropriate methods were used in order to measure the binding capacity for each of the configurations.

2.4.1 Batch Binding Capacity

Binding kinetics was evaluated using a simple batch system. A 100 mL beaker was initially filled with 6 mL of slurry at 70% (v/v%) in 20 mM phosphate buffer pH 7 solution containing 40 mM NaCl. The stirrer was turned on and a 34 mL of 20 mM phosphate buffer pH 7 solution containing 3 mg/mL of BSA was added to the beaker. This results in a final slurry concentration of 10% (v/v%). Samples of 200 µL were collected through an Acrodisc syringe filter (PM4612, Pall Corp., Washington, NY) containing a 0.2 µm pore size hydrophilic Super® membrane that was fully retentive to the resin particles. The sampling was done for 150 seconds. Each syringe and syringe filter were single used. The solutions were placed directly into 96-well full area plate, 200 µL per well. The free protein concentration per sample was determined using the fraction analyte concentration method previously explained in Section 2.3.3. The protein bound per resin volume was calculated using a mass balance on the form of Equation 4.

$$BBC\ (mg_{BSA}/mL_{resin}) = \frac{VC_0 - VC_i}{V_s} \quad (4)$$

where *V* is the total batch volume (mL), C_0 is the initial BSA concentration (mg/mL), C_i is the BSA concentration in sample and V_s is the volume of resin particles in the batch. The decrease of total batch volume and total amount of resin particles are neglected for the calculations as the solution is homogeneous and the concentration contents remain unchanged.

2.4.2 Batch Binding Capacity in Static Mixer

A 40% (v/v) slurry and a 3 mg/mL BSA solution were pumped with a double head peristaltic pump Watson Marlow through a series of 4 connected static mixers of diameter 1.0 cm with 12 elements. The static mixers were designed to give a theoretical residence time (RT) of 112 s, with a total flow rate of 51 mL/min (38 mL/min for the BSA solution and 13 mL/min for the slurry). The binding kinetics at the end of

the static mixers was measured and calculated in a similar fashion as described in Section 2.4.1 and Equation 4.

2.4.3 Batch Desorption Studies

Desorption experiments were performed in equal format as BBC studies using 40 mL of 20 mM phosphate buffer pH 7 solution with a slurry concentration of 10% (v/v). The slurry was equilibrated for 30 min with a starting concentration of 3 mg/mL of BSA. The appropriate amount of NaCl was added in order to increase the molarity up to 1 M, with a 100.0 mM increase. The sampling is similar as in Section 2.4.1 but the timing change to 20 seconds every time NaCl was added to the solution.

2.4.4 Dynamic Binding Capacity

The DBC measurements were established at 10% breakthrough. The 1 mL Bio-Scale Mini Macro-Prep High Q Cartridge (Bio-rad Laboratories, USA) and HiTrap Q FF (Sigma Life Science, USA) columns were mounted to an AKTA Explorer 100 system (GE Healthcare Life Sciences, USA). Both columns were equilibrated with 20 mM phosphate buffer pH 7. The DBC measurements were evaluated by saturating the column with 3.0 mg/mL of BSA solution at flow rates of 0.3 to 1 mL/min (linear flow velocities of 75 to 600 cm/h). The protein concentration was determined using the fraction analyte concentration method previously explained in Section 2.3.3, as well as with the UV absorption. The BSA bound to the resin was calculated as shown in Equation 5.

$$DBC\ (mg_{BSA}/mL_{resin}) = \frac{V_b C_0}{CV} \quad (5)$$

where V_b is the 10% breakthrough volume, C_0 is the initial BSA concentration and CV is the column volume.

2.5 Critical Flux Experiment

The inlet, outlet and permeate pressures were continuously monitored using Leo 2 digital manometer (Keller Druck, Switzerland). The system was equilibrated using a slurry of 5% (v/v) (diluted resin slurry), the permeate flow would start only after the stabilisation of all pressure readings. The permeate flow rate was increased gradually at equal intervals. The pressures were monitored at each permeate for a minimum of 15 min. The permeate flow rate was continuously increased until the TMP became unstable as indicated by a rise in TMP. Once the critical flux was recorded, the permeate pump was slowly ramped down to 0 mL/min and then flushed completely.

The TMP was calculated as a function of time with:

$$TMP = \frac{P_{in}+P_{out}}{2} - P_{permeate} \quad (6)$$

where P_{in} is the pressure at the feed inlet, P_{out} is the pressure at the retentate outlet and $P_{permeate}$ is the pressure in the permeate outlet. The diagram of the rig and its flow streams used for the critical flux experiment is shown in Figure 2.1. The rig has one hollow fibre module in total recirculation mode.

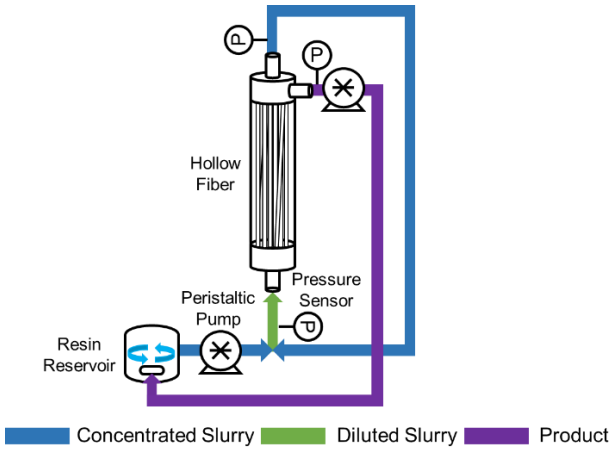

Figure 2.1. Hollow fibre configuration for critical flux studies. The system is operated in total recirculation maintaining the same concentration of resin slurry. The inlet flow rate remains constant at 51 mL/min while the permeate flow rate started at 0 mL/min and later increased every 15 min until the system became unstable to continue.

2.6 Particle Size Distribution

The experimental PSD was determined using a Mastersizer 3000 (Malvern, UK) using the Hydro SV unit to avoid contamination between samples and facilitate cleaning. The Hydro SV unit stirrer was set at 1,000 rpm to prevent resin damage and sedimentation. All buffers from the resin samples were buffer exchange to 20% ethanol for reading and storage. Each variable for all experiments was performed in triplicate and each sample was measured 5 times. The refractive and absorption indices for agarose were set at 1.34 and 0.001 and for methacrylate were 1.48 and 0.001 (numbers available in the software catalogue). The PSD was first measured before any other experiment was performed on the resin samples to avoid any deformation or damage of the matrix, i.e. DBC studies.

2.7 BSA and Myoglobin Separation in Packed-bed Chromatography

Packed-bed chromatographic runs were performed to create a baseline for the non-column membrane-based chromatography separation. The separations were done using a 1 mL prep-packed column BioScale Mini Macro-Prep High Q Cartridge and HiTrap Q FF, anion exchange resin. The purification of BSA took place via a non-gradient elution. The protein concentration in the solution was BSA 2 mg/mL and myoglobin 0.85 mg/mL for each matrix (ratio of 2.5:1). The loading volume was 6 mL for Bio-Scale Mini Macro-Prep High Q Cartridge and 12 mL for HiTrap Q FF column. A flow rate of 1 mL/min was employed to ensure enough residence time for total resin utilisation. The description of the steps is described in Table 2.1.

Table 2.1. Buffer solutions and volume durations for the anion exchange separation of BSA and myoglobin 1 mL Bio-Scale Mini Macro-Prep High Q Cartridge and HiTrap Q FF columns at a 1 mL/min flow rate.

Step	Buffer Solutions	Duration (CV)
Equilibration	20 mM phosphate buffer pH 7	6
Load	20 mM phosphate buffer pH 7 2 mg/mL BSA 0.85 mg/mL myoglobin	6 (Macro Prep High Q Cartridge) 12 (HiTrap Q FF)
Wash	20 mM phosphate buffer pH 7	12
Elution	0.4 M NaCl, 20 mM phosphate buffer pH 7	6
Strip	20 mM phosphate buffer pH 7	6
Regeneration/CIP	1 M NaOH and 0.5 M NaCl	6
Storage	20% Ethanol	6

2.8 BSA and Myoglobin Separation in CCTC

Figure 2.2 shows a schematic diagram of the batch 2-stage CCTC system used for bind, load, wash, elution and elution steps. The description and buffer concentrations of each step are shown in Table 2.2. Figure 2.3 shows the schematic representation of CCTC step sequence used for the separation. The permeate (both stages) streams were controlled by a double-head Watson Marlow peristaltic pump (Watson Marlow, UK), while the slurry and buffer flow rates were controlled by individual single-head Watson Marlow peristaltic pump. Each of the inlets and outlets in the hollow fibres were fitted with Leo 2 digital manometers (Keller, England).

First, the whole system was filled with the corresponding buffer for the step (Table 2.1) until all air is removed from the system. The concentrated slurry is first pumped into the first static mixer where it is mixed with the Stage-2 permeate. The diluted slurry enters the hollow fibre module where enough liquid is removed as permeate to concentrate the slurry to its original state. Then, the process is repeated for Stage-2 with the only difference is that the concentrated slurry is diluted with fresh buffer. All permeate peristaltic pumps were operated at a flow rate of 38 mL/min and the concentrated slurry peristaltic pump was operated at 13 mL/min. Samples from

stage-2 slurry retentate stream and stage-1 permeate stream were taken every minute for 20 min the moment the concentrated slurry exited stage 2.

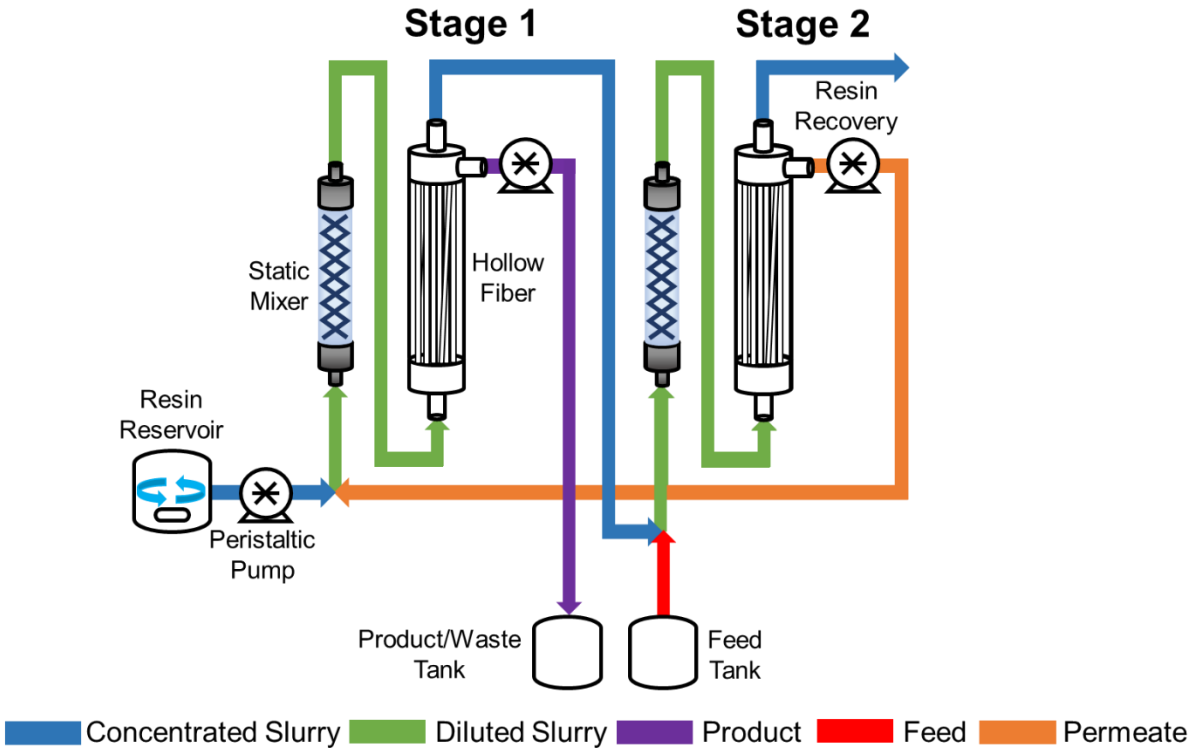

Figure 2.2. Schematic of the batch 2-stage CCTC system. The different streams are colour labelled according to their slurry or product concentration. The resin slurry starts in stage 1 and is recovered at the retentate stream in stage 2 for further use in the next steps; while the feed/buffers enter the system in stage 2 and get harvested/recovered in stage 1 in the permeate stream. The inlet resin slurry flow rate was kept at 13 mL/min while the permeate flow rate for both hollow fibres was kept at 38 mL/min.

Table 2.2. Buffer solutions for the separation of BSA and myoglobin in CCTC with Macro-Prep High Q and Q Sepharose FF with a concentrated resin slurry of 20% (v/v).

Step	Feed/Buffer Inlet	Resin Slurry
Equilibration	20.mM phosphate buffer pH 7	
Load	20 mM phosphate buffer pH 7 1 mg/mL BSA 0.5 mg/mL myoglobin	Macro-Prep High Q or Q Sepharose FF 20% (v/v) 20 mM phosphate buffer pH 7
Wash	20 mM phosphate buffer pH 7	
Elution	0.5 mM NaCl 20 mM phosphate buffer pH 7	
Strip	1 mM NaCl 20.0 mM phosphate buffer pH 7	

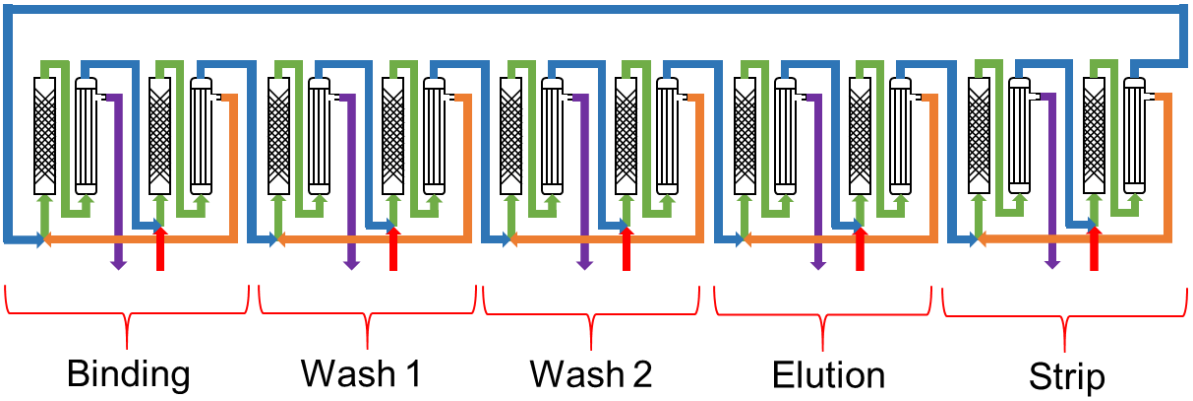

Figure 2.3. Schematic representation of the complete 2-stage CCTC system used for the separation of BSA and myoglobin. The schematic includes binding, wash 1, wash 2, elution and strip stages with a total recirculation of the resin from strip to binding stages. The clean resin recirculates at the end of the strip to binding step to have a closed resin cycle.

2.9 Ovalbumin Serotype Separation in Packed-bed Chromatography

Packed-bed chromatographic runs were performed for comparison between this mode and for the non-column membrane-based salt-gradient chromatography separation. The separation was done with a 1 mL Tricorn 5/50 column (GE Healthcare Life Sciences, United Kingdom) packed with a 5 cm bed height of Praesto Q anion exchange resin. The purification of ovalbumin took place via a 1 M NaCl gradient elution from 0 to 30% over the course of 50 CV. The ovalbumin concentration was of 1 mg/mL in 50 mM Tris buffer pH 8.5. A flow rate of 1 mL/min was used for all chromatography steps. Fractions volumes of 1 mL were taken for the whole duration of the elution step.

2.10 Ovalbumin Serotype Separation in CCTC

The separation of ovalbumin into different serotypes was performed in a similar manner as explained in Section 2.8. Figure 2.4 displays the sequence of chromatography steps used for the overall separation. The separations were done with an initial concentration 20% (v/v) of Q Sepharose FF anion exchange resin. The ovalbumin concentration was of 1.3 mg/mL (1 mg/mL after entering the static mixer)

in 50 mM Tris buffer pH 8.5. The corresponding buffers for each step are described in Table 2.3.

Table 2.3. Buffer solutions for the separation of ovalbumin into its major variants in CCTC with Q Sepharose FF with a concentrated resin slurry of 20% (v/v).

Step	Feed/Buffer Inlet	Resin Slurry
Equilibration	50 mM Tris buffer pH 8.5	
Load	50 mM Tris buffer pH 8.5	Q Sepharose FF 20% (v/v)
Wash	50 mM Tris buffer pH 8.5	
Elution 1	95 mM NaCl 50 mM Tris buffer pH 8.5	50 mM Tris buffer pH 8.5
Elution 2	155 mM NaCl 50 mM Tris buffer pH 8.5	
Strip	1 M NaCl 50 mM Tris buffer pH 8.5	

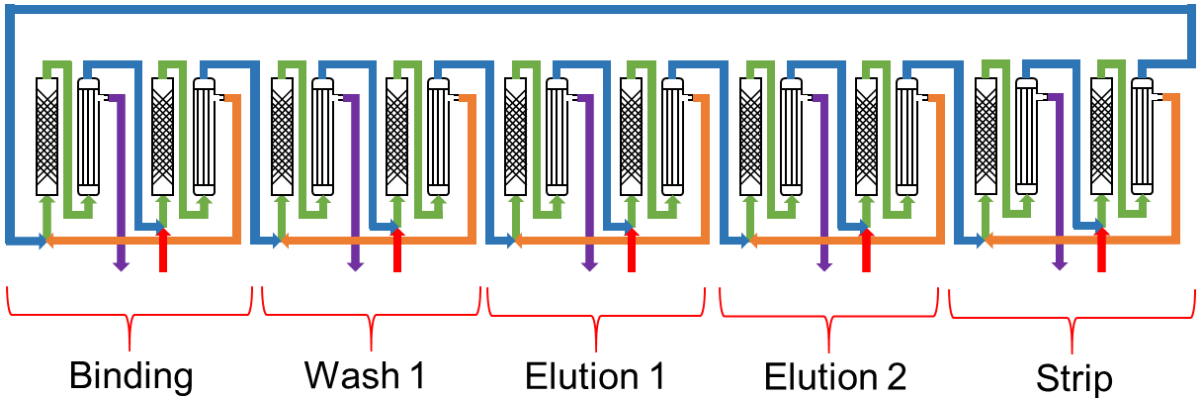

Figure 2.4. Schematic representation of the complete 2-stage CCTC system used for the separation of ovalbumin serotypes. The schematic includes binding, wash, elution 1, elution 2 and strip stages with a total recirculation of the resin from strip to binding stages. The two separate elution step allows to mimic a step-gradient separation. The clean resin recirculates at the end of the strip to binding step to have a closed resin cycle.

2.11 HPLC Ovalbumin Serotype Separation

The analysis of the fractions for the separation of the serotypes of ovalbumin in packed-bed chromatography and CCTC was done in an Agilent 1200 Infinity Series analytical LC system (Agilent Technologies, USA) using a 0.1 mL CIM-Q column (BIA Separations, Slovenia) by UV at 280 nm with mobile phases consisting of 50 mM Tris buffer pH 8.5 (Buffer A) and 1 M NaCl 50 mM Tris buffer pH 8.5 (Buffer B). Samples were eluted employing a linear gradient at ambient temperature of 0% Buffer B to 100% Buffer B over 30 CV. Flow rate was set at 0.1 mL/min.

2.12 High Shear Stress Resistance Studies in Small-Scale Device

The high shear stress experiments were performed using an USD rotating disc shear device. The device consisted of a 40 mm in diameter and 0.1 mm thick centrally mounted disc of stainless steel. The disc is connected to a high-speed motor powered via a power pack/speed controller unit (UCL mechanical workshop), capable of reliably controlling the rotating speed between 2,000 and 12,000 rpm. Figure 2.5 shows the external, internal diagram and shear distribution of the USD rotating disc shear device. The stainless steel chamber of 50 mm internal diameter and 10 mm height holds a volume of 20 mL. Three shear conditions were tested on Macro-Prep High Q and Q Sepharose FF: 2,000, 3,500 and 5,000 rpm. Each running condition lasted 20 seconds as it has experimentally been proven that it is enough time for the samples to experience the desired degree of shear comparable to the shear experience in an industrial-scale centrifuge. Also, because the system cannot withstand long operating times without a cooling jacket. The slurry concentration in each run for both resins was 20% (v/v) in 20 mM phosphate buffer pH 7.

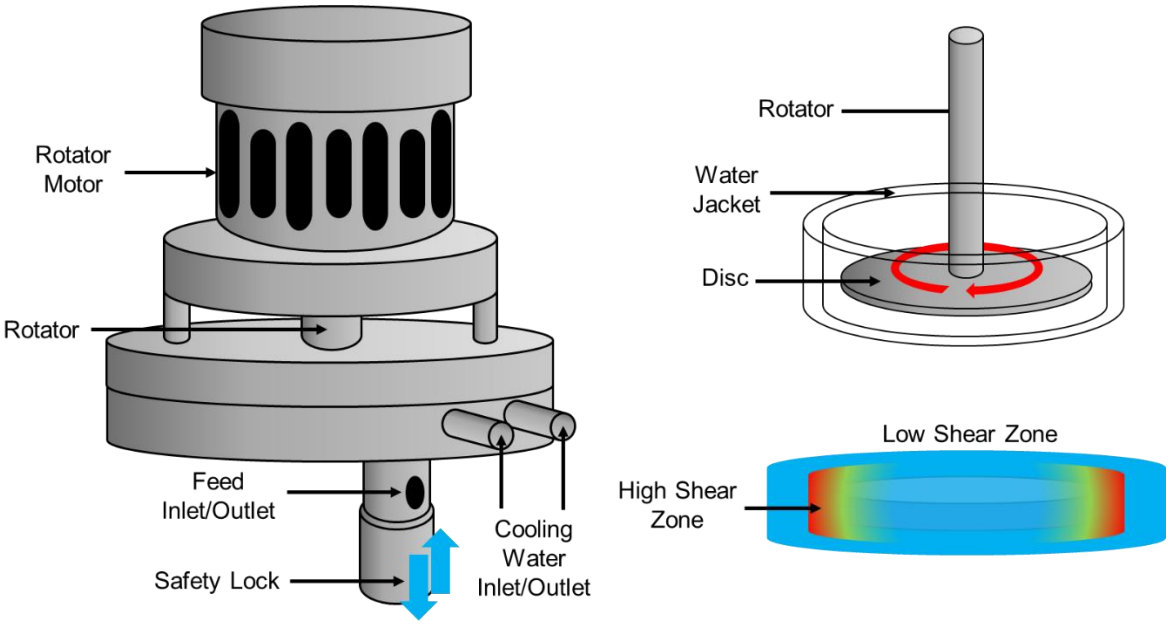

Figure 2.5. Schematic of: A) the outside of the USD Rotating Disc Shear Device depicting the sample inlet and outlet, B) the inside chamber of the device and the rotating disc and C) the different shear zones around the rotating disc. The highest shear is experience at the edges of the plate.

2.13 Low Shear Stress Resistance Studies in CCTC System

The low shear stress resistance experiments were performed to assess the damage of the resin after operation in a CCTC system for short and long term. The experiments were done in 6 configurations, as shown in Figure 2.6. The experiments were mainly divided in the type of stirring located inside the resin reservoir: magnetic stirrer and overhead impeller. Each of the type of stirring was performed in 3 different configurations: CCTC system coupled with a peristaltic pump and a resin reservoir in total recirculation, peristaltic pump and a resin reservoir in total recirculation and resin reservoir.

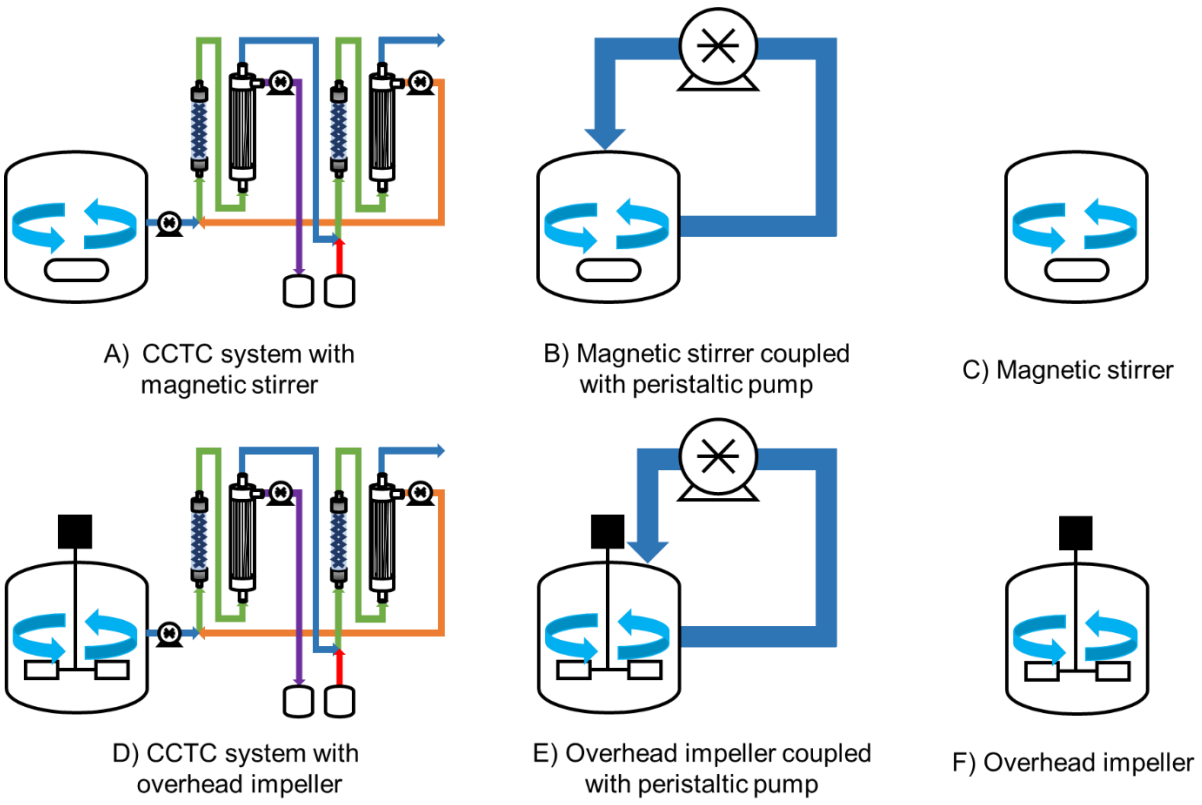

Figure 2.6. Different configurations used for testing resin resilience. A) CCTC system with a magnetic stirrer mixer, B) Magnetic stirrer coupled with peristaltic pump, C) Magnetic stirrer mixer, D) CCTC system with an overhead impeller mixer, E) Overhead impeller mixer coupled with peristaltic pump and F) Overhead impeller mixer.

A 20% (v/v) concentrated resin slurry in 20 mM phosphate buffer pH 7 was used for all the experiments. The inlet resin slurry peristaltic pump was set on 13 mL/min, while the permeate peristaltic pumps were set on 38 mL/min for the CCTC system coupled with a magnetic stirrer and overhead impeller in the resin reservoir; same conditions as described in Section 2.8. The peristaltic pump was set on 51 mL/min for the configuration with the resin reservoir coupled with a single peristaltic pump (B and E). The magnetic stirrer and overhead impeller were set to a speed of 400 rpm for all configurations.

2.14 DBC for High Shear and Low Shear Resistance Studies

The DBC measurements were carried in a similar manner as in Section 2.4.4 with the exception that the columns were manually packed for both Macro-Prep High Q, Q Sepharose HP and Q Sepharose FF. The resins were packed by gravity and then a gradual flow rate increase until no further compression in a XK 16 at a 2 cm bed height (4 mL of resin). The flow rate of 1 mL/min was used for all the steps. The asymmetry was maintained within a range of 1.6 to 2 and 0.9 to 1.1, respectively. The BSA load had a concentration of 20 mg/mL. All experiments were performed in triplicate.

2.15 Scanning Electron Microscope – Preparation and Techniques

20% (v/v) slurry samples of both resins of 1 mL obtained at different time points from Sections 2.12 and 2.13 were used for this study.

2.15.1 Freeze Drying

The protocol employed is an adaptation of previously reported freeze drying methodology (Nweke et al. 2017). The time for freezing and drying of the process was modified to completely dry completely the agarose- and methacrylate-based beads. A 0.5 mL aliquot of each sample 20% (v/v) slurry in 20% ethanol was poured into separate 60 x 15 mm sterile polystyrene petri dishes (Fisher Scientific, UK) and properly labelled. The petri dish was cover with a thin layer of laboratory film with holes made with a syringe to avoid cross-contamination among the same matrices inside the freeze-drying equipment. The samples were placed on different shelves according to their matrix in the Virtis Genesis 25EL freeze dryer (SP Scientific, US) to avoid cross-contamination. The samples were left in the equipment for 28 h. The freezing stage was held for 8 h with a step-wise temperature decrease from 25° to -40° C, 1 degree every 8 min. The drying stage was held for 20 h with a temperature step-wise increase from -40° to 25° C, 1° every 20 min. The samples were taken out of the equipment, sealed and stored in a dry place at room temperature until they were golden coated.

2.15.2 Sample Coating Preparation

The dried resin was placed onto the surface of a labelled 1 x 1 cm cylindrical aluminium specimen stub (Agar Scientific, UK) in order to be coated in gold. The resin managed to stick onto the stub due to a double sided sticky stamp.

The sample is placed into the Agar Manual Sputter Coater (Agar Scientific, United Kingdom). The coating consisted of a gold/palladium alloy with a thickness of 1 to 2 nm. The ion beam coater is operated at 240 V / 50 Hz at a 90° angle.

2.15.3 Scanning Electron Microscope - Imaging

After the samples were coated, the samples mounted onto the SEM carrier and inserted into the JSM6480LV field emission scanning electron microscope (JEOUL, U.S.A.) for imaging at 7 kV accelerating voltage.

2.16 Quantitative Analysis of Low and High Shear Resin SEM Images

ImageJ software was used for the quantitative analysis of all SEM images taken from samples obtained in Section 2.12 and 2.13. The scale was set manually by drawing a 2.5 cm on the scale bar of 1 μm, creating a pixel to length conversion. The image was smoothened to flatten the image and, if needed, the contrast was increased. All the colours of the smoothened image were turned into a binary scale of black and white. The software has a tool to find and select the edges of the black sections of the image. Finally, ImageJ tools were used to count the total number of pores, measure the average pore size and calculate the apparent porosity. Three different SEM surface images of the matrix were used for the quantitative analysis.

2.17 Reactor Rigs

The CFIR, HCR and SMR setup are illustrated in Figure 2.7. All of the reactor rigs basically consisted of 4 main components: buffer/resin reservoir, a double-head Masterflex peristaltic pump, a mixing T-piece connecting both streams and the reactor itself. The geometric parameters, such as coil pitch and number of turns per bend, were kept the same, whereas the tube diameter, coil diameter, number of 90° bends/inversions, tube length and velocity/flow rate were varied in order to obtain different RT, N_{Re} and λ, where applicable. All the different operational conditions for the different reactors are presented in Table 2.4.

The CFIR was built with PVC pipe joined with super glue for the coil and peristaltic tubing for the coiled arms. The HCRs were made from the same tube used for all CFIRs to keep consistent length. The HCR was coiled in order to have a diameter of 50 cm, mitigating some of the convective or secondary mixing phenomena. A straight reactor was not possible due to footprint limitations. The HCR with such coil diameter was chosen as the closest replacement within the restrictions. The SMR used for experiments are the same ones used in Sections 2.4.2, 2.8 and 2.10; each of the SMR segments had a length of 30 cm and a 1 cm internal diameter.

Table 2.4. Design and operational conditions for all the CFIRs ordered by λ number.

Coil Diameter (m)	Coiled Tube Internal Dia. (m)	Coiled Tube External Dia. (m)	Curvature Ratio (-)	Coil Pitch (m)	No. of Inversions (-)	Length (m)	Flow Rate (mL/min)	Flow Velocity (m/s)	Reynolds Number (-)	Dean Number (-)	Theoretical Mean Residence Time (s)
0.053	0.002	0.004	13.8	0.008	0	1.43	20	0.027	102.26	27.58	54.01
							35	0.046	178.95	48.26	30.86
							50	0.066	255.64	68.94	21.60
					1	2.87	20	0.027	102.26	27.58	108.01
							35	0.046	178.95	48.26	61.72
							50	0.066	255.64	68.94	43.21
					2	4.30	20	0.027	102.26	27.58	162.02
							35	0.046	178.95	48.26	92.58
							50	0.066	255.64	68.94	64.81
					3	5.73	20	0.027	102.26	27.58	216.03
							35	0.046	178.95	48.26	123.44
							50	0.066	255.64	68.94	86.41
0.068	0.002	0.004	17.5	0.008	0	1.81	20	0.027	102.26	24.44	68.22
							35	0.046	178.95	42.78	38.98
							50	0.066	255.64	61.11	27.29
					1	3.75	20	0.027	102.26	24.44	141.51
							35	0.046	178.95	42.78	80.86
							50	0.066	255.64	61.11	56.60
					2	5.70	20	0.027	102.26	24.44	214.79
							35	0.046	178.95	42.78	122.74
							50	0.066	255.64	61.11	85.92
					3	7.64	20	0.027	102.26	24.44	288.08
							35	0.046	178.95	42.78	164.62
							50	0.066	255.64	61.11	115.23

0.053	0.002	0.003	18.3	0.008	0	1.42	20	0.047	140.42	32.80	30.11
							35	0.083	245.74	57.40	17.21
							50	0.118	351.06	81.99	12.04
					1	2.85	20	0.047	140.42	32.80	60.49
							35	0.083	245.74	57.39	34.57
							50	0.118	351.06	81.99	24.20
					2	4.29	20	0.047	140.42	32.80	90.87
							35	0.083	245.74	57.39	51.93
							50	0.117	351.06	81.99	36.35
					3	5.72	20	0.047	140.42	32.80	121.25
							35	0.083	245.74	57.39	69.28
							50	0.117	351.06	81.99	48.50
0.073	0.002	0.004	18.8	0.008	0	1.94	20	0.027	102.26	23.62	72.96
							35	0.046	178.95	41.33	41.69
							50	0.066	255.64	59.04	29.18
					1	3.88	20	0.027	102.26	23.62	146.24
							35	0.046	178.95	41.33	83.57
							50	0.066	255.64	59.04	58.50
					2	5.82	20	0.027	102.26	23.62	219.53
							35	0.046	178.95	41.33	125.45
							50	0.066	255.64	59.04	87.81
					3	7.77	20	0.027	102.26	23.62	292.81
							35	0.046	178.95	41.33	167.32
							50	0.066	255.64	59.04	117.13
0.068	0.002	0.003	23.3	0.008	0	1.80	20	0.047	140.42	29.07	38.11
							35	0.083	245.74	50.87	21.78
							50	0.118	351.06	72.68	15.24
					1	3.74	20	0.047	140.42	29.07	79.33
							35	0.083	245.74	50.87	45.33
							50	0.118	351.06	72.68	31.73
					2	5.68	20	0.047	140.42	29.07	120.55

							35	0.083	245.74	50.87	68.89
							50	0.118	351.06	72.68	48.22
					3	7.63	20	0.047	140.42	29.07	161.78
							35	0.083	245.74	50.87	92.45
							50	0.118	351.06	72.68	64.71
0.073	0.002	0.003	25.0	0.008	0	1.92	20	0.047	140.42	28.08	40.77
							35	0.083	245.74	49.15	23.30
							50	0.118	351.06	70.21	16.31
					1	3.87	20	0.047	140.42	28.08	82.00
							35	0.082	245.74	49.15	46.85
							50	0.118	351.06	70.21	32.80
					2	5.81	20	0.047	140.42	28.08	123.22
							35	0.083	245.74	49.15	70.41
							50	0.118	351.06	70.21	49.29
					3	7.75	20	0.047	140.42	28.08	164.44
							35	0.083	245.74	49.15	93.97
							50	0.18	351.06	70.21	65.78

Table 2.5. Design and operational conditions for all the HCRs ordered to by their equivalent CFIR λ.

Coil Diameter (m)	Coiled Tube Internal Dia. (m)	Coiled Tube External Dia. (m)	Curvature Ratio (-)	Coil Pitch (m)	Length (m)	Flow Rate (mL/min)	Flow Velocity (m/s)	Reynolds Number (-)	Dean Number (-)	Theoretical Mean Residence Time (s)
0.5	0.002	0.004	125.5	0	1.43	20	0.027	102.26	9.13	54.01
						35	0.046	178.95	15.97	30.86
						50	0.066	255.64	22.82	21.60
					2.87	20	0.027	102.26	9.13	108.01
						35	0.046	178.95	15.97	61.72
						50	0.066	255.64	22.82	43.21
					4.30	20	0.027	102.26	9.13	162.02
						35	0.046	178.95	15.97	92.58
						50	0.066	255.64	22.82	64.81
					5.73	20	0.027	102.26	9.13	216.03
						35	0.046	178.95	15.97	123.44
						50	0.066	255.64	22.82	86.41
0.5	0.002	0.004	125.5	0	1.81	20	0.027	102.26	9.13	68.22
						35	0.046	178.95	15.97	38.98
						50	0.066	255.64	22.82	27.29
					3.75	20	0.027	102.26	9.13	141.51
						35	0.046	178.95	15.97	80.86
						50	0.066	255.64	22.82	56.60
					5.70	20	0.027	102.26	9.13	214.79
						35	0.046	178.95	15.97	122.74
						50	0.066	255.64	22.82	85.92
					7.64	20	0.027	102.26	9.13	288.08
						35	0.046	178.95	15.97	164.62
						50	0.066	255.64	22.82	115.23

0.5	0.002	0.003	167.3	0	1.42	20	0.047	140.42	10.86	30.11
						35	0.083	245.74	19.00	17.21
						50	0.118	351.06	27.14	12.04
					2.85	20	0.047	140.42	10.86	60.76
						35	0.083	245.74	19.00	34.72
						50	0.118	351.06	27.14	24.30
					4.29	20	0.047	140.42	10.86	91.4
						35	0.083	245.74	19.00	52.8
						50	0.118	351.06	27.14	36.45
					5.72	20	0.047	140.42	10.86	121.52
						35	0.083	245.74	19.00	69.44
						50	0.118	351.06	27.14	48.61
0.5	0.002	0.004	125.5	0	1.94	20	0.027	102.26	9.18	72.96
						35	0.046	178.95	15.97	41.69
						50	0.066	255.64	22.82	29.18
					3.88	20	0.027	102.26	9.13	146.24
						35	0.046	178.95	15.97	83.57
						50	0.066	255.64	22.82	58.50
					5.82	20	0.027	102.26	9.13	219.53
						35	0.046	178.95	15.97	125.45
						50	0.066	255.64	22.82	87.81
					7.77	20	0.027	102.26	9.13	292.82
						35	0.046	178.95	15.97	167.32
						50	0.066	255.64	22.82	117.13
0.5	0.002	0.003	167.3	0	1.80	20	0.047	140.42	10.86	38.11
						35	0.083	245.74	19.00	21.78
						50	0.118	351.06	27.14	15.24
					3.74	20	0.047	140.42	10.86	79.33
						35	0.083	245.74	19.00	45.33
						50	0.118	351.06	27.14	31.73
					5.68	20	0.047	140.42	10.86	120.55

						35	0.083	245.74	19.00	68.89
						50	0.118	351.06	27.14	48.22
					7.63	20	0.047	140.42	10.86	161.78
						35	0.083	245.74	19.00	92.45
						50	0.118	351.06	27.14	64.71
0.5	0.002	0.003	167.3	0	1.92	20	0.047	140.42	10.86	40.77
						35	0.083	245.74	19.00	23.30
						50	0.118	351.06	27.14	16.31
					3.87	20	0.047	140.42	10.86	82.00
						35	0.083	245.74	19.00	46.85
						50	0.118	351.06	27.14	32.80
					5.81	20	0.047	140.42	10.86	123.22
						35	0.083	245.74	19.00	70.41
						50	0.118	351.06	27.14	49.29
					7.75	20	0.047	140.42	10.86	164.44
						35	0.083	245.74	19.00	93.97
						50	0.118	351.06	27.14	65.78

Table 2.6. Design and operational conditions for all the SMRs ordered to by their length.

Internal Tube Diameter (m)	Number of Elements (-)	Length (m)	Flow Rate (mL/min)	Flow Velocity (m/s)	Reynolds Number (-)	Theoretical Mean Residence Time (s)
0.01	12	0.03	20	0.001	10.58	28.26
			35	0.002	18.52	16.15
			50	0.003	26.46	11.30
	24	0.06	20	0.001	10.58	56.52
			35	0.002	18.52	32.30
			50	0.003	26.46	22.61
	36	0.09	20	0.001	10.58	84.78
			35	0.002	18.52	48.45
			50	0.003	26.46	33.91
	48	0.12	20	0.001	10.58	113.04
			35	0.002	18.52	64.59
			50	0.003	26.46	45.22

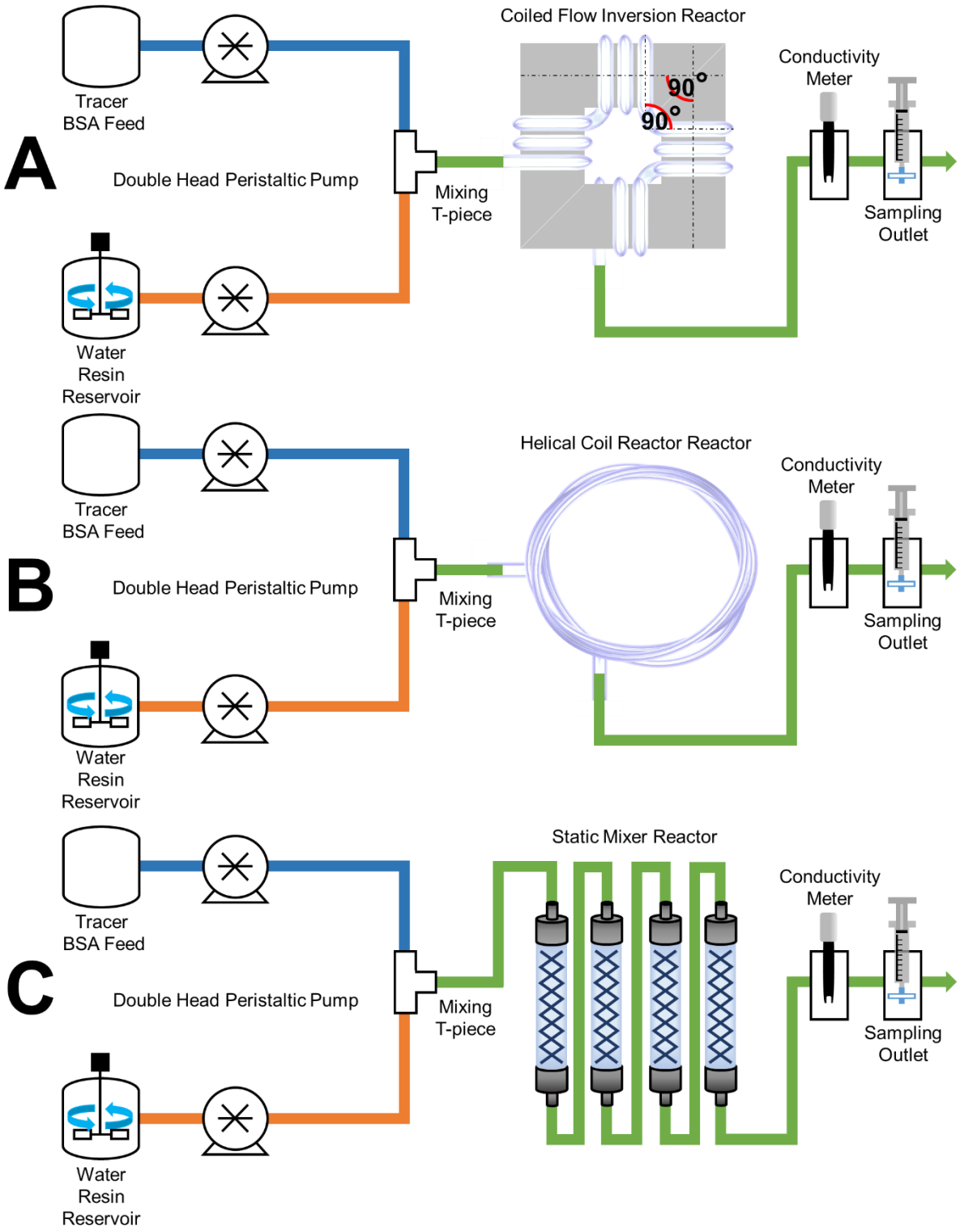

Figure 2.7. Schematic of the different reactors: A) CFIR, B) HCR and C) SMR. Each reactor had a mixing T-piece, an outlet for conductivity and sampling. The CFIR varied its number of inversions from 0 to 3. In turn, HCR reactor length varied to match the CFIR length. The SMR reactor length was varied by adding or removing individual modules.

2.18 Average Residence Time Distribution

In order to characterise the CFIR, HCR and SMR, average RTD studies were performed. Step functions with MilliQ water and 1 M NaCl solutions were used as tracers. The conductivity change in the solution was evaluated. The experimental rigs for the three type of reactors are displayed in Figure 2.7 in Section 2.17. All of the rigs were operated in the same manner. The flow rate for the double-head Masterflex peristaltic pump was set to three different flow rates of 10, 17.5 and 25 mL/min per head, giving a total unified flow rate of 20, 35 and 50 mL/min, disregarding the coil, coiled tube and static mixer diameter. The conductivity changes were made in both possible directions. First, the system was filled and equilibrated with MilliQ water or 1 M NaCl. Once the conductivity in the outlet was stable, the counterpart solution was pumped into the system. The measurements stopped when the conductivity stabilised.

2.19 Batch Binding Capacity in Reactors

The adsorption rate inside all the reactors was measured in a similar manner as adsorption in static mixers described in Section 2.4.2. The same experimental rigs for the three type of reactors used for average RTD studies were used. This are shown in Figure 2.7 in Section 2.17. The BBC studies were performed using 2 mg/mL BSA in 20 mM phosphate buffer pH 7 for solution A and 20 mM phosphate pH 7 for solution B. A final 5% (v/v) resin slurry concentration (diluted concentration) of Macro-Prep High Q was used for all the BBC studies in this set of experiments. In order to quantify the BBC, the free BSA at the outlet of each reactor was collected by an Acrodisc syringe filter containing a 0.2 μm pore size hydrophilic Super® membrane that was fully retentive to the resin particles and later, the UV-adsorption at 280 nm was read in 96-well samples. Finally, the free BSA signal was compared with the original BSA concentration to obtain the BBC.

Chapter 3: Design, Construction and Characterization of Continuous Counter-Current Tangential Chromatography System for Therapeutic Protein Purification

3.1 Summary

According to the creators of the CCTC technique, the system has superior capabilities at handling a binary mixture. However, the system itself is not commercially available. In order to review the CCTC design reported in literature, a recreation of the system was done at laboratory scale. This chapter describes the studies and steps done in order to build a functional 2-stage step CCTC system. It includes, the characterisation of the detection and concentration determination of BSA and myoglobin; the characterisation and modelling of the adsorption/desorption kinetics in different resin matrices for use in the mixing modules and the characterisation and modelling of the behaviour of the hollow fibre at different fluxes. Finally, the measurement of the PSD of both resins after being used for CCTC test runs is shown to review the structural conditions.

3.2 Introduction

It is essential for a study such as this to characterise the mixing and solid-liquid separation modules that make the CCTC system to test and assess the purification technique, as well as the protein adsorption and desorption kinetics of the proteins that will be used through the whole project. The characterisation of the static mixer and hollow fibres is the focus of this chapter.

This chapter describes the steps utilised for the characterisation and building of a 2-stage batch CCTC system. In order to test this separation technique a suitable analytical method is developed and its robustness tested in Section 3.4.1. Section 3.4.3 describes the measurement and calculation of the protein adsorption/desorption kinetics. Section 3.4.4 presents a binding kinetics model using the previous results presented for further use in Section 3.4.6, which determines the static mixer residence time method for protein adsorption and desorption. A description of the critical flux method and model for the operating condition for the hollow fibre is presented in Section 3.4.8 and 3.4.9. Finally, a measurement of the PSD of both resin types after use in the preliminary CCTC system in Section 3.4.10.

3.3 Theoretical Considerations

3.3.1 Protein Detection and Quantification

This section describes the accurate quantification of BSA and myoglobin, including the measurement of the 96-well plate volume path length. The operating procedure is described in Section 2.3.

Sample path length determination is done to increase precision and accuracy of the protein concentration measurement, as well as to mitigate some of the pipetting and human errors that might occur while handling the sample. Water is practically transparent between the wavelengths of 200 to 900 nm but has a particular absorbance peak near 977 nm. According to the Lambert law of light absorption, the characteristic absorbance of water can be used to measure the path length of any liquid sample. The wavelengths of 900 (baseline distant from water absorbance peak) and 990 nm (close to 1,000 nm to avoid any effect caused by varying temperatures) were selected for the determination. A standard curve was created as mentioned in Section 3.4.1.

In order to detect BSA and myoglobin via UV method, a wavelength scan was performed within the range of 200 and 1,000 nm as specified in Section 2.3.2. After selecting the specific wavelength for each protein (280 nm for both proteins and 500 nm for myoglobin), a standard curve was obtained for each protein independently explained in Section 3.4.3, as myoglobin to also absorbs light at 280 nm. A determination with both proteins is possible but the accuracy is significantly affected by doing so (Konstantinidis et al. 2018). Hence, an ion exchange packed column separation needs to be performed for each of the samples containing both proteins in order to ensure a correct concentration determination.

3.3.2 Protein Adsorption Kinetics

3.3.2.1 Protein Batch Adsorption Kinetics

Chromatographic resin performance is usually given by DBC but CCTC does not operate in the same manner. CCTC employs a binding capacity that will be established as BBC, as mentioned in previous sections. BBC varies from DBC in terms that the number of protein molecules remains constant throughout the experiment, unlike DBC that keeps a constant flux of protein feed throughout the whole run. The term BBC does not mean the system has reached equilibrium in terms of adsorption, it only refers to the binding capacity at a certain residence time at a certain protein concentration, usually at the moment where the rate of change of the binding capacity approaches to 0. The overall BBC determines the protein and slurry concentration in the system. If not, the type of matrix to accomplish the desired productivity.

In this chapter, the BBC at 3 min of Macro-Prep High Q and Q Sepharose FF is obtained in different initial BSA concentrations. As it is impossible to measure the protein inside the bead, the free protein in the solution gives an indication of the binding capacity of the resin at that certain point in time, calculated as described in Section 2.4.

After obtaining enough data, a BBC model was created for both resins. The model would allow us to predict and compare the BBC values that were not explored during any of the experiments, as well as to compare experimental data in order to quantify the level of adsorption in different reactors (Section 6.4.5.5). The modelled predictions will approximate a capacity according to a residence time, which will be translated into the static mixer design. The binding kinetics data were analysed using a simple lumped parameter model (Dutta, Tan, Napadensky, and Zydney 2016):

$$\frac{d\theta}{dt} = k_1 C_i (1 - \theta) \tag{7}$$

where

$$\theta = \frac{Q}{Q_{max}} \quad (8)$$

$$C_i = C_0 - \beta\theta \quad (9)$$

where

$$\beta = \frac{\varphi V_R Q_{max}}{V_S} \quad (10)$$

$$C_V = \frac{\sigma}{\bar{x}} \times 100 \quad (11)$$

$$V_S = V_M + V_R(1 - \varphi) + 0.3V_R\varphi \quad (12)$$

where Q is the binding capacity, Q_{max} is the maximum binding capacity, θ is the relationship between the capacity at any point in time and the maximum capacity, k_1 is the binding rate constant, C_i is the concentration of free protein at any point, C_0 is the initial concentration of free protein, φ is the slurry concentration, V_R is the slurry volume and V_S is the total volume of the solution.

3.3.2.2 Dynamic Binding Capacity

DBC is probably the most important aspect when choosing the most productive chromatography resin. There is always a need to keep looking for ways to improve the DBC by changing the nature or density of the ligands, support material or operating conditions. For this chapter, DBC studies were used to assess and establish operating conditions for the separation of BSA and myoglobin described in Section 2.8. However, these studies can also be used to assess the state of the matrix as described in Section 4.4.1.

All DBC experiments were performed in triplicate as described in Section 2.14. Column packing was assessed using an acetone 2% assay to verify the asymmetry of the pack-bed.

3.3.2.3 Protein Desorption Kinetics

The desorption kinetics of the target molecule from the resin matrix into the mobile phase is as crucial as the adsorption kinetics. Desorption kinetics is the phenomena that governs over the residence time of the resin slurry during the elution step. Typically, elution happens at a faster accelerated rate than adsorption. Thus, elution step times tend to be shorter. For this chapter, desorption studies were used to establish the ionic strength (salt concentration) and residence time required for total desorption of BSA from both resins. The residence time will impact on the design and dimensions of the static mixer required for the separation.

The desorption studies were performed in batch format to mimic the interactions inside the static mixer during a CCTC separation. The resins slurry was incubated for 30 min in a solution of 3 mg/mL to ensure total saturation and adsorption of the ligands. The experiments were performed in triplicate as described in Section 2.4.3.

3.3.2.4 Protein Batch Adsorption in Static Mixer Module

The role of the static mixer is to provide efficient mixing without any moving components. In this case, the mixing is indirectly involved with the adsorption and desorption of the material. However, it does not directly improve the kinetics in which the molecule of interest and the ligand interact. The adsorption and desorption in static mixers in CCTC work exactly as a batch adsorption but in a continuous mode, so sampling was done through a syringe fitted with a single use Acrodisc syringe filter as described in Section 2.4.2.

After recording the adsorption behaviour in batch mode and obtaining a reliable BBC model (Section 3.4.4), a set of static mixers were chosen considering the necessary residence time for a total adsorption and a total flow rate of 51 mL/min as reported in past literature and described in Section 3.4.6. Desorption was not tested in this particular case, as the target molecule desorbs from the matrix at a significant faster rate. Hence, the static mixer provided enough residence time for the elution step with the same dimension.

3.3.3 Critical Flux

The operating conditions for the whole CCTC system are mostly dictated entirely by the critical flux of the hollow fibre, as previously mentioned in Section 2.5. In order to obtain comparable results and test if the built CCTC rig is working as reported in literature, a similar hollow fibre model and the total flow rate (resin slurry + buffer feed) as the one reported in literature were used (Shinkazh et al. 2011).

The critical flux studies were tested with a peristaltic pump placed in the permeate outlet (Figure 2.1) rather than the retentate outlet, as the larger resin bead particles have the tendency to get stuck in the retentate inlet and outlet of the hollow fibre causing a false critical flux measurement. This problem gets accentuated when the slurry concentration is closer to 40% (v/v). Above 40% (v/v) the resin slurry starts to behave as a wet cake that is difficult to pump and eventually clogs the flow path. This makes a narrow tube diameter non-ideal because the risk of clogging increases drastically.

In order to characterise and predict any other critical flux under other parameters, the shear-induced diffusion model was applied to this instance. The one-dimensional convective-diffusion equation in the concentration polarization boundary layer is integrated over the accumulated deposit, assuming the ratio of the diffusion coefficient is equal to the bulk mass transfer coefficient, giving the following expression:

$$J = K\ ln\left[\frac{\phi_w}{\phi_b}\right] \quad (13)$$

where ϕ_w is the volume fraction at the membrane surface (usually 0.7 for spheres) and ϕ_b is the particle volume fraction in the suspension. The mass transfer coefficient, K, is derived from the Leveque solution for the corresponding heat transfer problem:

$$K = 0.81\left(\frac{\gamma_0 {D_s}^2}{L}\right)^{1/3} \quad (14)$$

$$D_s = 0.3\gamma_0 a^2 \quad (15)$$

$$\gamma_0 = \frac{4v}{r_0} \quad (16)$$

where γ_0 is the wall shear rate, L is the length of the hollow fibre and D_s is the effective particle diffusion coefficient, a is the particle radius (resin bead), v is the average suspension velocity and r_0 is the radius of the fibre. If we substitute all equations into Equation 13, we have a sole expression for the critical flux.

$$J = 0.312\ \frac{v}{r_0}\left(\frac{a^4}{L}\right)^{1/3} ln\left[\frac{\phi_w}{\phi_b}\right] \quad (17)$$

Equation 17 predicts the average pressure-independent flux correlated to the feed velocity and particle radius. The critical flux can also be correlated with the wall shear stress. The slope between the relation between the critical flux and the wall shear can be used for prediction for any particle size and slurry concentration, as well as the geometry o the hollow fibre.

$$\tau_w = \gamma_0 \mu \quad (18)$$

where τ_w is the wall shear stress and μ is the dynamic viscosity of the suspension.

3.3.4 Particle Size Distribution

In order to investigate the potential structural damage of the resin matrix due to the inherent flowing and pumping the system has during normal operation, PSD measurements were performed during the course of the first CCTC rig test runs as mentioned in Section 2.6. Structural integrity of the resin is crucial for any chromatographic operation, as the deviation from its original state or standard may cause a decrease in product quality or a safety hazard for the operator and consumer. The presence of fines or reduction of average particle size in the resin slurry already present or created by shear forces in the mixing or solid/liquid separation modules may foul the hollow fibre (increase system pressure), contaminate the product, reduce the cycle lifetime of the resin or hinder the binding capacity. The measurement of the particle size distribution is not an exact or definite measurement tool as the particle size approximation may find fines in the sample that are non-existent. This aspect is also explored as a possible explanation of the particle size shift.

3.4 Results and Discussion

3.4.1 Determination of Fraction Volume

The determination of the concentration of protein molecules on a 96-well plate format is affected if the experimental volume differs from the nominal value. The objective of the volume determination is to estimate the path length for each well for an accurate normalization and finally, estimate the protein concentration.

Experimental 20 mM phosphate buffer pH 7 volume fractions were calculated by linear regression based on Equation 1 with the resulting slope of 2,084.8 (d), and intercept of 3.1 (e) and a coefficient determination (R^2) of 0.99 as seen in Figure 3.1. Thus, the volume fit is considered as optimal to be used for all the measurements done throughout this project. The fraction path length was calculated by dividing the measured volume by the cross-sectional area of an individual well. The path length was further used to normalize all subsequent blanks and samples and it was also used as an indicator for any dispensing errors. The experiment was repeated with water but there was not a significant difference on the calibration curve between both solutions as the water itself is responsible for the wave length absorption at 990 and 900 nm. This was important to corroborate as buffer solutions with different components/salts were used for the variety of experiments.

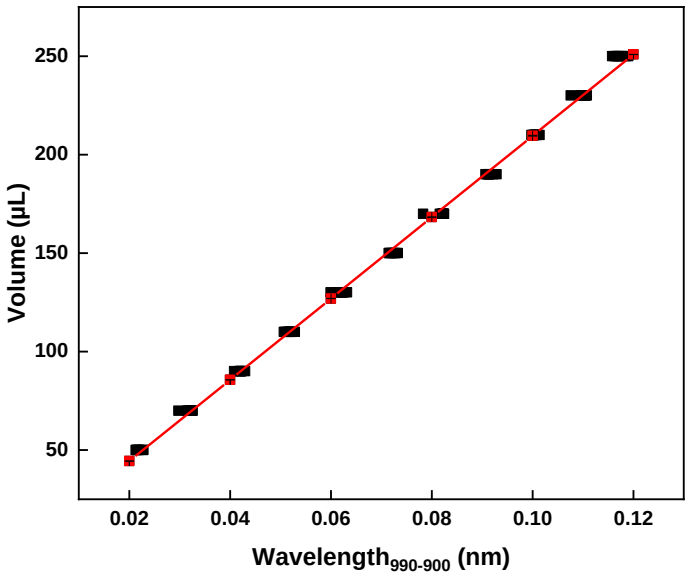

Figure 3.1. Volume measurements of 20 mM phosphate buffer pH 7 in a full area 96-well plate as a function of the difference between wavelength measurements of 990 and 900 nm. The red line represents the fitting line of the experimental data with a resulting slope of 2084.8 and a y-intercept of 3.1.

3.4.2 Selection of Wavelength for Protein Concentration

A complete wavelength scan was done for different BSA and myoglobin concentrations to determine the individual wavelengths for the construction of a standard concentration curve. Figure 3.2 and 3.3 show the normalized absorbance of BSA and myoglobin between 230 and 990 nm with and interval of 2 nm. BSA has an optimal absorbance at 280 nm, while myoglobin presents different peaks at 230, 280, 400, 500 and a minor peak at 630 nm. Both proteins presented some absorbance at 900 and 990 nm similar to the non-protein solutions. This absorbance is used for the volume determination mentioned in Section 3.4.3, evidencing that the concentration and volume determination absorbance measurements do not interfere with each other.

It was determined to use 280 nm for both proteins while being separated, as it is the most used wavelength for these species of proteins. However, myoglobin could also be reliably measured at 500 nm, as it does not overlap 280 nm and it gives a high enough signal to be quantified over a wide range of concentrations. Ultimately it was decided not to use 500 nm for myoglobin as most of the chromatography machines do not offer a possibility to choose a specific wavelength.

When both proteins are mixed, it is impossible to determine the quantity for BSA as myoglobin interferes with the absorbance at 280 nm. Even though a concentration determination curve for both proteins using the Lambert Law of light absorption can be done, the accuracy might be too low to be considered viable at low concentrations of a protein absorbing at 500 nm (Konstantinidis et al. 2018). In order to detect both proteins, an additional ion exchange separation step needs to be performed from the fractions obtained from the previous separation.

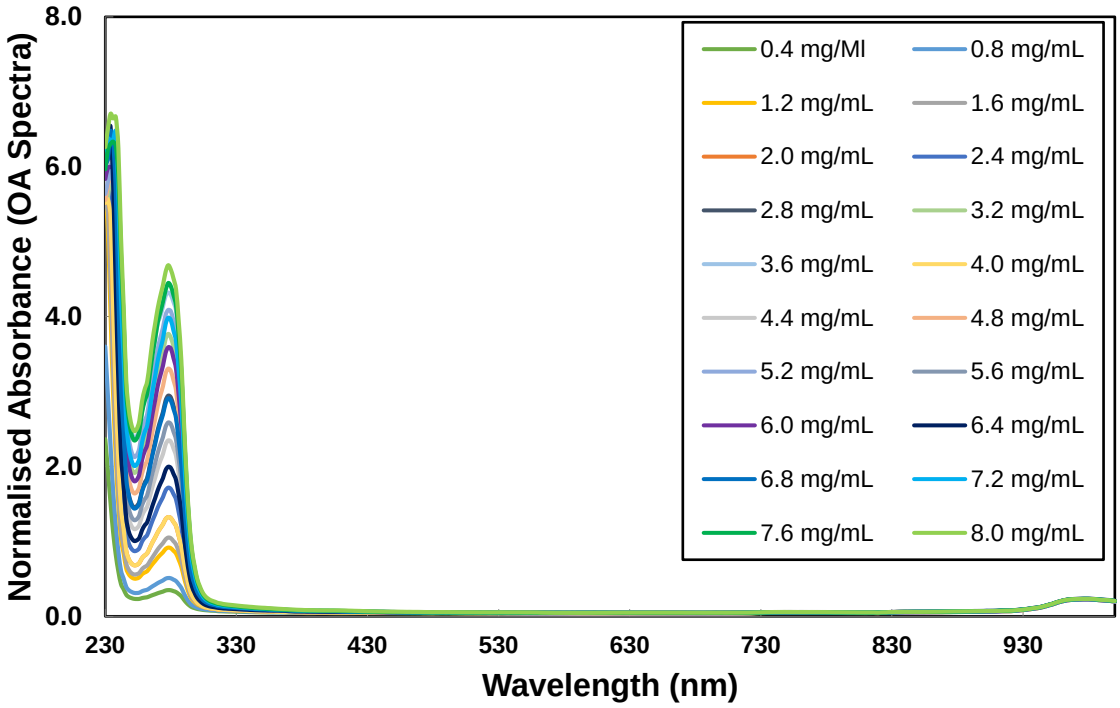

Figure 3.2. Wavelength absorbance data for a variety of BSA concentrations in 20 mM phosphate buffer pH 7 in a full area 96-well plate across a wavelength range of 230 and 990 nm.

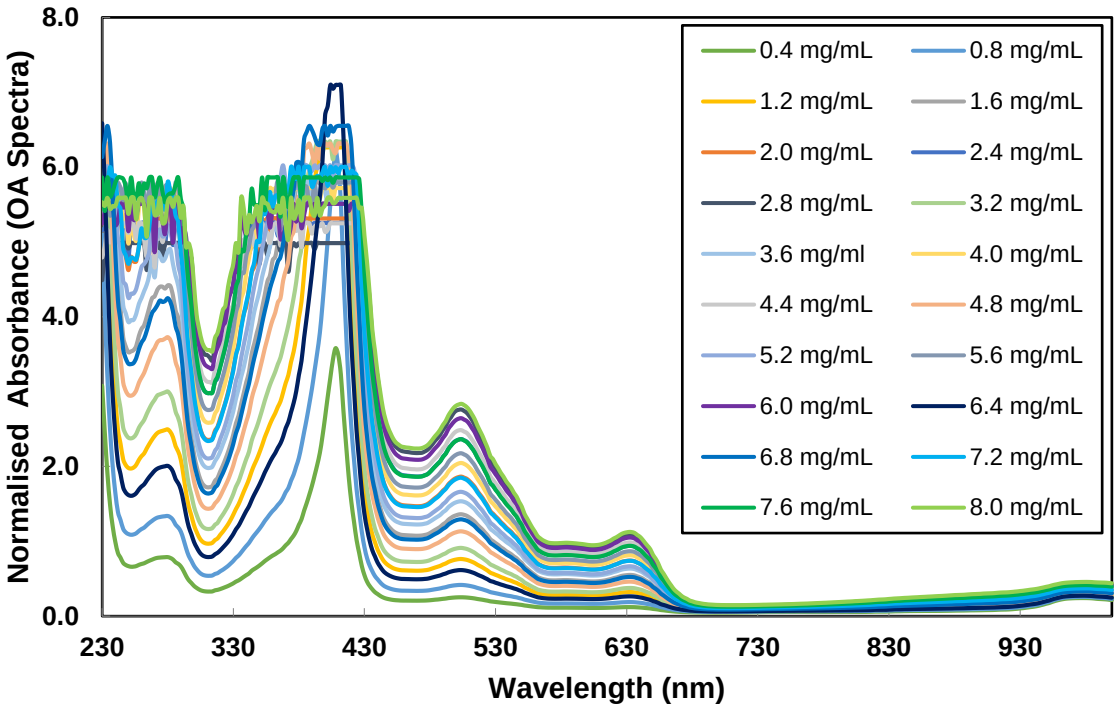

Figure 3.3. Wavelength absorbance data for a variety of Myoglobin concentrations in 20 mM phosphate buffer pH 7 in a full area 96-well plate across a wavelength range of 230 and 990 nm.

3.4.3 BSA and Myoglobin Concentration Determination

An individual concentration calibration curve was created for each protein. BSA and myoglobin calibration curve was based on the readings at 280 nm, as some of the chromatography equipment have limited wavelengths. However, a second separation in a separate ion exchange column is required in order to confirm the purity and yield of each protein.

Experimental BSA sample concentrations based on Equation 2 with the resulting slope of 1.7 (a_1), an intercept of –0.09 (b_1) and R^2 of 0.99. In similar manner, myoglobin experimental sample concentrations were calculated based on Equation 3 with the resulting slope of 2.4 (a_2), an intercept of -0.08 (b_2) and R^2 of 0.99. All coefficients were obtained from data presented on Figure 3.4 and Figure 3.5, respectively. There was a concern about the determination at high concentrations for both proteins as these points might escape the linear phase but the concentrations that are being used for the rest of the experiments do not exceed more than 5 mg/mL of protein.

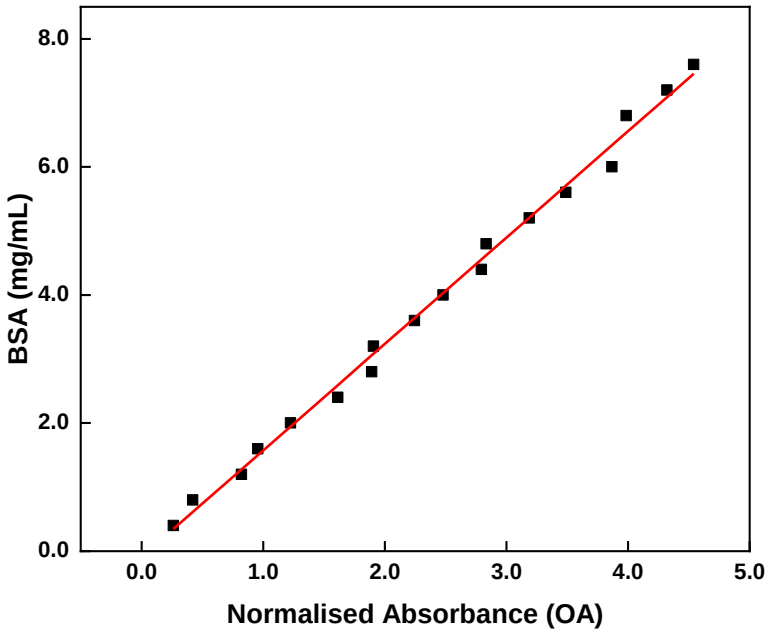

Figure 3.4. BSA wavelength absorbance measurements at 280 nm across different concentrations in 20 mM phosphate buffer pH 7. The red line represents the fitting line obtained from the experimental data with a resulting slope of 1.7 and a y-intercept of -0.09.

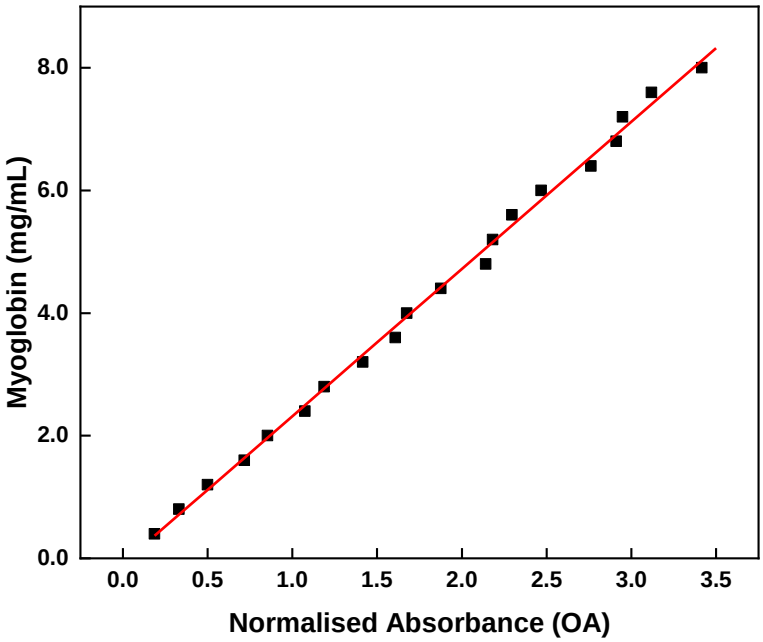

Figure 3.5. Myoglobin wavelength absorbance measurements at 280 nm across different concentrations in 20 mM phosphate buffer pH 7. The red line represents the fitting line obtained from the experimental data with a resulting slope of 2.4 and a y-intercept of -0.08.

3.4.4 Batch Binding Capacity for Residence Time Determination

The kinetics of BSA adsorption to the Macro-Prep High Q and Q Sepharose FF ion exchange chromatography resins were performed in a batch format. This studies are crucial in order to establish the minimum residence time needed to design the dimensions (diameter and length) of the set of static mixers in the system. Experimental data from BBC studies showing the BSA concentration in the mobile stationary phase (bound) as a function of time is presented in Figure 3.6. The data was obtained by mixing 6 mL of resin slurry 70% (v/v) with 34 mL of 3 mg/mL BSA. The initial concentration of BSA in the liquid phase at 0 s is 2.7 mg/mL assuming that the resin slurry contains 70% (v/v) solid particles and a porosity of 50%, giving 4.6 mL of liquid contained in the 6 mL of slurry, calculated with Equation 12. These assumptions were applied for both resins. The concentration in the liquid was calculated directly using the BSA calibration curve, as described in Section 2.4, while the adsorbed protein was calculated using Equation 4. The total volume for each calculation was assumed constant, as the total volume of the samples was less than 4% of the initial liquid volume and the protein and slurry concentration remains unchanged by the removal of liquid.

The initial concentration of free BSA decreases with time as the protein binds to the matrix until the bead reaches a saturation point. The bound protein to the resin increases within the same time. The binding kinetics are relatively fast but vary for each resin. Macro-Prep High Q reached a state of semi-equilibrium after 120 s, with a BBC of 18 mg/mL of resin; consistent to similar past literature (Shinkazh, et al., 2010). Q Sepharose FF reached a similar semi-equilibrium state after 200 s, with a BBC of 25 mg/mL.

The significant BBCs and binding time difference between both resins. The resins possess the same strong quaternary ligand. Therefore, ligand type does not explain the difference. The explanation for it can be attributed to bead size, ligand quantity and ligand density. Bead size directly affects the diffusion and mass transfer into the core of the bead (as mentioned in Section 1.5.2), slowing the process until it reaches saturation. A larger bead means a higher capacity, as there are more available ligands

for the protein to bind into but at a slower rate. The faster binding nature of Macro-Prep High Q is due to its 50 µm size while Q Sepharose FF struggles to keep up in this area due to its 90 µm diameter. Also, the type of support affects the ligand density, in this case Macro Prep-High Q is made out from methacrylate, while Q Sepharose FF from 4% agarose. A higher level of cross-linkage provides a higher surface area for the functionalisation of more ligands but increases the rigidity of the bead and in turn the pressure drop. These two resins present a trade-off between throughput and BBC. However, a thorough characterisation and analysis of each resin out of the scope of the project. The purpose of choosing these two types of resins is to observe the effects of CCTC in two beads with opposite rigid properties.

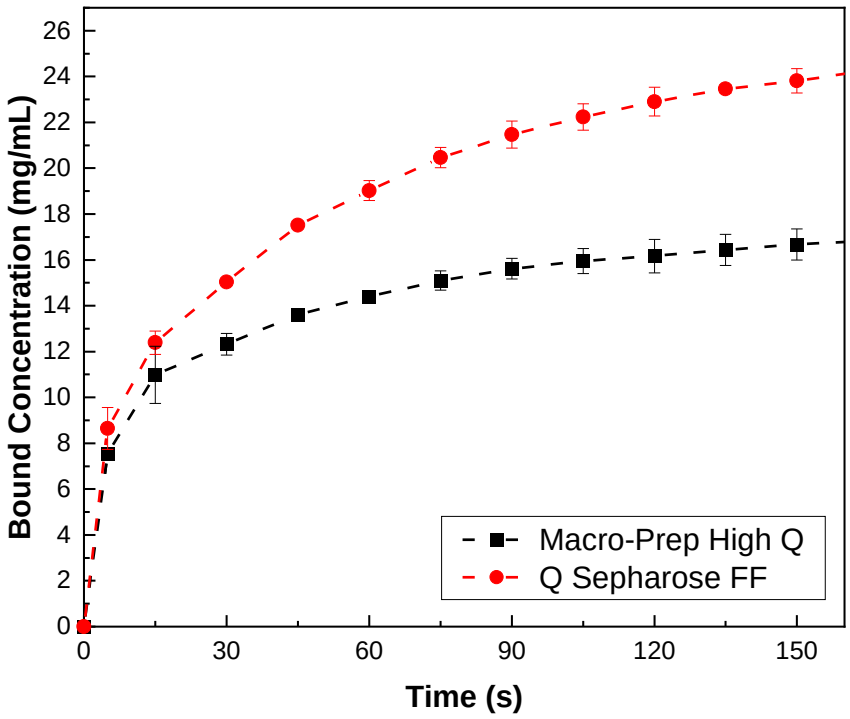

Figure 3.6. BBC experiment concentration results of BSA in solution bound to a resin slurry of 40% (v/v) Macro-Prep High Q (black) and Q Sepharose FF (red) in 20 mM phosphate buffer pH 7. The error bars represent the standard deviation of the samples (n=3).

The modelling of the BBC, as described in Section 3.3.2.1, was done to be able to predict the BBC values that were not explored; also to use the curve for comparison of the adsorption in the different mixing reactors discussed in Section 6.4.5.5. This prediction will approximate a BBC to a residence time, which will be translated into the static mixer design. Figure 3.7 and 3.8 show the lumped model over the experimental

data in Figure 3.6. The model is lumped at θ = 0.5 as the binding trend changes from a quasi-linear to a curved trend. The best fitting binding rate parameters in Equation 7 for the batch experiment for Macro Prep-High Q are k_1 = 1.3 min^{-1} and k_2 = 1.9 min^{-1}, and for Q Sepharose FF are k_1 = 0.9 min^{-1} and k_2 = 1.3 min^{-1}. These results make sense as the adsorption in Macro Prep-High Q happens at a much accelerated rate due to the decreased diffusive transport. The model had to be lumped into two halves due to the main ways of interaction (rate of adsorption) which are the external mass transfer through the film layer around the surface of the bead, the diffusion through the surface, the diffusion through the pore and the reaction rate at the binding site of the ligand (A. Rathore and Kumar 2017). The first half of the model is mainly controlled by the first two interaction ways (convective fluxes), while the second part is controlled by the diffusion of the target molecule into and through the pores of the bead (diffusive fluxes).

In order to validate the model, the percentage error was calculated for both resin types. Macro-Prep High Q had an average error of 0.08% and Q Sepharose FF an average of 0.4%. Figure 3.9 shows the individual percentage errors for each of the resins. The error seemed to increase for Macro-Prep High Q when the system is reaching an 80% to 100% BBC, suggesting the most difficult data to predict is mainly the diffusive flux section of the graph due to its smaller bead size. Furthermore, the highest error (-8.0%) detected in the model belonged to the time point at 0.5 min as it is where the model split into two. The steeper the curvature, the higher the error. For this reason, the model was divided into two sections to minimize the overall error. On the other hand, the error for Q Sepharose FF remained under 3% for the whole duration. In the end, the models for both resins are viable predictors because as a common practice in industry only 70% to 80% of the total capacity of the chromatographic resin is used in order to leave a safety region to avoid any product waste. Also, the error is lesser than 5% (except the isolated point where the model splits in two), making the model for Macro-Prep High Q a quite good approximation to the real value.

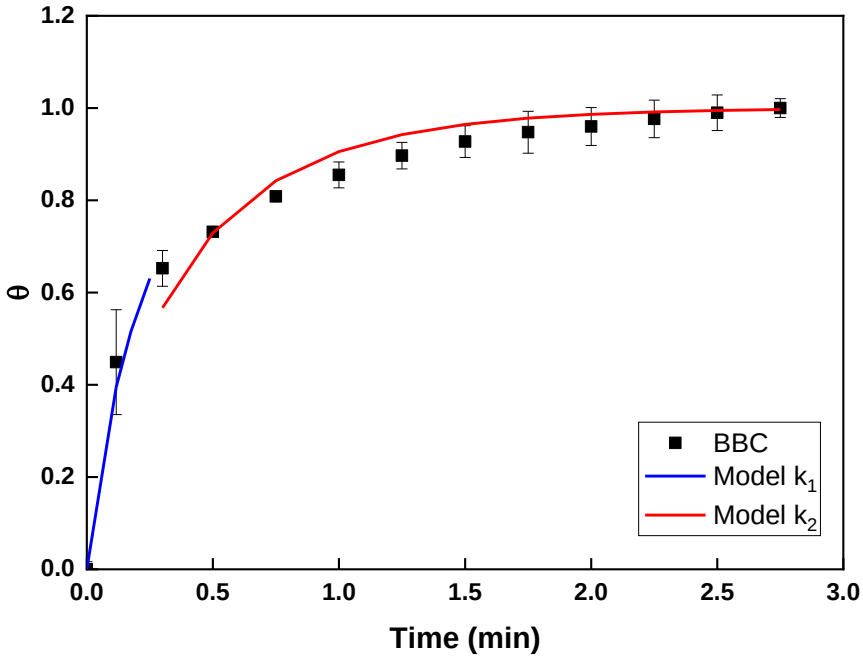

Figure 3.7. BBC model for the adsorption of 3 mg/mL BSA with 40% (v/v) Macro-Prep High Q resin slurry in 20 mM phosphate buffer pH 7. The constant model k_1 is 1.3 min^{-1} (< 50%) and k_2 is 1.9 min^{-1} (> 50%). The error bars represent the standard deviation of the samples (n=3).

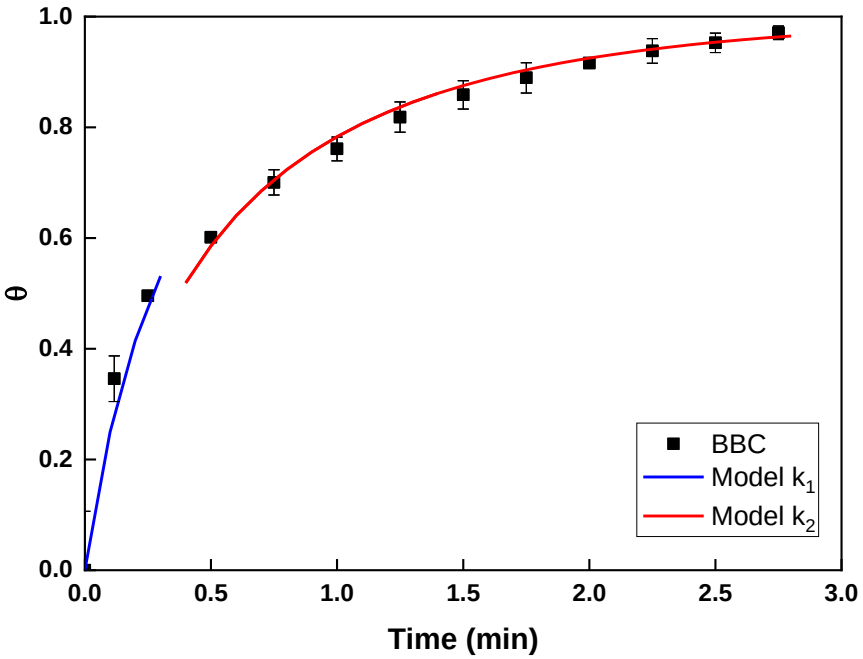

Figure 3.8. BBC model for the adsorption of 3 mg/mL BSA with 40% (v/v) Q Sepharose FF resin slurry in 20 mM phosphate buffer pH 7. The constant model k_1 is 0.09 min^{-1} (< 50%) and k_2 is 1.3 min^{-1} (> 50%). The error bars represent the standard deviation of the samples (n=3).

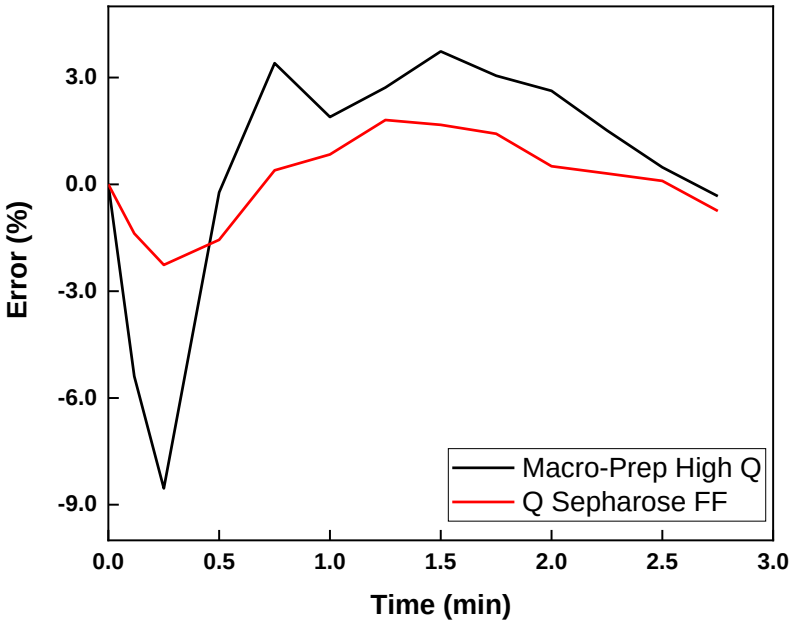

Figure 3.9. Percentage error of experimental data from the BBC studies for the adsorption of 3 mg/mL BSA with 40% (v/v) Macro-Prep High Q (black) and Q Sepharose FF (red) resin slurry in 20 mM phosphate buffer pH 7.

After reviewing the data, it was decided to purchase static mixers that would provide a minimum residence time of 120 s at 51 mL/min translated into four static mixers with a diameter of 1 cm and 30 cm length, even if the residence time needed for Q Sepharose FF is longer than that. The decision was made taking into account that as a common practice only 70% to 80% of the total BBC is used for manufacturing, as well as keeping the processing times as realistic and low as possible.

3.4.5 Batch Elution Studies for Residence Time Determination

Desorption studies were performed to determine the residence time required in the static mixer to achieve a complete elution of the product. The experiments were performed in the same batch format by increasing the ionic strength of the resin previously incubated with BSA by adding the adequate amount of NaCl. In both matrices a complete desorption happened < 60 s after reaching the concentration of 300 to 400 mM NaCl.

Both resins behaved similarly in spite of bead size and total number of ligands as seen in Figure 3.10. However, Q Sepharose FF takes slightly longer to reach the same free protein concentration due to the passive diffusion of the ion going into the pores of the bead and the passive diffusion of the BSA pouring out of the bead. This indicates that theoretically the static mixers for elution can be half the size from the ones used for binding, if the diameter and flow rate remains the same. The only parameter that cannot be changed between the steps is the flow rate. For the sake of the project, the chosen static mixers for binding will also be used for all the other stages, including elution. However, the reduction of residence time in other stages, such as elution and strip/CIP can further improve the overall productivity of the system.

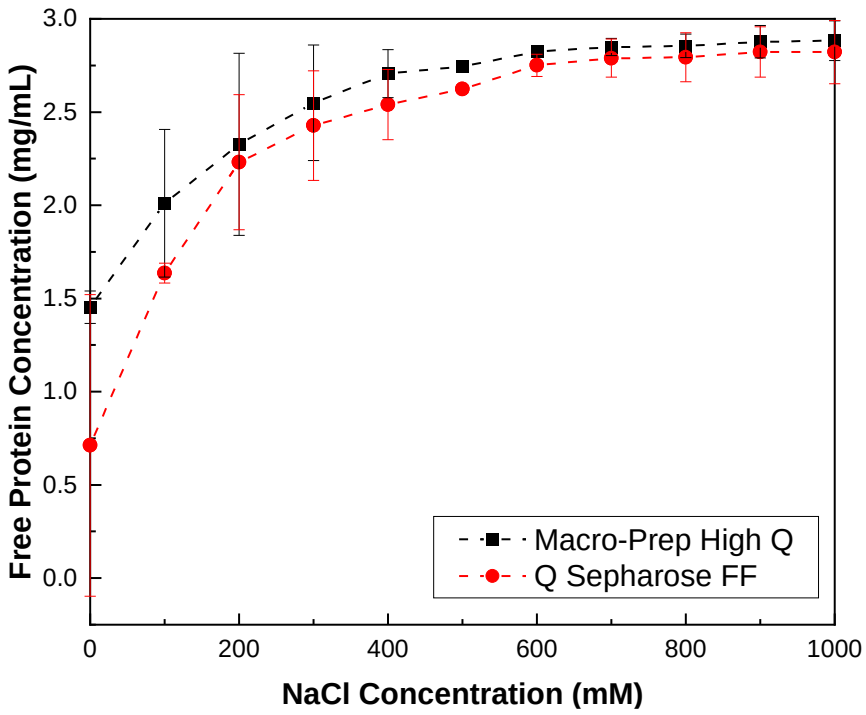

Figure 3.10. Batch desorption concentration results of free BSA concentration in the solution while the concentration of NaCl increased with time in 20 mM phosphate buffer at pH 7 using Macro-Prep High Q (black) and Q Sepharose FF (red) as stationary phases. The NaCl was raised every 20 s. The error bars represent the standard deviation of the samples (n=3).

3.4.6 Batch Binding Capacity in Static Mixer

The kinetics of BSA adsorption to the Macro Prep-High Q and Q Sepharose FF ion exchange chromatography resins were performed in a similar format as done in

Section 2.4.2 but in a continuous format. These studies were performed to ensure the resin slurry gets enough contact time for a complete adsorption. A resin slurry for both matrices of 20% (concentrated) and 5% (diluted) was used with a concentration of 3 mg/mL BSA for this experiment. The total theoretical residence time for the static mixers with dimensions already stablished in Section 3.4.4 was 120 s, a further analysis on the residence time was performed in Chapter 6 for comparison with other type of reactors.

The adsorbed BSA concentration for both chromatography resins in the static mixer outlet is shown in Figures 3.11. The BSA concentration could only be measured at the beginning and at the end of the flow path. The total concentration in each step reached steady state within about 90 s and 150 s for Macro Prep-High Q and Q Sepharose FF, respectively. The samples were taken for more than 500 s to ensure a steady state signal. The binding capacity was 16.1 mg/mL and 24.3 mg/mL, respectively. The measured BBC and residence time were compared to the models developed in Section 3.4.4 for validation and assessment of the performance of the static mixer. For both resins, the BBC and residence time match the modelled counterparts with an overall error of -3.8% for Macro-Prep High Q and +5.5% for Q Sepharose FF. ```

The results for both resins validated the design of the static mixers to give a sufficient residence time for adsorption of BSA under the operating conditions of 51 mL/min. Also, it has been confirmed that the adsorption happens uniformly and reaches steady state. As desorption occurs at least twice as fast as adsorption, the static mixers are also adequate for elution and strip steps.

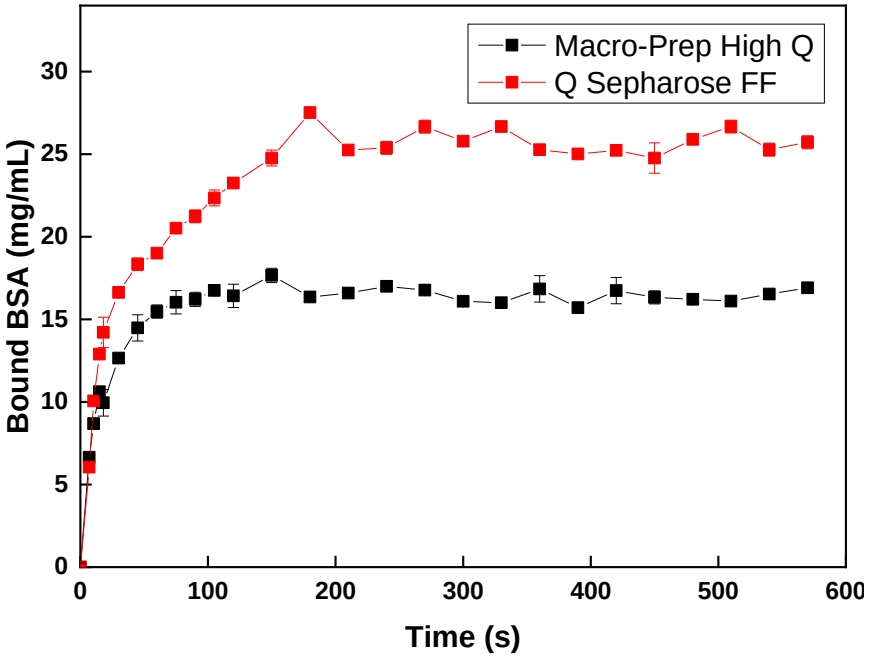

Figure 3.11. BBC concentration results of bound BSA in Macro-Prep High Q (black) and Q Sepharose FF (red) at the outlet stream of the static mixer modules with 48 elements and a total length of 1.2 m in 20% (v/v) resin slurry 20 mM phosphate buffer pH 7 at a flow rate of 51 mL/min. The error bars represent the standard deviation of the samples (n=3).

3.4.7 Dynamic Binding Capacity Studies

DBC studies are not directly relevant to a non-column membrane-based chromatography method, but are relevant for benchmark comparison, and for the quick assessment of the performance of the resin as BBC studies are lengthy and not automated. The DBC studies were carried out in 1 mL columns at different residence times that were further used in for the separation of BSA and myoglobin. The results are presented in Table 3.1, as well as the different flow rates and equivalent residence times for each column. These flow rates were chosen as the recommended velocities for normal operation as they wouldn't compromise the structural integrity of the resin.

Bio-Scale Mini Macro-Prep High Q Cartridge presented a constant DBC (10% breakthrough) of 34 to 36 mg/mL of resin, disregarding residence time. This constant DBC can be explained by the bead size and diffusive transport into the bead. HiTrap SP FF had a larger variation from 60.7 mg/mL to 75.4 mg/mL of resin, disregarding residence time. As explained before, the difference in DBC obtained with different flow rates and also in between the matrices is due to fact that Macro-Prep High Q resin

beads have an average size of 50 µm while Q Sepharose FF are 90 µm. This reduces the time for a single protein molecule to reach the core of the bead with diffusive forces. By the information shown in Table 3.1, it means that Macro-Prep High Q can be operated at a higher flow rate without losing any product, while Q Sepharose FF already experienced a product loss in the flow through at 0.5 mL/min.

The results in column format concur with the findings in batch mode. Macro-Prep High Q has an advantage in terms of residence time during adsorption, but Q Sepharose FF is capable of retaining a higher titre of product. For CCTC, the unchanged DBC within different flow rates is not relevant as the adsorption does not depend with velocity but it does depend on the total residence time and mixing.

Table 3.1. DBC results for both pre-packed columns with Macro-Prep High Q and Q Sepharose FF and the different RT/flow rates used for the experiments.

Column	Diameter (mm)	Height (mm)	Residence Time (min)	Flow Rate (mL/min)	DBC (mg/mL)
Bio-Scale Mini	5.6	40	1.0	1.0	34.6
Macro-Prep High			1.4	0.7	34.5
Q Cartridge			1.9	0.5	36.4
			3.3	0.3	36.4
HiTrap SP FF	7.0	25	1.0	1.0	60.7
			1.4	0.7	63.8
			1.9	0.5	70.0
			3.2	0.3	75.4

3.4.8 Critical Flux Experiments

Typical experimental data for the TMP from a critical flux experiments for water performed at permeate flow rate of 51 mL/min to provide a baseline for further slurry as feed. TMP values were averaged every 30 s at each permeate flow rate.

As seen in Figure 3.12, for t < 600 s, the permeate flux was maintained at a value of 31.8 L/m^{2}h (LMH) corresponding to a permeate flow rate of 15.4 mL/min and a feed conversion of 30%. The TMP remained constant over this amount of time. Similar results were obtained during the next flux increase intervals, with a statistically insignificant difference between the final and initial TMP. For t > 3,000 s, the permeate

flux was maintained at 63 LMH corresponding to a permeate flow rate of 30 mL/min and a feed conversion of 31%.

In Figure 3.13, a linear relationship between flux and TMP can be observed for all TMPs and fluxes registered. This indicates that there is no fouling in the system; hence, no critical flux was registered while operating with water. Individual pressure measurements are presented in Figure 3.14 confirming the constant TMP throughout all the intervals.

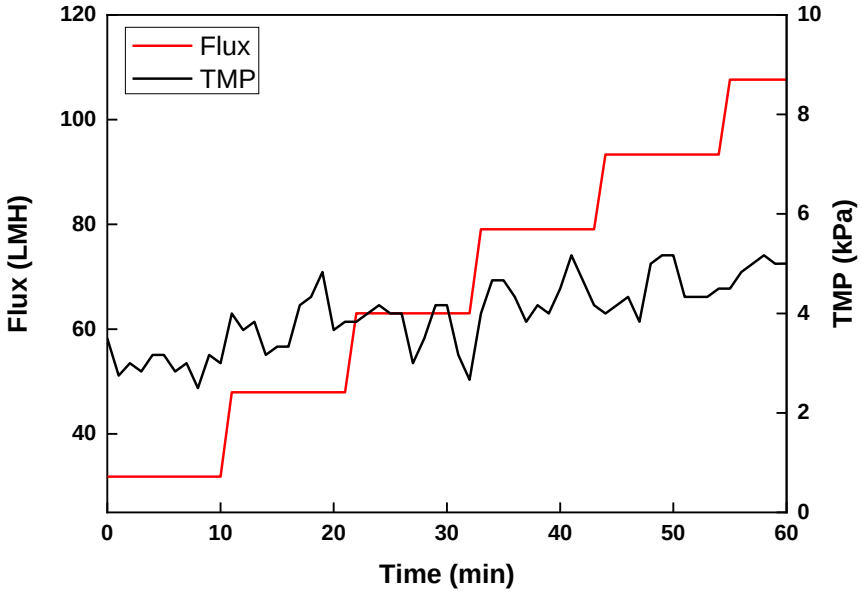

Figure 3.12. TMP and flux profiles in a hollow fibre module of modified polyethersulfone with a pore size of 0.65 µm, a tube length of 45 cm and a total membrane of 175 cm^2 against time during critical flux study in the hollow fibre module using deionised water. The flux was kept constant for 10 min before increasing it for each step.

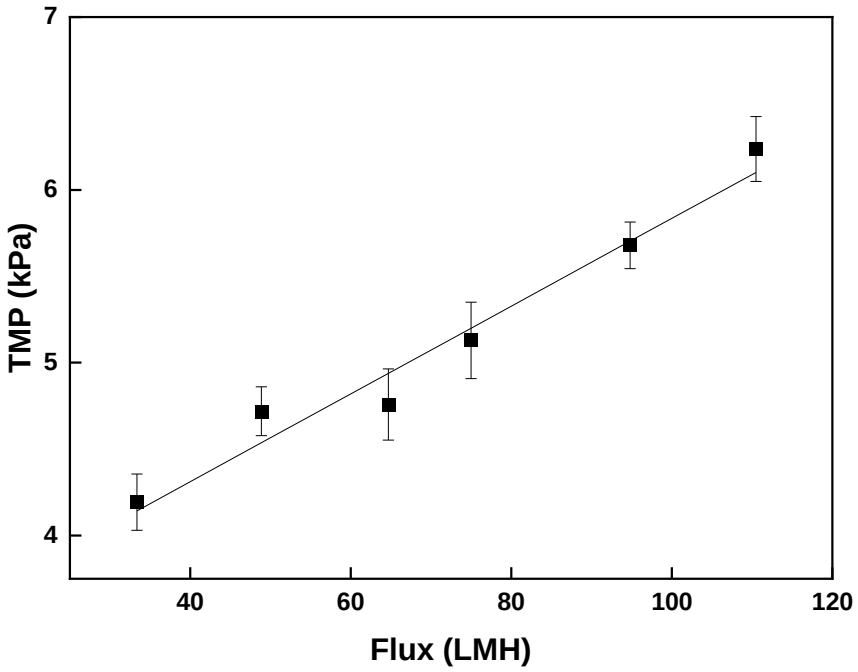

Figure 3.13. Relationship between the TMP and Flux during critical flux studies using deionised water in a single in a hollow fibre module of modified polyethersulfone with a pore size of 0.65 µm, a tube length of 45 cm and a total membrane of 175 cm^2. The flux was increased every 10 min to observe the resultant TMP. The error bars represent the standard deviation of the samples (n=3).

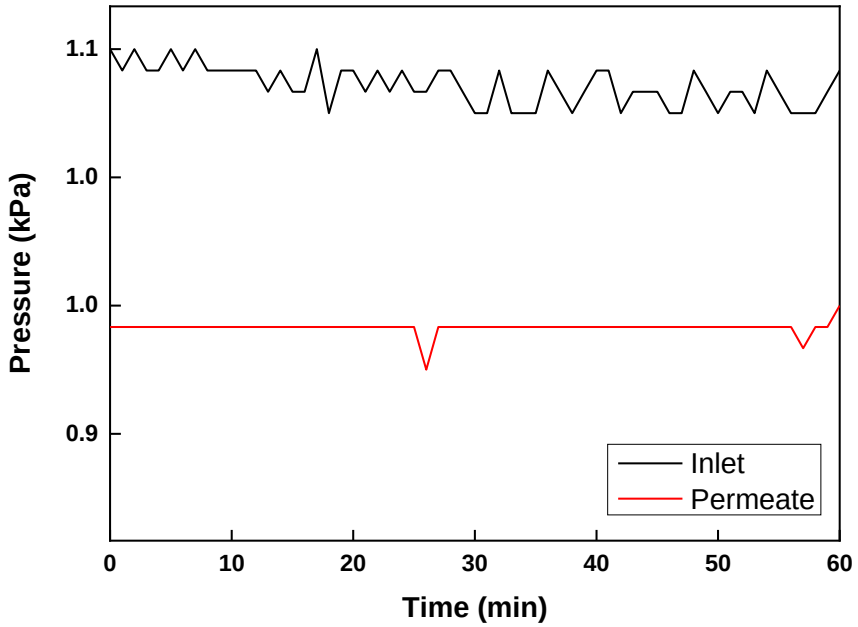

Figure 3.14. Inlet and permeate pressure profiles registered while performing the critical flux studies in a hollow fibre module of modified polyethersulfone with a pore size of 0.65 µm, a tube length of 45 cm and a total membrane of 175 cm^2 using deionised water.

Experimental results on TMP from a critical flux experiment performed with Macro Prep-High Q performed with 10% (v/v) slurry at a flow rate of 51 mL/mg are shown in

Figure 3.15. TMP values were averaged every 30 s at each permeate flow rate. For t < 6,000 s, the permeate flux remained at a value of 54.7 LMH corresponding to a permeate flow rate of 24.1 mL/min. This provided a conversion of 47.3% of feed to permeate and a final slurry concentration at the retentate outlet of 18%. A non-linear increase starter after 4,800 < t > 8,400 s reaching a maximum permeate flux of 93.4 LMH with a total flow rate conversion of 80% (40.8 mL/min). On the other hand, the TMP increased dramatically throughout the time interval above t > 8,400 s. This suggests the loss of membrane performance due to concentration polarization effects of the resin beads on the surface of the membrane. The critical flux for this set of operation conditions was determined to be around 55 LMH, it is the point where the TMP showed a linear behaviour. It was possible to run the system at higher fluxes above 55 LMH and below 93.1 LMH but the system seemed unstable, the permeate did not have a continuous flow and in several instances the inlet disconnected from the hollow fibre module during some of the test runs.

Figure 3.16 shows a clear linear relationship for t < 4,800 (< 54.7 LMH) and a non-linear relationship for t > 4,800, indicating the Flux/TMP in which the flux can be considered critical. The inventors of the CCTC system published some values for the critical flux data but it is not necessarily applicable to our experiments as they used a smaller resin bead with a discontinued hollow fibre module of unknown dimensions and pore size (Shinkazh et al. 2011). A total resin slurry of 6% (v/v) and 19% (v/v) resulted in a flux of 130 and 83 LMH. The results are not comparable, and they do not describe the physical behaviour of the system when reaching such high fluxes. However, different tests were done by maintaining a TMP of 15.5 kPa, which is translated to a flux of 76 LMH (75% permeate conversion), for at least 8 continuous hours and the system never fouled or stopped working as intended.

Individual pressure measurements are presented in Figure 3.17 showing that the permeate outlet has a steeper change after reaching the critical flux (>4,800 s). The critical flux run was reached but the system maintained an unstable and intermittent permeate outlet stream, however never reaching to a point where the tubing/connections connected to the hollow fibre snapped out of place due to the pressure. This behaviour is likely due to the formation of a cake layer on the membrane surface, decreasing the fibre radius. Also, this can be explained by the increase in

axial pressure drop caused by the increase in suspension velocity at the high particle polarization located at the exit of the hollow fibre.

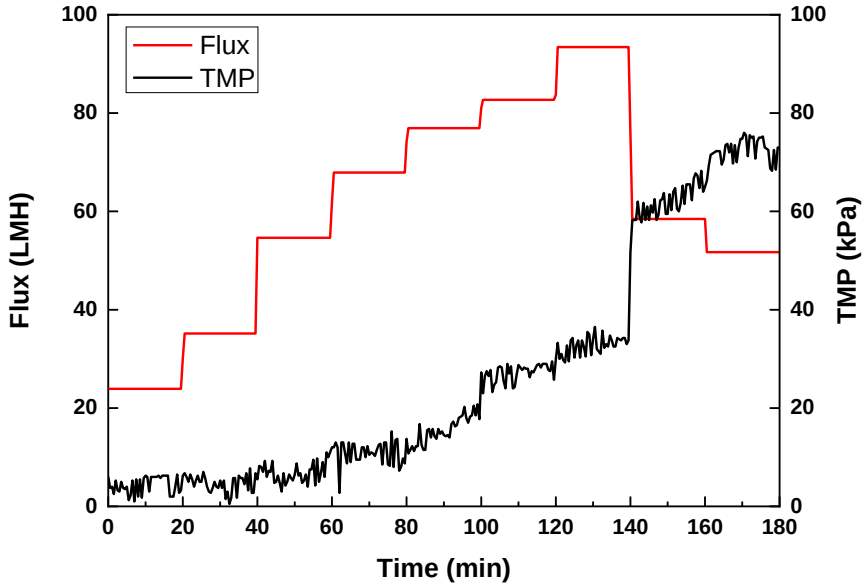

Figure 3.15. TMP and flux profiles against time during critical flux study in a hollow fibre module of modified polyethersulfone with a pore size of 0.65 µm, a tube length of 45 cm and a total membrane of 175 cm^2 using Macro Prep High Q 10% (v/v) resin slurry (diluted). The flux was kept constant for 10 min before increasing it.

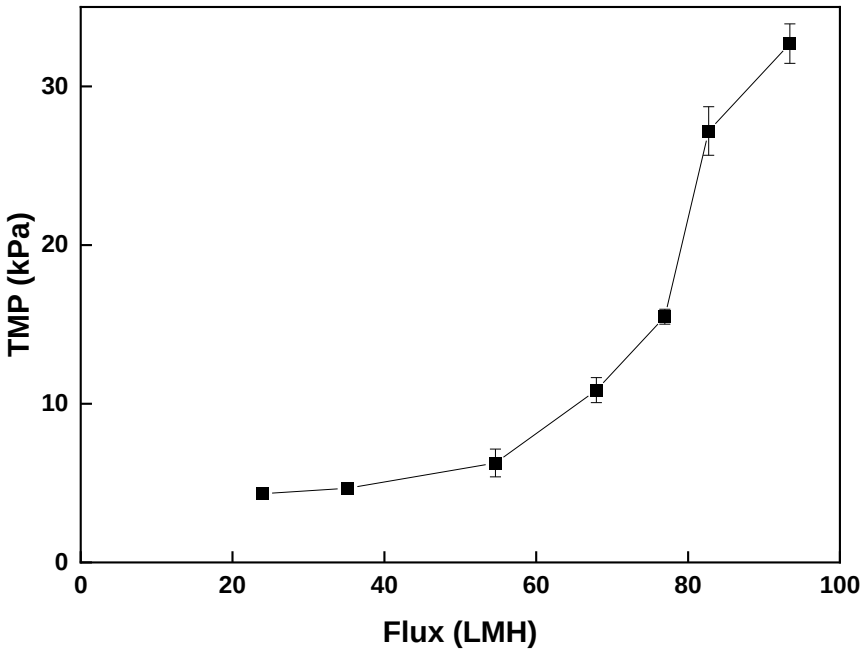

Figure 3.16. Relationship between the TMP and flux during critical flux studying using Macro Prep-High Q 10% (v/v) resin slurry (diluted) in in a hollow fibre module of modified polyethersulfone with a pore size of 0.65 µm, a tube length of 45 cm and a total membrane of 175 cm2. The flux was increased every 10 min to observe the resultant TMP. The error bars represent the standard deviation of the samples (n=3).

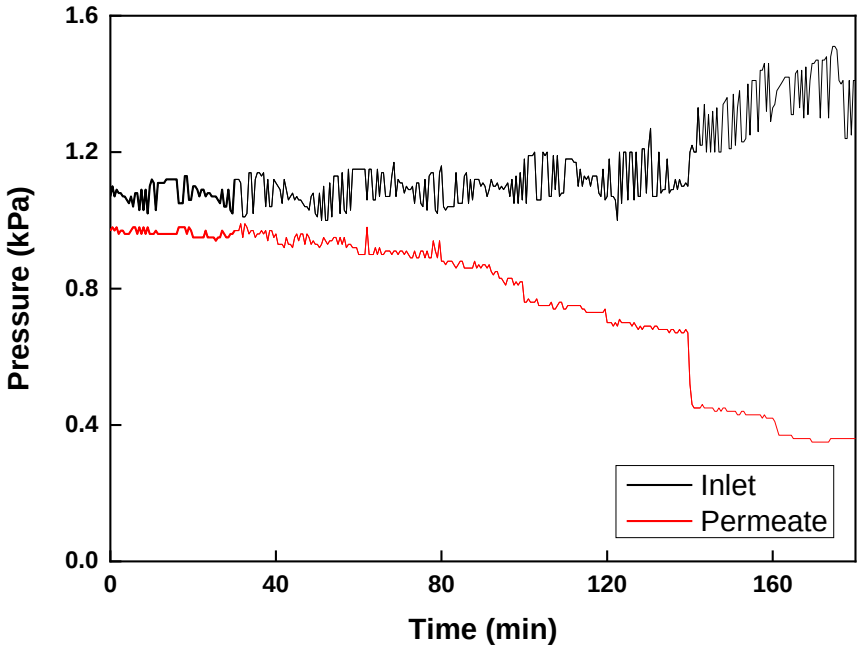

Figure 3.17. Inlet and permeate pressure profiles registered while performing the critical flux studies in a hollow fibre module of modified polyethersulfone with a pore size of 0.65 µm, a tube length of 45 cm and a total membrane of 175 cm^2 using 10% (v/v) Macro Prep-High Q resin slurry (diluted).

Experimental results for the TMP from a critical flux experiment performed with Q Sepharose FF performed with 10% (v/v) slurry at a flow rate of 51 mL/mg are shown in Figure 3.18. TMP vales were averaged every 30 s at each permeate flow rate. For t < 6,000 s, the permeate flux remained at a value of 74.6 LMH corresponding to a permeate flow rate of 36 mL. This provided a conversion rates of 69.6% of feed to permeate and a final slurry concentration at the retentate outlet of 34.1%. After t > 6,000 s, the permeate flux drastically increased up to 89.3 LMH with a feed conversion of 84.3% and a resin slurry of 32.9% until it abruptly stopped. The experiment was repeated several times but the ending result of inlet disconnection due to the increased pressure inside the hollow fibre was consistent in every test run, different from Macro-Prep High Q. On the other hand, the TMP increased dramatically during the time interval above t > 6,000 s. This suggests the loss of membrane performance due to concentration polarization effects of the resin beads on the surface of the membrane. The critical flux for this set of operation conditions was determined to be 74.6 LMH, as the last measurement where the TMP was operationally viable.

Figure 3.19 shows the linear relationship for t < 6,000 s and a non-linear relationship for t > 6,000 s, indicating the Flux/TMP in which the flux can be considered critical.

Compared to Macro-Prep High Q, it seems that the linear relationship between TMP vs flux is more prolonged for Q Sepharose FF

Individual pressure measurements are presented in Figure 3.20 showing that the inlet pressure profile seems to increase due to probable accumulation of resin in the exit of the fibre, as explained above for Macro-Prep High Q. However, the critical flux experiment drastically stopped every single time because the feed inlet abruptly disconnected from the hollow fibre due to high pressure. This behaviour is not observed in Macro-Prep High Q, this difference can be attributed to the larger resin bead size blocking completely the fibre radius or hollow fibre entry port.

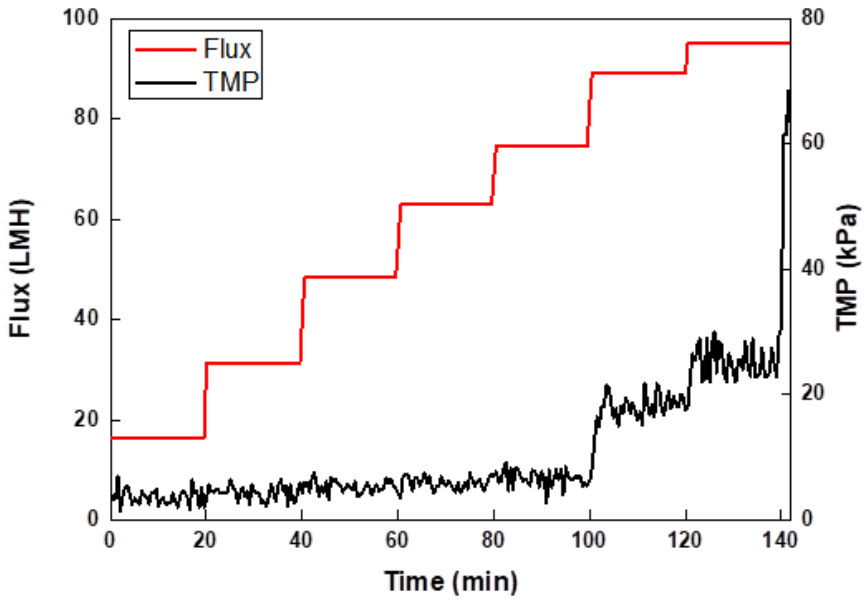

Figure 3.18. TMP and flux profiles against time during critical flux study in a hollow fibre module of modified polyethersulfone with a pore size of 0.65 µm, a tube length of 45 cm and a total membrane of 175 cm^2 using Macro Prep High Q 10% (v/v) resin slurry (diluted). The flux was kept constant for 10 min before increasing it.

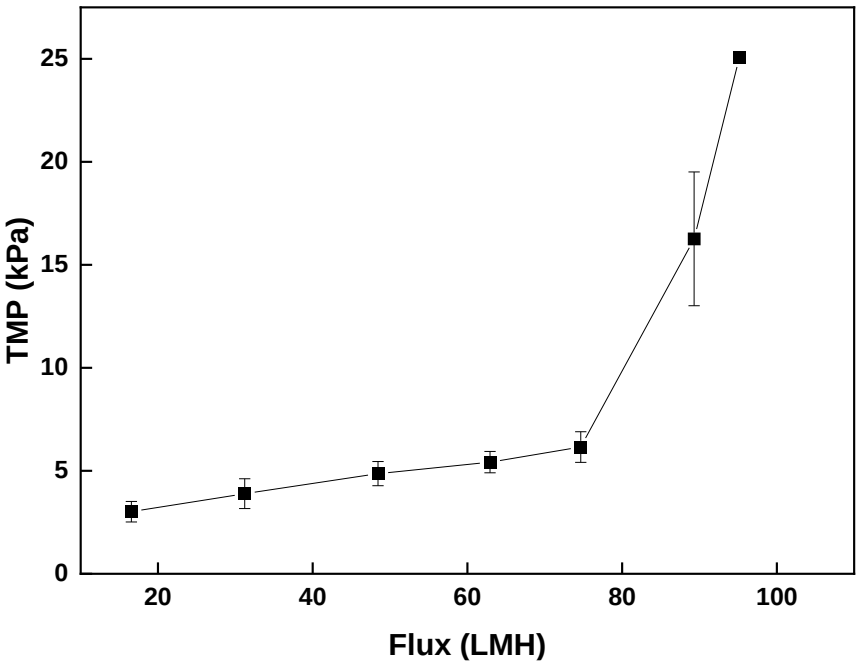

Figure 3.19. Relationship between the TMP and flux during critical flux studying using Q Sepharose FF 10% (v/v) resin slurry in a hollow fibre module of modified polyethersulfone with a pore size of 0.65 µm, a tube length of 45 cm and a total membrane of 175 cm^2. The flux was increased every 10 min to observe the resultant TMP. The error bars represent the standard deviation of the samples (n=3).

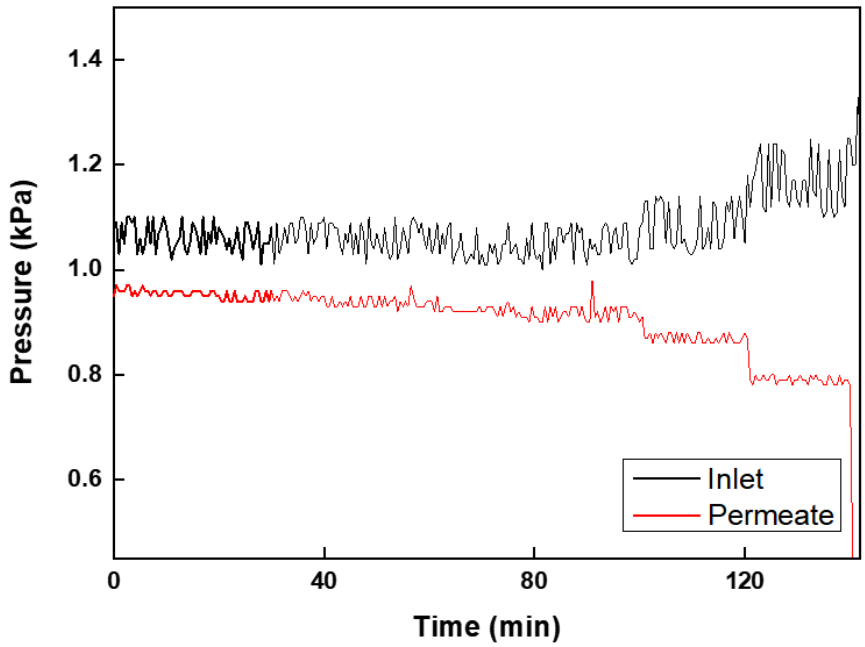

Figure 3.20. Inlet and permeate pressure profiles registered while performing the critical flux studies in a hollow fibre module of modified polyethersulfone with a pore size of 0.65 µm, a tube length of 45 cm and a total membrane of 175 cm^2 using 10% (v/v) Q Sepharose FF resin slurry (diluted).

In order to make sure the slurry concentration in the feed matched the one in the retentate outlet, the resin slurry concentration was monitored for both resins. The resin slurry feed (concentrated slurry) was initially pumped at 20% (v/v) and 40% (v/v) volume in 20 mM phosphate buffer pH 7. The feed flow rate was fixed at 51 mL/min, while the retentate flow rate was 13 mL/min and the permeate flow rate was 38 mL/min. The flow rates were established from literature and critical flux experiments. The resin beads were let to settle overnight before measuring the volume concentration.

The resin slurry concentration for both resin slurries and both resin concentrations reached a steady state after 6 min, after that point onwards the average concentration was 41.6% (v/v) and 21.4% (v/v) for Macro-Prep High Q and, 42.2% (v/v) and 21.7% (v/v) for Q Sepharose FF (Figure 3.21). This suggests that the slurry concentration at the inlet feed of the hollow fibre is approximately equal to the concentration in the rentate outlet at steady state. The slurry concentration takes around 5 min to reach steady state as the resin beads have to travel through the tubing and then a slight accumulation inside the fibres needs to happen first.

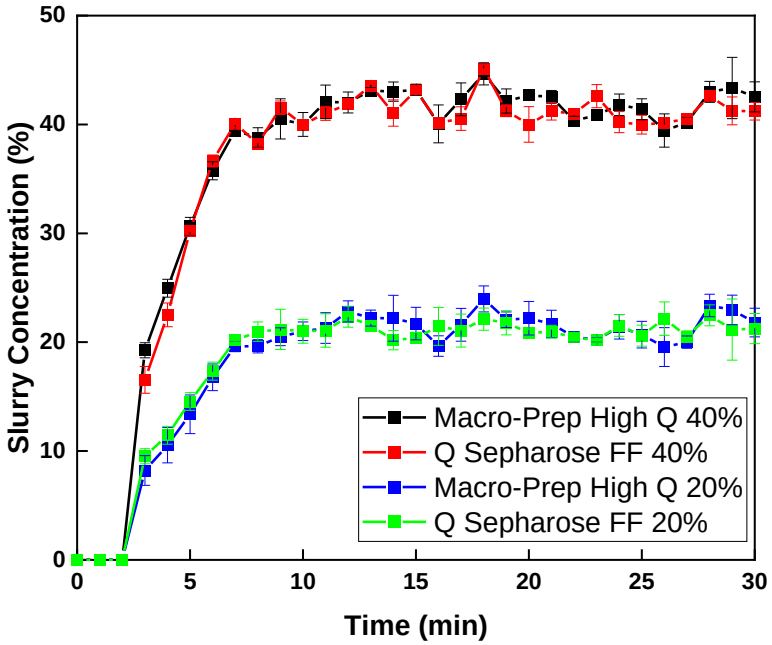

Figure 3.21. Resin slurry concentration measurements during a 30 min CCTC from the retentate outlet of a hollow fibre module of modified polyethersulfone with a pore size of 0.65 µm, a tube length of 45 cm and a total membrane of 175. cm^2 using 20% (v/v) and 40% (v/v) Macro-Prep High Q and Q Sepharose FF resin slurry. The error bars represent the standard deviation of the samples (n=3).

Based on these critical flux results for both resins, each stage in the CCTC system was designed to give an average flux of 70 LMH with a conversion of 75% corresponding to an inlet flow of 13 mL/min and a permeate flow of 38 mL/min. The intended slurry to be used for both matrices is 20% (v/v) for the concentrated slurry (retentate exit) and 5% for the diluted slurry (retentate inlet). The original experiments were done with a resin slurry of 40% (v/v) but it showed to be pushing the hollow fibres to their limits. As a consequence, a reduction of the resin slurry by half was decided to keep the system running without any unexpected interruptions due to a light polarisation effect on the membrane surface. The researchers involved in the development of the system seemed to notice this instability or limitation of the system as the concentrated resin slurry was reported to be 40% (v/v) for the first articles and then reduced by half or a third for the latest ones (Dutta et al. 2017; Shinkazh et al. 2011).

3.4.9 Critical Flux Model

Figure 3.22 displays the experimental and calculated values of the critical flux for Macro-Prep High Q and Q Sepharose FF 10% (v/v) slurry in a hollow fibre module of 45 cm, 0.65 μm and a total membrane of 175 cm^2 as a function of critical flux (J_{CRIT}) vs wall shear stress (τ_w). The critical flux data was evaluated using Equation 13 and the wall shear stress using Equation 18. The relationship is in agreement with the form given by the shear-induced diffusion model introduced and explain in Sections 1.8.1.8 and 3.3.3. However, the model heavily depends on accurate particle size measurements and assumes the total area is distributed under one single fibre. The model gives a good understanding as a starting point but for process manufacturing a dedicated resin slurry-hollow fibre model would be required for more accurate predictions.

In contrast, the inertial lift model was seen to not be a good critical flux model for the case of resin beads in form of a slurry in hollow fibres, as its data predictions are drastically different and predicts the data as a non-linear relationship.

As the data shows, the wall shear stress varies linearly with the critical flux. The data goes through the origin for both resins and has a residual error of -6.5% and -8.4% for Macro-Prep High Q and Q Sepharose FF, respectively. The fit of the data and the experimental data can be seen in Figure 3.22. The system was used to explore other conditions, i.e. a reduced slurry concentration in order to maintain a more stable chromatographic separation.

This model allows a starting point prediction of the overall operational conditions of the system as the feed, permeate and retentate flow rate (permeate flux), are all the crucial variables necessary in order to run the CCTC system safely. The change of flow rate before or mid-operational run can result in product loss due to insufficient residence time or even safety issues as pressure increases. The pressure increase causes clogging of the system due to the polarisation effect/cake formation and ultimately a rupture of any of the connections, static mixers or hollow fibres. A specialised CCTC model would be required in order to cement the solid/liquid separation design.

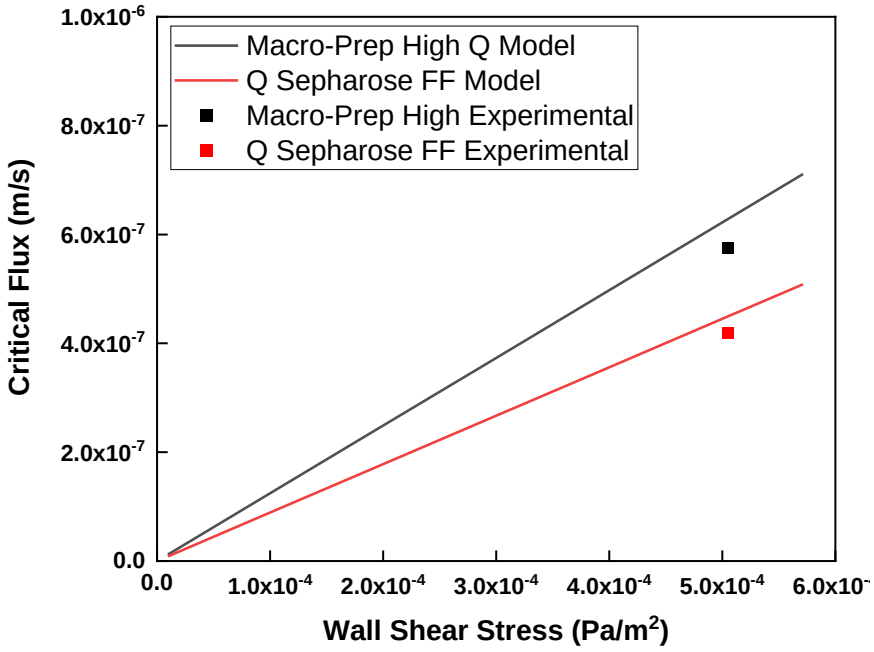

Figure 3.22. Theoretical and empirical critical flux for Macro-Prep High Q and Q Sepharose FF values as a function of wall shear stress with a feed resin slurry concentration of 10% (v/v) in a hollow fibre module of modified polyethersulfone with a pore size of 0.65 µm. The linear model is based in the critical flux theory known as the shear-induced model.

3.4.10 Particle Size Distribution

CCTC test runs were done in order to characterised, adjust and fix any operational condition before attempting the BSA and myoglobin separation. After a couple of hours of being recirculated through the static mixers and the hollow fibres, a PSD analysis of Macro-Prep High Q resin was performed to ensure there were no changes in resin slurry feed. The resin samples were buffer exchanged into 20% ethanol to reduce any background noise and non-existent fines. This buffer exchanged was done almost immediately after taking the samples by letting the samples settle. A fraction of the material was lost due to the small volumes.

Figure 3.23 shows the PSD of Macro-Prep High Q after being used for critical flux experiments and test for an equivalent of 8 h. The PSD for a fresh resin bead is 54 μm (10%), 74.2 μm (50%) and 101 μm (90%), while for the used resin is 31.2 μm (10%), 59.7 (50%) and 97.0 μm (90%). There was more than a 20% reduction on average particle size compared to new and unused chromatography matrices. The particle size reduction suggests that a component or a module in the CCTC system is exerting a significant shear upon the surface of the bead and, ultimately, chipping and/or cracking the bead open. The components that could cause this breakage would be the resin reservoir mixer, the static mixer (collisions into the sides of the tube and elements) and the TMP inside the hollow fibre membrane. This reduction can be clearly seen by the shifting of both peaks to a smaller particle size.

However, there is the presence of a secondary peak, even in the control/standard samples. This second peak is barely perceptible for some of the Macro-Prep High Q samples but it is quite prominent for Q Sepharose FF. These secondary peaks are not necessarily particles in the solution but a measurement or an analytical error done by the way the Mastersizer 3000 calculate the particle size values. The calculation method used by the machine is called the Fraunhofer approximation. The Fraunhofer approximation is a reliable approximation method as long as the sample sizes range below 50 μm and/or the material is not relatively transparent.

The particle size is measured by laser light diffraction spectrometry based on the fact that the scattering of light depends on the size of individual particles in the medium and on the particle collective. The smaller the particle, the more the light is scattered.

The scattered light forms a radially symmetric diffraction on the semi-circular detector. This procedure is particularly suitable for spherical and absorbing particles with diameters above 5 µm. Nevertheless, if the particles are transparent or semi-transparent it means that the particles do not absorb light. The transparency makes the particles to reflect or diffract it through, causing a miscalculation of the particle size. This miscalculation is presented in the presence of fine fractions (usually around 1 to 10 µm but can vary depending on the material and dispersant). This fictitious fraction is predicted by the Fraunhofer approximation but can be mitigated by using the appropriate values of the refractive index and absorption index of the material and, the dispersant in which the particles are being measured. Unfortunately, the manufacturer does not provide any of this values and obtaining them is time/resource consuming and out of scope. The software already has an approximation on those values (shown in Section 2.6) but they might not be good enough to mitigate all the transparency related issues. The relative refractive index for both materials is >1, which makes them appropriate for this piece of equipment in terms of scale (Teipel 2002; Storti and Balsamo 2010; Malvern Instruments Limited 2015; Ferraris, Bullard, and Hackley 2006).

By inspecting the data from Figure 3.23, the chromatography media made from agarose is the presenting these non-existent fines more prominently. This behaviour can be explained as agarose is more of a transparent material than methacrylate. These non-existent fines are attributed to the transparency and not to actual fines present in the samples as there are no fines present in samples shown in Chapter 4, where a more detailed look into the resin is displayed.

The dispersant in the samples played a major role on mitigating this non-existent fine peaks, being almost 100% successfully for Macro-Prep High Q. If the dispersant reflective index gets closer to the material, the Fraunhofer model would probably reduce or mitigate this non-existent fine peaks. The use of water during tests as a dispersant would increase the non-existent fine peak average size 10X. The replacement of water to a solution of 20% ethanol mitigated the problem but it did not solve it completely. This is due to the fact that the reflective index of ethanol is higher than the one of water and by replacing some of the water in the solution, it increases the average reflective index (approximately 1.33 for water and 1.36 for ethanol). Some tests with fresh resin and pure ethanol and isopropanol (reflective index of 1.38) were

also made with a higher success at removing the non-existent fine peaks. The replacement of all samples from a solution of 20% ethanol to an increased one was not possible due to the small sample volumes (significant material loss) and amount of samples. The samples had to be preserved in 20% as soon as possible as an increase percentage would damage them in the long-term and, the samples were not analysed immediately due to time constraints and equipment availability (Teipel 2002).

Another contributing factor would be the Mastersizer 3000 itself. This piece of equipment is made to measure particles of relatively large size, up to mm. This increased chamber would cause some particle overlapping for the particles in the smallest detectable range. This overlapping would make the peaks broader and less precise. Unfortunately, there is nothing to mitigate this effect as there was not another machine available for the measurement for this range of chromatography media sizes.

In general, there was a shift of 20% in the average particle size, disregarding the non-existent fines. The non-existent fines can be explained to mainly two factors: transparency of the material and dispersant. It was decided not to change the dispersant as the samples were measured in triplicate and for other analytical methods and the loss of material would be crucial. Also, the samples were not analysed immediately so exchanging them into pure ethanol/isopropanol and stored would definitely damage or destroy the sample. For this reason, Macro-Prep High Q samples did not display a significant of non-existent fines as it is the opaquer material compared to agarose.

Past literature has not thoroughly addressed this issue for commercially available chromatography media. Hence, Chapter 4 focuses on exploring the productivity hindrance and structural damage of the resin by exposing the resin to compartmentalised sources of shear before attempting a full separation in the custom CCTC rig.

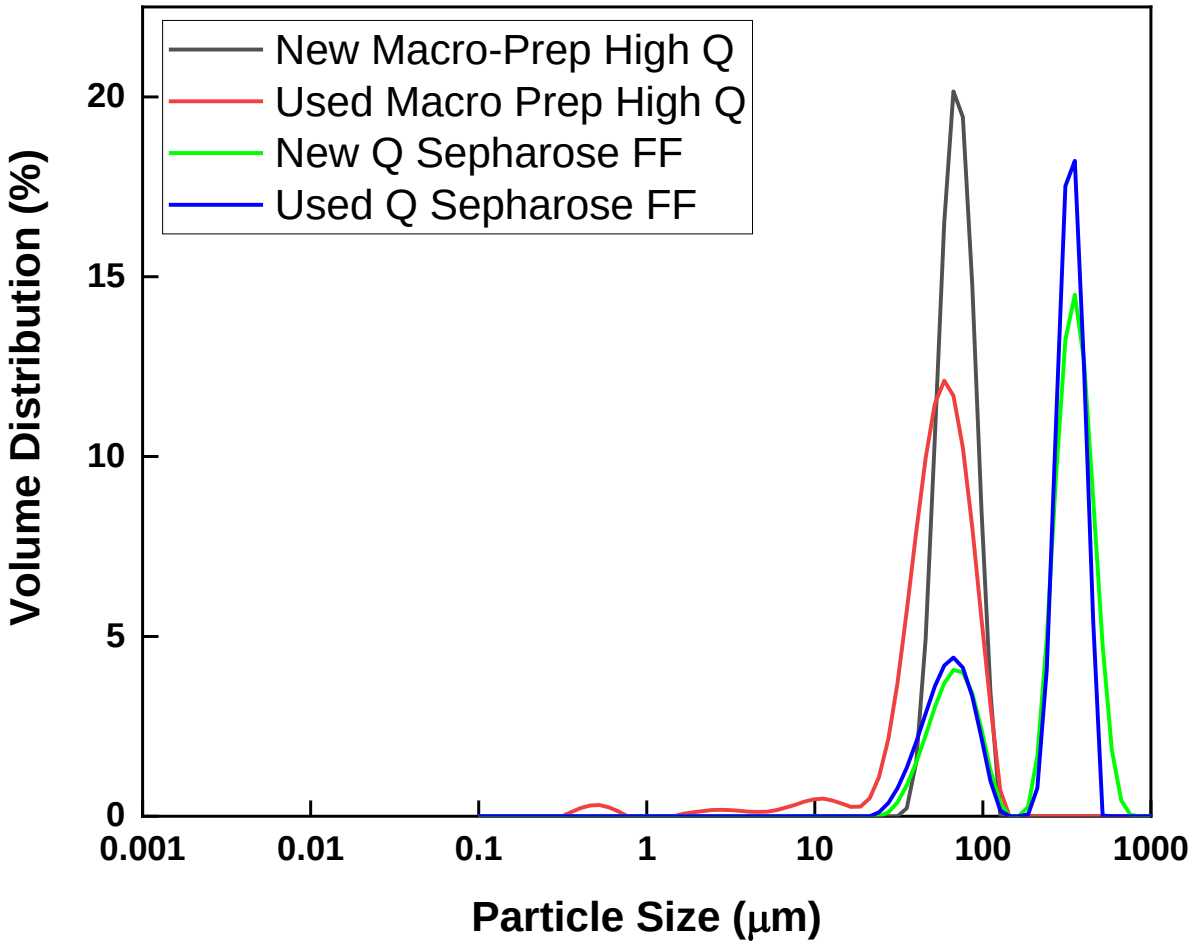

Figure 3.23. PSD diagram of fresh (black) Macro-Prep High Q and Q Sepharose FF (green) chromatography resin slurry and after using it for several cycles for BBC, batch desorption and critical flux studies (red and blue, respectively). Non-existent fines can be seen under the ranges of 0.1 to 100 μm.

3.5 Conclusion

As previously outlined, CCTC is a continuous manufacturing technique invented in 2010 with the intention to recreate traditional packed-bed AC separations without the need of a packed column by using the passive mixing provided by static mixers and the solid/liquid separation properties of hollow fibre modules (Shinkazh, et al., 2010). CCTC has proven to be a relatively simple (no packing needed), highly productive (major resin utilisation) and an efficient high throughput technique (low cycle time and continuous harvest) compared with to its competitors, such as SMB and PCC, but its novelty and lack of extensive literature backing these claims up have hidden the potential it can have to the public eye. The main limitation to stopping CCTC from becoming a highly studied chromatographic technique is the hurdle of acquiring or building a CCTC system and compatible materials involved in the separations.

This chapter explored the binding behaviour of BSA and myoglobin to the functionalised methacrylate (Q Sepharose FF) and agarose (Macro Prep-High Q) resin to determine the residence time needed for an efficient adsorption. Furthermore, the critical flux of the hollow fibre was tested under different flux and general flow rates with two resin slurries. The results showed that Q Sepharose FF had a higher BBC of almost 25 mg/mL but a longer residence time of 200 s due to its bead size of 90 µm compared to Macro-Prep High Q that had a BBC of 18 mg/mL and 120 s for residence time. The estimated critical flux was 76.4 LMH for Q Sepharose FF and 55 LMH for Macro-Prep High Q with a concentrated resin slurry of 20% (v/v). Appropriate models for BBC and critical flux were fully developed for the prediction of such values as well for the future references for determining BBC and CCTC operational conditions. According to these results and empirical tests, the mixing module was designed as a set of four 12-element static mixers with a combined minimum theoretical residence time of 120 s with a 1 cm diameter and 30 cm length, while the hollow fibre module of modified polyethersulfone with a pore size of 0.65 µm, a tube length of 45 cm and a total membrane of 175 cm^2 was set to be operated with an inlet/retentate flow rate of 38 mL/min and permeate flow rate of 13 mL/mL, for a total of 51 mL/min.

After all the characterisation and testing, Macro-Prep High Q particle size was measured. The average resin particle size had decreased around 20%, from 72.4 µm

to 59.7 µm. Some non-existent fines were measured predominantly in the samples with the agarose-based media, even after being mitigated by using a different dispersant. However, this noise did not change the fact that the media is being damaged or torn apart by the constant use in the system. This suggests that the constant use of the resin under the wall shear stress conditions inside the hollow fibre or shear stress caused by the peristaltic pump causes a wear and tear to the bead. This is a crucial aspect that needs to be addressed as the resin is intended to be used for several cycles to be cost-effective as it usually 70% to 80% of the total DSP costs, especially referring to Protein A resin. These are addressed in the next chapter before separating any proteins using a complete batch 2-stage CCTC system.

The main challenges faced while characterising the modules and building the CCTC system involved the consistency, sampling and repeatability of results as everything is done manually, without any automated help from an AKTA system as the elements or the system are not commercially available yet from Chromatan. As stated in the designated articles, the buffer usage for this system is approximately more than 3 times than traditional chromatographic techniques, especially if done in batch fashion mode as the priming, flushing and cleaning of the static mixer and hollow fibres has to be done after every step. Every experiment or test for BBC, critical flux or CCTC test required a minimum amount of 100 mL of resin and 2 L of the designated buffer for the step. A crucial aspect that is not touched upon in the articles is the resin slurry behaviour, performance and damage inside the system. The resin beads tend to quickly sediment at low flow rates and high slurry concentrations in tubes with larger diameters. This can be a problem if something goes wrong or the system needs to be paused or shut off mid-run, the beads will sediment inside the hollow fibre and tubing causing high pressure and even damage to the CCTC modules or pieces such as sensors or pumps. If a problem occurs, there is no other solution than flushing and cleaning the entire system.

At the point of characterisation and testing off the system, CCTC presents a lot of potential theoretically and empirically. Nonetheless, there is probably a long way to go in having CCTC as a staple biomanufacturing chromatography technique, mainly due to its novelty, lack of general knowledge and the requirement for troubleshooting for problems caused by resin sedimentation inside the hollow fibre.

Chapter 4: Revision of Current Continuous Counter-current Tangential Chromatography Design Aimed to Characterised the Structural Damage and Resin Productivity

4.1 Summary

It appeared that the use of the chromatography resin in a CCTC system is causing some unmeasured damage to the structure and possibly to its binding capacity. In order to review the lifetime of two types of media (agarose and methacrylate) after use in a CCTC system. This chapter describes the studies and steps done to assess quantitatively and qualitatively the degree of damage of the overall bead structure and surface. Additionally, the binding capacity of the beads is investigated after a prolonged operational time under different system configurations consisting of different parts of the CCTC design. The efficiency of the resin was studied by tracking the DBC after certain time intervals. The qualitative analysis was done by using a combination of freeze-drying techniques with SEM imagery; whilst the qualitative analysis is done by tracking the PSD and using an imagery software analysis tools.

4.2 Introduction

In the previous chapter, the design and characterisation of the mixing modules (static mixer) and solid/liquid separation modules (hollow fibre) was used for the building a custom batch 2-stage CCTC rig. Before attempting the binary separation of BSA and myoglobin, as well as the salt step-gradient ovalbumin separation into its major variants, a difference of PSD in the resin beads was observed after several critical flux and test runs of the CCTC system. Even though the resins were seemingly performing as intended, there was evidence that prolonged use (flow and pump of the resin slurry inside the CCTC system) was crucially damaging the beads.

This chapter looks to investigate whether the CCTC system can or cannot hinder the productivity (binding capabilities) and damage the structure of the bead in the short- and medium-cycle time. The hindrance is thought to be caused by either the difference of pressure/shear experienced inside the hollow fibre, the shear stress from the peristaltic pump or the mixing method in the resin reservoir. The damage was naturally recreated by using the CCTC system in different modes for a certain amount and time, as well as exposing the resin beads to a controlled shearing environment. The USD shear rotating disc device is an established method of mechanical characterisation

developed for high throughput studies. It is mainly used to determine the shear resistance of cells and aggregated proteins for further homogeniser, centrifuge or precipitation studies (Chatel, Kumpalume, and Hoare 2014; Voulgaris et al. 2016; Q. Li et al. 2013). However, it can be used for the purposes of this study. This chapter reviews the importance of safe and homogeneous process operations in terms of resin matrix.

The techniques will be applied to the two types of resin used mentioned beforehand in Chapter 2. The resin matrices are made up of agarose (Macro-Prep High Q) and methacrylate (Q Sepharose HP). The resin capacity is probably the most important characteristic for these types of technique as the resin is required to be working non-stop at a certain standard to guarantee the purity of the target molecule. Both materials represent the two opposite sides of the rigidity spectrum of chromatographic beads; Macro-Prep High Q being a rigid matrix and susceptible to break or chip under high forces and Q Sepharose HP being a softer one, which is susceptible to deformation. The productivity was analysed via DBC studies due to its higher consistency, repeatability and pragmatism; unlike BBC studies that require higher precision in terms of resin slurry concentration, manual sampling and analysis, and troublesome cleaning at small scale.

On the other hand, the resin beads need to withstand continuous shear, not present in traditional column chromatography, for a minimum number of cycles in order to ensure the quality of the product and justify the expensive production costs. The structural damage will be analysed by two means: PSD measurements and SEM imaging. The PSD allowed us to track quantitatively the breakage of the resin bead while SEM showed qualitatively the physical state of the resin at a certain given point in time. The correlation between the productivity with structural damage and PSD shift of both resins is discussed in this chapter.

4.3 Theoretical Considerations

4.3.1 Ultra Scale-down Rotatory Disc Device

The high shear studies were performed in order to push the matrices to their limits in terms of shear stress endurance under a short amount of time. It is necessary to convert the rotary speed into a quantifiable force. The rotary disc speed was related to maximum dissipation rate, ε (W/kg), which was derived empirically by previous studies (Chatel, Kumpalume, and Hoare 2014; Zhang et al. 2007) as follows:

$$\varepsilon\ (Wkg^{-1}) = \ 1.7\ \times\ 10^{-3}N^{3.71} \quad (19)$$

$$\varepsilon(Wkg^{-1}) = \gamma^2 \times \mu \quad (20)$$

where N is the disc speed (rev s^{-1}) and μ is the kinematic viscosity of the liquid. Three conditions were used: 2,000, 3,500 and 5,000 rpm. These conditions were chosen as 6,000 rpm is equivalent to conditions experienced in the feed zone of hydro-hermetic disc stack centrifuges, making these conditions harsh for the resin and still realistic. The wall shear stress can be theoretically calculated with Equation 18 and subsequently converted into a theoretical velocity with Equation 16 in Section 3.3.3. The viscosity of the slurry was assumed to be the viscosity of water at room temperature as the concentration was 10% (v/v) to mimic the maximum diluted resin slurry that the CCTC can handle. The USD rotary disc device studies were performed as stated in Section 2.12.

4.3.2 Continuous Counter-current Tangential Chromatography

Potential resin damage caused by shear from being pumped and flowing through pipes/tubes for prolonged amounts of time is central to CCTC, specially as structure

stability tests are mainly targeted for packed-bed columns. According to Amit K. Dutta, the CCTC system has been used for cycles of up to 8 h or longer (Dutta et al. 2015a). None of the articles expand on the fact that the commercially available resins might crack, chip, break, introduce a new contaminant/leachable or lower the overall quality of the final product on this regard. The first article explaining the CCTC system only presents a PSD after the short-use of the resin. There was no dedicated resin for this kind of system or operating fashion in the past. Until recently, Purolite Corporation has published the first article about a commercially available resin specifically done to withstand the CCTC binding and shearing conditions (Fedorenko et al. 2020). The creation of a dedicated resin increases the confidence that the companies might employ the use of this type of chromatography but also discourages the use or experimentation with any other type of resin (matrix, ligand or brand), reducing the choices for a better cost-effective decision.

According to the results in Section 3.4.10, the resin beads for both types (agarose and methacrylate) have changed in particle size after their use in the CCTC system. All the major variables that might influence on the extent of the performance and structural hindrance are outlined below:

- Rigidity of resin: type of matrix
- Resin reservoir: mixing/suspension method
- Peristaltic pump
- Pressure inside the hollow fibre module
- Flow through peristaltic tubing

The first 4 variables were put into test as depicted in Section 2.13. The rigidity of the resin was tested by having two kind of matrices. The resin reservoir was tested by having a magnetic stirrer and an overhead impeller as the mixing methods. The peristaltic pump and the 2-stage CCTC system (representing the pressure inside the hollow fibre) was tested by removing each element at a time. Unfortunately, it is impossible to get rid of the potential damage caused by flowing the resin slurry through the system but it can be minimised by reducing the void volume between components, such as resin reservoir, peristaltic pump, static mixer and hollow fibre. Figure 2.6 shows the different rigs and components used for the experiment.

4.3.3 Dynamic Binding Capacity for Binding Performance

The DBC of both resins was measured after every 4 h of continuous operation in all configuration modes. The 4 h sampling time was determined by assuming an ion exchange CCTC with 5 steps: equilibration, bind, wash 1 (sometimes wash step 2), elution and strip/clean. The resin slurry takes around 5 to 8 min to enter and leave a single step at a steady state (according to tests in Section 2.5), while a whole cycle would take about half an hour. In total recirculation for 4 h, each bead would be going approximately 8 full theoretical cycles. These time approximations were also based on step, cycle and processing times reported in literature. The cycle time was about 5 to 8 h using clarified cell culture fluid for the purification using Protein A affinity media for the capture of mAbs in CCTC systems (Dutta et al. 2017). Also, the sample numbers were limited due to the amount of material needed to run each experiment and the amount of resin slurry required for each sample (10 mL of resin, translated into 30 mL of 20% (v/v) concentrated resin slurry). It is worth noting that each sample removes a small amount of resin from the system and cannot be recovered. The resin slurry was packed in a XK 16 column until it reached a bed height of 2 cm (approximately 4.0 mL) to ease the packing process and operated with a flow rate of 1 mL/min. The BSA load concentration was 20 mg/mL to keep the loading step short due to the number of samples. The DBC experiments were performed in triplicate for all configurations.

Even though the experiments were done for a CCTC, returning to BBC studies for the binding capacity studies would require more resources with less reliable results as an automated AKTA machine would not be able to be used. The slurry samples would have to be settled, buffer exchanged with 5 to 9 resin volumes for equilibration and then elution in batch mode. The amount of time and resources for the sheer number of samples would make it impossible to finish in a realistic timeframe.

4.3.4 Scanning Electron Microscopy Imaging

The SEM imaging was done in 3 different steps: freeze drying, coating preparation and imaging. The chromatographic media needed to be completely dry in order to be properly coated and yield high quality images with the least amount of noise possible. The freeze-drying was done as described in Section 2.15.1, the protocol was chosen as it had been proven to successfully remove all the liquid inside agarose beads. It is known that resin drying may bring performance and structural damage in the future. However, the reported process accomplished the liquid removal without compromising the structure of the matrix in the process (Nweke, Rathore, and Bracewell 2018; Nweke, McCartney, and Bracewell 2017).

The dried resin beads needed to be coated in a gold/palladium alloy as the inherent properties of agarose and methacrylate are not electrically conductive. Non-conductive materials tend to charge when scanned by the electron bean, affecting the final results. The coating was done by the machine operator as described in Section 2.15.2.

Finally, the prepared samples were placed into the field scanning electron microscope for imaging. The SEM resin pictures were taken by picking different individual beads at random to represent the whole population, as well as single layered-clusters for a better visualization of the population. The surface of the resin was photographed for measuring the porosity deviation quantitatively. Section 2.15.3 and 2.16 describes the SEM imaging procedure as well as the processing of the pictures in ImageJ for porosity analysis.

4.3.5 Quantitative Analysis of SEM Images

A quantitative analysis helps to give further insight on the effects of the use of commercially available resin in a CCTC system. ImageJ was selected as the image processing software to numerically analyse the SEM images. This software has several advantages. It is a public domain open source software with no required specific expertise. Furthermore, it contains a vast number of tools and inbuilt plug-ins

that are specifically relevant for this type of analysis. Additionally, ImageJ has been widely used in research to quantify the characteristics of a diverse number of biotechnological related materials (Jensen 2013; Helmy and Abdel Azim 2012; Schneider, Rasband, and Eliceiri 2012; Nweke et al. 2017).

Average pore count, average pore size and apparent porosity are properties that can be calculated with the aforementioned software to characterize the effects of CCTC on the surface of the resin bead. Different from PSD, these properties are not reported by the manufacturers or easily obtainable. Average pore count (number of pores in an image) and apparent porosity (pore to matrix ratio) may seem directly related, as a larger number of pores would translate to less matrix on the image. However, it may not be correlative, as the 3D nature of image is flattened for the analysis or most of the pores might be of the lower area in the picture. This can be seen in some of the samples in Section 4.4.3.

There were a number of steps performed in order to prepare the images before being ready to be analysed. The scale was set by manually drawing a line of 2.5 cm over the scale bar of 1 μm. Then, the software assigns an equivalent number of pixels to 2.5 cm and calculates the actual length of the sample. The “Smooth” filter is applied to flatten the surface. The contrast of the image is increased or decreased depending on the image, avoiding it if possible. The “Binary” option is selected to enhance the location of the pores. The threshold limit is then set to filter as much background noise as possible. The “Find Edges” tool selects all the enclosed black pixels to facilitate the measurement of the pores and enable the next step. The “Particle Analyser” is selected to allow the count of the total number of the black enclosed pixel spaces, the measurement of the area of these areas and the percentage between enclosed black pixels and the rest of the picture. Afterwards, the pores are selected, encircled and numbered in the image. Two new windows appear, one contains the individual information for each pore and a second one gives the summary with the information mentioned above. The results are displayed in units specified in the scale in Step 1. The pore diameter is approximated based on a circumference, area of a circle, as πr^2. This may cause some discrepancies between the apparent porosity and the average pore count as mentioned beforehand.

4.3.6 Particle Size Distribution Analysis

PSD studies were used to quantitatively register the reduction of size the media beads and appearance of fines that can be translated to damage in the form of cracking, chipping or fragmentation of the structure. These results were complimented with SEM pictures, providing a visual and quantitative perspective on identifying and solving the problem about the shifting particle size and the non-existent fine particles. The PSD experiments were done in the same manner following the same reasoning as the explained in Section 3.4.10.

The 20% (v/v) resin slurry samples in 20% ethanol were dispersed in 20% ethanol as pure 20 mM phosphate buffer pH 7 or deionized water would increase the background noise and the presence of non-existent fine fractions in the samples, especially for the agarose-based beads (as explained in section 3.4.10). Buffer exchange was reduced to a minimum after the samples were collected as the samples needed to be stored for long after taken. Also, because the volume was minimal and the material loss between each buffer exchange would be significant and would compromise feasibility of the subsequent analysis.

4.4 Results and Discussion

4.4.1 Binding performance

The binding capacity was used as a reference for resin performance after being experiencing high shear in the USD rotary device and low shear in the resin reservoir mixer, pumped through a peristaltic pump and/or pass through a batch 2-stage CCTC system.

4.4.1.1 High Shear Stress

The resin slurry at 20% (v/v) was sheared in the USD rotary disc device in 3 different rotary speed velocities: 2,000, 3,500 and 5,000 rpm; which correspond to three shear levels: 30, 70 and 140 Pa. The control would be no shear at all, a sample retrieved from a fresh buffer. Afterwards, the DBC was measured in order to track the performance of the resin. The objective for this experiment was to test the commercially available resins under excruciating shearing conditions as a controlled and accelerated shearing environment to track the possible loose of performance.

Figure 4.1 shows the different DBCs for each of the resins vs the different shearing conditions. The normalised DBCs for Macro-Prep High Q were 1.02, 1.01 and 0.99 and for Q Sepharose FF were 1.00, 0.98 and 0.99 for 2,000, 3,500 and 5,000, respectively. An ANOVA test showed that there is no significant difference among the sheared samples with p-values of 0.97 and 0.98, respectively, and a significance level of 5%. These results suggest that the high shear environment did not affect the binding capabilities of the matrix in any way. However, this does not prove that the resin itself it is not getting damaged by these conditions. The resin bead may crack or fractionate but the surface of the cracked bead and fines still have functional ligands capable of capturing BSA under the right conditions. Thus, explaining the consistency of the DBC. It is important to mention that the USD rotatory disc device was design to shear cellular material and protein aggregates. A second approach to these results might be required

for establishing a proper chromatography resin shear test. The resin performance and structural damage is further investigated in Section 4.4.2 and 4.4.3 to confirm these claims.

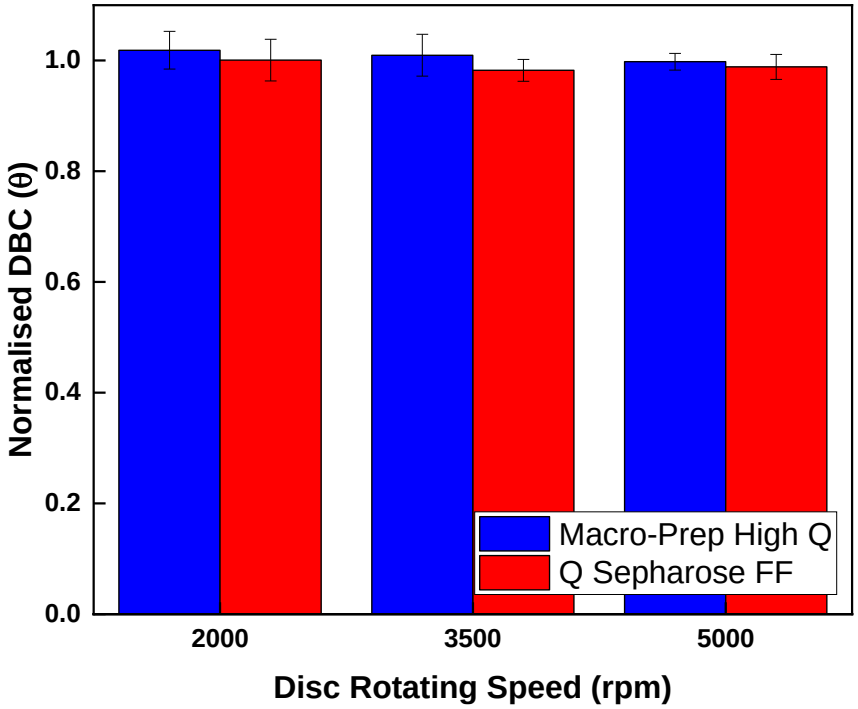

Figure 4.1. Normalised DBC results of BSA in Macro-Prep High Q (blue) and Q Sepharose FF (red) resins after being sheared in the USD rotary disc device at 2,000, 3,500 and 5,000 rpm. The resin slurries were packed in a XK 16 with a 2 cm bed height (4 mL of resin) and operated at a flow rate of 1 mL/min. A load of 20 BSA mg/mL was used for every run. The error bars represent the standard deviation of the samples (n=3). An ANOVA test showed that there is no significant difference among the sheared samples with p-values of 0.97 and 0.98, respectively, and a significance level of 5%.

4.4.1.2 Low Shear Stress

The resin slurry at 20% (v/v) was operated for a total of 36 h in each of the 6 different configurations shown in Figure 2.6. The purpose of testing each configuration is to identify if any of the components in the CCTC system might be hindering the binding capacity of the resin in short- and long-term under realistic CCTC operating conditions (low shear environment). This is especially important for the peristaltic pump, as it cannot be replaced and the pumping of the resin slurry is what distinguishes this continuous non-column system with the traditional column format.

Figure 4.2 shows the normalised DBC for Macro-Prep High Q for the configurations involving a magnetic stirrer mixer in the resin reservoir and Figure 4.3 for the configurations involving an overhead impeller mixer. The average normalised DBC were 0.99, 0.96 and 1.00 for the CCTC configuration, pump and magnetic stirrer mixer configuration and the magnetic stirrer mixer, respectively. According to the ANOVA test with a 5% significance level and p-values above 0.32, there is no significant difference between the DBC of any of these resin samples. The average normalised DBC were 1.00, 0.95 and 0.96 for the CCTC configuration, pump and overhead impeller mixer configuration and the overhead impeller mixer, respectively. According to the ANOVA test with a 5% significance level and p-values above 0.33, there is no significant difference between the DBC of any of these resin sample.

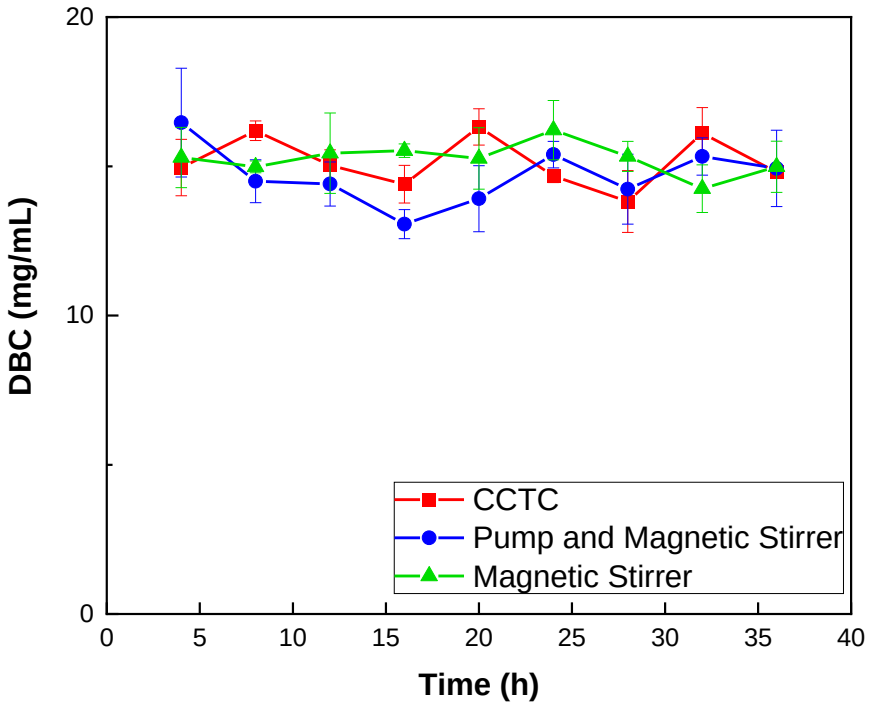

Figure 4.2. Normalised DBC of BSA in Macro-Prep High Q resin slurry after being used in a CCTC system with a magnetic mixer in the resin reservoir (red), rig consisting of a peristaltic pump and a magnetic stirrer mixer in the resin reservoir (blue) and a magnetic stirrer mixer in the resin reservoir (green). Each sample was taken every 4 h of continuous operation. The resin slurries were packed in a XK 16 with a 2 cm bed height (4 mL of resin) and operated at a flow rate of 1 mL/min. A load of 20 BSA mg/mL was used for every run. An ANOVA test showed that there is no significant difference among the sheared samples with p-values of 0.32 and a significance level of 5%. The error bars represent the standard deviation of the samples (n=3).

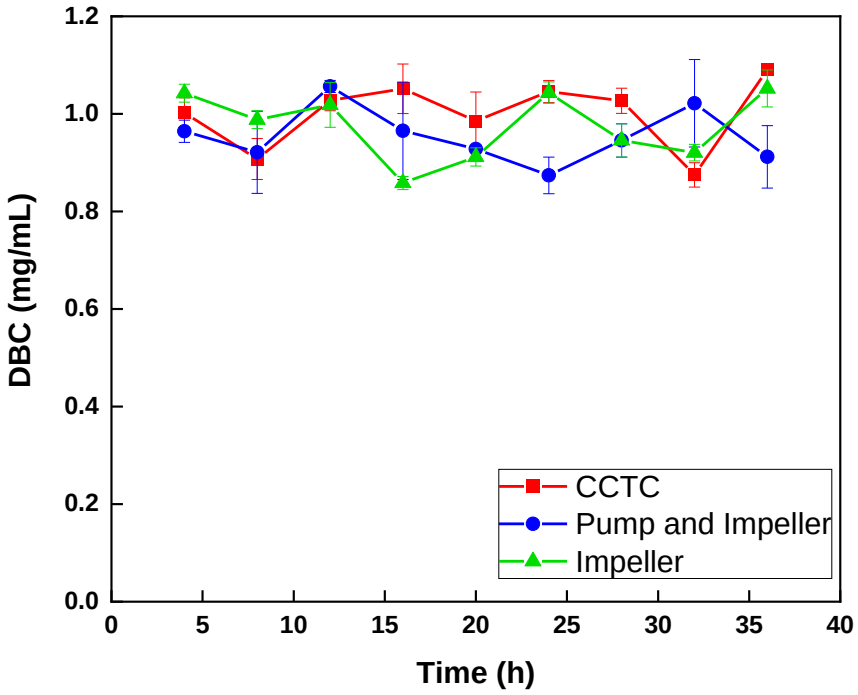

Figure 4.3. Normalised DBC of BSA in Macro-Prep High Q resin slurry after being used in a CCTC system with an overhead impeller mixer in the resin reservoir (red), rig consisting of a peristaltic pump and an overhead impeller mixer in the resin reservoir (blue) and an overhead impeller mixer in the resin reservoir (green). Each sample was taken every 4 h of continuous operation. The resin slurries were packed in a XK 16 with a 2 cm bed height (4 mL of resin) and operated at a flow rate of 1 mL/min. A load of 20 BSA mg/mL was used for every run. An ANOVA test showed that there is no significant difference among the sheared samples with p-values of 0.32 and a significance level of 5%. The error bars represent the standard deviation of the samples (n=3).

Figure 4.4 shows the normalised DBC for Q Sepharose HP for the configurations involving a magnetic stirrer mixer in the resin reservoir, and Figure 4.5 for the configurations involving an overhead impeller mixer. The average normalised DBC were 0.99, 1.00 and 1.04 for the CCTC configuration, pump and magnetic stirrer mixer configuration and the magnetic stirrer mixer, respectively. According to the ANOVA test with a 5% significance level and p-values above 0.26, all the DBCs are not significant different through time and configurations. The average normalised DBC were 0.99, 1.00 and 1.03 for the CCTC configuration, pump and overhead impeller mixer configuration and the overhead impeller mixer, respectively. According to the ANOVA test with a 5% significant level and p-values above 0.27, all the DBCs are statistically the same for all the samples.

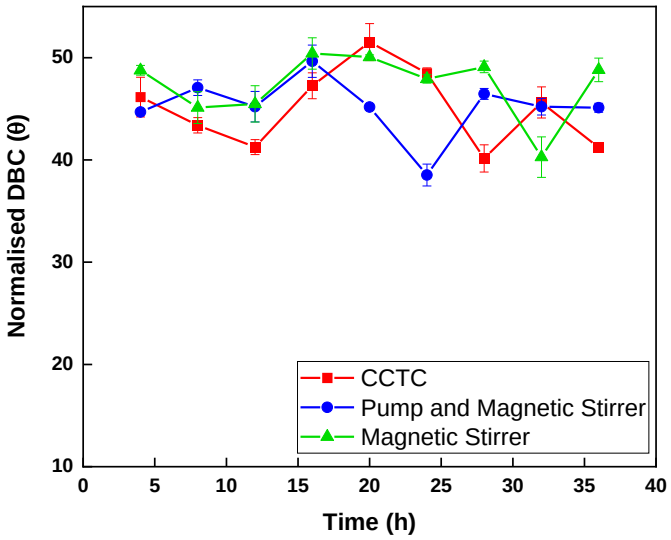

Figure 4.4. Normalised DBC of BSA in Q Sepharose HP resin slurry after being used in a CCTC system with a magnetic mixer in the resin reservoir (red), rig consisting of a peristaltic pump and a magnetic stirrer mixer in the resin reservoir (blue) and a magnetic stirrer mixer in the resin reservoir (green). Each sample was taken every 4 h of continuous operation. The resin slurries were packed in a XK 16 with a 2 cm bed height (4 mL of resin) and operated at a flow rate of 1 mL/min. A load of 20 BSA mg/mL was used for every run. An ANOVA test showed that there is no significant difference among the sheared samples with p-values of 0.26 and a significance level of 5%. The error bars represent the standard deviation of the samples (n=3).

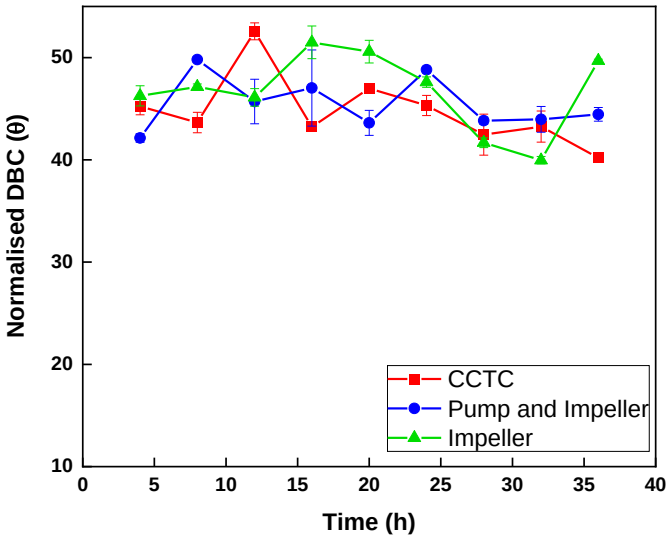

Figure 4.5. Normalised DBC of BSA in Q Sepharose HP resin slurry after being used in a CCTC system with an overhead impeller mixer in the resin reservoir (red), rig consisting of a peristaltic pump and an overhead impeller mixer in the resin reservoir (blue) and an overhead impeller mixer in the resin reservoir (green). Each sample was taken every 4 h of continuous operation. The resin slurries were packed in a XK 16 with a 2 cm bed height (4 mL of resin) and operated at a flow rate of 1 mL/min. A load of 20 BSA mg/mL was used for every run. An ANOVA test showed that there is no significant difference among the sheared samples with p-values of 0.26 and a significance level of 5%. The error bars represent the standard deviation of the samples (n=3).

Figure 4.6 shows a graphical representation of the average normalised DBC for both resins of all the samples in the 36 h operation against the configuration they were used in. The DBC for all types of configurations and types of resins shows no deviation or hindrance from its original DBC, suggesting any shear experienced from any of the modules in the CCTC system can hinder the performance of both rigid and flexible matrices. As stated in Section 4.4.1.1, this does not translate to undamaged resin matrix. The ligands on and in the bead can still remain intact even after cracking and fragmenting, capable of binding and eluting charged molecules at specific buffer conditions. However, this confirms that the CCTC system, including peristaltic pumps, do not have an impact on the DBC in any way after short or long cycle runs for both types of resins.

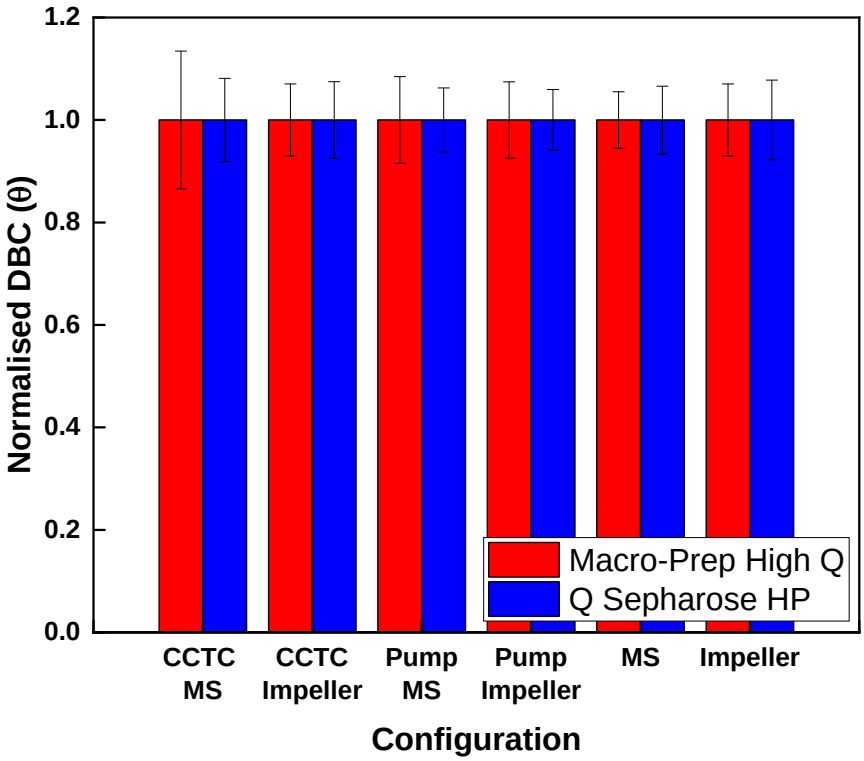

Figure 4.6. Comparison between the normalised DBC of BSA in Macro-Prep High Q (red) and Q Sepharose HP (blue) resin slurries after being used in a CCTC system, peristaltic pump with a resin reservoir mixer and only a resin reservoir mixer. Each configuration was used with a magnetic stirrer mixer and an overhead impeller mixer. Each sample was taken every 4 h of continuous operation. The resin slurries were packed in a XK 16 with a 2 cm bed height (4 mL of resin) and operated at a flow rate of 1 mL/min. A load of 20 BSA mg/mL was used for every run. The error bars represent the standard deviation of the samples (n=3).

4.4.2 Particle Size Distribution Studies

DBC studies can only show resin performance but they cannot give evidence of a damaged bead. PSD experiments were done in order to measure the extent of the damage in both types of resins under all the different system configurations.

4.4.2.1 High Shear Stress

PSD readings were taken immediately after shearing the 20% (v/v) resin slurry samples in the USD rotary disc device for 20 seconds at the determined disc velocities. Figure 4.7 and 4.8 show the PSD results for new and sheared Macro-Prep High Q and Q Sepharose FF, respectively. Table 4.1 shows the particle sizes at different volume distributions, as well as the theoretical energy dissipation rate and shear stress the resin slurry was exposed to during the shearing run. Also, it shows the theoretical linear and flow velocity that the particles would travel inside a 4 mm diameter peristaltic tube to achieve that shear stress.

The slurry samples for Macro-Prep High Q present a deviation of less than 1.8% from the control for all shear levels. Macro-Prep High Q presented a single peak but the measured average particle size (50%), 69.7 μm, does not match the one reported with the manufacturer, 50 μm. This might be due to the refractive and adsorption indices for methacrylate and the buffer or diluent used for the experiments as the manufacturer does not give any details on how the PSD was measured. These refractive indices for the materials are one of the reason why there is a presence of non-present fraction fines in the PSD, as well as the transparency of the materials (specially agarose); as explained in Section 3.4.10.

Q Sepharose FF PSD results show a deviation of less than 14.5% compared to the control values for all shear levels. Due to its agarose nature, Q Sepharose FF is susceptible to slight deformation under high physical forces. Thus, explaining the slight decrease of its average PSD but keeping the 10% and 90% distribution, which was practically unchanged with a deviation of 7.5% and 2.4%, respectively. These claims are qualitatively corroborated in Section 4.4.3.1.1 with the SEM images. It was thought

that the fines were caused by smaller particles in the buffer media, so several buffer exchanges on the resin before being processed were performed to remove the fine particles that range from 1 to 10 μm without any success. Later, these fines were explained as an error in the Fraunhofer approximation due to the difference in reflective indices between the dispersant (20% ethanol solution with a reflective index approx. if 1.3 and the reflective index of agarose of 1.34), the transparency of the matrices and the approximation in itself. Agarose is the more transparent material, causing the light to diffract and scatter in such a way that makes the Mastersizer 3000 detect fine particles when there are none. This phenomena could not be sorted out as the sample could not be buffer exchanged into pure ethanol or isopropanol (loss of sample due to volume and storing conditions) and unknown specific reflective indices. After revising the numbers, the real average PSD is no more than 5% to10% different under the apparent value. On top of that, if this error was present for all Q Sepharose FF and Q Sepharose HP samples then it would not interfere with the conclusions. It seems that the proportion of this non-existent fine fraction was consistent with all type of samples. It was decided to leave the fines in the calculations and figures, as the results did not vary more than 5% to 10%.

It can be said that both resins were practically unaffected by the high shear stress experienced. Disregarding the matrix type, both slurries were exposed to a shear stress of 29.98 to 142.23 N/m^2 during 20 seconds which can be translated to 880.82 to 4,820 mL/min. These flow rates seem unrealistic as operational conditions for a CCTC separation process but set a precedent that both resins are able to withstand extremely high flow or shear stress without any significant consequences. Q Sepharose FF was the resin that was most structurally affected due to its soft material but the PSD profile of both peaks practically remained intact.

It is stated that the rotary disc device is a machine to produce high levels of shear, comparable to the ones in a centrifuge. As stated previously, the low shear experiments are denominated as such because the maximum shear experienced by the resin slurry is just a fraction of the ones discussed in this section. Table 4.1 shows not only the shear upon the resin slurry inside the rotary disc device but also inside the different modules of the CCTC system, being the resin reservoir mixer, static mixer and peristaltic tube (hollow fibre was neglected as the time of the slurry inside of it was almost non-existent).

The maximum shear the slurry is experiencing while being operated in a batch 2-stage CCTC system as the slurry is suspended in the resin reservoir by the mixer with a total shear of 1.5 Pa, while the minimum shear experience is in the static mixer with 0.01 Pa. The peristaltic tube is slightly higher than the one register for the static mixer but not close to the resin reservoir mixer or the rotary disc device. The rotary disc device provided approximately a shear stress magnitude 3,000X to 14,000X higher than the one calculated for the static mixer and, 20X to 96X higher than the one calculated for the resin reservoir mixer. This shear stress comparison aids to visualize the magnitude difference between the conditions and devices that were used for the characterisation of the slurry.

With all of these shear stress magnitude numbers in mind, it can be assumed that the chromatography media beads are probably not significantly damage to the exposure of high shear levels. It can also be thought that the low shear on the low shear experiments do not have a significant impact on the damage suffered by the resin slurry. This claim is supported by the results presented in all high and low shear experiments throughout this Chapter. However, this does not eliminate the possibility that any other form of interaction, such as the grinding effect of a magnetic stirrer in the resin reservoir mixer can exert of the beads, which is further thoroughly discussed in Section 4.4.2.2 and 4.4.3.

These results, in conjunction with the results in Section 4.4.3, demonstrated that commercially available synthetic and agarose-based resins are able to withstand extreme conditions for a short term of time without any hindrance to their DBC or serious structural damage.

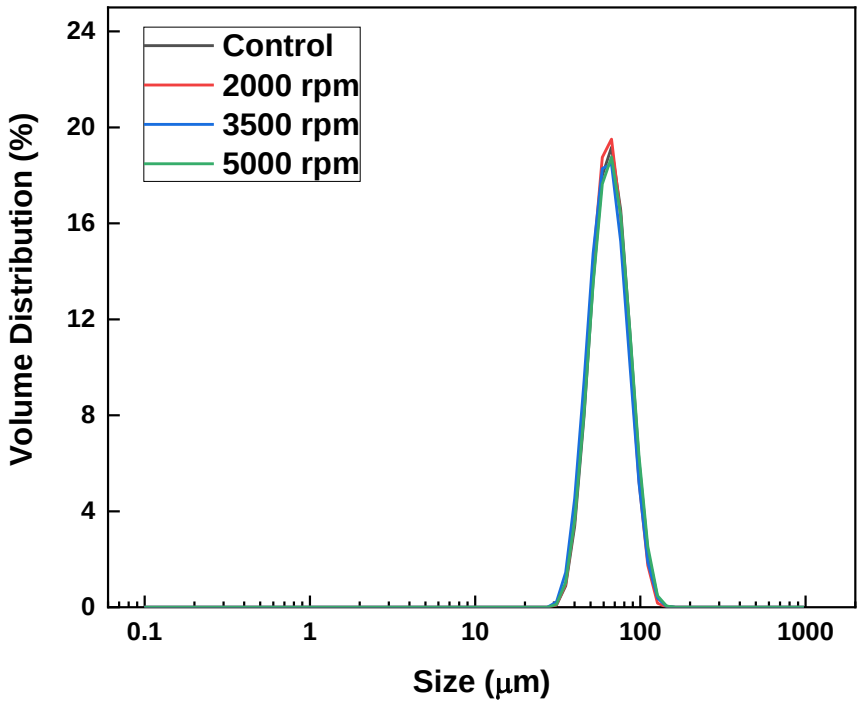

Figure 4.7. PSD diagram of fresh Macro-Prep High Q (black) and sheared samples at 2,000 (red), 3,500 (blue) and 5,000 (green) rpm in a USD rotary disc device for 20 s. The resin slurry was dispersed in 20% ethanol.

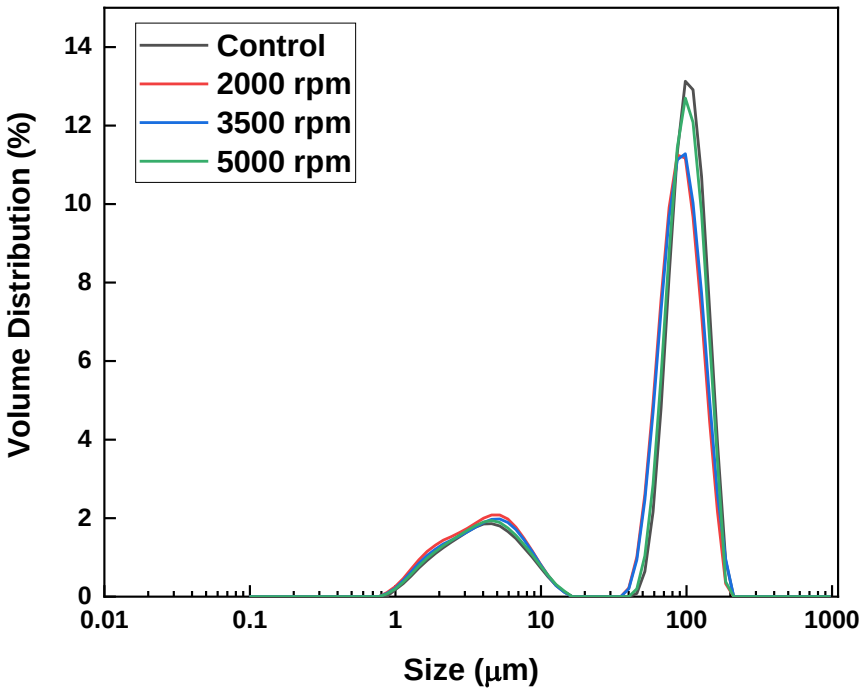

Figure 4.8. PSD diagram of fresh Q Sepharose FF (black) and sheared samples at 2,000 (red), 3,500 (blue) and 5,000 (green) rpm in a USD rotary disc device for 20 s. The resin slurry was dispersed in 20% ethanol. Non-existent fines can be seen under the ranges of 0.1 to 100 μm.

Table 4.1. High shear theoretical parameters (Equations 19 and 20) for Macro-Prep High Q and Q Sepharose FF after being sheared in a USD rotary disc device for 20 s in 20 mM phosphate buffer pH 7. Low shear theoretical parameters (Equation 16 and 18) for the module components of resin reservoir mixer, peristaltic tube and static mixer for a flow velocity of 50 mL/min in 20 mM phosphate buffer pH 7.

Resin	Material	Disc Velocity (rpm)	Energy Dissipation Rate (W/kg)	Shear Stress (Pa)	Theoretical Linear Velocity (cm/s)	Theoretical Flow Velocity (mL/min)	PSD 10% (-)	PSD 50% (-)	PSD 90% (-)
Macro-Prep High Q	Methacrylate	Control	0	0	0	0	49.90	69.70	96.90
		2000	7.59E+02	29.98	29.21	880.83	49.40	68.50	94.90
		3500	6.05E+03	73.39	82.47	2487.29	49.50	69.30	96.30
		5000	2.27E+04	142.23	159.83	4820.26	48.50	68.70	96.80
Q Sepharose FF	Agarose	Control	0	0	0	0	3.66	96.90	149.00
		2000	7.59E+02	29.98	29.21	880.83	3.38	83.10	138.00
		3500	6.05E+03	73.39	82.47	2487.29	3.44	85.00	141.00
		5000	2.27E+04	142.23	159.83	4820.26	3.53	92.70	145.00

Module Component	Disc Velocity (rpm)	Shear Stress (Pa)	Theoretical Linear Velocity (cm/s)	Theoretical Flow Velocity (mL/min)
Mixer	400	1.48	30.18	N/A
Peristaltic Tube	N/A	0.04	6.65	50.0
Static Mixer	N/A	0.01	1.05	50.0

4.4.2.2 Low Shear Stress

PSD measurements were done before any DBC experiments and only after all samples for that configuration set were taken and in 20% ethanol. The resins tested for this experiment were Macro-Prep High Q and Q Sepharose HP. Q Sepharose HP is made of 6% cross-linked agarose (approximately the same as Q Sepharose FF) with a particle size reported by the manufacturer of 34 µm. Q Sepharose HP was not used for any of the previous experiments due to the cost of the resin as it is around 4X more expensive than the original counterpart. Both resin bead particle sizes are comparable according to their own manufacturers.

Figures 4.9 and 4.10 shows the measured PSD at time 0, 4 and 36 h for Macro-Prep High Q in the configurations with a magnetic stirrer and an overhead impeller mixer. Figure 4.9 clearly shows a deviation from the original PSD, while Figure 4.10 displays no visible change. As mentioned in Section 3.4.10, the measured average PSD do not match to the ones reported by the manufacturer but this does not interfere with the final results. This can be explained by the errors in the calculations of the Fraunhofer approximation used by the Mastersizer 3000. However, this error calculation is manageable as it was consistent and not variable. The manufacturers or literature did not specify the method of PSD measurement. Table 4.2 shows the PSD for all of the samples according to their respective configurations. All the configurations with the magnetic stirrer mixer showed a maximum reduction of 80%, 60% and 40% for 10%, 50% and 90% PSD after 36 h. All PSDs of all the configurations after 36 h using an overhead impeller showed no significant reduction, with some size increase under the normal random variation of no more than 7%. This suggests that the magnetic mixer stirrer is the main component causing the breakage and fractionation of the methacrylate resin bead. It seems that the shear created by the peristaltic pump or hollow fibre pressure difference had no significant or measurable effect on the resin.

Figures 4.11 and 4.12 shows the measured PSD at time 0, 4 and 36 h for Q Sepharose HP in the configurations with a magnetic stirrer and an overhead impeller mixer. As seen in Section 3.4.10, Q Sepharose HP also presents the same Fraunhofer approximation errors seen for Q Sepharose FF. It was decided to also continue with it following the logic explained in Sections 3.4.10 and 4.4.2.1. In both figures, a shift in

the PSD is barely noticeable for both peaks compared with the control sample. Table 4.2 shows the PSD for all the samples according to their respective configurations. All the configurations with the magnetic stirrer mixer showed a variation of +-5%, -5% and -13% for 10%, 50% and 90% PSD after 36 h. As seen for Macro-Prep High Q, the magnetic stirrer mixer in the resin reservoir is having a noticeable negative effect on the size of the beads but probably not as drastic due to the soft nature of the material, only reducing the size by plastic deformation of the bead but not fragmenting completely it apart. The configurations with CCTC and the peristaltic pump with the overhead impeller presented similar PSD variations of -15%, 1% and 5% for 10%, 50% and 90% PSD after 36 h. The configuration of only the overhead impeller mixer presented a PSD variation of -1%, 5.5% and 1.5% for 10%, 50% and 90% PSD after 36 h. This overhead impeller mixer configuration, compared to the other two, proposes that the peristaltic pump is having a direct impact on the smallest particles signal. The algorithm, in which the PSD is calculated, assumes the particles to be spherical and measures the PSD accordingly. However, Q Sepharose FF and Q Sepharose HP are made out of a soft material, prone to deformation, causing a different light scattering for those molecules. This is most probably caused to the change of shape (as seen in Section 4.4.3) and consequently the diffracted light through the transparent bead. This change of shape comes with a small diffraction/scattering variation of the light going through the bead due to its transparency. This is suggested in Sections 3.4.10 and 4.4.2.1, where the agarose-based beads are not spherical to begin with, the shape is susceptible to the forces in their environment and the misleading non-existent fine fractions. It seems the shear stress was not the significant factor affecting the PSD but it was more about the deformation the agarose bead was experiencing in each mixer.

In contrast, each resin type behaved differently to the shear stimulus in their environment after 36 h. Macro-Prep High Q seemed to be fragmented substantially by the magnetic stirrer mixer, this was caused by the grinding effect the magnetic stirrer had over the rigid beads coming in contact with the bottom part of the magnetic stirrer. On the other hand, the rigidity of the methacrylate when used in the configurations coupled with an overhead impeller mixer showed no bead damage. This, coupled with the shear stress calculation results in section 4.4.2.1, infer that the shear stress is not a significant factor affecting the PSD. Q Sepharose HP showed a mild decrease in 90% PSD probably as the beads are able to withstand the grinding/crushing effect as

smallest and medium sized particles are able to elastically deform, with the largest particles showing a plastic deformation. However, the agarose-based bead clearly showed a slight plastic deformation. Finally, neither system was affected by the wall shear stress effect inside the hollow fibre as none of the PSD showed any variation compared to the ones without the CCTC system (complemented with the observations made in Section 4.4.2.1). Macro-Prep High Q showed a consistent pattern every 4 h due to its rigidity, while Q Sepharose HP was prone to more variation due to its softness and wider particle sizes.

Taking into account the previous discussion in this Section and the shear stress results in Section 4.4.2.1, it seems that the resin slurry is not significantly affected by shear stress. The set of PSD results and shear stress results from Table 4.1 and 4.2 show that the resin slurry particle size is not significantly affected by the shear stress level in the system. As stated before, the resin reservoir magnetic mixer seems to be the one causing the breakage or erosion of the beads due to its grinding mechanical nature, while the overhead impeller had a minimal impact on the slurry. The shear levels in the CCTC while using an overhead impeller are 3,000X to 14,000X higher than the ones recorded for the rotary disc device.

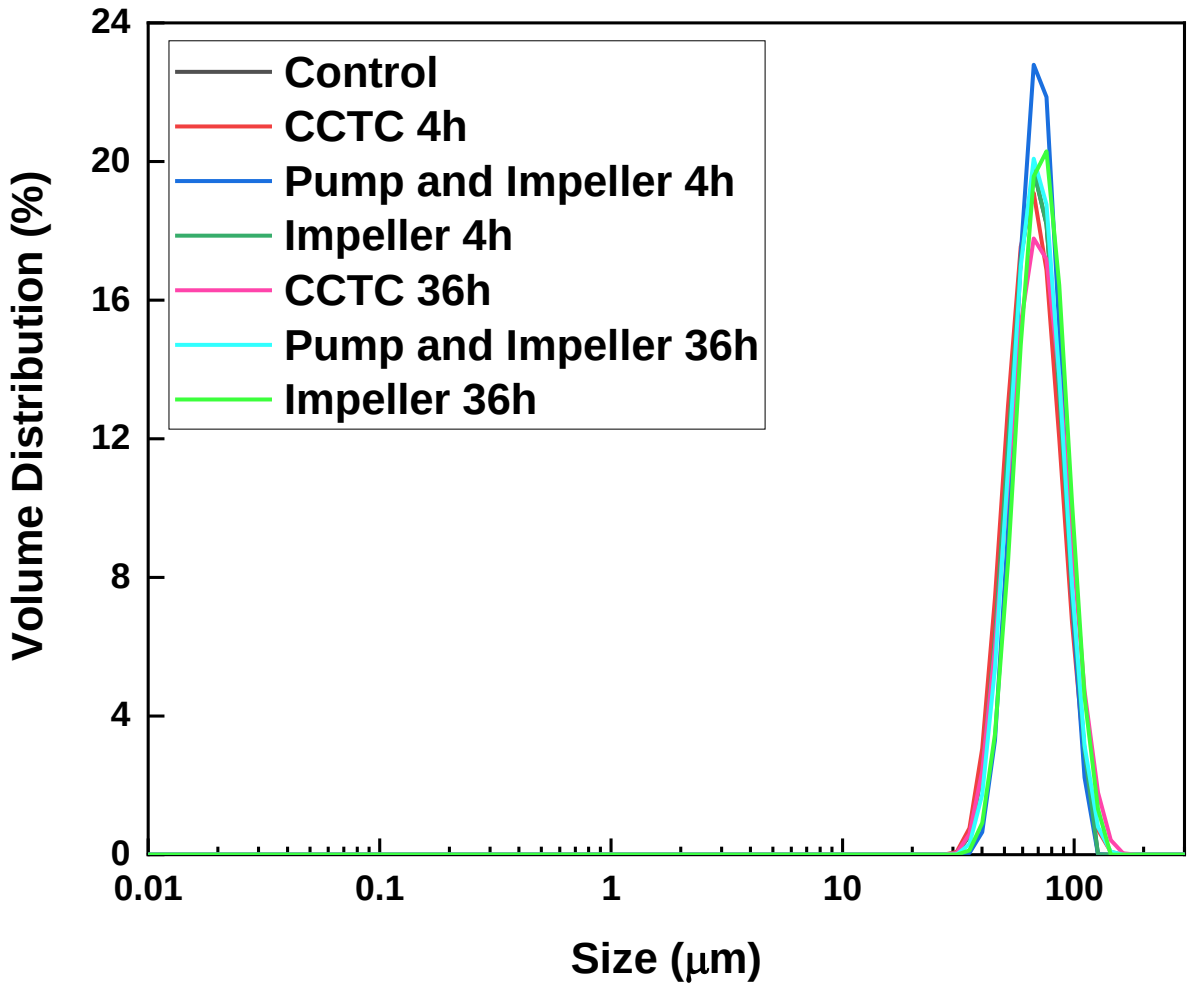

Figure 4.9. PSD of fresh Macro-Prep High Q (black) and resin used in different system configurations: CCTC system with an overhead impeller mixer for 4 h (red), peristaltic pump with an overhead impeller mixer for 4 h (dark blue), an overhead impeller mixer (dark green), CCTC system with an overhead impeller mixer for 36 h (pink), peristaltic pump with an overhead impeller mixer for 36 h (light blue) and an overhead impeller mixer for 36 h (light green). The resin slurry was kept at a 20% (v/v) concentration in 20 mM phosphate buffer pH 7. The overhead impeller mixer was kept at 400 rpm for all system configurations.

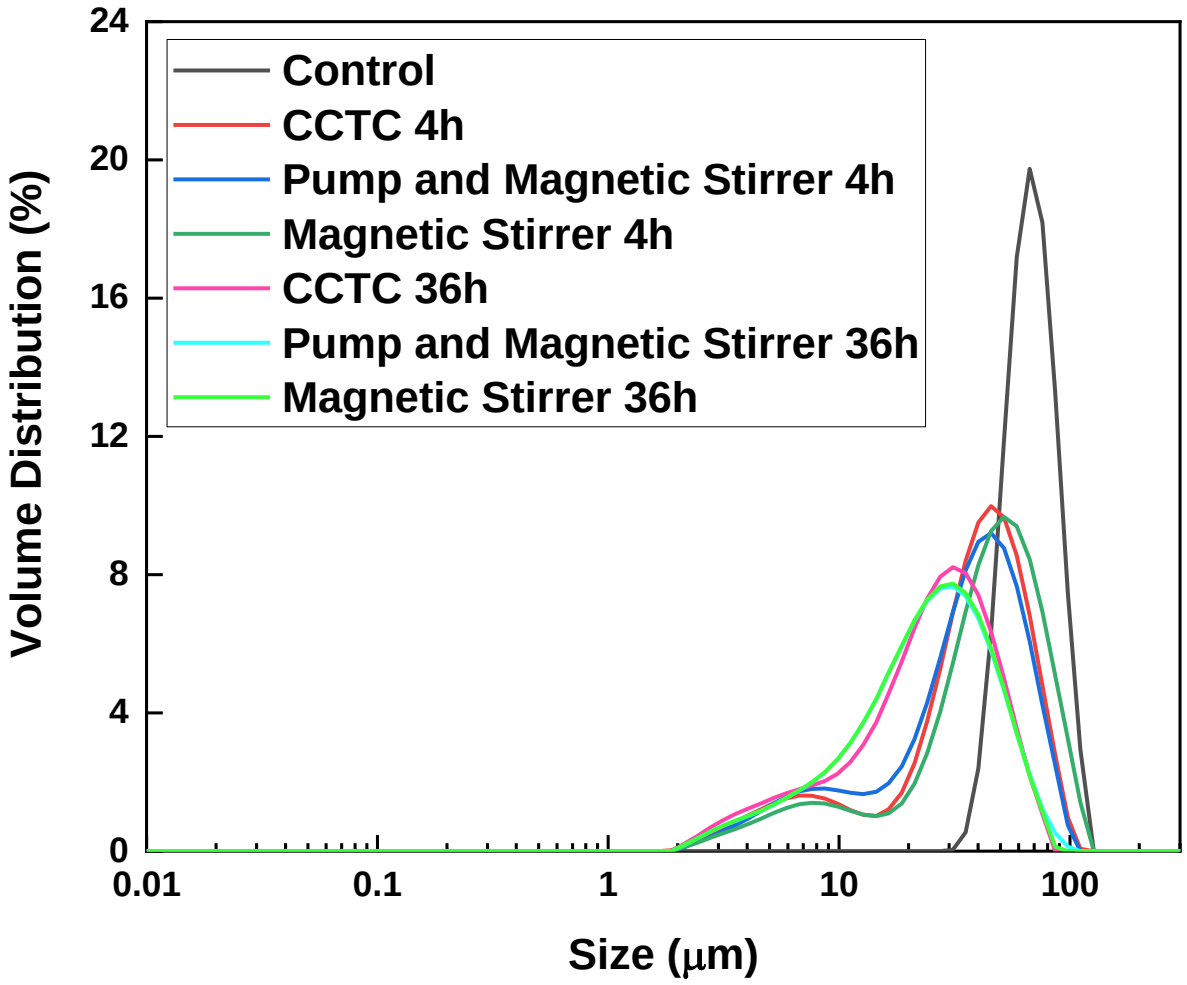

Figure 4.10. PSD of fresh Macro-Prep High Q (black) and resin used in different system configurations: CCTC system with a magnetic stirrer mixer for 4 h (red), peristaltic pump with a magnetic stirrer mixer for 4 h (dark blue), a magnetic stirrer mixer (dark green), CCTC system with a magnetic stirrer mixer for 36 h (pink), peristaltic pump with a magnetic stirrer mixer for 36 h (light blue) and a magnetic stirrer mixer for 36 h (light green). The resin slurry was kept at a 20% (v/v) concentration in 20 mM phosphate buffer pH 7. The magnetic stirrer mixer was kept at 400 rpm for all system configurations.

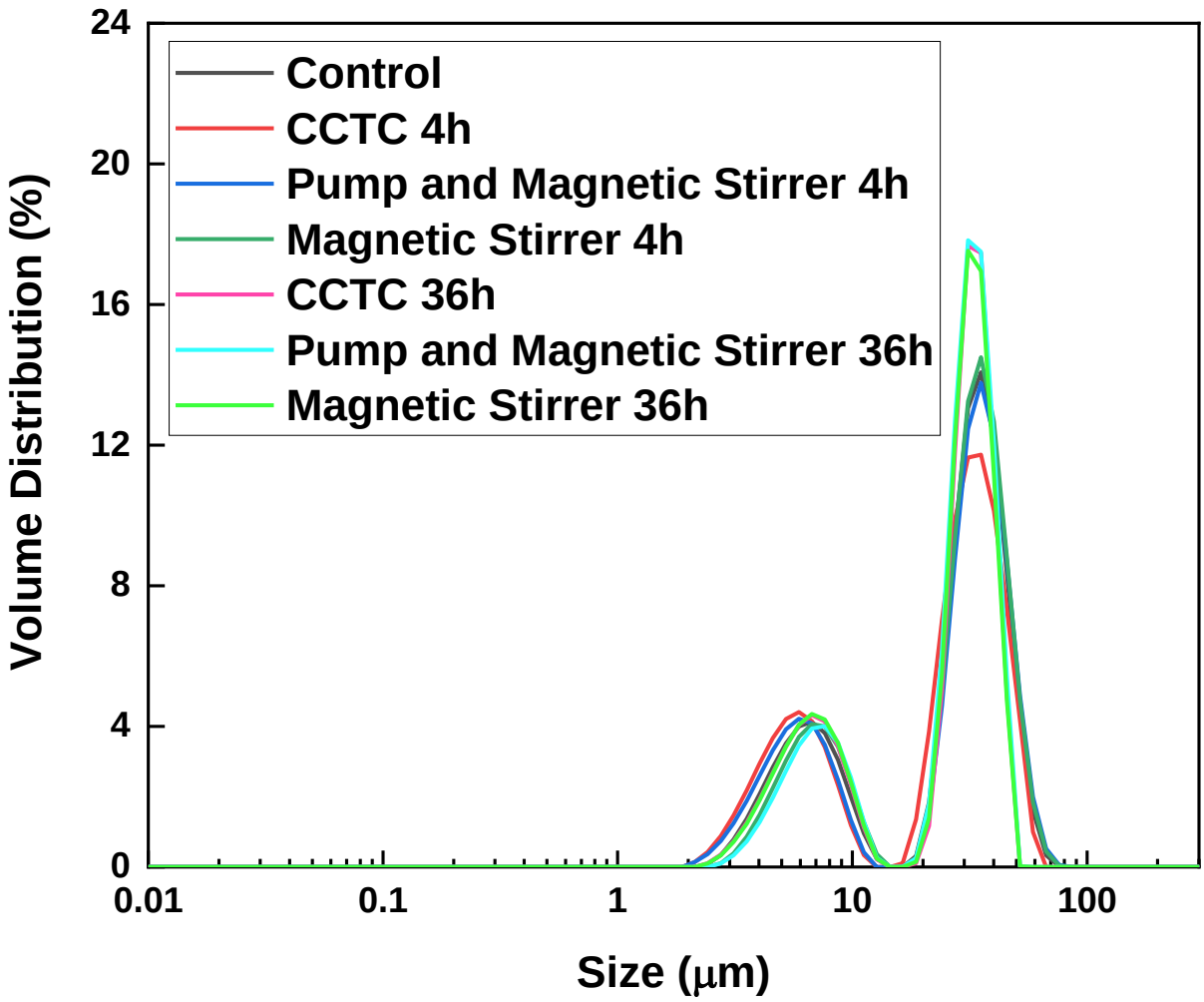

Figure 4.11 PSD of fresh Q Sepharose HP (black) and resin used in different system configurations: CCTC system with a magnetic stirrer mixer for 4 h (red), peristaltic pump with a magnetic stirrer mixer for 4 h (dark blue), a magnetic stirrer mixer (dark green), CCTC system with a magnetic stirrer mixer for 36 h (pink), peristaltic pump with a magnetic stirrer mixer for 36 h (light blue) and a magnetic stirrer mixer for 36 h (light green). The resin slurry was kept at a 20% (v/v) concentration in 20 mM phosphate buffer pH 7. The magnetic stirrer mixer was kept at 400 rpm for all system configurations. Non-existent fines can be seen under the ranges of 0.1 to 100 μm.

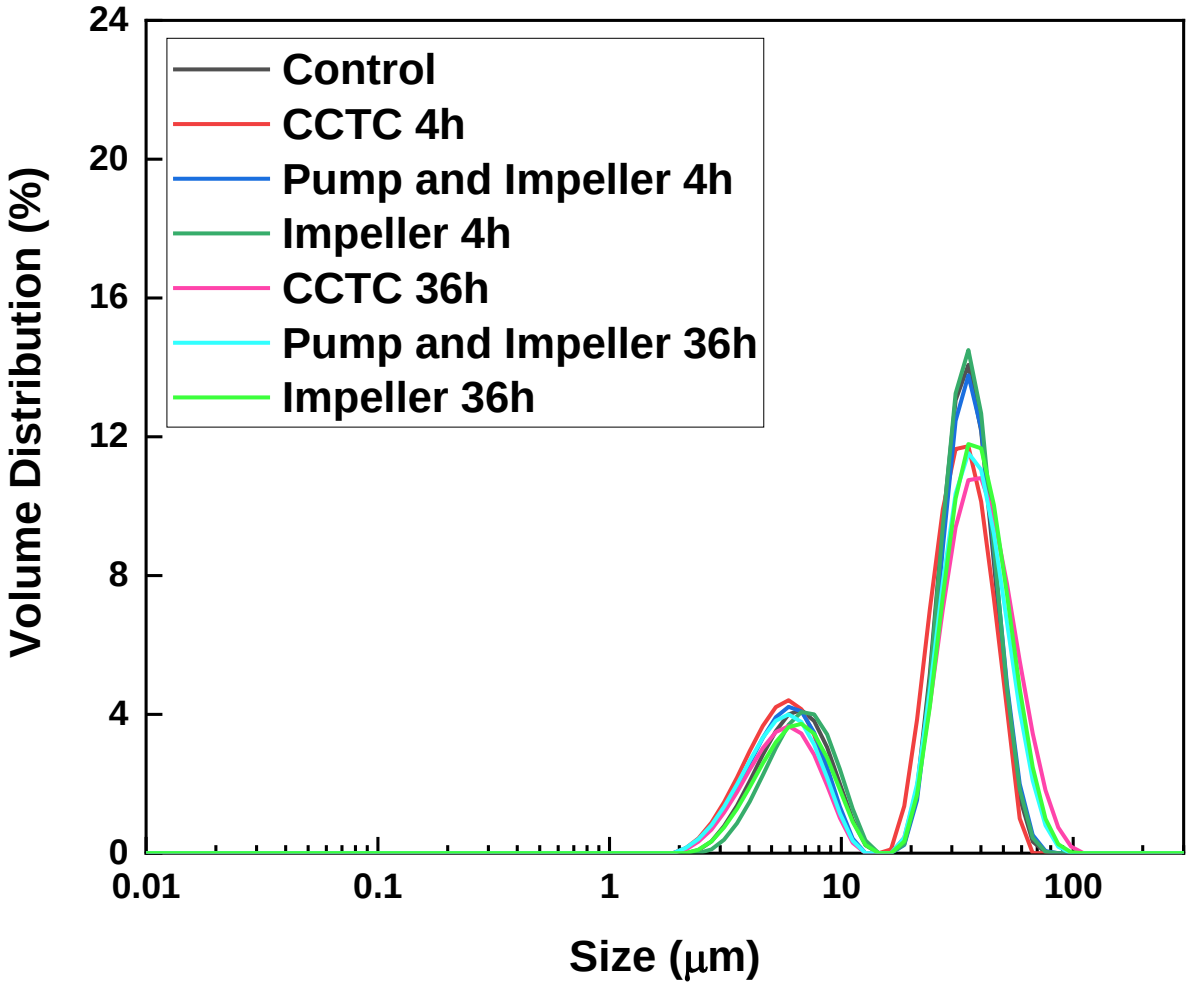

Figure 4.12 . PSD of fresh Q Sepharose HP (black) and resin used in different system configurations: CCTC system with an overhead impeller mixer for 4 h (red), peristaltic pump with an overhead impeller mixer for 4 h (dark blue), an overhead impeller mixer (dark green), CCTC system with an overhead impeller mixer for 36 h (pink), peristaltic pump with an overhead impeller mixer for 36 h (light blue) and an overhead impeller mixer for 36 h (light green). The resin slurry was kept at a 20% (v/v) concentration in 20 mM phosphate buffer pH 7. The overhead impeller mixer was kept at 400 rpm for all system configurations. Non-existent fines can be seen under the ranges of 0.1 to 100 μm.

Table 4.2. PSD values for 10%, 50% and 90% for Macro-Prep High Q resin slurry after being used for prolonged continuous hours in different system configurations.

Resin	Material	Configuration	Time (h)	Particle Size (10%)	(50%)	(90%)
Macro-Prep High Q	Methacrylate	Control	0	51.7	71.8	99.3
		CCTC	4	8.05	41.99	74.14
		Magnetic Stirrer Mixer	8	9.82	47.93	70.48
			12	8.37	33.30	63.28
			16	8.69	30.94	68.93
			20	10.25	29.95	60.79
			24	7.17	27.37	54.30
			28	7.17	28.48	58.42
			32	8.56	30.62	57.36
			36	8.46	28.52	55.83
		Peristaltic pump	4	8.60	40.11	73.24
		Magnetic Stirrer Mixer	8	9.51	46.23	83.32
			12	7.31	34.66	64.31
			16	7.29	33.31	65.68
			20	6.73	27.90	61.59
			24	7.06	25.89	51.54
			28	6.23	25.12	50.75
			32	7.07	26.92	53.55
			36	7.87	26.13	54.51
		Magnetic Stirrer Mixer	4	9.82	47.91	86.29
			8	8.05	41.90	74.14
			12	8.37	33.37	63.27
			16	8.69	30.99	68.93
			20	10.24	40.28	82.81
			24	7.17	27.33	54.33
			28	7.17	28.47	58.44
			32	8.56	30.69	57.30

	36	8.46	28.55	55.89
CCTC	4	50.2	70.62	99.66
Overhead Impeller Mixer	8	51.92	71.53	99.78
	12	54.03	75.27	104.93
	16	53.02	73.73	102.98
	20	53.40	74.82	105.98
	24	53.70	74.18	101.05
	28	52.20	72.80	102.84
	32	53.71	77.57	112.34
	36	52.48	74.44	107.02
Peristaltic pump	4	56.24	74.58	97.86
Overhead Impeller Mixer	8	56.16	74.62	98.65
	12	56.46	74.98	98.74
	16	55.42	74.56	99.74
	20	55.38	74.82	100.83
	24	53.54	72.76	98.53
	28	54.22	73.74	99.28
	32	53.63	73.10	99.63
	36	56.16	74.62	98.24
Overhead Impeller Mixer	4	52.35	72.20	99.34
	8	53.87	73.83	100.42
	12	53.74	73.36	99.00
	16	52.80	72.54	98.77
	20	54.73	75.19	103.38
	24	51.99	72.96	103.23
	28	52.45	73.74	104.01
	32	53.62	74.44	103.81
	36	54.89	76.63	106.53

Table 4.3. PSD values for 10%, 50% and 90% for Q Sepharose HP resin slurry after being used for prolonged continuous hours in different system configurations.

Resin	Material	Configuration	Time (h)	Particle Size 10%	50%	90%
Q Sepharose HP	Cross-linked Agarose	Control	0	5.93	33.20	49.71
		CCTC Magnetic Stirrer	4	5.89	32.45	44.84
			8	5.68	31.99	43.57
			12	5.69	31.63	43.27
			16	5.88	30.38	44.36
			20	5.73	31.74	43.63
			24	5.72	31.90	43.08
			28	5.61	31.71	43.27
			32	5.96	32.01	44.44
			36	5.81	31.58	43.15
		Peristaltic pump Magnetic Stirrer	4	5.79	32.59	48.35
			8	5.71	32.46	47.73
			12	5.85	32.49	45.68
			16	6.01	32.64	46.71
			20	5.97	32.25	47.40
			24	6.33	32.13	45.22
			28	6.14	31.82	44.72
			32	6.17	31.83	45.25
			36	6.17	31.74	43.57
		Magnetic Stirrer	4	5.76	32.73	44.78
			8	5.99	32.29	45.34
			12	5.99	31.31	43.42
			16	6.05	32.36	49.76
			20	6.01	32.18	43.79
			24	5.99	31.89	43.75
			28	5.93	31.88	44.31
			32	6.19	32.63	45.39

	36	6.14	31.74	43.50
CCTC	4	4.92	30.48	49.66
Overhead Impeller	8	5.04	32.64	50.54
	12	5.05	33.44	51.48
	16	5.26	32.27	48.28
	20	5.27	32.33	49.11
	24	5.09	30.34	46.38
	28	5.39	32.44	50.22
	32	5.13	32.39	51.24
	36	5.05	33.48	52.54
Peristaltic pump	4	5.11	33.54	51.80
Overhead Impeller	8	5.09	33.16	53.68
	12	4.97	33.12	51.21
	16	5.06	32.04	50.73
	20	4.84	32.86	52.25
	24	4.97	33.74	53.84
	28	4.87	34.52	50.86
	32	5.02	34.42	50.90
	36	5.00	33.43	51.35
Overhead Impeller	4	5.88	33.44	50.94
	8	6.00	33.45	50.22
	12	5.93	33.28	49.92
	16	5.84	33.55	50.74
	20	5.77	33.01	49.69
	24	5.71	33.5	53.76
	28	5.88	35.4	52.63
	32	6.10	34.14	51.40
	36	5.88	35.19	50.47

4.4.3 Scanning Electron Microscopy Imaging

SEM imaging was used to support the claims in Section 4.4.2 about resin bead damage, chipping and fragmentation. All the samples of both resin types were subjected to the same freeze-drying conditions, gold/palladium alloy coating and SEM imaging conditions.

4.4.3.1 High Shear Stress

4.4.3.1.1 Qualitative Analysis

Figures 4.13 and 4.14 depicts SEM images of an average bead, population and surface of the fresh and sheared samples in 2,000, 3,500 and 5,000 rpm in the USD rotary disc device. Each figure labelled as A represents the whole bead images, B represents the population and C represents the surface for their respective resin and shear level.

Figure 4.13.A.1 shows a randomly selected fresh bead of Macro-Prep High Q. The sample shows that the individual bead is uniformly spherical in structure and shows no visible signs of strain or fragmentation. Figure 4.13.B.1 shows a randomly selected fresh bead population of Macro-Prep High Q. As seen in the individual bead, the population seems to share the same characteristics with some with the exception of the presence of some fragments/fine particles of < 20 µm. This fines could have been created at the moment of drying or are particles of dust that do not represent the slurry. The image also shows the wide PSD of the samples (50 to 100 µm), as measured in Section 4.4.2.1. Figure 4.13.C.1 presents the surface of a typical bead with clear and defined visible pores at a µm scale without any damage. All these properties were also shared by the Macro-Prep High Q sheared samples (Figures 4.13.A.2 to A.4, B.2 to B4 and C.2 to C.4) with the exception of some of the beads that presented more prominent indentations compared to the control.

Figure 4.14 has a similar structure as Figure 4.13 but with Q Sepharose FF as the resin subjected to SEM. Figure 4.14.A.1 displays a non-uniform spherical structure and a flatten or un-even surface. In Figure 4.14.B.1, the same characteristics can be seen for the whole population; some of the beads do not have a spherical shape but their surface does appear even and undamaged. Furthermore, the image shows the disparity of sizes, as measured in their PSD (90.0 to 150.0 µm, excluding fines). Figure 4.14.C.1 shows a visible highly packed/deformed but undamaged surface. Figures 4.14.B.2 to B.4 showed a population formed by deformed spherical beads with flat sides, even more compared to Figure 4.14.B.1. Aside from that, all the other properties were shared among all the Q Sepharose FF sheared samples (Figure 4.14.A.2 to A.4, B.2 to B.4 and C.2 to C.4).

According to the state of the bead and surface of both types of resins, it seems to indicate that the freeze-drying process and the high shear conditions do not have any significant or drastic effect on the integral structure of the beads. However, Q Sepharose FF (Figure 4.14.B.2 to B.4) appear to have suffered a plastic deformation by displaying flat surfaces in most of the beads. This can be explained due to the lack of rigidness of the agarose, making it flexible and harder to fragment, as opposed to Macro-Prep High Q (Figure 4.14.B.2 to B.4) that showed no signs of deformation or deviation from its spherical form. The flat surfaces in Figure 14.A.1 can be attributed to the beads adhering before the freeze-drying due to their viscous nature and then disjoined when the water is removed. Post-shearing, the flat surface might have worsened by the centrifugal force and shear stress experienced inside the USD rotatory disc device. Each resin shows surface structural differences as they do not share the same chemical and physical compositions. Q Sepharose FF seems to display a relatively thicker or “gel-like” matrix, it appears to have a more viscous structure and smaller and uniform pores compared to Macro-Prep High Q, that shows pores closer and larger to the surface that extend inwards with a more randomised pore distribution.

This section confirms the non-existent fine fraction measured by the Mastersizer 3000. There is not a significant amount of agarose fragments in any of the pictures. We can confidently confirm the suspicions about the inherent errors the measuring technique has for agarose-based materials, also applicable for methacrylate at a minor extent.

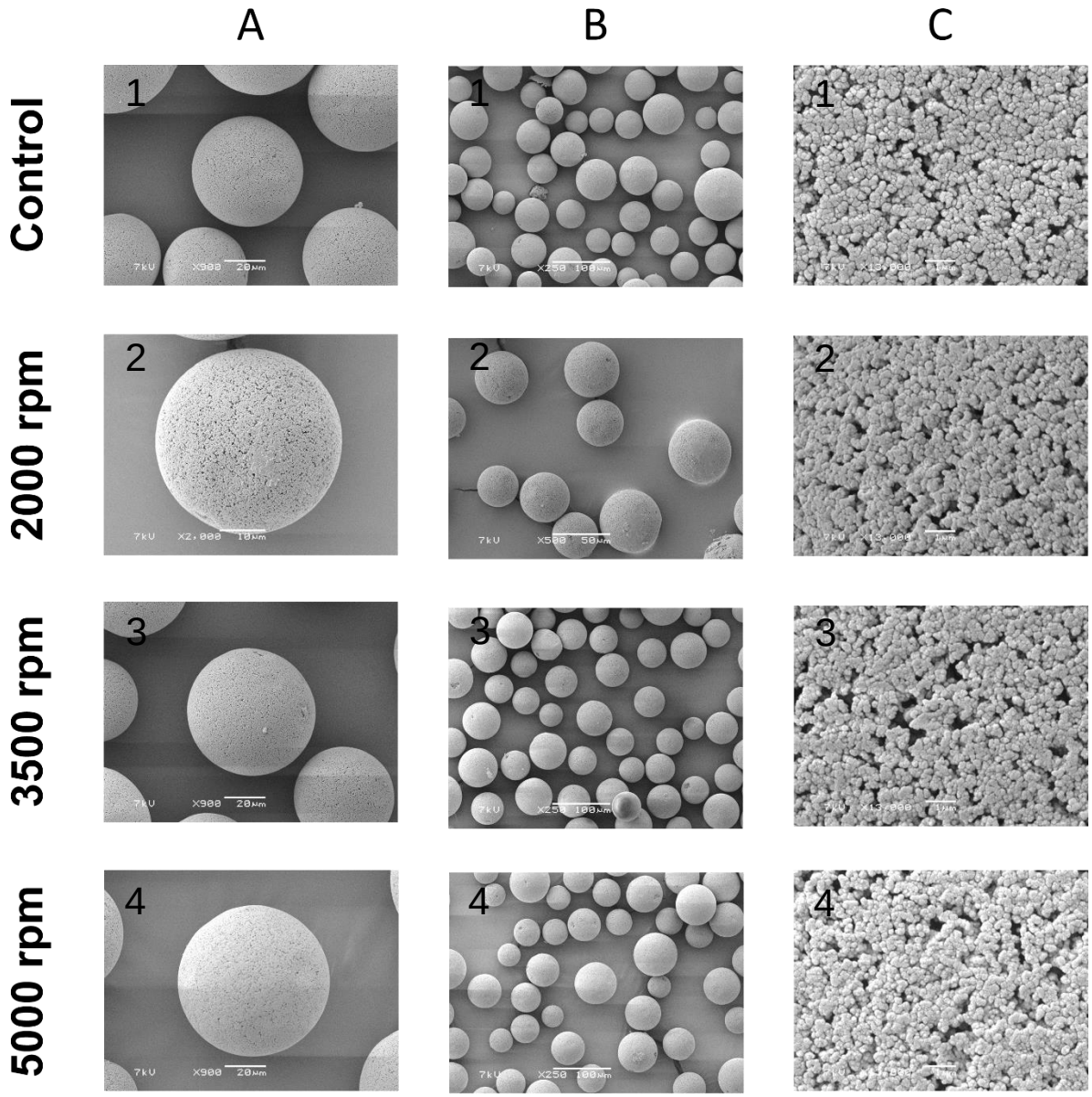

Figure 4.13. A) Scanning electron micrograph showing fresh Macro-Prep High Q post-freeze drying. Whole bead (X900), average bead population (x250) and bead surface (x13,000), 7 kV images in that respective order. B) Scanning electron micrograph showing 2,000.0 rpm sheared Macro-Prep High Q post-freeze drying. Whole bead (X2,000), average bead population (x500) and bead surface (x13,000), 7 kV images in that respective order. C) Scanning electron micrograph showing 3,500 rpm sheared Macro-Prep High Q post-freeze drying. Whole bead (X900), average bead population (x250) and bead surface (x13,000), 7 kV images in that respective order. D) Scanning electron micrograph showing 5,000.0 rpm sheared Macro-Prep High Q post-freeze drying. Whole bead (X900), average bead population (x250) and bead surface (x13,000), 7 kV images in that respective order. The scale bar represents 20, 100 and 1 µm, respectively.

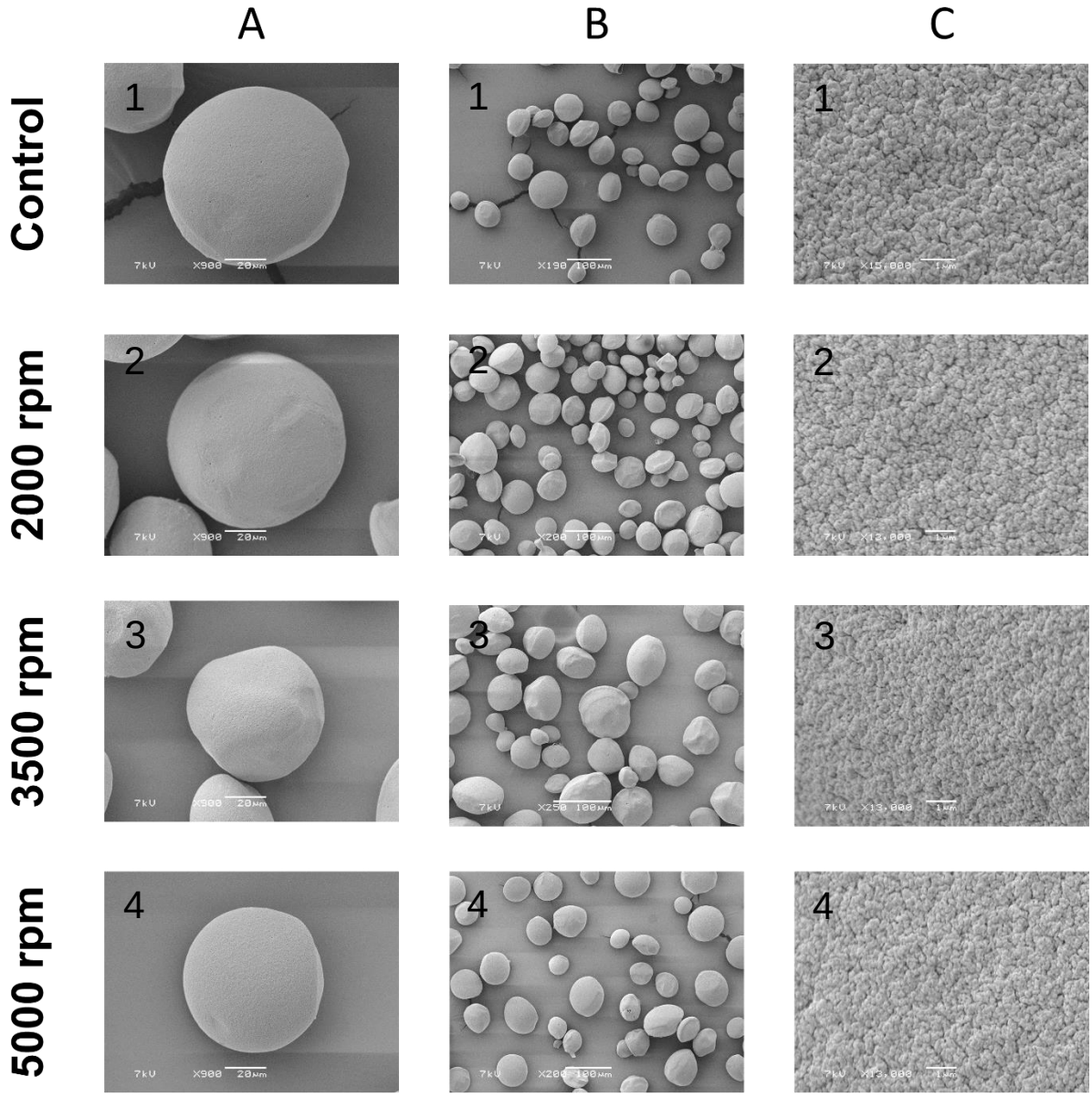

Figure 4.14. A) Scanning electron micrograph showing fresh Q Sepharose FF post-freeze drying. Whole bead (X900), average bead population (x190) and bead surface (x1500), 7 kV images in that respective order. B) Scanning electron micrograph showing 2,000.0 rpm sheared Q Sepharose FF post-freeze drying. Whole bead (X900), average bead population (x200) and bead surface (x1300), 7 kV images in that respective order. C) Scanning electron micrograph showing 3,500 rpm sheared Q Sepharose FF post-freeze drying. Whole bead (X900), average bead population (x250) and bead surface (x1300), 7 kV images in that respective order. D) Scanning electron micrograph showing 5,000 rpm sheared Q Sepharose FF post-freeze drying. Whole bead (X900), average bead population (x200) and bead surface (x1300), 7 kV images in that respective order. The scale bar represents 20 (10 for 2,000 rpm), 100 (50 for 2,000 rpm) and 1 µm, respectively.

4.4.3.1.2 Quantitative Analysis

The average pore size, apparent porosity (ratio of pore-to-fibre) and total number of pores can be quantified and calculated using ImageJ to have a quantifiable degree of change of the surface of the bead. Table 4.4 shows the average pore count, pore size and apparent porosity of both resins in this experiment (Macro-Prep High Q and Q Sepharose HP) based on 3 bead surface images. ImageJ counts the number of enclosed black pixels and converts this into micrometres, based on the procedure described in Section 2.16. After this, the properties are determined by translating the number of enclosed black pixels into the pore count, the average area of all enclosed black pixels into the average pore size, and the area percentage of the black enclosed pixels to the whole image into apparent porosity.

The results show that any sample from Macro-Prep High Q has the highest pore count among both matrices. This can be misleading as Q Sepharose FF seems to be thicker or more viscous maybe due to the cross-linking between the agarose, making it harder for the machine to distinguish a pore from the actual bead. The average pore count for both resins in all shear levels had low variability. This suggests that the high shear levels did not create or obstruct a significant amount of pores or holes. This property can be observed in Section 4.4.3.1.1, both qualitative and quantitative analyses are in agreement, as the surface remained somewhat unchanged.

The average pore size seemed to increase after being exposed to a high shear, as this property increased 10%, 15% and 12% for the shear levels of 2,000, 3,500 and 5,000, respectively; while Q Sepharose FF deviation from the control was -10%, 20% and 10%. The high shear can erode small particles surrounding the pores (enlarging the pore area) as Macro-Prep High Q is made off from a brittle material. In contrast, a possible explanation for such variability is the elasticity of the Q Sepharose FF, protecting the surface from cracking or “peeling off” but deforming the pores in the process causing a higher error in ImageJ as the average area of the pore is calculated by approximating the enclosed black pixels to a circle. This characteristic can be perceived during the qualitative analysis, as the surface of Q Sepharose FF looks flexible and thicker compared to the robust and rigid but brittle look of Macro-Prep High

Q. This change of average pore size cannot be immediately perceived while doing a qualitative analysis for any of the resins.

Macro-Prep High Q appeared to have the highest apparent porosity of both resins, as it can be observed in Figures 4.13 and 4.14. Q Sepharose FF presented half of the apparent porosity, explained by the “gel-like” surface and high cross-linkage. The apparent porosity for Macro-Prep High Q increased 37%, 32% and 42% for the shear level of 2,000, 3,500 and 5,000 rpm, respectively; while for Q Sepharose FF it was a -10%, 34% and 20%. Direct comparisons of these results to other similar studies done by Mauryn Nweke show similar values for all these properties for Q Sepharose FF, while the studies for Macro-Prep High Q are limited on past literature (Mauryn C. Nweke 2017).

Overall, pores on the Macro-Prep High Q surface were significantly affected to the same degree no matter the shear level, while Q Sepharose FF showed more consisted properties due to its soft and flexible nature. The results also show a correlation between the properties observed in the qualitative analysis (Section 4.4.3.1.1) and the quantitative analysis.

Table 4.4. Quantitative analysis for average pore count, average pore size and average porosity for 20% (v/v) fresh and sheared Macro-Prep High Q and Q Sepharose FF resin slurry in 20 mM phosphate buffer pH 7.

Resin	Shear Level (rpm)	Average Pore Count (-)	Average Pore Size (µm)	Apparent Porosity
Macro-Prep High Q	0	465.15	0.043	21.04
	2000	471.05	0.044	28.80
	3500	436.58	0.046	27.63
	5000	442.98	0.045	29.75
Q Sepharose FF	0	276.12	0.022	8.25
	2000	275.46	0.018	7.47
	3500	301.42	0.024	11.03
	5000	300.80	0.022	9.93

4.4.3.2 Low Shear

4.4.3.2.1 Qualitative Analysis

Figures 4.15 and 4.16 depicts SEM images of an average bead at two different time points of the experiment in each of the configurations used to test the durability and performance of Macro-Prep High Q and Q Sepharose HP under low shear stress environments for short and long cycles. The configuration modes were CCTC (A), peristaltic pump coupled in total recirculation to the resin reservoir (B) and the resin reservoir mixer alone (C). Figure labelled 1 and 2 represent the resins 4 h after the experiment started using a magnetic stirrer mixer or an overhead impeller, respectively. Figures labelled 3 and 4 show resin beads after 36 h after the experiment started using a magnetic stirrer mixer and an overhead impeller, respectively.

Figure 4.15 shows a randomly selected fresh bead of Macro-Prep High Q. The control sample depicts a uniformly spherical in structure and shows no visible signs of damage, with the exception of some neighbouring beads with slight indentations. Figure 4.15.B.1 show that the magnetic stirrer mixer has already started to drastically indent and chip all over the surface of the bead, in addition the surface looks somewhat eroded; while the overhead impeller (Figure 4.15.B.2) counterpart seems to be intact and comparable to the control. Figure 4.15.B.3 shows most of the resin beads are cracked open completely with only some spherical structures remaining. Confirming the deviation from the original PSD (from 50-100 µm to 8-55 µm) measured in Section 4.4.2.2. On the other hand, Figure 4.15.B.4 presents a resin bead that represents the whole population, the surface and shape look undamaged. All the rest of the samples for the other configurations (Figures 4.15.C.1 to C.4 and D.1 to D.4) shared all the characteristics described above to their counterparts of the same resin reservoir mixer with no significant visible variations. This samples also confirm the miscalculations error by the Mastersizer by showing minimal traces of non-existent fine fractions.

Figure 4.16 has the same structure as Figure 4.15 but Q Sepharose HP was the resin subject for SEM imaging. The control showed had quasi-spherical with flatten sides in the most-part and a less dense or lowly-packed surface but no signs of damage or fragmentation. In Figure 4.16.B.1, beads quasi-spherical with flatten side with no

visible damage or fragmentation on the surface can be observed. In contrast, Figure 4.16.B.2 shows a more spherical shape resin bead with flatten sides. Figure 4.16.B.3 and B.4 showed similar results, they display a population of barely sphere-shaped beads with flatten sides and some of them with fragments missing or signs of the resins bursting due to a high force; however, Figure 4.16.B.4 presented more sphere-like beads. Beads in Figures 4.16.C.1, C.2, C.3, C.4, D.1 and D.3 showed the same characteristics as in their respective configurations. Figures 4.16.D.2 and D.4 showed similar observations, the resin beads have a uniformly spherical shape and show no signs of flatten sides or significant surface damage. The disparity behaviour of the 3 different configurations using the overhead impeller mixer confirms the difference in PSDs obtained in Section 4.4.2.2. This samples also confirm the miscalculations error by the Mastersizer by showing minimal traces of non-existent fine fractions.

Q Sepharose HP is able to withstand the freeze-drying process just like its similar resin, Q Sepharose FF. The magnetic stirrer mixer seemed to have a negative impact for all samples subjected to it. The magnetic stirrer might have a grinding effect on the resin beads, as the most rigid one cracked and fragmented while the flexible one got permanently deformed. There are not any publications addressing this issue as a magnetic stirrer mixer is not intended for any of these applications up to this point. Also, overhead impellers are used for the manufacturing of chromatography media but never used for actual experiments. High shear stress or high flow velocities can be discarded, as seen in Section 4.4.2.1, as the possible cause of the structural damage. Low shear for a longer period of time seems unlikely as the samples in the resin reservoir with only the overhead impeller presented characteristics comparable to the ones seen in the control samples. Macro-Prep High Q seemed like a more robust resin once the magnetic stirrer mixer was removed, showing almost no disparity between all the samples and the control. This suggests that the CCTC system and, more importantly, peristaltic pump action do not have a bigger impact on the physical structure of rigid beads. On the other hand, Q Sepharose HP was affected in a similar manner by all the configurations, excluding the overhead impeller mixer alone. This implies that the force induced by the peristaltic pumps upon the softer resin beads causes a plastic deformation and a minor fragmentation. The unique spherical shape seen in Figure 4.16.D.2 and D.4 might be explained by the constant overall shear the bead was experiencing around all its surface causing a slight deformation of the

surface layer. The flatter sides seen in all the other samples from Figure 4.16, can be attributed to the manufacturer or the freeze-drying process as mentioned in Section 4.4.3.1.1.

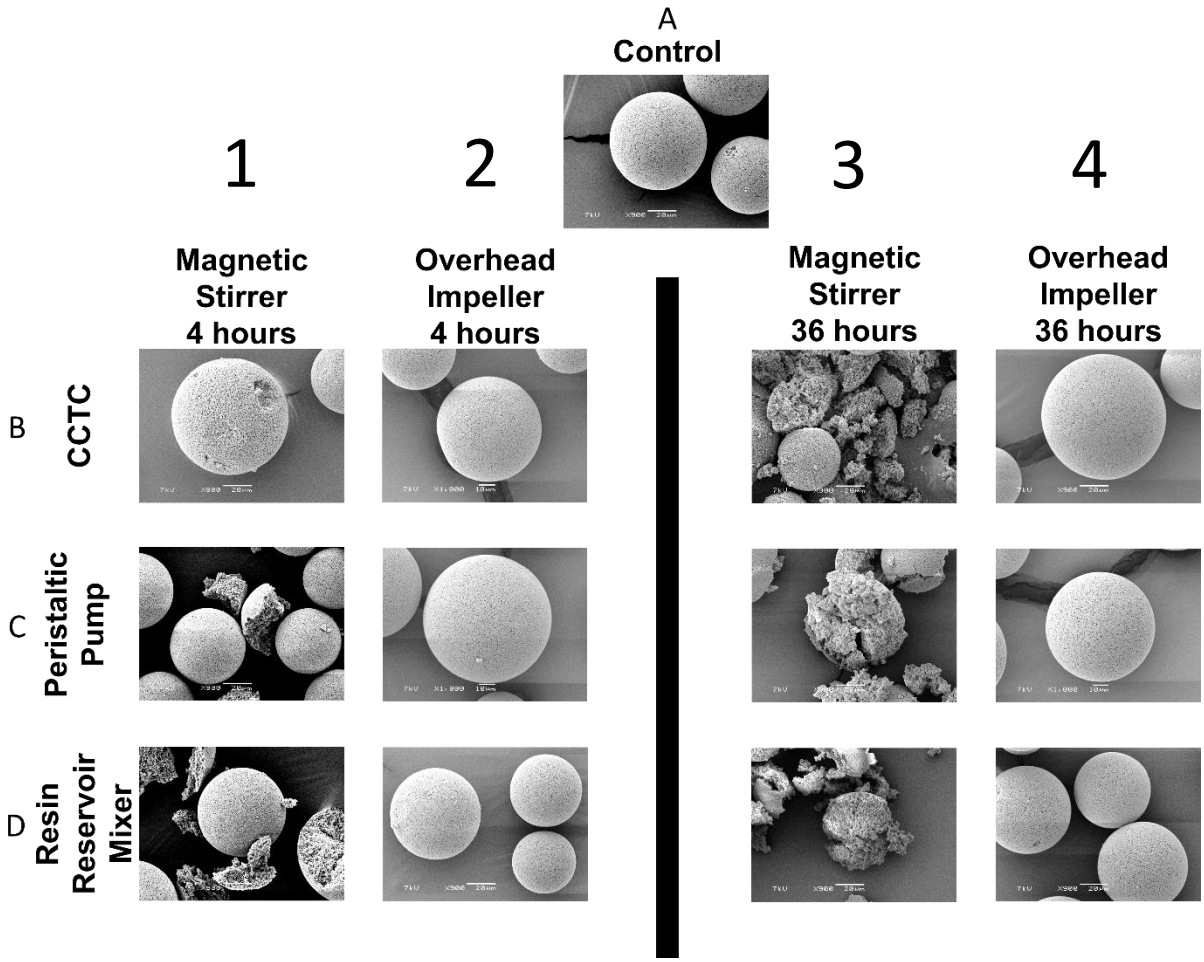

Figure 4.15. A) Scanning electron micrograph showing fresh Macro-Prep High Q post-freeze drying. Whole bead (x900) 7 kV image. B) Scanning electron micrograph showing resin Macro-Prep High Q post-freeze drying after being used in a CCTC with a magnetic stirrer and overhead impeller mixer in the resin reservoir after 4 and 36 h, respectively. Whole bead (x900, x1000, x900 and x900) 7 kV image. C) Scanning electron micrograph showing resin Macro-Prep High Q post-freeze drying after being used in a system consisting of a peristaltic pump and a magnetic stirrer and overhead impeller mixer in the resin reservoir after 4 and 36 h, respectively. Whole bead (x900, x1000, x900 and x1000) 7 kV image. D) Scanning electron micrograph showing resin Macro-Prep High Q post-freeze drying after being mixed using a magnetic stirrer and overhead impeller mixer in the resin reservoir after 4 and 36 h, respectively. Whole bead (x900, x900, x900 and x900) 7 kV image. The scale bar represents 20 µm, with the exception of image C – Overhead Impeller 4 h and 36 h being 10 µm.

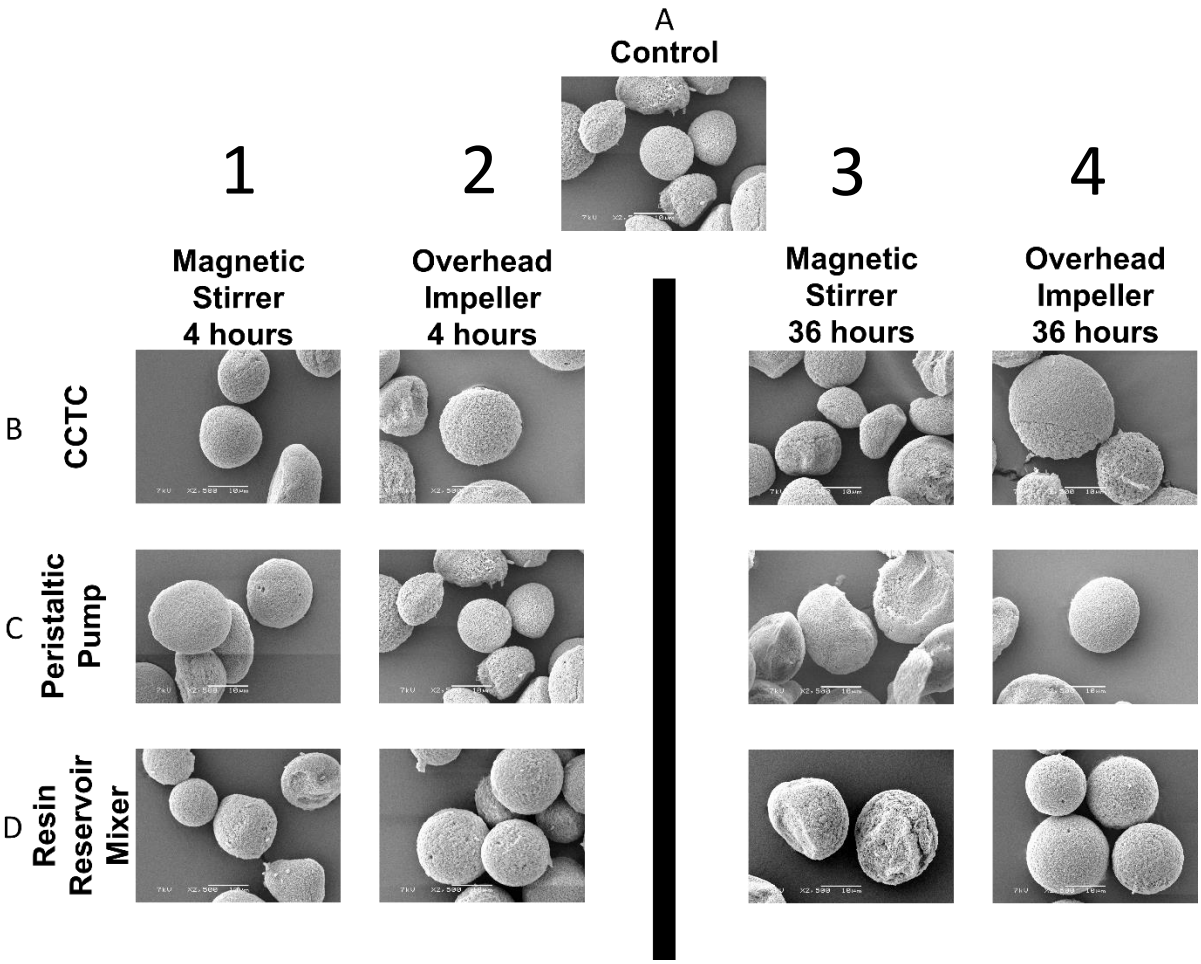

Figure 4.16. A) Scanning electron micrograph showing fresh Q Sepharose HP post-freeze drying. Whole bead (x2500) 7 kV image. B) Scanning electron micrograph showing resin Q Sepharose HP post-freeze drying after being used in a CCTC with a magnetic stirrer and overhead impeller mixer in the resin reservoir after 4 and 36 h, respectively. Whole bead (x2500, x2500, x2500 and x2500) 7 kV image. C) Scanning electron micrograph showing resin Q Sepharose HP post-freeze drying after being used in a system consisting of a peristaltic pump and a magnetic stirrer and overhead impeller mixer in the resin reservoir after 4 and 36 h, respectively. Whole bead (x2500, x2500, x2500 and x2500) 7 kV image. D) Scanning electron micrograph showing resin Q Sepharose HP post-freeze drying after being mixed using a magnetic stirrer and overhead impeller mixer in the resin reservoir after 4 and 36 h, respectively. Whole bead (x2500, x2500, x2500 and x2500) 7 kV image. The scale bar represents 10 µm.

4.4.3.2.2 Quantitative Analysis

ImageJ software allowed us to quantify the average pore size, apparent porosity (ratio of pore-to-fibre) and total number of pores on the surface of Macro-Prep High Q and Q Sepharose HP after 36 h of use either a magnetic stirrer mixer or an overhead impeller mixer in a CCTC system, a peristaltic pump with the mixer and the mixer

alone. Table 4.5 shows the average pore count, pore size and apparent porosity for the aforementioned samples based on 3 bead surface images. The method for calculating each property was done similar to what was described in Section 4.4.3.1.2 and thoroughly described in Section 4.3.5.

According to the results of Macro-Prep High Q, the average pore count did not show any trend for both of the mixing configurations, with some samples having a variability of +-20%. Even though the resin bead is fragmenting, the rigid surface keeps its original shape from being deformed or blocked. Additional pores could have been created but the pictures were taken of the original surface, excluding any sites where the bead was fragmented or chipped. On the other hand, Q Sepharose HP showed less pores on its surface for the configuration with the magnetic stirrer mixer for CCTC (-15%), peristaltic pump and mixer (28%), and mixer (-50%). This decrease in average pore count might be caused by the blockage of pores as the resin bead gets squeezed and compressed by the external forces in the peristaltic pump and the magnetic stirrer mixer. The deviation is highest when using the magnetic mixer as the resin beads remain in contact for longer with the magnetic stirrer compared to the other configurations where the resin has to travel from the resin reservoir to the peristaltic pump and finally, the hollow fibre. For the overhead impeller mixer configurations, the CCTC (-2%) and peristaltic pump with mixer (-29%) showed a decreasing trend, while the overhead impeller mixer alone had an increase of 26%. As the qualitative analysis showed, the resin beads in the first two configurations suffer a plastic deformation, bringing a possible squeezing (widening or narrowing) and blocking of the pores, making them unable to be detected by the software. On the other hand, the resin beads gain a uniformly spherical shape with unblocked or squeezed pores due to the shear experience in the overhead impeller mixer.

The average pore size for Macro-Prep High Q had two different trends depending on the mixer used in the resin reservoir. For the magnetic stirrer mixer, a deviation of -38%, -43% and -45% was measured for the configurations of CCTC, peristaltic pump with mixer and mixer alone, respectively. While for overhead impeller, a change of 4%, 18% and 8% was measured, respectively. The decrease in average pore size can be explained to the excessive grinding caused by the magnetic stirrer upon the bead resulting in the eroding and chipping of the external layer of the bead. As the external layer disappeared, the smaller pores start to show on the surface. Conversely, the

overhead impeller mixer configurations showed a small increase in average pore size without a specific trend. In this case, the perimeter of the top layer pores gets chipped or eroded but not enough to reveal the smaller inside pores. For Q Sepharose HP, the magnetic stirrer mixer caused the average pore size to increase 510%, 446% and 545% for the configurations of CCTC, peristaltic pump with mixer and mixer, respectively. For the overhead impeller mixer configurations, an increase of 64%, 82% and 46% was measured, respectively. The magnetic stirrer mixer drastically wears down the surface due to the compressing and stretching of the bead; while, with the overhead impeller mixer, the wear is reduced but still significant to cause plastic deformations of the shape of the bead. The qualitative analysis of the resin (Section 4.4.3.2.1) provides support to the information gained in this section.

Macro-Prep High Q shows an increased average porosity for all configurations with both mixers without any specific trend with a maximum increase of 39% and a minimum of 6%. Q Sepharose HP shows an increased apparent porosity of 37%, 57% and 48% for the CCTC system, peristaltic pump with mixer and mixer using a magnetic stirrer mixer, respectively, and 20%, 23% and 50% for the ones using an overhead impeller mixer. The increase of apparent porosity, even when the average pore size has decreased, might be due to the fact that the software calculates the pore size in relation to a perfect circumference. The apparent porosity is just the ratio of dark enclosed pixels to the non-dark pixels in the whole image and does not take into account any other data. The porosity is an approximation as it is measured as a 2D property, when in reality the 3D nature of the pores is not accounted for in this study. This probably increases the error as parts of the bead should or should not be accounted for the calculation. The SEM images (Section 4.4.3.2.1) show a higher porosity for both resins and both samples, indicating that there is an agreement between both analyses.

In general, the magnetic stirrer mixer showed to have the biggest negative impact on both resins. The CCTC and the peristaltic pump have a minor impact or no impact, suggesting that the whole CCTC system (excluding the resin reservoir mixer) is safe to use with both types of resin. The overhead impeller was the better choice for mixing the resin slurry in the resin reservoir as it does not have a grinding effect and showed the overall lowest deviation from the fresh resin. The average pore size and the apparent porosity increase as the resin experiences shear for long cycle times, with

the exception of Macro-Prep High Q with the magnetic stirrer mixer as the resin beads fragment causing an uneven surface. In most cases, the results show a correlation between the properties observed in the qualitative analysis (Section 4.4.3.2.1) and the quantitative analysis.

Table 4.5. Quantitative analysis for average pore count, average pore size and average porosity for 20% (v/v) Macro-Prep High Q and Q Sepharose HP resin slurry in 20 mM phosphate buffer pH 7 under different system configurations.

Resin	Configuration	Mixer Type	Average Pore Count (-)	Average Pore Size (μm)	Apparent Porosity
Macro-Prep High Q	Control	-	465.21	0.040	21.04
	CCTC	Magnetic Stirrer	576.65	0.025	25.38
	Peristaltic Pump	Magnetic Stirrer	490.89	0.023	21.50
	Mixer	Magnetic Stirrer	407.32	0.022	29.14
	CCTC	Overhead Impeller	457.02	0.040	25.50
	Peristaltic Pump	Overhead Impeller	741.30	0.048	23.50
	Mixer	Overhead Impeller	345.84	0.043	29.15
Q Sepharose HP	Control	-	611.77	0.011	12.71
	CCTC	Magnetic Stirrer	513.15	0.067	17.46
	Peristaltic Pump	Magnetic Stirrer	438.36	0.06	19.93
	Mixer	Magnetic Stirrer	303.08	0.071	18.86
	CCTC	Overhead Impeller	596.90	0.018	15.20
	Peristaltic Pump	Overhead Impeller	432.56	0.020	15.69
	Mixer	Overhead Impeller	826.43	0.016	19.03

4.5 Conclusion

As previously mentioned, CCTC as an emergent purification technology has not been fully explored. The inherent nature of the system raises an alarm about resin performance and structural integrity after short and long cycle times. The hindrance of any of these two qualities may compromise the quality and safety of the therapeutic product, the CCTC system and the users.

In order to investigate these concerns, high and low shear experiments were performed upon synthetic (Macro-Prep High Q) and agarose-based (Q Sepharose FF and Q Sepharose HP) resins. The high shear studies were conducted in a USD rotary disc device at different shear levels. The low shear experiments were performed in 3 different configurations (CCTC, peristaltic pump with mixer and mixer) with 2 different mixers (magnetic stirrer mixer and overhead impeller mixer).

The high shear studies showed that the shear experienced was not enough to cause a significant change in the performance/productivity (DBC) or PSD in any of the resin samples. Comparing the high shear stress values to the ones calculated for the CCTC system, it can be implied that the shear stress in the latter does not have a significant effect on the resin beads. The high shear stress magnitude was 3,000X to 14,000X larger than the low shear ones. Observations upon SEM images supported these claims as both resins seemed to be intact. Quantitative analysis of the SEM images showed an overall increase in average pore size (up to 15%) and apparent porosity (38%) for Macro-Prep High Q due to its rigid nature, while Q Sepharose FF had a less of an impact due to its flexible nature.

It seemed that using the low shear configuration rigs for 36 h had a significant impact on the physical structure both of the resin but the performance remained unchanged. The DBC of all resin samples in all configurations remained unchanged with a variability of up to +-5.%. This shows that the ligands on the surface and inside of the bead (if fragmented or deformed) are unaffected by the physical stress experienced after 36 h. The PSD and average particle size of Macro-Prep High Q was extremely affected by the magnetic stirrer mixer, disregarding of using it with the CCTC or the peristaltic pump, with a decrease in average particle size of at least 60% (from 70 to 28 μm); while the configurations with the overhead impeller did not show a significant

change, even if the full 2-stage CCTC system was in use or not. This suggests that the CCTC or the peristaltic pump do not have a significant effect on the methacrylate bead, unlike the magnetic stirrer. On the other hand, Q Sepharose HP was not as significantly affected due to its flexible nature. The magnetic stirrer mixer had an overall increase of 6% in the average bead size, while the overhead impeller mixer had an overall decrease of 5%. In a general manner, the CCTC system (including the use of stand-alone peristaltic pumps) does not have any significant effect on the average bead size. Non-existent fine fractions were mainly found in the agarose-based samples due to the transparency of the material and the Fraunhofer approximation used for the calculation of the PSD.

SEM images of high and low shear samples were qualitatively and quantitatively analysed. Both resins showed similar visible properties to their control counterparts, Macro-Prep High Q looking rigid but brittle and Q Sepharose FF flexible but lacking of a defined shape. Macro-Prep High Q showed an increase in average pore size (0.04 to 0.45 µm) and apparent porosity (21% to 28%) among all shear levels. Q Sepharose FF exhibited a similar increase for both, the average pore size (0.02 to 0.023 µm) and apparent porosity (8 to 10%). It can be said that both resins are robust enough to withstand high shear forces comparable to being feed into a large scale centrifuge. The non-existent fine fractions were nowhere to be found in any of the samples, confirming the non-existence of such particles.

Images from low shear studies showed that Macro-Prep High Q is highly susceptible to grinding or crushing forces as it got fragmented in all configurations that the magnetic stirrer mixer was used but apparently intact for the ones with an overhead impeller. On the contrary, Q Sepharose HP showed visible damage but no signs of fragmentation or chipping due to its flexible nature. However, this seemed to have permanently deformed some of the bead. The only exception to this was the use of an overhead impeller mixer, as its even shear forces reshaped the bead into a uniform sphere. The qualitative analysis of the surface of the pictures helped to give a larger insight on the damage. The average pore size for Macro-Prep High Q got drastically reduced (0.04 to 0.023 µm) for the configurations with a magnetic stirrer mixer, probably to the erosion or crack of the outer layer and displaying some of the smaller pores on the inside. In contrast, the configurations using an overhead impeller mixer had an increase of average pore size (0.04 to 0.047 µm) due to the edges of the pore

constantly being eroded by mild shear forces. Q Sepharose HP showed an overall increase in its average pore size for the magnetic stirrer mixer (0.1 µm to 0.07 µm) and for the overhead impeller mixer (0.01 to 0.02 µm), might be due to wear and tear of the surface due expansion and the compression of the bead, a “balloon-like effect”. The apparent porosity increased all aboard both resins and configurations probably related to the increased pore sizes with the exception of Macro-Prep High Q in constant contact with the magnetic stirrer, probably calculation errors by the software and shape of the pores.

The main challenges faced in terms of resin stability when using the CCTC system were addressed in this chapter by analysing the performance, PSD and surface properties. SEM images provided a valuable asset at determining the effect the configurations were having on the resin slurry at a macro- and microscopic level. These experiments proved that the 2-stage CCTC system has no significant impact on the long run for a rigid-based resin and a slight structural change for a more flexible one such as an agarose-based one. It is important to note, that the constant mechanic compression and shear flow caused by the peristaltic pump has the same impact as the whole CCTC system. The overhead impeller mixer is the ideal mixing device for the slurry at the resin reservoir with practically its only impact being the slight deterioration of the surface of the resin bead. The magnetic stirrer mixer has been discarded as a viable option for resin mixing at this scale or scales smaller than this (BBC studies). Finally, a rigid resin is recommended for the separation of biomolecules in a CCTC system as it showed to retain the original DBC, PSD and shape as the control, making it a more robust option to ensure a homogeneous quality throughout the run and further cycles.

The binary and step-gradient separations in a CCTC system were resumed in the next chapter, as the issue of damage of the resin was identified as being caused by the magnetic stirrer mixer and not the CCTC system (including peristaltic pumps) itself. On top of that, the best adapted commercially available resin was selected for such purification due to its rigidness and robustness.

Chapter 5: Binary and Step-Gradient Anion Exchange Separations in a Custom Built Continuous Counter-current Tangential Chromatography System

5.1 Summary

After establishing the possible impact each major CCTC system component, the custom batch 2-stage CCTC rig was built with the specifications and operational parameters explored previously. This chapter describes the two separations in the custom 2-stage CCTC rig. The first experiment was the separation of BSA and myoglobin to assess claims in literature and identify possible draw backs only present in this technique. The second study focused on the separation of ovalbumin into its major variants in order to explore an elution in a salt-gradient elution in a CCTC system. Previous column-based separations were performed as preliminary studies in order to avoid the waste of resources during the CCTC runs.

5.2 Introduction

The previous chapters established the design of the static mixers and the operational conditions for the hollow fibres, as well as addressing the potential detrimental effects the CCTC system, the peristaltic pumps or the resin reservoir mixer use may have upon the resin. Also, the identification of the optimal matrix to be used for the system in general. Following the logical progression of the project, the final CCTC rig was put into test with two different separations. Both separations, in conjunction with all the experience gathered throughout the experiments reported in Chapter 3 and 4, will help evolve the work and the design of the CCTC system. The system has tremendous potential but it needs to pushed into its limits to grow as a chromatography technique.

This chapter looked to test the full scale custom built batch 2-stage CCTC rig under all chromatography steps in order to achieve a binary and a step-gradient separation. The first purification consists of the separation of an ideal mixture of BSA and myoglobin using Macro-Prep High Q as the anion exchange resin due to its rigidity and robustness. The second experiment looks to recover ovalbumin into its different variants in a 2 step-gradient process using Q Sepharose HP due to its higher capacity and limited resources. The first separation looks to identify the strong points of the system, also for areas of opportunity or limitations the current design presents. The

second separation aims to push the system to its limits in terms of a gradient-based purification by including 2 elution steps with close elution behaviours.

For the first separation, the system separated myoglobin (contaminant) and BSA (molecule of interest). This non-challenging separation exemplifies the original intended use of the system by just adsorbing 1 target molecule in 1 step and eluting the molecule in its totality in a further step while the contaminants are collected as flow through during the first steps of the process. The CCTC separation was done by performing a set of individual chromatographic steps (bind, wash-1, wash-2, elution and strip) in succession in order to replicate a full scale CCTC system. The buffer conditions only allowed the adsorption of BSA into the Macro-Prep High Q beads, leaving the myoglobin free in the mobile phase. The myoglobin exited the system during the bind, wash-1 and wash-2 steps. BSA was harvested during the elution step. In order to check the possible interaction between the two molecules and/or the matrix, column-based separations were performed first for convenience.

For the second separation, the CCTC was challenged with the separation of ovalbumin into its different variants. This separation was done to mimic a separation where two molecules of interest bind to the chromatography resin and they need to be collected separately at different pools. Ovalbumin is a protein with different molecular conformations which mainly differ with respect to different phosphorylation and glycosylation patterns. The different ovalbumin forms allow the protein to desorb at different ionic strength points of the salt gradient. The nature of the CCTC system does not allow a real salt gradient as is possible in a column-based technique. However, a salt step-gradient can be achieved by having multiple elution steps in the process train. An ionic strength characterisation was done first in order to fix the salt concentrations for each elution step and define what ovalbumin variants would be obtained from them. Because the CCTC has a diluting nature and ovalbumin is an expensive resource, a total of 2 elution steps were planned to keep the molecule above the sensible limits of the spectrophotometer.

The separations were theoretically and empirically analysed step by step in order to measure purity and yield of the CCTC process. The protein concentration was tracked from the start of the run and after it reaches a steady state. Other characteristics such as the system pressure or slurry concentration at the outlet of the hollow fibre were

also recorded to assess the stability of the system. Also, the results and experience gained with the system were used to obtain a bigger insight into the capabilities and windows of opportunity the system shows at the present moment.

5.3 Theoretical Considerations

5.3.1 BSA and Myoglobin separation in Packed-bed Chromatography

Before attempting the separation of BSA and Myoglobin in the CCTC system, a packed-bed chromatography purification run was planned to explore the interaction between the matrix and the molecules in the same buffer conditions planned for CCTC. The separation conditions were chosen taking into considerations the DBC results in Section 3.4.7 and the method described in Section 2.14. The separation was done by using a 1 mL Bio-Scale Mini Macro-Prep High Q Cartridge pre-packed column to avoid the packing procedure and the errors related to the process. The mixture of BSA and myoglobin had a concentration of 2 mg/L and 0.85 mg/mL, respectively. To avoid saturation, the protein load was calculated with 70% of the original DBC. A different pH could have been used to improve the loading, resolution and elution pooling. Nonetheless, none of these parameters (except for loading) are a crucial aspect for the purpose of this characterisation and a typical CCTC separation.

On top of the separation pattern, the overall purity and yield were calculated as follows:

$$Purity = \frac{m_{BSA}}{m_{BSA}+m_{myo}} \quad (21)$$

$$Yield = \left(1 - \frac{m_{BSA,load}-m_{BSA}}{m_{BSA,load}}\right) \times 100 \quad (22)$$

where m_{BSA} is the total BSA mass collected in the elution step, m_{myo} is the total myoglobin mass collected in the elution step and $m_{BSAload}$ is the BSA mass loaded into the system.

5.3.2 Design of the 2-Stage Continuous Counter-current Tangential Chromatography Rig

The CCTC rig was design to be a batch 2-stage CCTC system. A 2-stage CCTC system theoretically guarantees approximately 93% protein recovery, assuming all the product had enough residence time to bind onto the resin ligands and the resin had enough binding capacity for the load (Napadensky *et al.*, 2013; Amit K. Dutta *et al.*, 2016). The key parameters for each step of the separation of BSA and myoglobin are presented in Section 2.8 - Table 2.2. A diagram of the rig portraying all the elements, including tubing and connections, and its dimensions is shown in Figure 5.1. A simplified schematic of a single stage detailing all inlets and outlets for the theoretical mass balance calculations is presented in Figure 5.2. Even though the system used for these studies is a 2-stage system, the simplified 1-stage system can be used for all the intended calculations showed in Section 5.4.2. The mass balance only involves the inlets and outlets, meaning that streams going from stage 1 to stage 2, and vice versa are left unknown as their theoretical or experimental calculation are out from the scope of the project.

The system is intended to run in batch mode, with each chromatography step performed sequentially afterwards. The whole system was primed with the respective step buffer before every step. The step started when the pressure achieved a steady state and there were no bubbles inside any of the tubes or hollow fibres. After each step, the resin was recovered. The mobile phase in the resin slurry was left untouched to avoid any protein loss. Nevertheless, the pH and ionic strength was measured and registered. The resin slurry was left to settle for 1 or 2 hours to confirm the concentrated resin slurry concentration (20% (v/v%)) for the next step. In some instances, a fraction of the mobile phase had to be removed to achieve such concentrations. While the resin slurry was settling, the cleaning of the whole CCTC was done by pumping water into the whole system to get rid of as much protein material or resin beads that were left in the static mixers and hollow fibres. The cleaning was done until the ionic strength and pH became steady; then, sodium hydroxide was used to get rid of any protein material and finally, a second water wash was performed.

Based on the results in Section 3.4.4, 3.4.5 and 3.4.6, the static mixers were designed to provide an approximate minimum residence time of 120 s. Each static mixer counts with 12 elements, even increasing the average residence time without any measurable pressure drop. The hold-up volume of each static mixer is approximately 30 mL. Hence, sets of 2 static mixers for each stage (4 in total per chromatography step) were needed to provide a total hold-up volume of 120 mL (disregarding the hold-up volume between each static mixer and hollow fibre). An after-binder (an extra static mixer the resin slurry would have to go through after the second stage and before being collected for the next step) was considered but discarded due to the experiments on Chapter 3, the settling time and the utilisation of 70% of the total BBC. Another improvement that can be done in respect to this module is that the volume/length/RT of the module can be increased or decreased if necessary to increase productivity; i.e. the elution step requires a shorter average residence time than binding. Table 5.1 shows all the specifications and dimensions of each static mixer.

The hollow fibre modules in the CCTC system were designed based on inlet (diluted) and outlet (concentrated) slurry of 5% and 20%, respectively. The critical flux for this specific concentration is 70 LMH, giving a maximum conversion of 75%. The final membrane surface area for each of the modules was 175 cm^2. The total flow rate was set to 51 mL/min; this was done by pumping 38 mL/min of buffer (feed for binding step) and 13 mL/min of concentrated resin slurry. The value of γ (ratio of buffer flow rate to the concentrated resin slurry flow rate) was set to be 3. Table 5.1 shows the dimensions and specifications of each hollow fibre.

The integration of both modules through flexible peristaltic tubing and peristaltic pumps creates the CCTC system; as well as a buffer/resin reservoir acting as the beginning and end for the waste/product/resin for each step.

Table 5.1. Mixing module and hollow fibre module product dimensions and specifications for the 2-stage CCTC rig.

Module	Fibre Internal Dia. (mm)	Total Length (cm)	Effective Length (cm)	Fibre Count (-)	Total Area (cm^2)	Pore Size (µm)	Material	Supplier
Hollow Fibre	0.75	45	41.5	18	175	0.65	Modified Polyethersulfone	Repligen

Module	Diameter (cm)	Length (cm)	No. of Elements (-)	Material	Supplier
Static Mixer	1	30	12	Clear PVC pipe	Cole-Palmer

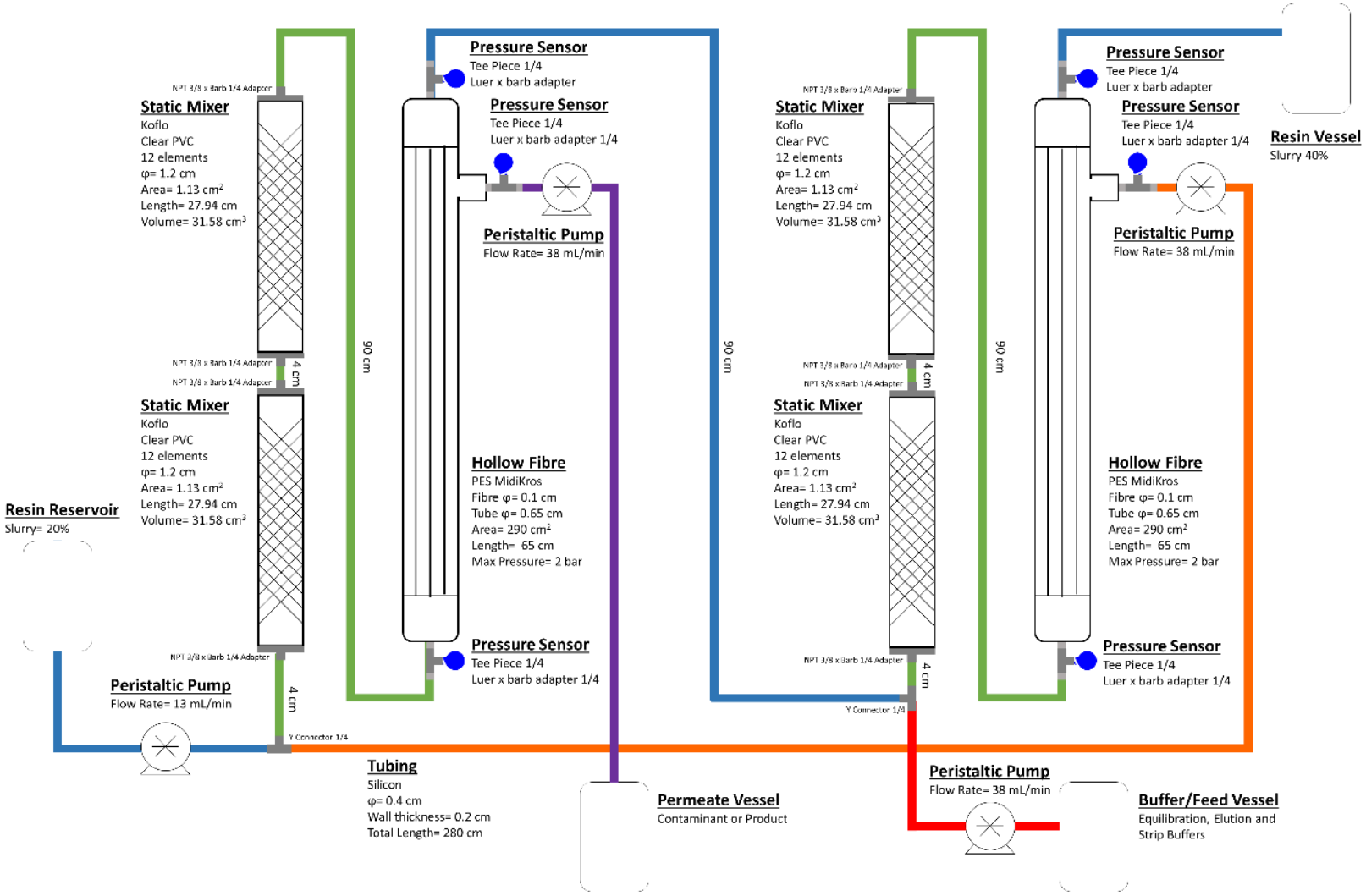

Figure 5.1. Schematic of the flow path, specifications and dimensions of the parts in the 2-stage CCTC rig. The flow path has been labelled in different colours depending on its resin slurry or buffer identity: concentrated slurry (blue), diluted slurry (green), waste/product harvesting stream (purple), waste/product recirculated stream (orange) and fresh load/buffer (red).

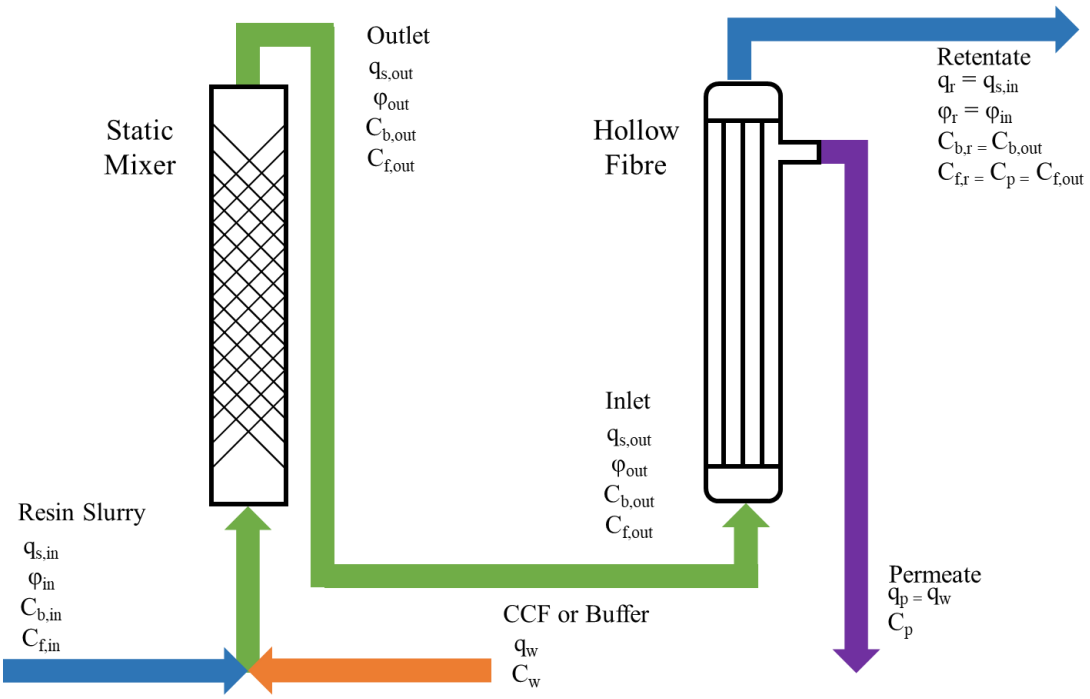

Figure 5.2. Schematic of the mass balance for a 1-stage CCTC system. The flow path has been labelled in different colours depending on its slurry or buffer identity: concentrated slurry (blue), diluted slurry (green), waste/product harvesting stream (purple) and fresh load/buffer (orange).

5.3.3 General Mass Balance

The governing mass balances for each static mixer are (Amit K. Dutta *et al.*, 2016):

$$q_{s,in} + q_w = q_{s,out} \tag{23}$$

$$q_{s,in}\varphi_{in} = q_{s,out}\varphi_{out} \tag{24}$$

$$q_{s,in}\varphi_{in}C_{b,in} + q_{s,in}(1-\varphi_{in})C_{f,in} + q_w C_w = q_{s,out}\varphi_{out}C_{b,out} + q_{s,out}(1-\varphi_{out})C_{f,out} \tag{25}$$

where $q_{s,in}$ and $q_{s,out}$ are the slurry flow rates in the inlet and outlet streams of the static mixer; q_w is the flow rate into the inlet of the mixer from fresh buffer or permeate from the subsequent stage (wash buffer, elution buffer, feed); φ_{in} and φ_{out} are the resin slurry volume fractions in the inlet and outlet streams; $C_{b,in}$ and $C_{b,out}$ are the concentrations of bound target molecule in the inlet and outlet streams; and $C_{f,in}$, $C_{f,out}$ and C_w are the concentrations of free target molecule in the inlet, outlet and fluid streams.

The mass balance equations for the hollow fibre module are (Amit K. Dutta *et al.*, 2016):

$$q_{s,out} = q_r + q_p \tag{26}$$

$$q_{s,out}\varphi_{out} = q_r\varphi_r \tag{27}$$

$$q_{s,out}\varphi_{out}C_{b,out} + q_{s,out}(1-\varphi_{out})C_{f,out} = q_r\varphi_r C_{b,r} + q_r(1-\varphi_r)C_{f,r} + q_p C_p \tag{28}$$

$$C_p = C_{f,r} \tag{29}$$

where the subscripts r and p represent the retentate and permeate streams.

5.3.3.1 Bind Step

The bind step provides enough contact time between the clean resin bead and the buffer containing the molecule of interest. $C_{b,in} = C_{f,in} = 0$ and C_w and C_F is the molecule of interest. $C_{b,out}$ and $C_{f,out}$ are determined by the binding kinetics already explored in Section 3.4.4. The residence time for binding kinetics in the hollow fibre is disregarded for calculations due to its small volume giving $C_{b,r} = C_{b,out}$ and $C_{f,r} = C_{f,out} = C_p$. The amount of target molecule can be calculated as:

$$Load = \frac{C_{b,out}}{Q_{max}} = \frac{\gamma_b C_f}{Q_{max}\varphi_{in}} \quad (30)$$

$$\gamma_b = \frac{q_w}{q_{s,in}} \quad (31)$$

The bind step can be more efficient by increasing the number of stages; hence, the total residence time. Also, an after-binder (static mixer) can be incorporated at the end of the bind step, in order to let the residual free target molecules in the solution at the outlet of the retentate stream.

The yield can be calculated from the following equation:

$$Y_b = \left(1 - \frac{C_{f,out}}{C_0}\right) \quad (32)$$

where C_0 is the target molecule concentration before entering the static mixer. The concentration is expressed as:

$$C_0 = \frac{C_w q_w}{[q_w + \{q_{s,in}(1-\varphi_{in})\}]} \quad (33)$$

5.3.3.2 Wash Step

The purpose of the wash step is to get rid of the unbound impurities through the permeate stream. The counter-current staging is used to reduce buffer usage and increase impurity removal. The binding of the impurities into the resin was assumed to be negligible, making C_b for the impurities 0. The resin slurry concentration (φ_r) from the binding step (or previous step) is equal to the slurry concentration in the inlet of

the static mixer (φ_{in}). The impurity removal is presented as (Dutta, Tan, Napadensky, and Zydney 2016; Dutta et al. 2015a; 2017):

$$R_1 = \frac{\alpha(\alpha^N - 1)}{\alpha^{N+1} - 1} \tag{34}$$

$$\alpha = \gamma SK \tag{35}$$

$$K = \frac{1}{1 - \varphi_{ave}(1 - \omega)} \tag{36}$$

$$\varphi_{ave} = \frac{\varphi_{in}(\gamma + 2)}{2\gamma + 2} \tag{37}$$

where R_1 is the fractional impurity removal from the wash step, N is the number of stages in the step, S is the average sieving coefficient for the species of interest, K is a correction factor that accounts the solid content in the slurry, φ_{ave} is the average slurry volume fraction in the hollow fibre, and ω is the liquid fraction contained in the settled resin bed. The total impurity removal if two steps are used is characterised by (Dutta, Tan, Napadensky, and Zydney 2016):

$$R_{total} = [1\{(1 - R_1)(1 - R_2)\}] \tag{38}$$

The buffer usage for the wash steps is defined as the volume of buffer required per gram of target molecule and can be expressed as (Dutta, Tan, Napadensky, and Zydney 2016):

$$V_b = \frac{(\gamma_{w,1} + \gamma_{w,2})}{\gamma_b C_f Y} \tag{39}$$

where Y is the overall yield, C_f is the concentration of the target molecule in the feed and $\gamma_{w,1}$ and $\gamma_{w,2}$ are the ratios of buffer flow to slurry flow rates in each of both wash steps.

5.3.3.3 Elution Step

The ionic strength used for the elution step is assumed to cause complete desorption from the matrix, making $C_{b,out}$ and $C_{b,r}$ equal to 0. The resin slurry in the retentate stream (φ_r) of the hollow fibre is set equal to the inlet stream (φ_{in}) of the static mixer. The same principle/calculations for the contaminant retrieval applies to elution. The counter-current nature of the system provides an increased yield while minimizing buffer usage. The yield for a multistage elution step can be derived using Equations 34 with (Dutta, Tan, Napadensky, and Zydney 2016):

$$Y_e = R \tag{40}$$

5.3.3.4 Strip Step

The strip step can be considered as a wash step as the target molecule is considered a contaminant and located in the mobile phase. The same assumptions made for elution step (Section 5.3.3.3), which is related to wash step (Section 5.3.3.2), were made for the strip step. As complete desorption already took place in elution, $C_{b,out}$ and $C_{b,r}$ are equal to 0. The BSA entering the system is equal to the BSA coming out the retentate outlet stream in stage 2 in elution step (Elution $C_{f,r}$ = Strip $C_{f,in}$) The resin slurry in the retentate stream (φ_r) of the hollow fibre is set equal to the inlet stream (φ_{in}) of the static mixer. The protein that remains in the system after the strip step can be calculated as follows:

$$Y_s = R \tag{41}$$

5.3.3.5 Staging

All the experiments in Chapter 3 and 4 were performed with a 2-stage CCTC system; however, all the experiments can be done in a single-stage or 2-stage CCTC system. The contaminant reduction and the yield for the elution step would be affected. The yield for the elution was reported to be 78% +-2% to more than 98% +-1% for the 3-stage CCTC system. The values can be calculated as following:

$$Y_n = \frac{\frac{q_p}{q_r}\left[\left(\frac{q_p}{q_r}\right)^n - 1\right]}{\left(\frac{q_p}{q_r}\right)^{n+1} - 1} \tag{42}$$

where n is the total number of stages in the elution step. The equation is derived by assuming total desorption from the stationary phase upon addition of elution buffer. The same concept can be applied for contaminant removal.

5.3.4 Separation of Ovalbumin in Packed Chromatography

A challenging multi-step gradient elution separation in a CCTC system has not been attempted before. A packed-bed chromatography separation was executed beforehand to establish the different ovalbumin variants and the respective ionic strength concentrations required to elute the stationary phase. The fractions were collected and used to create an HPLC method for further analysis and comparison of the traditional packed-bed chromatography and CCTC samples.

The method for this separation (Section 2.9 and 2.10) was an adaptation of the separation of ovalbumin in a SMB system (Chris Wayne 2019). The 1 mL 5 cm Tricorn 5/50 column pre-packed with Praesto Q anion exchange resin was used for these studies to support other project and the required ovalbumin is extremely expensive.

Nevertheless, it was decided that the results could be used for the use of Q Sepharose HP for the CCTC separation because the resin properties of both resin are similar or even identical in some instances; i.e. same chemical stability, same quaternary amine as functional group, same binding capacity, similar particle size (30% smaller), highly cross-linked, agarose-based and similar rigidity. The salt gradient from 0% to 30% NaCl was applied over 50 CVs to have a good resolution and view of all the peaks.

All the elution steps were collected in 1 mL fractions for further individual HPCL analysis. The 280 nm UV signals containing the same species according to the elution volume were compared, compiled and a specific ionic strength concentration was recorded. All the signals were compiled for comparison with the whole ovalbumin variants. Finally, the correlation of ionic strength concentration with each of the peaks was established for the upcoming CCTC separation.

5.3.5 Separation of Ovalbumin in CCTC

The ovalbumin variant separation was successfully performed in a pre-packed column and the ionic strength elution points for all the major variants were established. As the CCTC system requires high volumes of resin slurry, buffer and molecule of interest, only a 2 elution and a strip step were planned to test the 2-stage CCTC system under challenging elution conditions. The first elution was designed to recover the first variant peak eluting at an ionic strength of 7% and the second elution, the second variant peak at 12%. When referring to the ionic strength concentration for each elution step, it is meant to be the concentration inside the static mixers and not the fresh elution buffer fed in stage 2 (unless specified). The strip step was planned to remove the rest of the variants.

The method for this purification (Section 2.10) is similar to the one described for the separation of BSA and myoglobin (Section 2.8). Q Sepharose HP was used instead of Macro-Prep High Q due to the similar or equal properties to the resin used for the column separation. The BBC of Q Sepharose HP approximately doubles the one of Macro-Prep High Q. Also, ovalbumin was limited and previous BBC studies were not able to be performed. The resin slurry concentration at the resin reservoir and the

outlet retentate of the hollow fibre was kept at 20% (v/v), while the diluted slurry inside the static mixers and the inlet of the hollow fibre was 5% (v/v). The total flow rate was set to 51 mL/min (38 mL/min for the permeate flow rate and 13 mL/min for the resin reservoir pump), giving a value of γ_{flow} equal to 3. The aforementioned parameters were kept to same as for the BSA and myoglobin separation, as they work without any membrane fouling or inconvenience at a manageable buffer volume under the planned time cycle.

Samples for every step were taken from the moment the resin slurry mixed with the permeate from the second stage in the T-piece at the entrance of the static mixer. A volume of 2.5 mL was directly taken every minute it passed from the permeate outlet of the hollow fibre located on stage 1. The same occurred for the samples obtained from the retentate outlet of the hollow fibre on stage 2 but the resin was filter using a syringe filter, similar to the method used for BBC studies in Section 2.4.1. Samples taken past the 10 to 15 min mark (steady state already achieved) were used to be individually analysed in the HPLC machine.

5.4 Results and Discussion

5.4.1 Separation of BSA and Myoglobin in a Packed-bed Chromatography

The chromatogram showing the separation of BSA and myoglobin in BioScale Mini Macro-Prep High Q Cartridge pre-packed column is shown in Figure 5.3. A flow rate of 1 mL/min and a concentration of 2 mg/mL BSA and 0.85 mg/mL myoglobin were used. The loading volume was scaled to achieve a total DBC utilisation of approximately 70% to 80% to have a more realistic approach and avoid having large amounts of BSA in the flow through that could overlap with the myoglobin signal. The aim of this separation was to record the behaviour of BSA and myoglobin under these buffer conditions. Hence, the residence time and flow rate from the CCTC operational conditions was not replicated for practical reasons and limitations of the AKTA Explorer.

The results show that myoglobin escapes the column as soon as possible during the loading and wash step. BSA seems to be retained almost completely during these two phases, as the signal coming from myoglobin has no fluctuations or extra plateaus. The wash step lasted longer than a usual step due to the 2 wash steps planned for the CCTC step. There is no evidence of traces of BSA or myoglobin for the rest of the step. The elution of BSA after the ionic strength reached approximately 30% (final 50%) was almost instantaneous, as seen previously in the BBC and DBC studies (Chapter 3). The BSA peak presented an “elbow”, this could have been caused by the presence of naturally occurring dimers or aggregates already in the product as specified by the manufacturers. The same separation was replicated using a HiTrap Q FF column (Q Sepharose FF) with similar results with the only difference being the total residence time of myoglobin inside the column; probably due to the different interaction between BSA and agarose. All the steps were collected in different fractions. Each fraction was loaded into its separate chromatography separation run in order to detect any BSA in the loading and wash steps, as well as myoglobin in the

elution or strip steps. No measurable traces of the molecules were found in the respective steps.

The overall BSA purity and yield after the analysis of each fraction were calculated (Equations 21 and 22) to be 99.6% and 99.1%. This shows that myoglobin has virtually no interaction with BSA or with the ligands in the matrix at these buffer conditions. Also, BSA was recovered in almost its totality.

This separation served as the foundation to what to expect on each chromatographic step while doing it in a CCTC system. The recovery (yield) cannot be translated to the CCTC technique, as depends on the number of stages during the elution step (assuming no protein was lost in previous steps). The purity observed in this separation can be expected in the CCTC system.

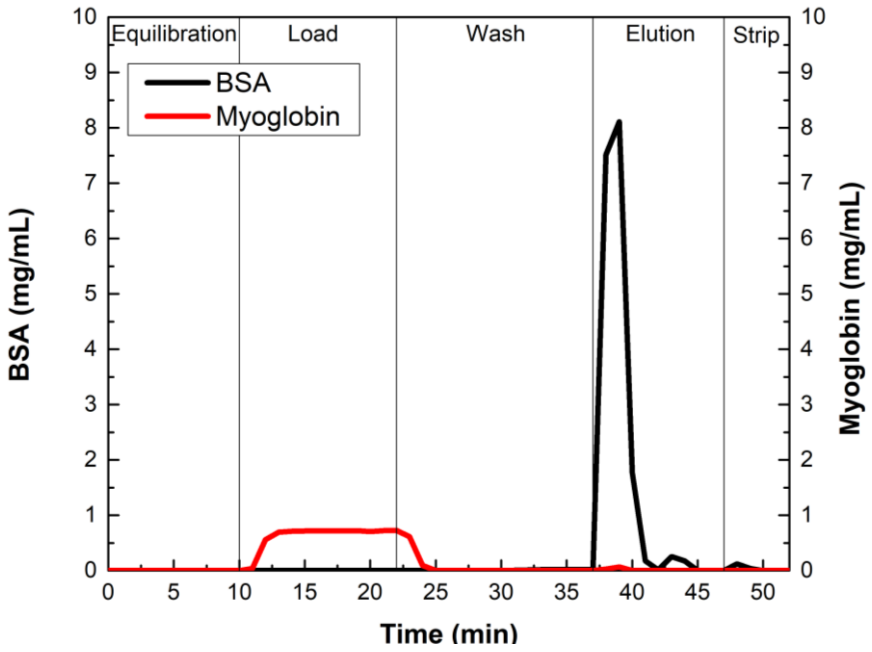

Figure 5.3. Chromatogram of BSA and myoglobin separated using a 1 mL BioScale Mini Macro-Prep High Q Cartridge. The loading concentration was 2 and 0.85 mg/mL of BSA and myoglobin, respectively. All steps were carried out at a flow rate of 1 mg/mL. The BSA yield and purity were above 99%.

5.4.2 Separation of BSA and Myoglobin in CCTC

After the characterization of the mixing and solid/liquid separation module and the column separation test, the CCTC system was tested with the separation of BSA (target molecule) and myoglobin (contaminant). Five different steps were planned: bind, wash 1, wash 2, elution and strip. The samples for all steps were collected from the permeate collected from stage-1 and retentate from stage-2 using syringes fitted with syringe filters similar to the sampling done for BBC studies in Section 2.4.1. The conductivity was manually measured with a probe before and after every step. The samples were individually loaded into a Bio-Scale Mini Macro-Prep High Q to separate and quantify the BSA and myoglobin, as the concentrations cannot be directly measured out of the CCTC system.

5.4.2.1 Bind Step

The purpose of the bind step is to give enough residence time to the target molecule to bind the ligands on the resin and serve as a first wash step to remove some of the contaminants. For the mass balances, it was assumed that all the BSA in the mobile phase binds to the resin bead, while myoglobin has no interaction with it. The general mass balance equations in Section 5.3.3 were used for all the calculations. Figure 5.4 shows a schematic map of the proteins and resin slurry inside each stage and stream during the bind step for a better comprehension of the process.

The load concentration of BSA 1 mg/mL was calculated with an approximate of 80% of the maximum BBC using Equation 30. The theoretical yield for this step was assumed to be 100% (Equation 32) as the assumption was that all free BSA will bind to the resin under the minimum residence time of approximately 120 s (disregarding the tubing between modules). Myoglobin was loaded at a concentration of 0.5 mg/mL to keep a ratio about 2:1.

The bind step was presumed to be a quasi-wash step, as it gets rid of most of the contaminants while the binding interaction between the target molecule and resin slurry happens. Though, the Equations 34 to 37 presented in Section 5.3.3.2 cannot

be used as those equations are only correct when fresh buffer is pumped into the system in stage 2. It must not be feed material or contain the contaminant. Nevertheless, the final concentration for the outlet streams can still be calculated with the general mass balance equations (Equations 26 to 28). The final average concentration calculated in the retentate outlet in stage 2 and the permeate outlet in stage 1 were of 0.46 mg/mL and 0.34 mg/mL, respectively, with a total waste removal of 73%. The concentration in the retentate outlet in stage 2 is higher than the one recovered giving a false sense of waste removal. However, this happens because the retentate outlet stream volume is 3 times smaller than the one at the permeate outlet (γ_{flow} = 2.9) but most of the myoglobin mass coming out of the CCTC system is in the permeate outlet stream in stage 1, as well as the diluting effect the system has at the inlet of every stage.

Figure 5.5 shows the average experimental concentration of BSA and myoglobin throughout the bind step. The BSA in the mobile phase was below detection in almost all the samples, agreeing with the theoretical assumption that practically all BSA binds to the resin slurry before leaving the system. It can also be attributed to the diluting nature of the system, bringing the concentration of the trace BSA in the mobile phase to undetectable limits. The myoglobin concentration increased as expected and reached to a steady state around the 10 min time mark until the end of the step run. The average myoglobin concentration for the retentate in stage 2 was 0.43 mg/mL and 0.35 mg/mL for the permeate in stage 1. The former concentration is carried into the wash 1 step, after assuring the resin slurry concentration is 20% (v/v). The average contaminant removal for the binding step was 67.7%. All empirical number are in agreement with the theoretical numbers calculated beforehand doing the experiment.

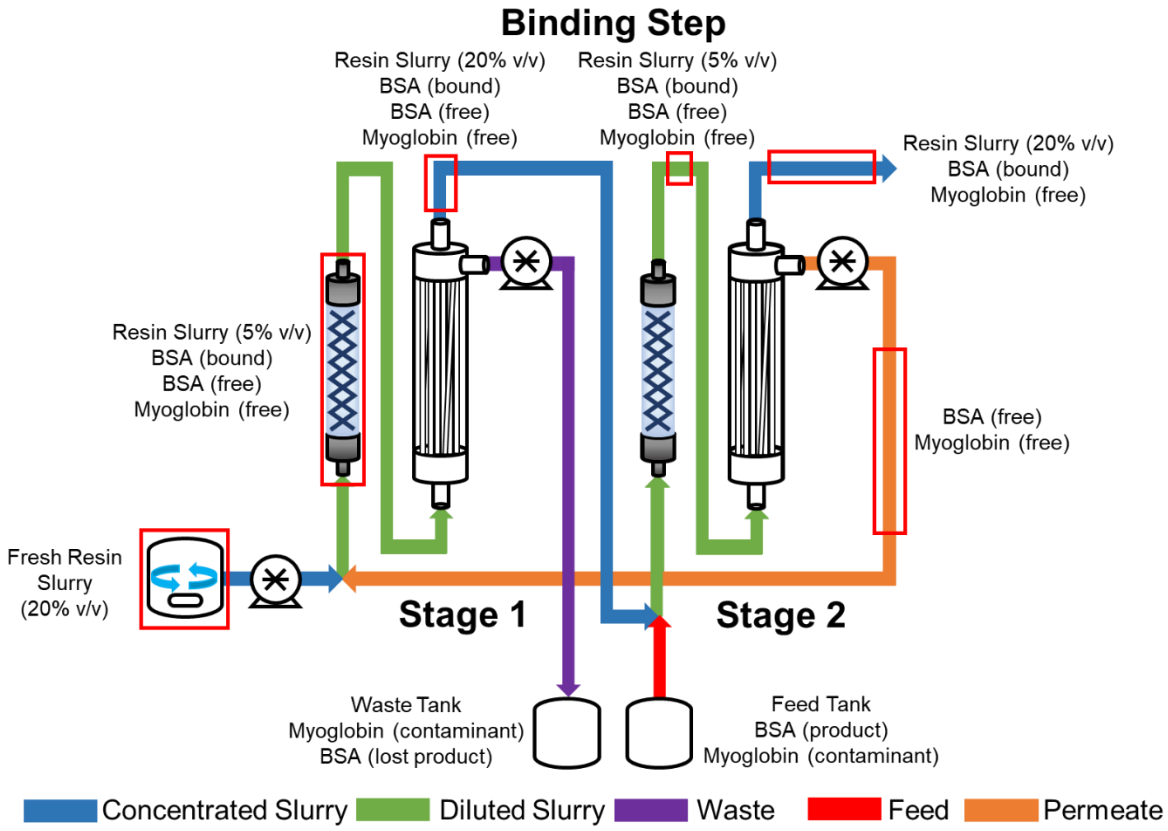

Figure 5.4. Diagram of a 2-stage CCTC system during binding step. The flow paths have been coloured depending on the resin slurry or buffer identity: concentrated slurry (blue), diluted slurry (green), waste/contaminant harvesting stream (purple), recirculated product and contaminant permeate (orange) and fresh loading buffer (red). The red squares on some parts on the flow path signal the concentration of the resin slurry and the state of the product and contaminant molecules.

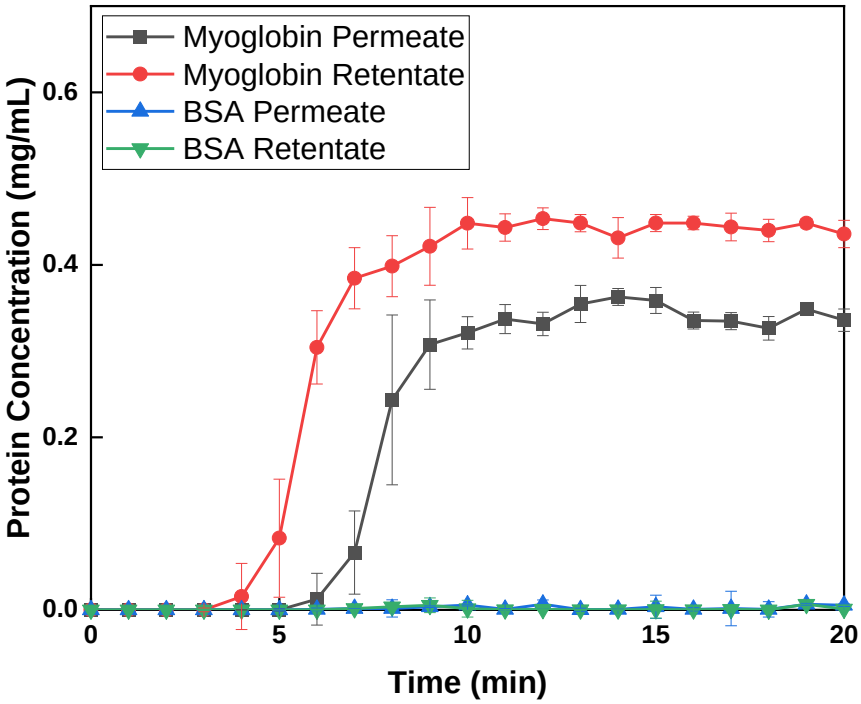

Figure 5.5. Free protein concentration of BSA and myoglobin in 20 mM phosphate buffer pH 7.0 in permeate (stage 1) and retentate (stage 2) streams during the binding step using 20% (v/v) Macro-Prep High Q anion exchange resin slurry in a 2-stage CCTC system from the start of operation until 20 min (steady state). The error bars represent the standard deviation of the samples (n=3).

5.4.2.2 Wash Step

The remaining myoglobin at the end of the binding step was further removed in 2 washing steps. The contaminant removal equations in Section 5.3.3.2 can be used as the fresh buffer does not contain more of the contaminant and the step is exclusively dedicated to the removal of such molecules. The slurry containing the absorbed BSA (approximately 14 to 15 mg of BSA / mL of resin) was concentrated to 20% (v/v) (φ_{in}). The myoglobin concentration at the retentate stream coming out of the binding step was measured to be approximately 0.43 mg/mL. Figure 5.6 shows a schematic map of the proteins and resin slurry inside each stage and stream during the wash steps for a better comprehension of the process.

The previous myoglobin concentration was used in Equations 34 to 37 to calculate the theoretical waste removal and final concentration for each step. According to the CCTC system and resin slurry specifications, the waste removal percentage is given to be 92.9% for both of the wash steps as this removal does not depend on the initial

concentration of the contaminant. The first wash step was assumed to start with a myoglobin concentration of 0.43 mg/mL in the resin reservoir and finish with a concentration of 0.036 mg/mL in the retentate stream of stage 2 and 0.11 mg/mL for the permeate stream in stage 1. In the second wash step, the myoglobin concentration was assumed to be 0.036 mg/mL in the resin reservoir and finished with a concentration of 0.0029 mg/mL in the retentate stream in stage 2 and 0.0091 mg/mL in the permeate stream in stage 1. The accumulated contaminant removal percentage for the bind stage, wash step 1 and 2 were 67.7%, 98.1% and 99.9%, respectively.

Figure 5.7 and 5.8 show the concentration of free BSA and myoglobin during the CCTC wash step 1 and 2. If there are traces of BSA in the permeate and retentate samples, they were below the detection limits or bound the resin at this point. The myoglobin concentrations for wash step 1 in the retentate in stage 2 and permeate in stage 1 were 0.13 mg/mL and 0 mg/mL, respectively. Whereas the concentrations for the wash step 2 were 0 mg/mL and 0 mg/mL, respectively. The myoglobin appeared to be absent from the samples because the protein concentration is below the detection level of the method. The theoretical calculations agreed with the supposed low concentrations. The quantifiable accumulated removal percentage for the bind, wash step 1 and 2 were 67.7%, 96.5% and 96.5%, respectively. As the myoglobin cannot be quantified in wash step 2, it was assumed that the minimum removal remained unchanged from step 1 to 2. The relative high error bars were attributed to the manual handling of the system and the sample concentrations for being close to the limit of measurement. All the aforementioned theoretical calculations were in agreement with the results obtained from the wash steps in the CCTC system.

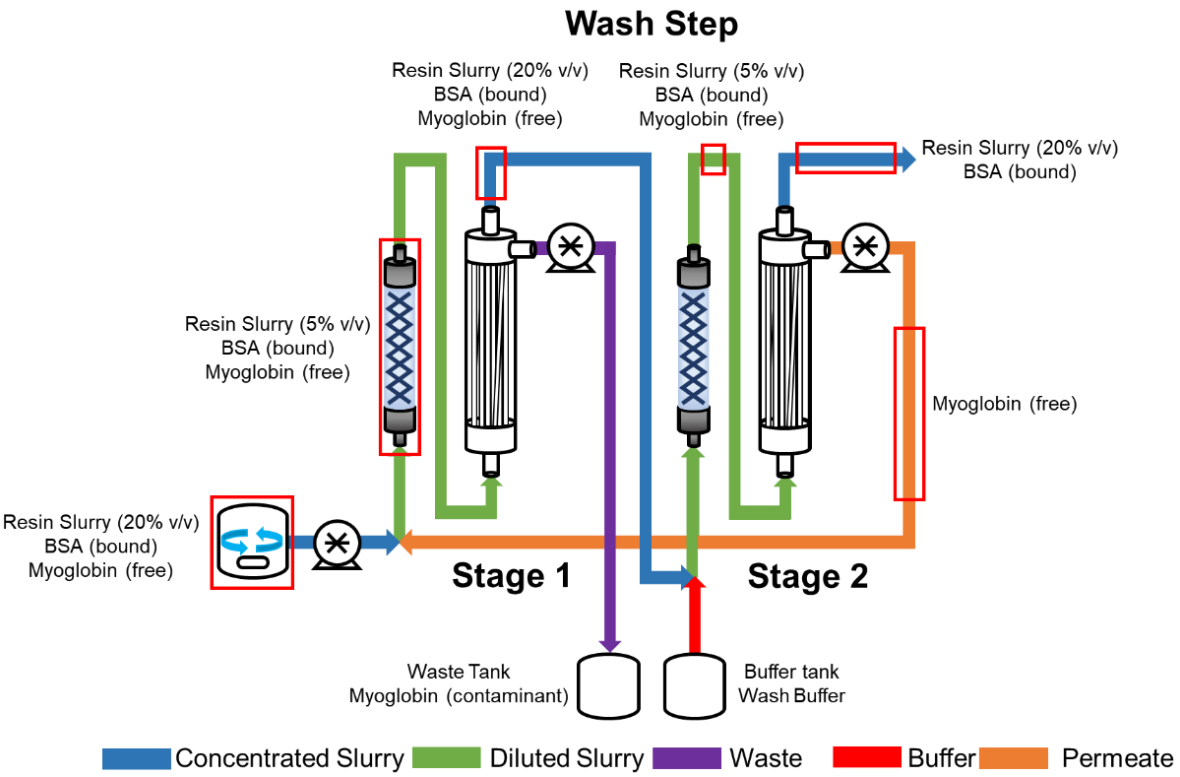

Figure 5.6. Diagram of a 2-stage CCTC system during wash step. The flow paths have been coloured depending on the resin slurry or buffer identity: concentrated slurry (blue), diluted slurry (green), waste/contaminant harvesting stream (purple), recirculated contaminant permeate (orange) and fresh buffer (red). The red squares on some parts on the flow path signal the concentration of the resin slurry and the state of the product and contaminant molecules.

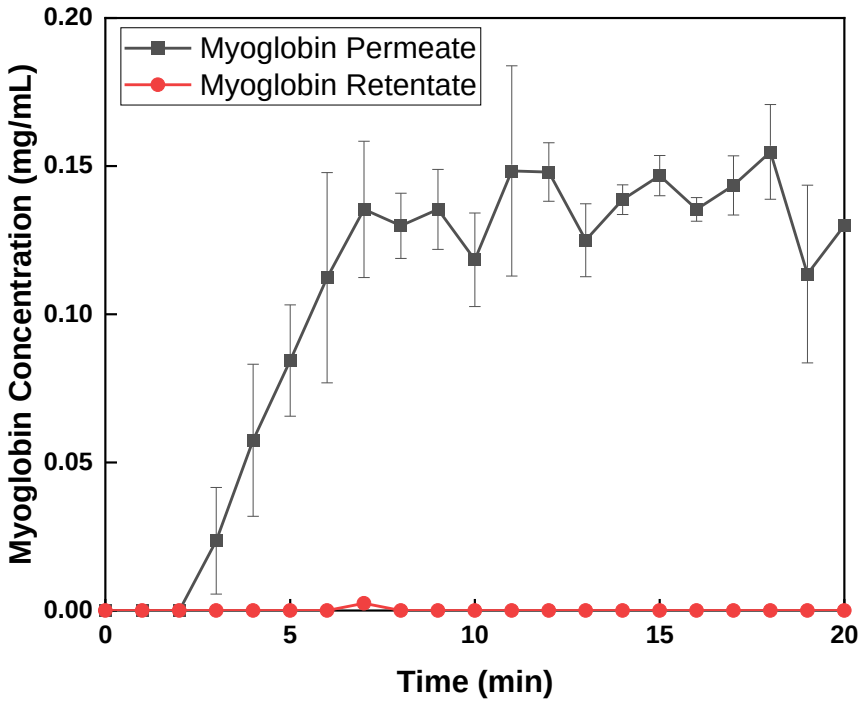

Figure 5.7. Myoglobin concentration in 20 mM phosphate buffer pH 7 in permeate (stage 1) and retentate (stage 2) streams during the wash-1 step using 20% (v/v) Macro-Prep High Q anion exchange resin slurry in a 2-stage CCTC system from the start of operation until 20 min (steady state). The error bars represent the standard deviation of the samples (n=3).

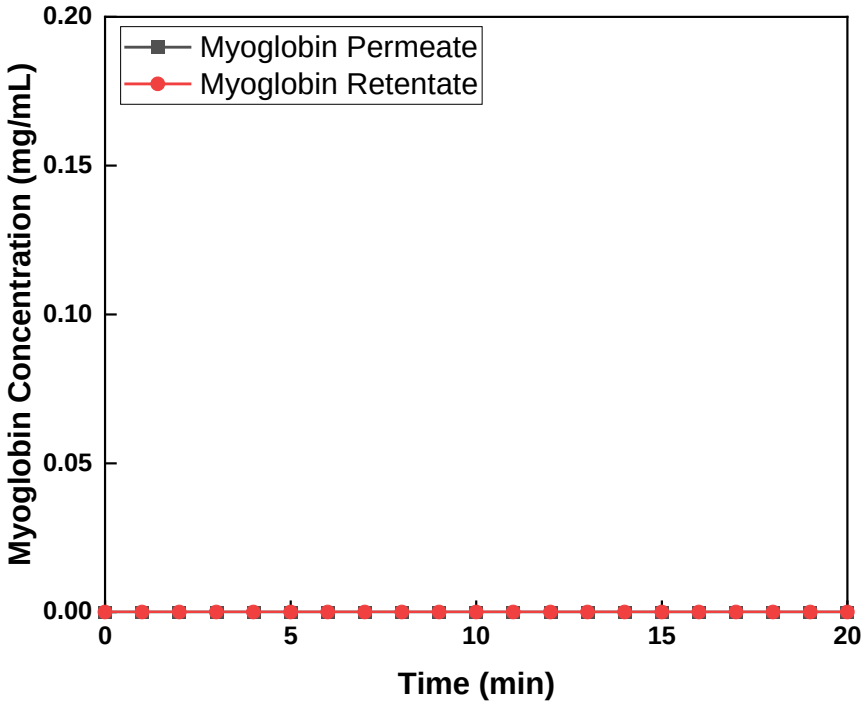

Figure 5.8. Myoglobin concentration in 20.0 mM phosphate buffer pH 7.0 in permeate (stage 1) and retentate (stage 2) streams during the wash-2 step using 20% (v/v) Macro-Prep High Q anion exchange resin slurry in a 2-stage CCTC system from the start of operation until 20 min (steady state). The error bars represent the standard deviation of the samples (n=3).

5.4.2.3 Elution Step

The BSA adsorbed to the resin was recovered during the elution step. The slurry collected during the second step of wash was collected and re-concentrated to 20% (v/v), making sure the BSA concentration levels did not change. Previous experiments showed that a complete elution was obtained at NaCl concentrations above 300 mM. Thus, the elution buffer was prepared with 500 mM NaCl (buffer B 50% in column chromatography terms) after being diluted in the static mixer inlet. The bound BSA was calculated to be 14 to 15 mg of BSA / mL of resin. The traces of myoglobin from wash step 2 were accounted in the theoretical calculations but were disregarded in the empirical ones as the concentration cannot be quantified. Figure 5.9 shows a schematic of the proteins and resin slurry inside each stage and stream during the elution step for a better comprehension of the process.

The mass balance equations and yield equations in Sections 5.3.3.2 and 5.3.3.3 were used for all the calculations. The overall yield for a 2 stage CCTC system using a resin

slurry of 20% (v/v) is 92.9%. According to this recovery percentage and 14 mg of bound BSA / mL of resin, the BSA concentration in the retentate outlet stream in stage 2 and permeate outlet stream in stage 1 were planned to be 0.91 and 0.21 mg/mL, respectively. According to the recovery percentage and the theoretical remaining myoglobin, the purity of the permeate stream should be 99.9%.

Figure 5.10 shows the BSA concentration in the permeate and retentate outlet streams over the course of the chromatography step after elution buffer was pumped into the system. The average BSA concentration in the permeate outlet stream in stage 1 samples was 0.93 mg/mL, while the retentate was 0.20 mg/mL during the time mark of 10 and 20 min. Myoglobin was not detected in the step. The high error bars before the 10 min mark is due to the stabilization/homogenization of the system, as well as the lack of an automated machine handling the CCTC system. The average empirical yield for the elution step was 93.2%. The purity could not be calculated due to the undetectable amount of myoglobin in the system. However, if the theoretical myoglobin concentration is taken as a true value, the purity of the permeate stream was estimated to be 99.9%. These values were in good agreement with the mentioned theoretical calculations.

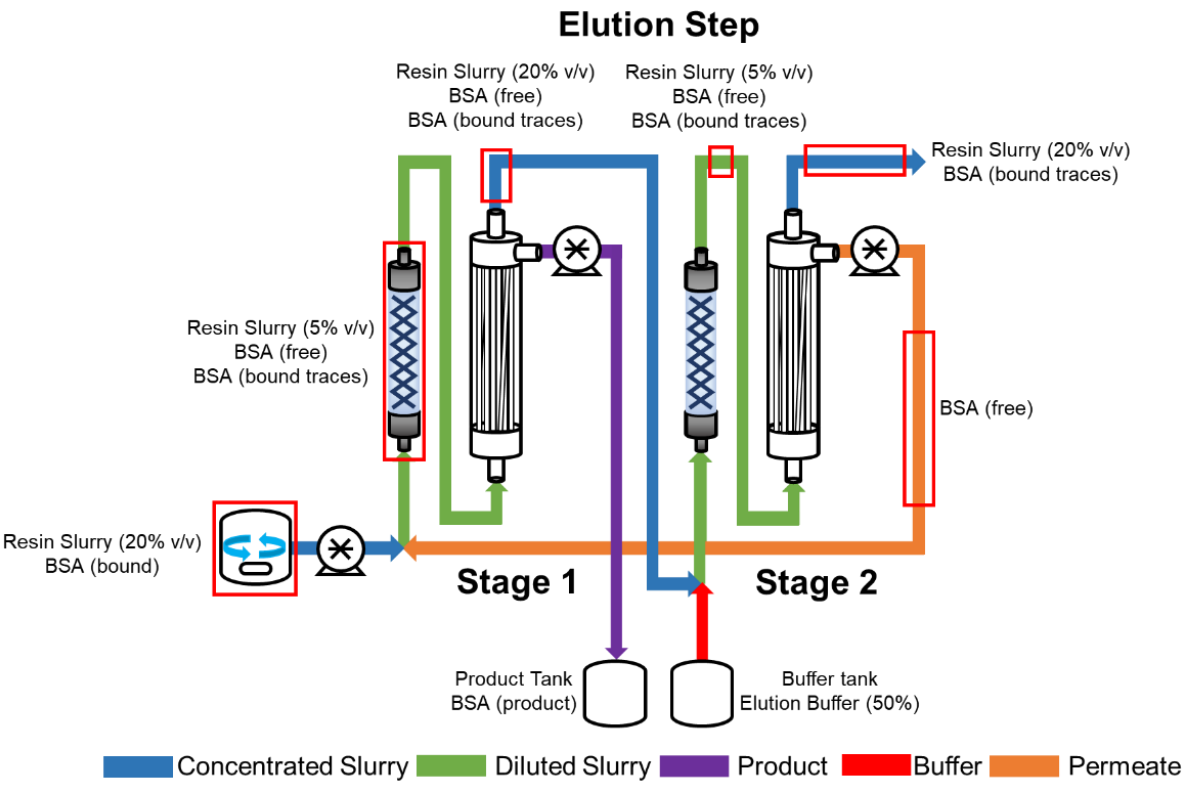

Figure 5.9. Diagram of a 2-stage CCTC system during elution step. The flow paths have been coloured depending on the resin slurry or buffer identity: concentrated slurry (blue), diluted slurry (green), product harvesting stream (purple), recirculated product permeate (orange) and fresh elution buffer (red). The red squares on some parts on the flow path signal the concentration of the resin slurry and the state of the product and contaminant molecules.

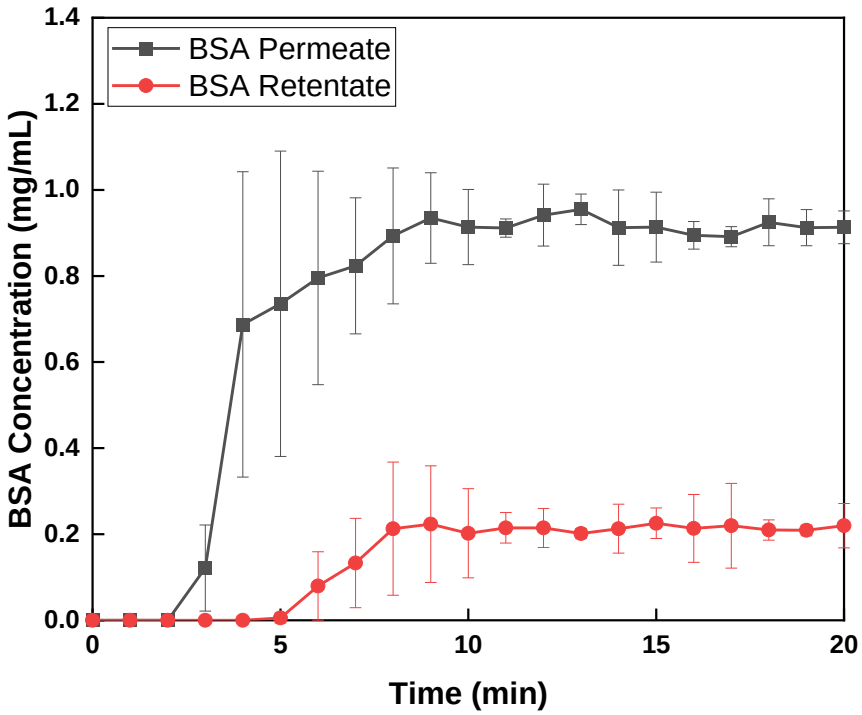

Figure 5.10. Free BSA concentration in 20 mM phosphate buffer pH 7 in permeate (stage 1) and retentate (stage 2) streams during the elution step using 20% (v/v) Macro-Prep High Q anion exchange resin slurry in a 2-stage CCTC system from the start of operation until 20 min (steady state). The error bars represent the standard deviation of the samples (n=3).

5.4.2.4 Strip Step

The resin was cleaned through a stripping step for further use in new cycles. The recovered slurry was collected and re-concentrated to 20% (v/v) by removing any extra mobile phase liquid. The strip was carried out using an ionic strength of 1 M NaCl (100% gradient) to make sure the resin and the CCTC system were clean for the next separation run. The strip step works as a wash step for the target molecule and all the traces left from other steps. Equation 41 (Section 5.3.3.4) was used for the prediction of the BSA in all outlet streams. Figure 5.11 shows a schematic map of the proteins and resin slurry inside each stage and stream during the elution step for a better comprehension of the process.

For the theoretical calculations, the remaining BSA concentration in the resin slurry was taken as 0.20 mg/mL. At this point, the BSA in this step is considered lost. Like a wash or elution strip, the removal of a molecule in a 2-stage CCTC system is 92.6%, the rest of the BSA will remain in the resin slurry solution ready to enter an equilibration step (not done for this cycle). The theoretical BSA concentration in the retentate stream outlet in stage 2 and permeate outlet stream in stage 1 were 0.015 mg/mL and 0.063 mg/mL.

Figure 5.12 displays the BSA concentration in the outlets of the CCTC system throughout the strip step. The average BSA concentration in the retentate outlet stream in stage 2 and permeate outlet stream in stage 1 were 0.07 mg/mL and 0.01 mg/mL. After all the previous steps, the amount of BSA that remains in the system is less than 0.01%. The high variability of the samples could be explained by the quantification method, which is reaching its lower detection limits resulting lower accuracy and/or in some cases the inability to detect any protein at all (retentate outlet stream in stage 2). Even with high error bars, there is a clear trend of the system reaching a steady state around the 8 min time mark. The theoretical calculations were in agreement with the exemption of the concentration in the permeate outlet stream in stage 1, probably due to the protein detection limit of the method.

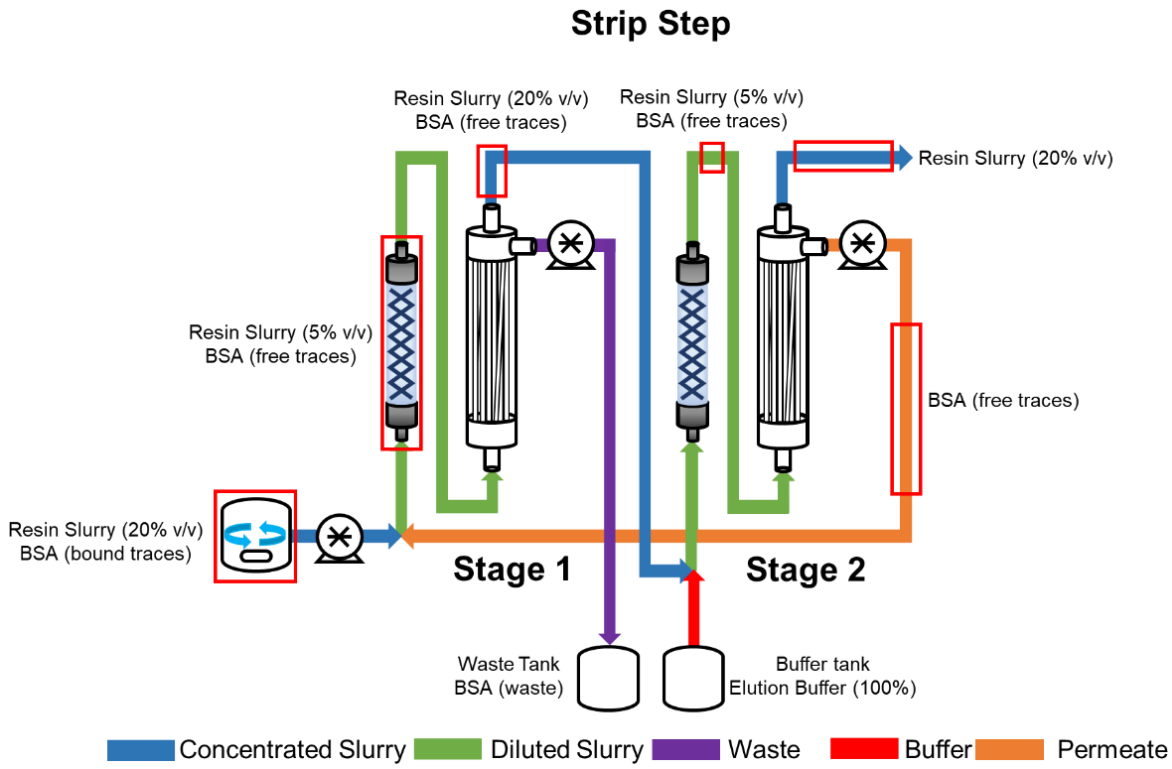

Figure 5.11. Diagram of a 2-stage CCTC system during elution step. The flow paths have been coloured depending on the resin slurry or buffer identity: concentrated slurry (blue), diluted slurry (green), waste product harvesting stream (purple), recirculated waste permeate (orange) and fresh elution buffer (red). The red squares on some parts on the flow path signal the concentration of the resin slurry and the state of the product and contaminant molecules.

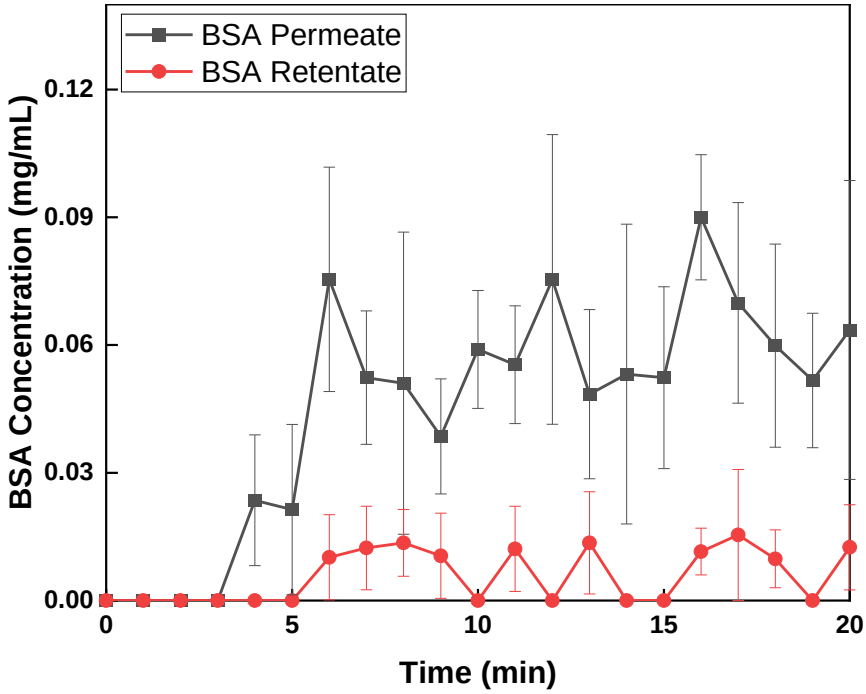

Figure 5.12. Free BSA concentration in 20 mM phosphate buffer pH 7 in permeate (stage 1) and retentate (stage 2) streams during the strip step using 20% (v/v) Macro-Prep High Q anion exchange resin slurry in a 2-stage CCTC system from the start of operation until 20 min (steady state). The error bars represent the standard deviation of the samples (n=3).

5.4.2.5 Hydrodynamics

The CCTC separation of BSA and myoglobin was performed in batch fashion with each step taking a period of time of 20 min. The stability of the system is crucial as the system cannot be stopped or paused once the resin slurry is inside the system.

Typical TMP profiles during all the steps are presented in Figure 5.13. The system was completely stable throughout the bind, wash 1, wash 2, elution and strip steps according to the TMP/flux measurements. All pressure readings showed a constant trend throughout the whole step, giving a TMP below 40 kPa. The up and down of the TMP is due to the nature of the peristaltic pump, the highest pressure readings when the liquid is being physically pushed by the rotating mechanism in the head of the pump. The increase at the beginning of every step is due to the resin slurry entering the hollow fibre and reaching a steady pressure. The bind step (31.4 kPa) showed the highest TMP as there are more molecules (BSA and myoglobin) traveling through the hollow fibre. The first wash step (27.9 kPa) was second as there is still a substantial amount of myoglobin in the system, while wash step 2 (15.4 kPa) is practically operating only with resin slurry at 20% (v/v). The elution step (22.6 kPa) was third highest, even though almost all BSA is circulating in the system. The strip step (20.9 kPa) was the second to last, above the wash step 2, due to the remaining BSA in the system after the elution step. It seemed that the salt concentration in the system had a positive effect on the TMP by decreasing it 20% to 3%. The membrane pores in the hollow fibre seemed to expand with the presence of salt in the mobile phase. This explains why the elution and strip steps were the lowest in the process (excluding wash step 2). Similar results were experienced while testing the hollow fibre with the different buffer for extended periods of time. The low pressure in the system allows it to be built with plastic single-use static mixer and hollow fibres, reducing the cost and easing the handling of the system.

The total volume of buffer pumped into the system, for all streams and steps, was approximately 300 mL/min. The total amount of resin needed to run a step a whole CCTC system was 79.6 mL, which translates to 0.26 L of resin per L of pumped buffer into the system (3.8 L of buffer per L of resin) or 6.4 L of buffer per g of product (without any recycling and an equilibration step). The resin slurry concentration (concentrated)

in the inlet and outlet of the CCTC system remained stable at approximately 20% (v/v). As seen previously, the system is capable of operating at this flux even at a slurry concentration (concentrated) of 40% (v/). This amount does not take into account the priming and flushing of the system which usually took around 400 mL to 600 mL of fresh buffer. On top of that, the system was cleaned with 400 mL to 600 mL of water, sodium hydroxide and, again, water. However, the priming and flushing would only occur once in a whole CCTC system after several cycles (3.3 cycles per hour approximately with this setup). The buffer consumption was clearly higher than a traditional column separation (0.8 to 1.1 L of buffer per g of product) but the cost-effectiveness of the smaller amount of resin absorbs the increased buffer costs.

Taking all the previously mentioned BSA concentration numbers in Section 5.4.2.1 to 5.4.2.4 and the resin volume, the productivity of the system was calculated to be 22.3 g of BSA per L of resin per h. This productivity was expected. A conventional column operated at a residence time of 5 min operates with a productivity of 5 to 8 g/L/h (Mahajan, George, and Wolk 2012), with a potential to achieve almost 30 g/L/h. Though, the CCTC system can achieve such productivities with a few litters of resin in shorter cycle times. The productivity can increase with optimization approaches and changing the resources used for the separation. The value can at least double by using a different kind of resin (Macro-Prep 25Q) and increasing the resin volume concentration in the resin slurry. Also, a hollow fibre with different pore size and membrane can be utilized to achieve a higher flux at higher resin slurry concentrations. The static mixer volume (residence time) in the wash, elution and step volume can be reduced to provide a smaller residence time; hence, shorter cycle times. Finally, replacing the static mixers for a different mixing module that has not been explored for a columnless chromatography technique in the past.

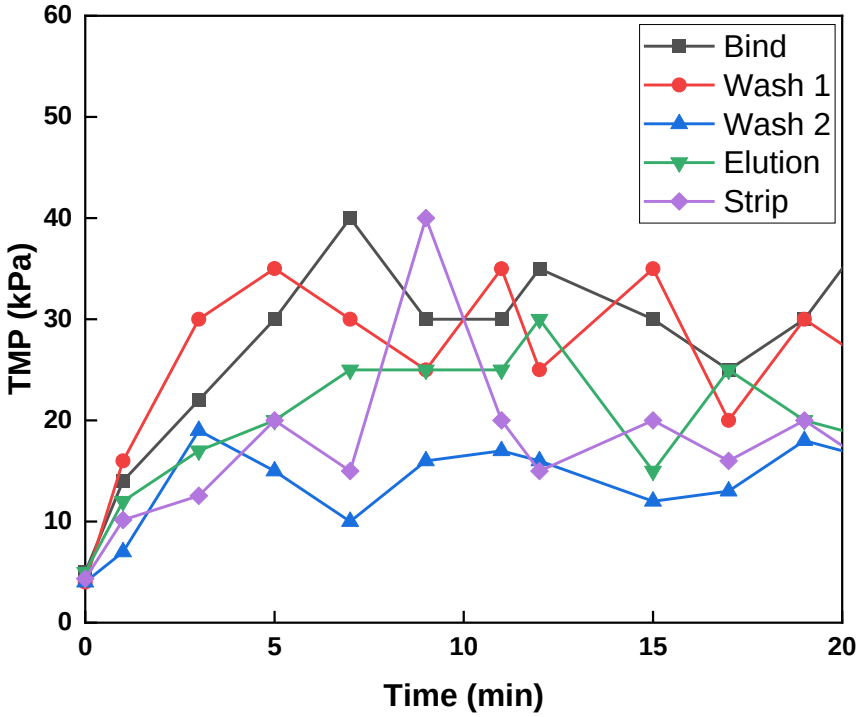

Figure 5.13. TMP profiles recorded for each step while separating BSA and Myoglobin using Macro-Prep-High Q as the chromatography resin in a 2-stage CCTC system. The resin slurry flow rate and buffer/permeate flow rate were fixed at 13 mL/min and 38 mL/min, respectively.

5.4.3 Salt Gradient Separation of Ovalbumin in Packed Bed Chromatography

The separation of ovalbumin into its different variants in column chromatography was planned to screen the elution salt gradient for further step-gradient separation in the custom CCTC rig. Ovalbumin at a concentration of 1 mg/mL was loaded into the 1 mL 5 cm bed height of Praesto Q anion exchange column, as described in Section 2.9. Some of the properties of the resin cannot be disclosed but 3 different ligand densities were used for this experiment.

Figure 5.14 shows the resulting chromatogram from the separation using the highest ligand density Praesto Q of ovalbumin variants using a NaCl gradient. The chromatogram showed 5 defined peaks. The peaks were numbered 1 to 5, depending on their ionic strength elution point (retention time). The pattern of the variants was consistently defined with the three different ligand density resins and reported data (Chris Wayne 2019). Variant peak 3 was the one with the highest concentration, followed by variant peaks 4, 2, 1 and 5, respectively. An extra peak between 2 and 3

was seen but it is an overlapping signal between the aforementioned peaks. Table 5.2 shows each peak variant elution CV with its respective salt gradient mark. The elution point for the first 4 peaks were close to each other with 2% to 5% of difference between each other. The overall resolution could be improved by using a larger column but it was discarded as the feed material was limited, especially as the CCTC system requires a substantial amount for one single cycle. In addition to these variants, an additional peak was measured after the gradient reached 30% at 50 CV (not shown in the chromatogram). The peak seems to consist of the most prevalent ovalbumin variant, without the presence of any other species around it. This last peak was excluded from further analysis as the gradient concentration was too far apart from the previous 5, defeating the purpose of the experiment CCTC. As expected, the separation of the variants is significantly challenging. The HPLC analysis of the elution fractions was performed before selecting the step gradients for the CCTC separation.

Figure 5.15 shows the ovalbumin variant peak UV absorbance signals obtained from the analysis of the fractions in HPLC. The compiled and separate ovalbumin peak pattern from the HPLC analysis and the column separation agree with each other. The number of defined main variants were 5. Peak variant 2 seems to have 2 peaks/variants but it is the overlapping signal from signal 3. Variant 3 is the more prevalent species, while variants 1 or 5 are the least prevalent. Due to the overlapping of all the peaks it was impossible to tell if there are different major or a combination of species of ovalbumin in between these peaks. The last peak after the 30% gradient also appeared but did not show any signs of different species in it.

The characterisation or concentration determination of each variant or separation optimisation was out of the scope for this project. The main focus was to define the peaks that were going to be separated in the CCTC system. After this set of experiments, it was decided to obtain ovalbumin variant peak 1 in the first elution step and ovalbumin peak 2 (with a slight overlap with peak 3) for the second elution step. The salt gradient for elution step 1 and 2 were fixed to 7% and 12%, respectively. The rest of the peaks were planned to be obtained in the strip step with 100% of the gradient. These gradient concentrations were chosen due to their narrow, but feasible, range apart between each other and their lowest amount of overlapping among their neighbours.

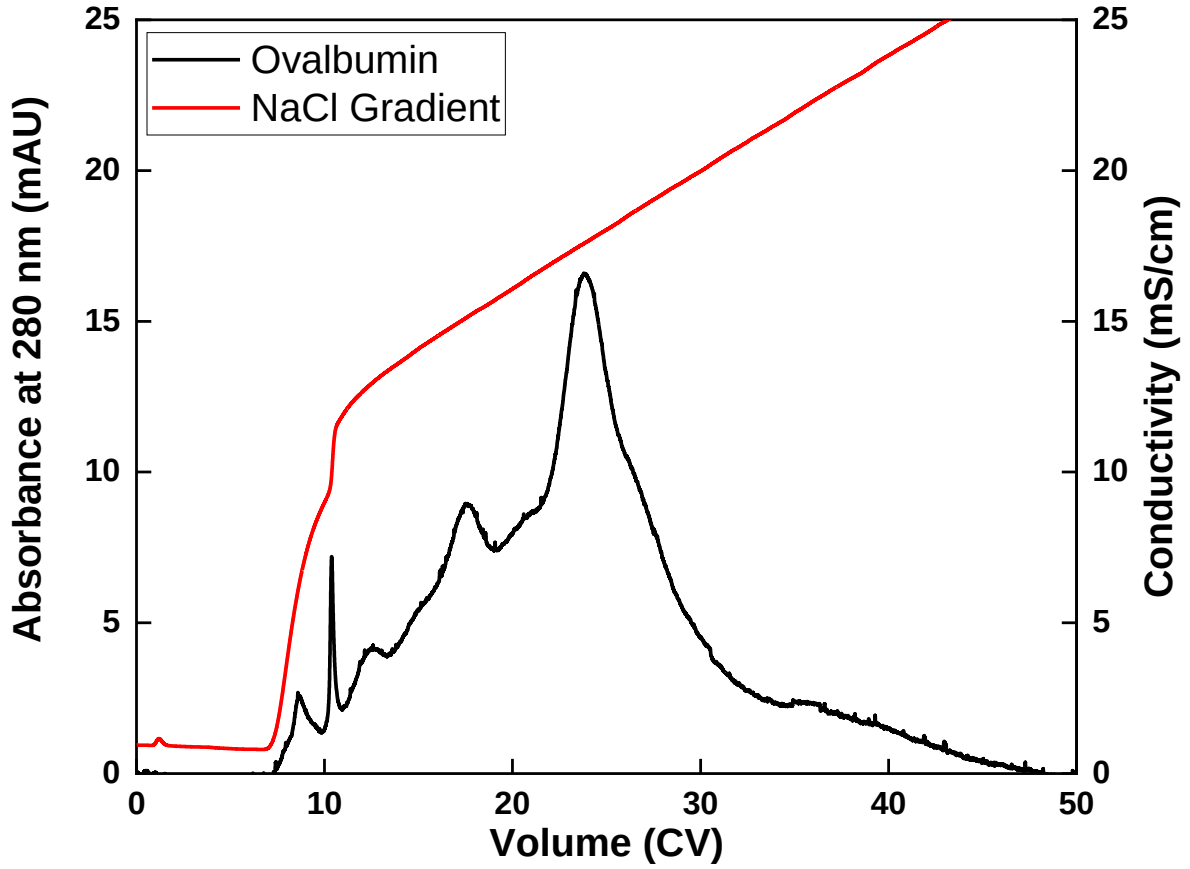

Figure 5.14. Separation of ovalbumin into its major variants using a 1 mL 5 cm height Tricorn 5/50 column packed with Praesto Q anion exchange resin. The salt gradient elution starts at 0% and ending at 30% over the course of 50 CVs. The separation was done using 50 mM Tris buffer pH 8.5 at a constant flow rate of 1 mL/min.

Table 5.2. Elution peaks of ovalbumin variants found in the separation of commercially available whole albumin in a 1 mL 5 cm height Tricorn 5/50 column with Praesto Q anion exchange resin using a 0% to 30% salt gradient.

Ovalbumin Peak Variant	Column Volume Elution (CV)	Salt Gradient Elution (%)
1	8.5	6.6
2	10.4	11.9
3	17.6	15.2
4	23.4	17.6
5	35.2	22.1

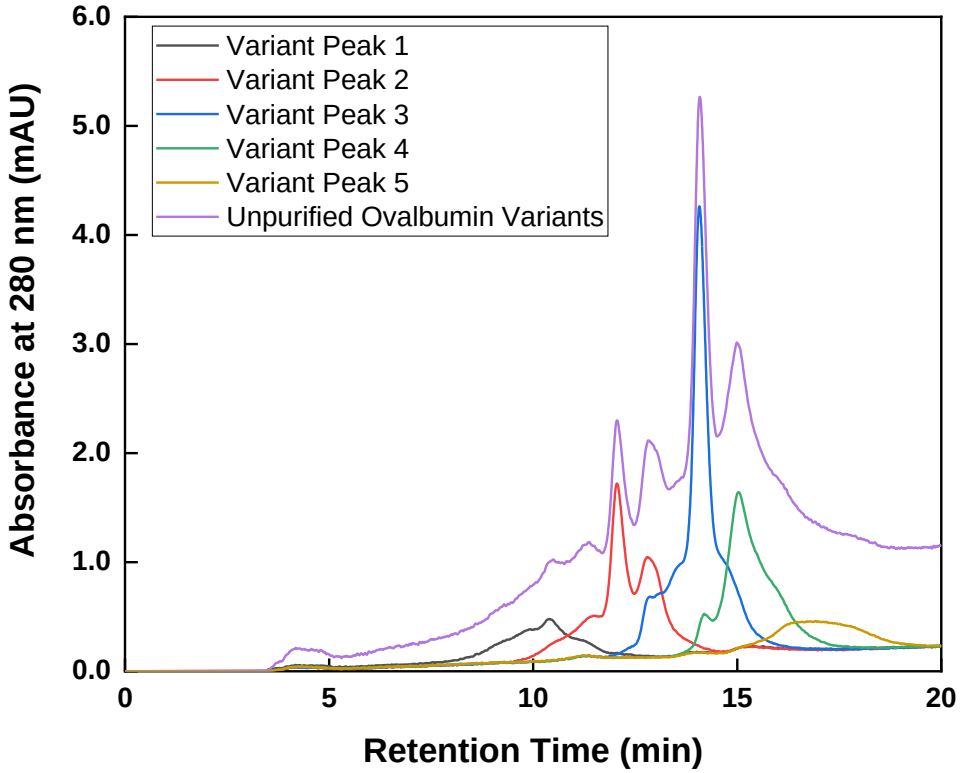

Figure 5.15. HPLC analysis of ovalbumin variant fractions at 280 nm using a 0.1 mL CIM-Q column. The solutions used were 50 mM Tris buffer pH 8.5 (Buffer A) and 1 M NaCl 50 mM Tris buffer pH 8.5 (Buffer B). A linear gradient of 0% to 100% was applied over 30 CVs at a flow rate of 0.1 mL/min.

5.4.4 Salt Step-gradient Separation of Ovalbumin in Continuous Counter-current Tangential Chromatography

In order to test the CCTC system for the purification of ovalbumin into its major variant groups, a pack-bed base separation was done beforehand to explore the separation based on the gradual difference of the ionic strength of the mobile phase. As seen in Figure 5.15 and Table 5.2 in Section 5.4.3, ovalbumin can be separated in 5 major variants at specific ionic strength concentrations. In order to test the CCTC system in a salt-step gradient purification, two elution steps were done. The first elution step at a 7% salt gradient and the second elution at 12% of a 1 M NaCl 50 mM Tris buffer pH 8.5. All samples analysed in HPLC were taken after 15 min of operation, as it was when the respective step was working at steady-state.

5.4.4.1 Bind Step

The bind step mixing modules were not designed for the adsorption kinetics of ovalbumin; although, the ovalbumin and resin slurry concentration were chosen to provide enough time to bind most of the material. A concentration of 1 mg/mL of ovalbumin and a Q Sepharose FF resin slurry of 20% (v/v) were fed into the CCTC system. Q Sepharose FF was chose due to its similarity to Praesto Q and its higher BBC compared to Macro-Prep High Q. Results from Chapter 4 were also considered and decided that the impact on the reason would not affect the outcome of this set of experiments.

Figure 5.16 shows the UV signal from the permeate outlet stream in stage 1 and the retentate outlet stream in stage 2 from the binding step after 15 min of operation after being analysed in HPLC. Both outlets show all 5 major peaks of the original ovalbumin as seen in Section 5.4.3 - Figure 5.15. The permeate stream had the higher signal, suggesting the residence time for ovalbumin was not enough and some of the protein was lost. The retentate stream showed almost a similar pattern but variant peaks 2, 3, 4 and 5 seemed to have flattened significantly (30% to 80%). It is likely that each ovalbumin variant has its own adsorption binding kinetics, these variants take longer to be adsorbed or diffused into the resin bead. The remaining ovalbumin (if not adsorbed while waiting for the resin to settle) will be removed from the resin slurry in the wash step. The ovalbumin that eluted after the 30% salt-gradient mark was still detected at a higher concentration compared to the first 5 peaks, around 4 mAU. Though, the presence of this species did not compromise the separation of the first two peaks as it elutes at a higher salt concentration and does not overlap any of the other peaks.

This difference in concentration is attributed to the lack of optimisation of the residence time provided by the stage 1 set of static mixers, which impacts the binding between the ovalbumin and the ligands on the matrix surface. Theoretically, the flow rate can be decreased in order to provide a longer residence time for a complete adsorption; however, a lower flow rate would make the resin inside the tubes and static mixer settle inside the system, increasing the risk of a pressure overshoot inside the hollow fibre module. On top of that, a slower flow rate would require flux studies.

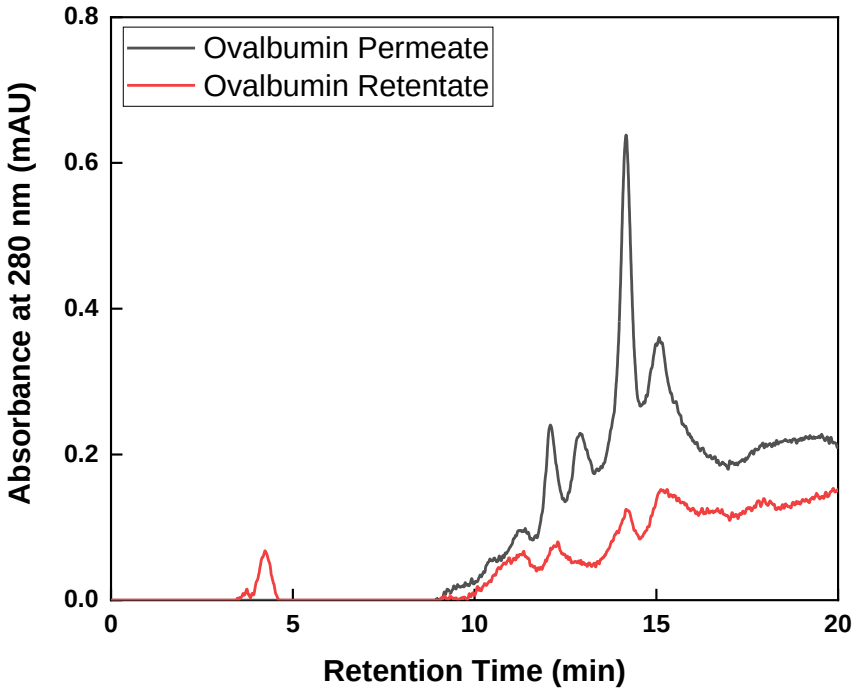

Figure 5.16. HPLC analysis of ovalbumin variant samples obtained from the permeate (stage 1) and retentate (stage 2) outlets during bind step of a 2-stage CCTC system at 280 nm using a 0.1 mL CIM-Q column. The solutions used were 50 mM Tris buffer pH 8.5 (Buffer A) and 1 M NaCl 50 mM Tris buffer pH 8.5 (Buffer B). A linear gradient of 0% to 100% was applied over 30 CVs at a flow rate of 0.1 mL/min.

5.4.4.2 Wash Step

The wash step was required to get rid of any remaining ovalbumin in the mobile phase of the resin slurry. As the custom CCTC rig was not modified, the contaminant recovery should be approximate to 92.6% (Equation 34 to 37). However, in this case there is no contaminant as all the major variants should be absorbed in the chromatography resin. The ovalbumin that could not be absorbed due to the ligand saturation is expected to be detected in this step. The overall UV absorbance signal was expected to disappear completely or decreased to a proportionate manner to the wash step contaminant removal percentage.

Figure 5.17 displays the UV absorbance signal from both outlets of the wash step after 15 min of operation after being analysed in HPLC. The permeate outlet stream in stage 1 had traces of variant peaks 3, 4 and 5. The retentate outlet stream in stage 2 showed signal of traces of the aforementioned variants, approximately 90% lower. The

majority of the remaining ovalbumin from the bind step might have partially absorbed into the resin or got diluted to an undetectable concentration. The sixth peak detected after a column-based salt gradient of 30% was also present in these samples. The absorbance signal of this peak was reduced around 90%, as the other variant peaks.

The resin slurry is practically free of unbound major ovalbumin variants and the remaining contaminants, such as the sixth peak, will be highly diluted in the next CCTC step.

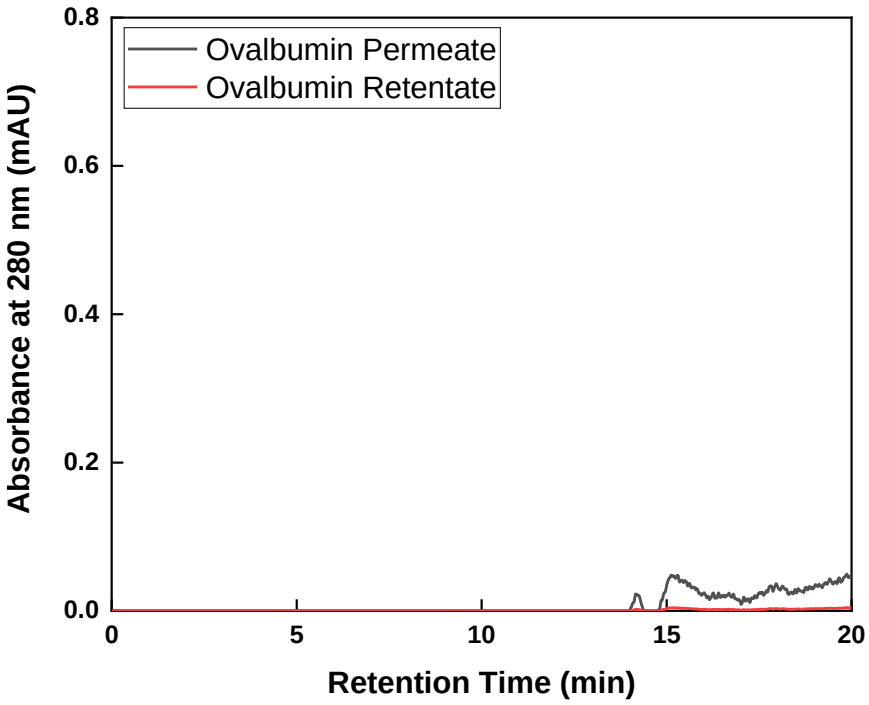

Figure 5.17. HPLC analysis of ovalbumin variant samples obtained from the permeate (stage 1) and retentate (stage 2) outlets during wash step of a 2-stage CCTC system at 280 nm using a 0.1 mL CIM-Q column. The solutions used were 50 mM Tris buffer pH 8.5 (Buffer A) and 1 M NaCl 50 mM Tris buffer pH 8.5 (Buffer B). A linear gradient of 0% to 100% was applied over 30 CVs at a flow rate of 0.1 mL/min.

5.4.4.3 Elution Step 1 and 2

The elution steps were designed to recover peak variant 1 in the first elution step and peak variant 2 in the second elution. The first elution had a step gradient of 7%, while the second one had one of 12%. The success of this section was based on the absence or traces of the undesired variant peaks in each of the steps. The presence

of any of the variant peaks would suggest a poor and slow initial mixing at the inlet of the static mixer between the resin slurry (20% v/v) and the permeate buffer coming from stage 2.

Figure 5.18 shows the permeate and retentate UV absorbance at 280 nm from elution 1 (7% salt-gradient) and elution 2 (12% salt-gradient) after being analysed in HPLC. Both elution steps, disregarding the outlet stream, showed the 5 peak variants. This meant that the separation of the variant peak 1 and peak 2 into two different elution pool was unsuccessful. Each product stream was contaminated with almost all the ovalbumin variant peaks, including the species eluting after the 30% gradient mark. The variant peak 1 is not present in any of the outlet streams in elution step 2.

The permeate outlet stream in stage 1 from elution step 1 showed a peak signal 54% and 24% times higher for variant peaks 1 and 2, respectively, compared to the retentate outlet stream in stage 2. The elution step 2 presented a concentration 20%, 31% and 33% times higher on variant peaks 3, 4 and 5. This asymmetrical pattern was probably caused by the counter-current design of the system, as all the stages inside an elution will have different ionic strengths due to the diluting nature of operation. Stage 2 retentate stream has the intended gradient concentration (7%) while the prior step has a lower gradient concentration (approximately 5.3%) at steady state. However, this concentration gradient would not cause the elution of the more strongly bound variants into the mobile phase, as the gradient never goes above the intended concentration. The premature elution of the “contaminant” variant was probably caused by the initial contact between the buffer containing the salt and the resin slurry. The fresh elution buffer has to be loaded at a higher concentration to compensate for the dilution that happens at the entrance of the static mixer with the resin slurry. Probably, the pulsating nature of peristaltic pump and the lack of a plug flow caused an initial uneven gradient for enough time at the point where both streams become in contact. All other samples at different time marks and repetition showed the same behaviour.

For elution step 2, the retentate and permeate outlet streams had a practically identical pattern and a similar concentration among all its variants, with the retentate outlet stream in stage 2 being 23% times lower. It was assumed that the asymmetric pattern was not seen in this step as a large percentage of variants 4 and 5 was lost in the

previous step, causing this even peak height among variants. The variant peak 1 was absent, meaning that this variant was assumed to be eluted in the previous step and the remaining molecules in the resin slurry got diluted to undetectable levels at the entrances of the first stage. The low concentration of the rest of the variants was due to the amount protein loss that happened in the previous elution step.

As mentioned beforehand, the CCTC technique was invented with the aim of separation biotherapeutics by AC. The experiments showed that the CCTC system failed in separating molecules with narrow elution points. The elution of each molecule was dependent on the gradient created inside the static mixers. This suggested that salt gradient microenvironments were created and persisted long enough at the entrance of the static mixer to make the latter variants elute.

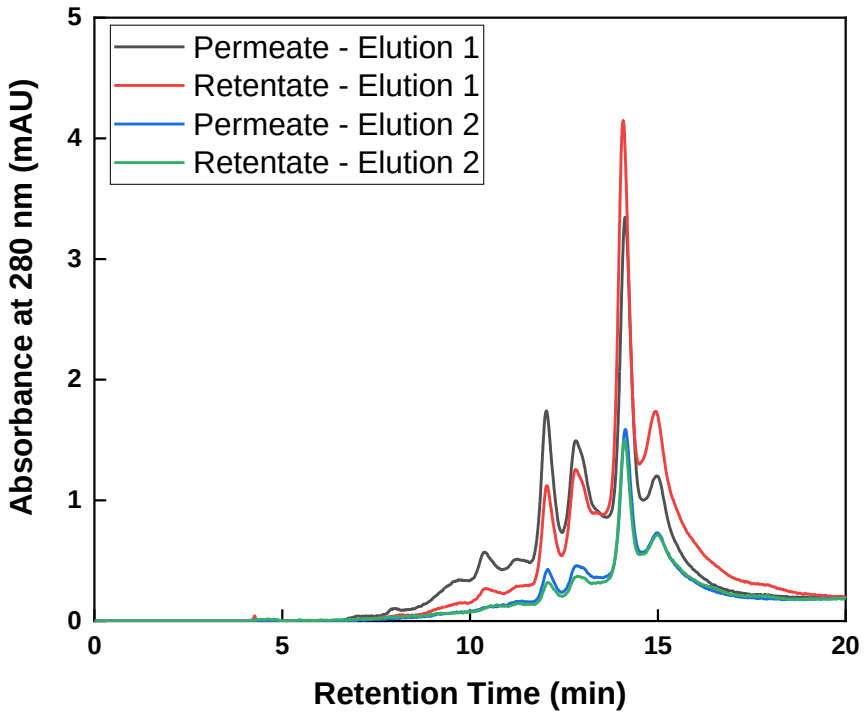

Figure 5.18. HPLC analysis of ovalbumin variant samples obtained from the permeate (stage 1) and retentate (stage 2) outlets during elution step 1 (7%) and elution step 2 (12%) of a 2-stage CCTC system at 280.0 nm using a 0.1 mL CIM-Q column. The solutions used were 50.0 mM Tris buffer pH 8.5 (Buffer A) and 1 M NaCl 50 mM Tris buffer pH 8.5 (Buffer B). A linear gradient of 0% to 100% was applied over 30 CVs at a flow rate of 0.1 mL/min.

5.4.4.4 Strip Step

The strip step aimed to elute the rest of the “contaminant” variants and clean the resin for further use. The salt step gradient used for this step was of 100%. The absence of any the variant peak 3, 4 and 5 would suggest that the previous step was unable to separate the first ovalbumin variants using two elution steps with fixed salt concentrations.

Figure 5.19 displays the UV signal from the permeate and retentate outlet stream sample after being analysed in HPLC. Both outlet streams showed the same peak pattern with the permeate outlet stream in stage 1 being 30% higher. The expected variant peaks 3, 4 and 5 could be identified even at such low concentrations. However, variant 2 was also detected in all the samples. The variants were probably present as the microenvironments created by the heterogeneous mixing did not reach its required ionic strength elution point for its complete elution. The variant peak that elutes after a gradient of 30% was also measured in all the samples but was 10% and 11% times higher than the ones recorded on elution step 1 and 2, respectively.

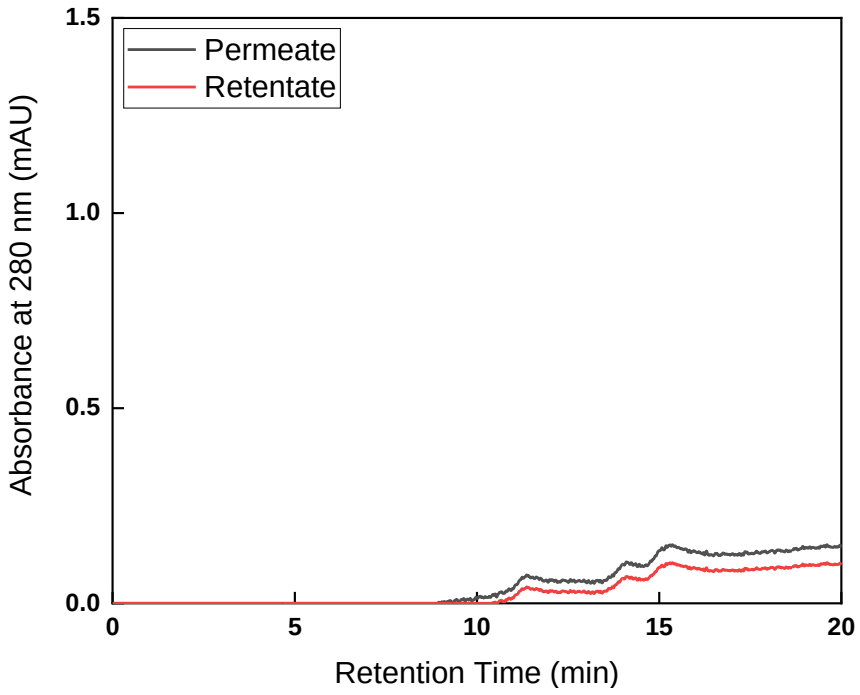

Figure 5.19. HPLC analysis of ovalbumin variant samples obtained from the permeate (stage 1) and retentate (stage 2) outlets during strip step (100%) of a 2-stage CCTC system at 280 nm using a 0.1 mL CIM-Q column. The solutions used were 50 mM Tris buffer pH 8.5 (Buffer A) and 1 M NaCl 50 mM Tris buffer pH 8.5 (Buffer B). A linear gradient of 0% to 100% was applied over 30 CVs at a flow rate of 0.1 mL/min.

5.4.5 Assessment of the Continuous Counter-current Tangential Chromatography Technique

This section addresses different observations about the use and design of the system that could not be discussed in previous segments. As the literature about CCTC is limited and focused on AC separations, and the system cannot be currently commercially acquired, aside from the qualitative results of the separations, it is common that the operational qualities of the technique have not been properly explained.

The few articles corresponding to the separation of biotherapeutic molecules already highlighted the advantages of the technique, these are also mentioned in Section 1.8.1. The CCTC technique is unique as it eliminates the necessity for column packing, which is usually time consuming and it is quite laborious to get a perfectly packed column. This makes the system inherently more efficient as it reduces idle times. The efficiency is further increased by using all the resin in the system at all times; unlike its column counterpart that uses the resin from top to the bottom. The bound material is only retained on/in the bead only for approximately 10 min (depends on the stages and steps), reducing the risk of denaturisation or change of quaternary structure of the product. The system pressure does not depend on the bead size, which means that a smaller bead size can be used without any repercussion. Also, this same low pressure allows plastic single use technologies for all modules. The scale-up is straightforward by increasing the dimensions of the static mixer and hollow fibre modules. The system is a truly continuous system when it reaches steady state. This true continuous nature allows real time operational changes (pH, salt concentration and resin slurry concentration), useful for planning and executing a design of experiments (DoE) approach (Dutta, Tan, Napadensky, and Zydney 2016; Dutta et al. 2015b; Napadensky et al. 2013b; Dutta et al. 2017).

One of the biggest oversights in the literature and something articles do not mention is the inability of the system to pause or stop the cycle run at all. The moment when the CCTC technique stops the flow of liquid through the tubes, the resin beads start to

settle in the mixing modules and solid/liquid separation modules. If the system is re-initialised before any proper flushing and cleaning, it causes imminent clogging of the inlets of the hollow fibres. The clogging causes an increase in TMP inside the fibres, this might damage the hollow fibre performance and sudden tube disconnections from the inlet of the hollow fibre or even a sudden burst of the hollow fibre tube. Any of these two consequences are a safety hazard for the operator and compromises the quality of the product. If the system is stopped, flushed and re-initialised, a percentage of the product is lost in the process. As the CCTC system only holds up a relatively low amount of product at all times, the loss would not be that impactful. However, it is not a desirable outcome. Alternatively, these “waste” streams can be collected and processed to be re-introduced into the CCTC system but the quality of such product would not be guaranteed.

The column packing is completely eliminated while using this type of chromatographic technique; nevertheless, the resin slurry needs to be prepared beforehand. First, the preparation consists of buffer exchanging the resin slurry into the desired equilibration buffer. Then, the resin slurry in the desired mobile phase must settle in order to be able to fix the slurry concentration (v/v). The settlement of the resin slurry can be done by centrifugation or gravity. The centrifugation is quick and effective but requires another unit operation; on the other hand, gravity settlement is lengthy but inexpensive. After each cycle, the resin slurry has to be collected and stored in 20% ethanol (or equivalent storing solution) causing the resin slurry preparation to be repeated for the next cycle. However, the resin can be stored in measured containers if possible to aid and reduce times in the resin slurry concentration fix step.

The total and partial flow rate are limited by a minimum and maximum range of operation. The flow rate can only be reduced up to a point as the resin will start settling inside the mixing modules or tubes. The tube diameter also plays a role here, as a larger diameter would require higher flow rates (larger diameters are translated to lower N_{Re}). However, larger flow rates require larger mixing modules and more resources used per unit time. This is not a system flaw but it is something to take into account while building and operating a CCTC system. The diameter of the tubing and modules has to be kept to a minimum to avoid this problem.

Up until now, there are no commercially available sensors dedicated for process control for the CCTC equipment. An UV absorbance sensor for the resin slurry streams is crucial to monitor the binding/desorption rate of the process; yet, such accessory does not exist. This makes resin slurry sampling time and resource consuming, as each of the samples has to be taken via a syringe fitted with a membrane/filter disc. Recently, an article about a turbidity meter made just for the CCTC system was developed but unfortunately is not commercially available at this moment (further discussed in Chapter 8) (Fedorenko et al. 2018). This turbidity meter would help by showing an early deviation from the original resin slurry concentration before the hollow fibre fouls completely. The lack of accessories lowers the throughput of the system and the precision of the measurements.

As seen in Chapter 4, chromatography resin deformation and damage after its prolonged flow/use in a CCTC system was shown and quantified. After every use, the resin slurry takes longer to settle and the mobile phase loses its original clear look. The fines of the resin beads can be visually seen with the naked eye in some instances. This potentially has the risk of contaminating the product with resin chromatography fines/leachables, which is not much of a risk while operating a packed-bed chromatography format. Macro-Prep High Q showed a better performance in this regard. Nonetheless it is something that has to be addressed for quality and validation tests.

The CCTC system has a higher buffer usage compared to column chromatography. There are solutions that mitigate this characteristic such as the re-use of the wash buffer on the strip step but it requires extreme process control and optimisation. Running test experiments even in a batch 2-stage CCTC rig required litres of buffer for the preparation, run and cleaning; as well as at least 50 mL 100% (v/v) of chromatography resin for one step to run for approximately 20 min.

As seen in this chapter, the CCTC struggles to achieve a successful separation when the molecules of interest have closely elution points. After all, the CCTC technique was made for AC in mind. Still, it has been proven in the past and in this chapter that an ion exchange separation is possible with different types of resin (Dutta et al. 2017; Napadensky et al. 2013b; Dutta et al. 2015b). The CCTC system would not be able to compete in terms of purity in extremely challenging separations with species with close

elution points compared to a traditional column format. However, the system can be used for a double elution process as long as the elution points are relatively further away from each other. This would require a tight valve and peristaltic pump control in the system in order to avoid initial uneven mixing.

In general, the custom batch 2-stage CCTC rig confirmed what was already published but raised a few oversights or design concerns if this technology aims to move forward in the industry. After analysing the design, it was decided that the more logical way of studying and simplifying the rig was to focus on the mixing module, as seen in Chapter 6.

5.5 Conclusion

A 2-stage CCTC rig was assembled and tested with a simple binary and a challenging step-gradient separation. The binary separation consisted of the separation of BSA, as the product, and myoglobin, as the contaminant. The second separation entailed the separation of ovalbumin using two different elution steps. These separations allowed to determine the advantages and drawbacks of the system.

The binary separation parameters were first tested using a column chromatography technique to save resources. Myoglobin was not retained by the chromatography media and left the system during the wash step; whilst BSA was adsorbed during these steps. 99.1% of the BSA was recovered during elution with a purity of 99.6%. This showed that myoglobin had no interaction either with the BSA or the Macro-Prep High Q resin during any of the steps.

The separation of BSA and myoglobin in a 2-stage CCTC system was done in 5 chromatography steps: bind, wash 1, wash 2, elution and strip step. Macro-Prep High Q was used at a 20% (v/v) resin slurry concentration. The retentate streams and permeate streams had a flow rate of 13 mL/min and 38 mL/min, respectively. This was translated to a TMP between 15 and 40 kPa and a 70 LMH flux.

The bind step was loaded with BSA 1 mg/mL and myoglobin 0.5 mg/mL. As assumed, all BSA was adsorbed by the methacrylate resin and no outlet signal was detected. The BSA bound concentration was calculated to be 14 to 15 mg of BSA / mL of resin. The bind step worked as a pre-wash step, removing 67.7% of the total myoglobin. The myoglobin concentration from the retentate outlet stream in stage 2 and permeate outlet stream in stage 1 were 0.46 mg/mL and 0.34 mg/mL, respectively. The remaining myoglobin in the retentate was removed in the sequential wash steps, each step was designed to remove 92.6%. At the end of wash step 1 and 2, 98.1% and 99.9% of the initial amount of myoglobin was removed from the cycle run. The final retentate outlet stream concentration in stage 2 was calculated to be 0.003 mg/mL. The elution was fed with 50% elution buffer. Respectively, the retentate outlet stream in stage 2 and permeate outlet stream in stage 1 had an average concentration of 0.93 mg/mL and 0.20 mg/mL. This concentration can be converted into a recovery of 93.2% with a 99.9% purity, as undetectable traces of myoglobin are assumed to be in

the system. The remaining BSA was removed in the strip step, giving a concentration retentate outlet stream in stage 2 and permeate outlet stream in stage 1 of 0.68 mg/mL and 0.0062 mg/mL, respectively. After the strip step, the remaining BSA in the system is approximately 0.01%. The system operated under a TMP of 40 kPa for step with higher viscosities (bind and wash 1) and above 15 kPa for the higher salt concentrated ones or lowest viscosities. The system presented a productivity of 22.3 g of BSA per L of resin per h. This productivity can be boosted at least twice by shortening the wash, elution and strip step residence times, as well as using a different resin and slurry concentration (modifying the hollow fibre dimensions and membrane). The second wash step can be eliminated by adding 1 or 2 stages to the first wash step; this would decrease the processing time and buffer usage while maintaining a 99% contaminant removal. All the theoretical calculations agreed with the experimental results mentioned above.

The operational parameters for the ovalbumin separation into its different variant species were first explored by doing a column separation. A 1 mL 5 cm Praesto Q anion exchange column was loaded with 1 mg/mL of ovalbumin. The separation was done using a salt gradient. The ovalbumin was separated into 5 different major variants with different elution points. The variant peaks had some overlapping sections, as well as having different mass ratios. The elution points in the gradient for the 5 peaks were: 6.6%, 11.9%, 15.2%, 17.6% and 22.1%.

The ovalbumin separation was planned to follow the same flow rates and system modules used for the separation of BSA and myoglobin. However, a wash step was removed and replaced for a second elution step. The elution steps were planned to follow a step gradient separation: elution step 1 with a gradient of 7% (variant peak 1) and elution step 2 with a gradient of 12% (variant peak 2). Q Sepharose FF resin slurry 20% (v/v) was used to keep the system at steady operating conditions.

The bind step showed the residence time for the aforementioned separation was not enough, as all variants were present in both outlet streams. The wash step showed an approximate 90% removal on the peak signal. Elution step 1 presented all major variants, with a higher concentration of peak 1 and 2 in the permeate outlet stream in stage 1. Elution step 2 showed all variants without major difference between both of the outlet streams. Finally, the strip step showed minor remnants of ovalbumin, an

approximately 4.7% of the original elution signal. The patterns during the elution and strip steps showed that most of the protein was desorbed during elution step 1 and the remainder was released during the second step. Conductivity measurements were taken in the inlet and outlets of each step, showing that the probable mixing/gradient issue was happening at the entry point of the mixing modules. This suggested that the CCTC technique was not capable of separating 2 molecule species with such narrow ionic strength elution points. This was attributed to different reasons: creation of microenvironment, pulsating nature of the peristaltic pump flow and uneven plug flow. Even though the separation was not successful, it was interesting to push the operational parameters to show the potential and draw backs of the system in the current configuration.

After testing the CCTC rig and analysing its advantages and draw backs, it was decided to focus the last part of the project on the mixing module for a couple of reasons. First, Chromatan is currently investigating the replacement of the solid/liquid separation module (Chapter 8). Secondly, the mixing module has the potential to become more flexible by replacing the static mixers with a CFIR as the length can be modified at the moment. Finally, the CFIR would be a more cost-effective technique at a smaller and larger scale.

Chapter 6: Proof of Concept: Coiled Flow Invertor Reactors Used as Replacement for Mixing Modules in Continuous Counter-current Tangential Chromatography Design

6.1 Summary

After characterization and testing of the individual modules, the resin and everything as a whole, the next step in this project was to explore alternatives the current CCTC system design. This chapter explores the proof of concept for CFIRs as viable alternatives to the current static mixers as the mixing modules for the CCTC system. Three types of reactors are explored in this chapter: CFIRs, HCRs and SMRs. The assessment is divided into: RTD experiments, dispersion number modelling and BBC studies. The RTD experiments give the necessary insight and data in order to obtain and model axial dispersion numbers, which are necessary for the characterization of each reactor geometry. BBC experiments using Macro-Prep High Q were conducted for each type of reactor. The BBC data is contrasted with the axial dispersion numbers in order to calculate the effectiveness of the CFIRs against the HCRs and SMRs. In addition, simple foot print and costs were calculated in order to reach an overarching conclusion.

6.2 Introduction

It is essential for a system like CCTC to have the most effective mixing in the cheapest and simplest mode possible. The most commonly employed techniques to achieve this is to add a second/third phase, mechanical agitation or placing obstacles in the flow path. Depending on the operating conditions and/or unit operation this results in energy dissipation, temperature rise, high pressure drops and non-uniform shear when done inside a tube. Clearly, any of these is not desired for therapeutic manufacturing as the pharmaceutical products might be heat or shear sensitive (Paul, Atiemo-Obeng, and Kresta 2004).

This chapter describes the basic characterization of a variety of reactors as a replacement for the set of static mixers in the current CCTC system. The reactors described in this section are: CFIR, HCR and SMR. In order to compare the different reactor configurations, the average RTD and axial dispersion parameters were measured and calculated in Section 6.4.1. Section 6.4.6 shows the measurement

results from the BSA adsorption kinetics in the different reactors obtained by BBC studies. Next, Section 6.4.6.4 presents the experimental BBC results compared with the BBC kinetics models shown in Section 3.4.4. Finally, a performance, footprint, operation and cost contrast between the reactors is done in Section 6.4.7 and Section 6.4.8. Thus, the scope of the present chapter is a proof of concept for CFIR as mixing modules for a columnless chromatography adsorption.

6.3 Theoretical Considerations

6.3.1 Design Model for Reactors

Recently, CFIR is being seen as a viable mechanism for achieving the desired mixing even at low velocities under the laminar region. This technology has already seen success under the areas of continuous refolding, heat exchanger, precipitation and viral inactivation as its compactness, low manufacturing cost and efficacy are unprecedented (A. K. Sharma et al. 2016; David et al. 2019a; Klutz et al. 2016; Kateja et al. 2016a; Kumar et al. 2007).

The structure of a standard CFIR looks like a square duct (coil/frame) with helically coiled arms. The mixing and homogeneous velocity profile is due to a double vortex (also known as Dean vortices) circulation (recirculation in the radial direction) pattern that the cross section of the tube formed by centrifugal force. On top of that, the coil bends itself to 90° for a complete flow inversion that enhances radial mixing than that of a straight helical coil or a simple tubing. This mitigates some of the radial velocity gradients (Rossi et al. 2017; Soni et al. 2019).

The CFIR reactor was designed to be able to work with the operating conditions of the functional CCTC rig used in Chapter 5. The CFIRs were fabricated from PVC pipe of 70, 65 and 50 mm internal diameter and 72, 67 and 52 mm external diameter (D_c) surrounded by peristaltic tubing of 3 and 4 mm internal diameter (d_{ti}) and 5.0 and 6.0 mm outer diameter ($d_{te)}$, respectively. A second reactor was fabricated as a HCR arrange in a wide circle with a diameter (D_{HCR}) of 50 cm. The length of the HCRs matches their CFIR counterparts. The HCR was not a straight reactor due to space limitations in the bench space; however, the large D_c was chosen to diminish any major contributions from the secondary flow (Dean vortices) form inside the reactor due to the curved geometry. Finally, a third reactor was fabricated from interconnected static mixers of 30 cm length and 1 cm internal diameter.

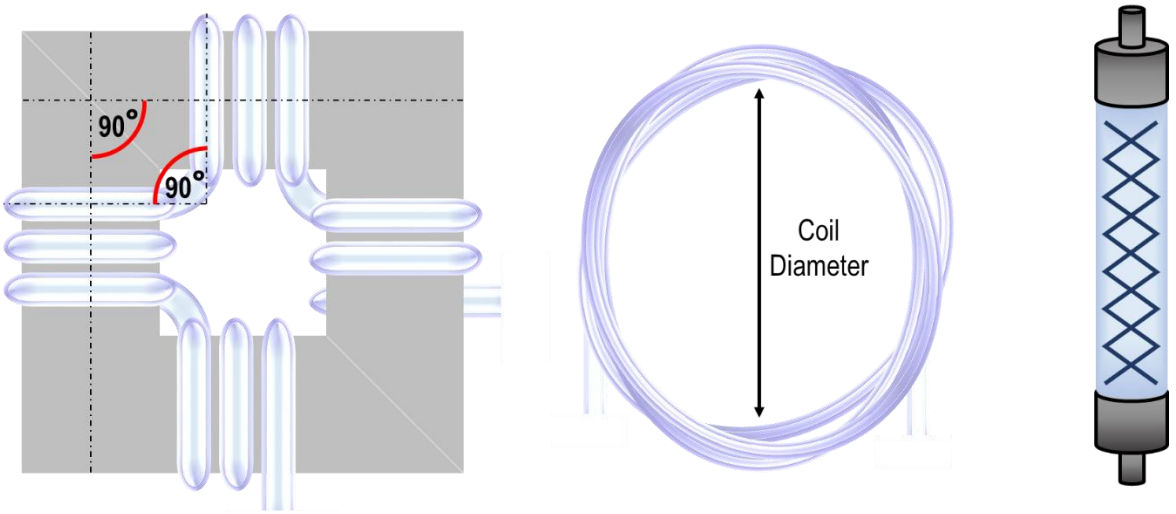

Figure 6.1. Diagrams of CFIR, HCR and SMR. A) CFIR: The coil base made from PVC pipe coiled by peristaltic silicon pump tubing. After a certain number of turns the coiled tubing makes an inversion towards to adjacent side of the base coil. B) HCR: No physical coil, the peristaltic silicon pump tubing is coiled and fixed with restriction pins. C) SMR: Each static mixer was connected by using a piece of peristaltic silicon pump tubing with minimum length.

Before presenting the design of the reactors a couple of parameters employed in this chapter need to be mentioned:

Coil-to-tube diameter ratio (λ) is the number related to the effect of centrifugal force and is defined as:

$$\lambda = \frac{D_c}{d_{ti}} \tag{43}$$

where D_c is the diameter of the cylindrical coil and d_{ti} is the internal diameter of the coiled tube. The curvature of a circle is defined by the inverse of its radius; consequently, λ represents the ratio of curvature between the coil and the coiled tube. Decreasing λ, increases the centrifugal force due to the increased curvature between of the coil with respect to the coiled tube.

The dean number (De) is the parameter that relates the balance between inertial, centrifugal and viscous forces, it is calculated as follows:

$$De = N_{Re}\lambda^{-0.5} \quad (44)$$

As De decreases, viscous forces dominate while centrifugal forces vanish. It is suggested to operate above a De > 3 in order to flatten the velocity profile (Klutz et al. 2015).

The focus in this chapter is on the effect of λ and number of 90° bends on the adsorption of BSA onto a chromatography resin. For this reason, the number of turns of coiled tube in each and number of bends was kept constant for all experiments. Due to the size and resources a total number of 32 turns and a total number 3 bends were selected for the experiments. The optimal number turns per bend was calculated as (Saxena and Nigam 1984):

$$n_{o,t} = \frac{n}{n_b+1} \quad (45)$$

where n_{turns} is the optimal number of turns per arm, n is the total number of turns in the CFIR and n_b is the total number of bends.

Design details such as number of units per reactor, total length (L), pitch distance (p), λ of coil radius (λ), number of turns (n_{turns}), number of 90° bends (n_{bends}), flow velocity, Dean number (De) and theoretical residence time are given in Table 2.4. By changing the D_c and d_{te} in the CFIRs, it was possible to obtain different values of λ ranging from 13.8 to 25. All the reactors were operated at the same 3 different flow rates, regardless of the difference in N_{Re} due to the difference of t_{te} of 3 and 4 cm. The N_{Re} could have been matched for both t_{te} but ultimately it was decided to keep the same volumetric throughput for all the reactors.

The minimization/optimization of area and volume were not part of the scope for the CFIR design and model but it has already been successfully done with symmetrical and asymmetrical mechanisms in the past (Soni et al. 2019).

6.3.2 Residence Time Distribution

Residence time distribution analysis is crucial in order to obtain parameters that allow direct comparison between the reactors with different diameters, flow velocities and number of inversions.

The normalization of time and other variables were calculated by a numerical integration using the trapezoidal rule. The parameters were defined as follows (Soni et al. 2019):

$$(t_{ave}) : t_{ave} = \int_0^\infty tE(t)dt \quad (46)$$

$$E(t) = \frac{C(t)}{\int_0^\infty C(t)dt} \quad (47)$$

$$(\sigma^2) : \sigma^2 = \int_0^\infty (t - t_{ave})^2 E(t)dt \quad (48)$$

$$(\sigma_\theta{}^2) : \sigma_\theta{}^2 = \frac{\sigma^2}{t_{ave}{}^2} \quad (49)$$

$$\frac{UL}{D} : \ \sigma_\theta{}^2 = 2\left(\frac{D_{ax}}{uL}\right) - 2\left(\frac{D_{ax}}{uL}\right)^2 \left[1 - e^{-\frac{UL}{D}}\right] \quad (50)$$

where t_{ave} is the average residence time, t is the time at an specific moment, C is the concentration of the particle, σ is the variance, σ_θ dimensionless variance, u is the mean axial velocity, L is the total length of the tube, D_{ax} is the axial dispersion coefficient and D/uL is an estimate of the dimensionless dispersion number (Levenspiel 1999). The dispersion number is used to measure the axial dispersion of each reactor, as explained in Section 6.3.3.

The concentration measurements and time were normalized and evaluated between the normalized concentration value at 0.5% and 99.5% The narrowness of the residence time distribution expresses how close the pattern resembles an ideal plug flow. The narrowness or relative width (R_w) was calculated as followed:

$$R_w = \frac{\theta_{0.005}}{\theta_{0.995}} \quad (51)$$

6.3.3 Axial Dispersion Model

The axial dispersion model (ADM) is an extension of the plug flow reactor (PFR) model that accounts longitudinal dispersion of a particle in the axial dispersion in straight tubes (Rossi et al. 2017; Schaschke 2014). The ADM can be used in this instance to calculate different parameters that are useful for the comparison of the different reactors in this chapter.

The particle concentration is assumed to be uniformed around the radial axis and is based on the following equations:

$$\frac{\partial \mathrm{C}}{\partial \mathrm{t}} = -\mathrm{u}\frac{\partial \mathrm{C}}{\partial \mathrm{z}} + \mathrm{D_{ax}}\frac{\partial^2 \mathrm{C}}{\partial \mathrm{z}^2} \quad (52)$$

where C is the particle concentration, dependent on the time t and on the axial coordinate z and u is the mean axial fluid velocity. If the model is expressed under dimensionless numbers a parameter known as Peclet number (N_{Pe}) can be obtained as (Rossi et al. 2017; Rojahn et al. 2018):

$$N_{Pe} = \frac{uL}{D_{ax}} \quad (53)$$

Or an approximation with:

$$Pe \approx \frac{2{t_{ave}}^2}{{\sigma_\theta}^2} \quad (54)$$

The N_{Pe} can be derived from the inverse number of D/uL from Equation 50 in Section 6.3.2. This parameter is also known as the Bodenstein number or the reciprocal of the vessel dispersion number.

As the ADM coefficient cannot be calculated directly from experiments, it is possible to obtain an approximation by fitting a model to the experimental data obtained in the RTD studies. Assuming open-open boundary conditions, the ADM delivers two E(t) fitting expressions depending on the N_{Pe} number (Rojahn et al. 2018):

$N_{Pe} < 100$: $E_{ADM}(t) = \sqrt{\frac{N_{Pe}}{4\pi t t_{ave}}}\, exp\left[-\frac{N_{Pe}}{4t/t_{ave}}\left(1-\frac{t}{t_{ave}}\right)^2\right]$ (55)

$N_{Pe} > 100$: $E_{ADM}(t) = \frac{1}{t_{ave}}\sqrt{\frac{N_{Pe}}{4\pi}}\, exp\left[\frac{N_{Pe}}{4}\left(1-\frac{t}{t_{ave}}\right)^2\right]$ (56)

The experimental data is fitted to Equation 55 or 56 in order to corroborate the theoretical N_{Pe} calculated with Equation 53 or 54.

As this model is focused on CFIRs, HCRs, and SMRs; the applicability of the ADM in these reactors is not guaranteed. Therefore, the following conditions have to be fulfilled in order to validate all the previous calculations as valid (Rojahn et al. 2018; Rossi et al. 2017).

Condition 1: $\frac{4L}{d_{ti}/_2} \gg 6.9$ (57)

and

Condition 2: $\frac{t_f/_{t_{ave}} D_m}{\left(d_{ti}/_2\right)^2} \gg 0.25$ (58)

$N_{Pe} < 100$: $D_{ax} = D_m + \frac{u^2 {d_t}^2}{192 D_m}$ (59)

$N_{Pe} > 100$: $D_{ax} = \frac{u^2 {d_t}^2}{192 D_m}$ (60)

Where t_f is the final time point of the run (dimensionless time) and D_m is the molecular diffusion coefficient.

Finally, the fitting was based on the least squares method and the residual error (ε) was used to assess the quality of the fitting. The error was calculated as follows:

$$\varepsilon = \sum_i [E_{ADM}(\theta_i) - E(\theta_i)]^2 \quad (61)$$

Where $E_{ADM}(\theta_i)$ is the value of the analytical RTD curve obtained from Equation 55 or 56 at any time θ_i and $E(\theta_i)$ is the experimental RTD value.

6.3.4 Batch Binding Capacity in Reactors

The BBC was calculated similarly to way it was done in Section 2.4.2. In order to guarantee the best quality of results, each reactor was built independently, and no valves were used in between inversions for CFIR, determined length for HCR and SMR.

All reactors operated in the same manner. The system was first equilibrated with 20 mM phosphate pH 7, then the BSA solution of 2 mg/mL (final concentration) was pumped into the system and finally the 5% (v/v) Macro-Prep High Q resin slurry (final concentration) was introduced into the system. Samples before the introduction of the resin slurry into the system were taken for reference. The samples obtained after the resin slurry was circulating through the system were taken after the system was functioning in steady state. In other words, after the measured maximum residence time had already passed by (Section 6.4.1).

The BBC results for each of the reactors were compared to the BBC kinetics model explained and developed in Section 3.4.4.

6.4 Results and Discussion

6.4.1 Average Residence Time Distribution Characterisation

RTD studies with water and NaCl solution were performed to characterize the CFIRs, HCRs and SMRs. The RTD of each reactor was calculated by increasing and decreasing the salt concentration from 0% to 50% and 100% to 50% salt gradient, respectively. Each CFIR had an equivalent HCR in length and tube diameters. Figures 6.2 to 6.8 display the comparison of each theoretical and experimental CFIR and its HCR counterpart, as well as the RTD for the SMRs. The result values for the RTD measurements are displayed in Table 6.1 (CFIR), 6.2 (HCR) and 6.3 (SMR).

The CFIRs and HCRs showed an average RT 30% times narrower with a standard deviation of 17 s for CFIRs and +-22 s for HCRs than their minimum theoretical counterparts, whilst the SMRs was 88% times narrower with a standard deviation of +-50 s. Similar trends in RTD narrowing have been reported for viral inactivation studies (David *et al.*, 2019) This indicates that most of the geometries CFIRs and HCRs did not show any significant difference in narrowness in average RT at these tube and coil diameters disregarding λ, length and flow velocities. This similarity might be attributed to the secondary flow present in both types of reactors. HCRs had an inherently worse design than the CFIRs but it has been established that a De > 3 is enough to significantly flatten the velocity profile and promote a secondary flow in the reactor (Rossi et al. 2017). The slight difference in internal tube diameters (3 and 4 mm) has no significant effect on the RTD or performance of the reactors (Rojahn et al. 2018). The SMRs were superior due to the elements inside the cylinder (12 elements per 30 cm length for each static mixer). The elements enhance the mixing while at the same time retaining the fluid for longer at the cost of a pressure drop in the system. This pressure drop was insignificant while doing CCTC experiments for Chapter 3 and 5 due to the short flow length and multiple number of peristaltic pumps in each chromatography step. The average RT had a linear decrease as the flow velocities increased for all geometry lengths and number of inversions. In addition, the theoretical RT was calculated using idealized conditions. This theoretical value

assumed all particles are not interrupted by any wall effect or pumping action (pulse pumping). The difference between both the RTD recorded for the reactors and the theoretical one is closer in reality.

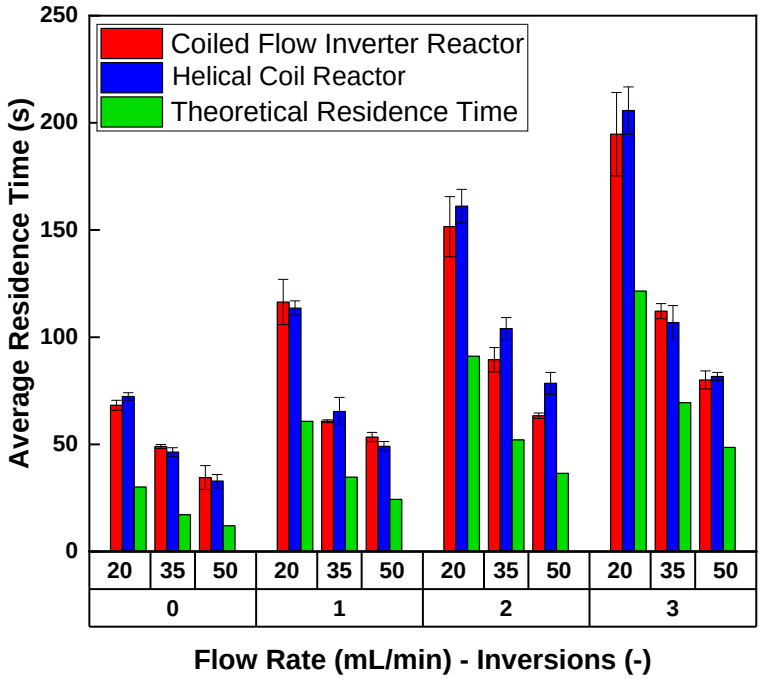

Figure 6.2. Average RT characterisation for CFIR and HCR with an internal coiled tube diameter of 3 mm, along with the minimum theoretical RT (green). The CFIR (red) had a coil of 52 mm and a λ of 18.3. The HCR (blue) had a coil of 0.5 m and a λ of 167.3. The RT was calculated by using NaCl as a tracer element by measuring the increase and decrease of conductivity (0 to 50% and 100% to 50%) at the end of the reactor. The error bars represent the standard deviation of the samples (n=3).

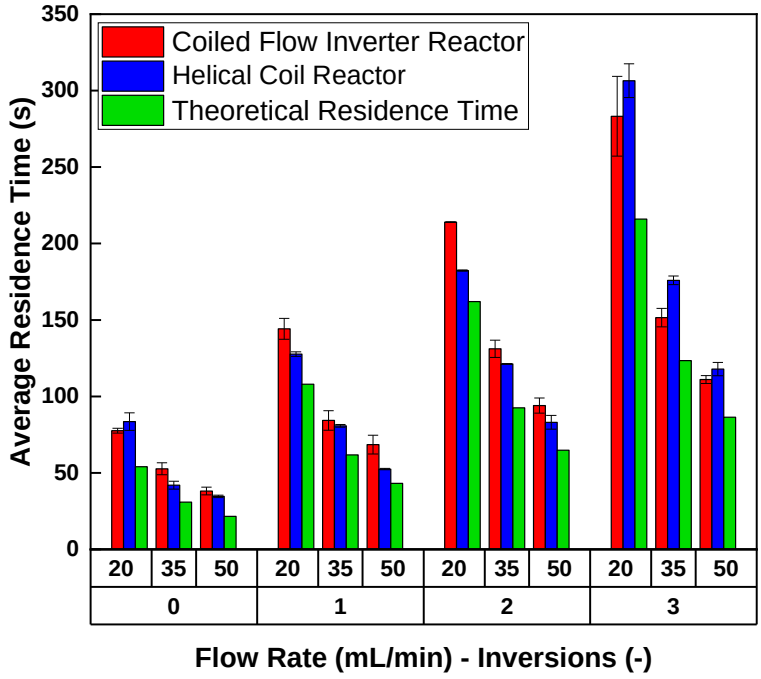

Figure 6.3. Average RT characterisation for CFIR and HCR with an internal coiled tube diameter of 4 mm, along with the minimum theoretical RT (green). The CFIR (red) had a coil of 52 mm and a λ of 13.8. The HCR (blue) had a coil of 0.5 m and a λ of 125.5. The RT was calculated by using NaCl as a tracer element by measuring the increase and decrease of conductivity (0 to 50% and 100% to 50%) at the end of the reactor. The error bars represent the standard deviation of the samples (n=3).

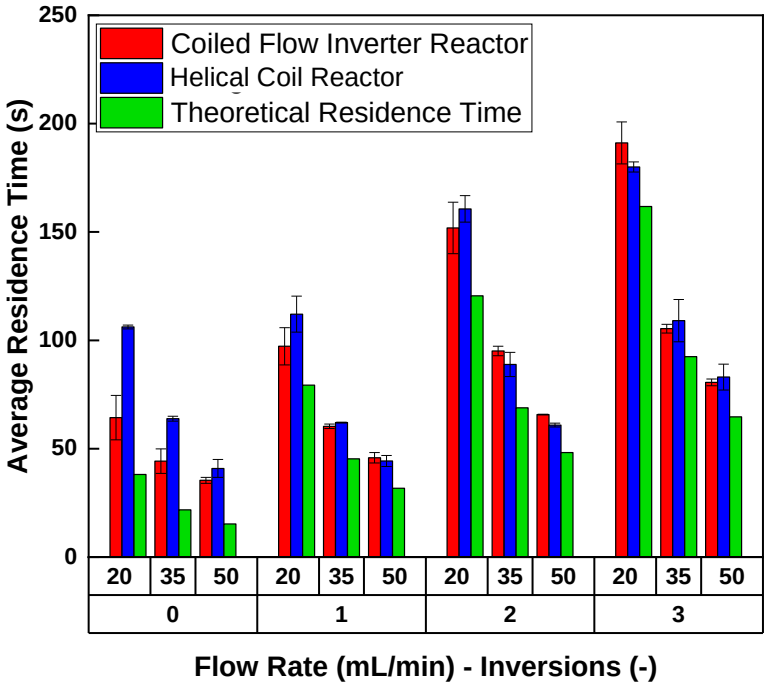

Figure 6.4. Average RT characterisation for CFIR and HCR with an internal coiled tube diameter of 3 mm, along with the minimum theoretical RT (green). The CFIR (red) had a coil of 67 mm and a λ of 23.3. The HCR (blue) had a coil of 0.5 m and a λ of 167.3. The RT was calculated by using NaCl as a tracer element by measuring the increase and decrease of conductivity (0 to 50% and 100% to 50%) at the end of the reactor. The error bars represent the standard deviation of the samples (n=3).

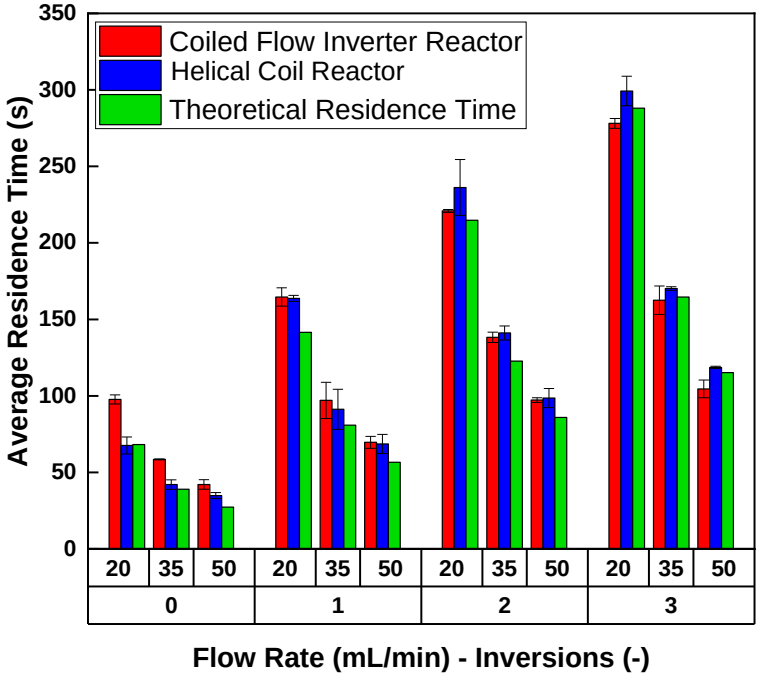

Figure 6.5. Average RT characterisation for CFIR and HCR with an internal coiled tube diameter of 4 mm, along with the minimum theoretical RT (green). The CFIR (red) had a coil of 67 mm and a λ of 17.5. The HCR (blue) had a coil of 0.5 m and a λ of 125.5. The RT was calculated by using NaCl as a tracer element by measuring the increase and decrease of conductivity (0 to 50% and 100% to 50%) at the end of the reactor. The error bars represent the standard deviation of the samples (n=3).

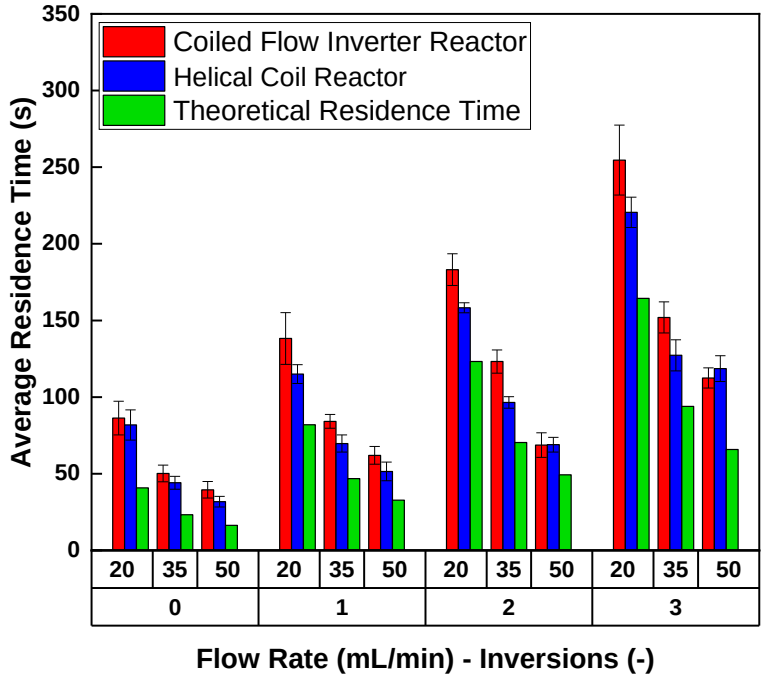

Figure 6.6. Average RT characterisation for CFIR and HCR with an internal coiled tube diameter of 3 mm, along with the minimum theoretical RT (green). The CFIR (red) had a coil of 72 mm and a λ of 25. The HCR (blue) had a coil of 0.5 m and a λ of 167.3. The RT was calculated by using NaCl as a tracer element by measuring the increase and decrease of conductivity (0 to 50% and 100% to 50%) at the end of the reactor. The error bars represent the standard deviation of the samples (n=3).

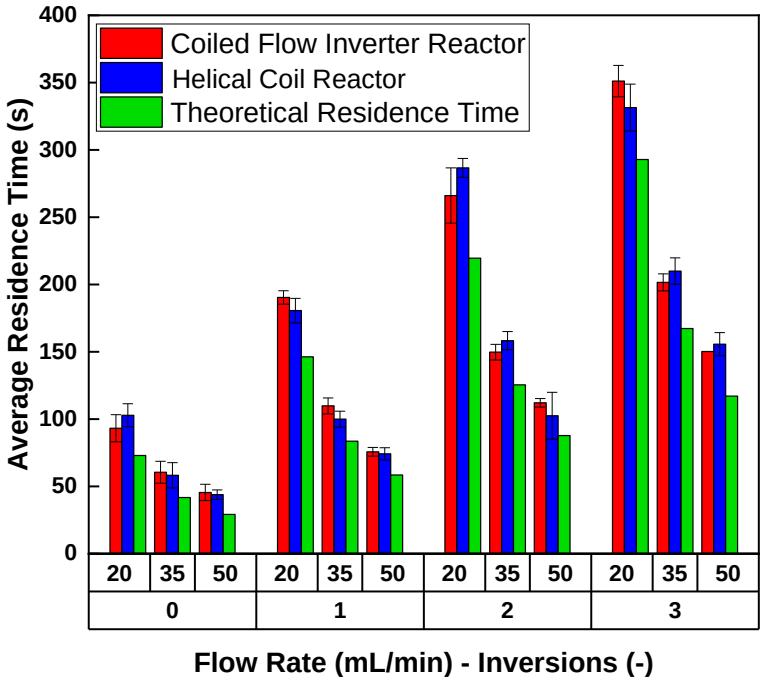

Figure 6.7. Average RT characterisation for CFIR and HCR with an internal coiled tube diameter of 4 mm, along with the minimum theoretical RT (green). The CFIR (red) had a coil of 72 mm and a λ of 18.8. The HCR (blue) had a coil of 0.5 m and a λ of 125.5. The RT was calculated by using NaCl as a tracer element by measuring the increase and decrease of conductivity (0 to 50% and 100% to 50%) at the end of the reactor. The error bars represent the standard deviation of the samples (n=3).

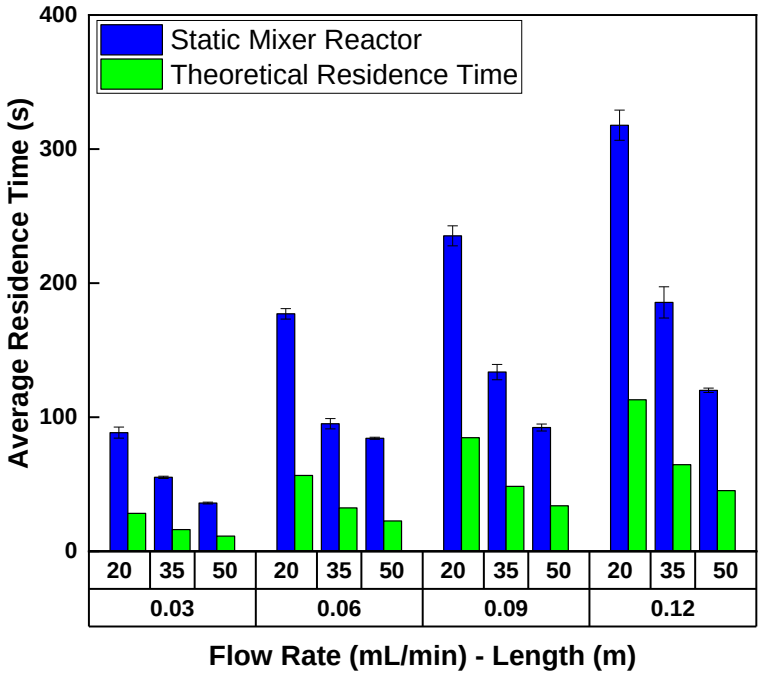

Figure 6.8. Average RT characterisation for SMR (blue) made from 1 to 4 modules, along with the minimum theoretical RT (green). Each of the modules has total length of 30 cm, an internal diameter of 1 cm and 12 elements. The RT was calculated by using NaCl as a tracer element by measuring the increase and decrease of conductivity (0 to 50% and 100% to 50%) at the end of the reactor. The error bars represent the standard deviation of the samples (n=3).

Table 6.1. Average RT values for all the different geometries of each CFIR. The data is ordered by rising λ value. The RT was calculated by using NaCl as a tracer element by measuring the increase and decrease of conductivity (0 to 50% and 100% to 50%) at the end of the reactor.

Coil Dia. (m)	External Tube Dia. (m)	Internal Tube Dia. (m)	λ (-)	Number of Inversions (-)	Length (m)	Flow Velocity (m/s)	Flow Velocity (mL/min)	N_{Re} (-)	Theoretical Average RT (s)	Experimental Average RT (s)
0.053	0.002	0.004	13.8	0	1.43	0.027	20	102.27	54.01	77.60
						0.046	35	178.95	30.86	52.70
						0.066	50	255.64	21.60	38.14
				1	2.87	0.027	20	102.25	108.01	144.23
						0.046	35	178.95	61.72	84.28
						0.066	50	255.64	43.21	68.46
				2	4.30	0.027	20	102.26	162.02	213.97
						0.046	35	178.95	92.58	131.16
						0.066	50	255.64	64.81	94.03
				3	5.73	0.027	20	102.27	216.03	283.21
						0.046	35	178.95	123.44	151.56
						0.066	50	255.64	86.41	111.06
0.068	0.002	0.004	17.5	0	1.81	0.027	20	102.26	68.22	97.71
						0.046	35	178.95	38.98	58.52
						0.066	50	255.64	27.29	42.10
				1	3.75	0.027	20	102.256	141.51	164.61
						0.046	35	178.95	80.86	97.05
						0.066	50	255.64	56.60	69.64
				2	5.70	0.027	20	102.26	214.79	220.90
						0.046	35	178.95	122.74	138.26
						0.066	50	255.64	85.917	97.27
				3	7.64	0.027	20	102.26	288.08	278.10
						0.046	35	178.95	164.62	162.49
						0.066	50	255.64	115.23	104.57
0.053	0.002	0.003	18.3	0	1.42	0.047	20	140.42	30.11	68.22
						0.083	35	245.74	17.21	48.98

						0.118	50	351.06	12.04	34.52
				1	2.85	0.047	20	140.42	60.49	116.39
						0.083	35	245.74	34.57	60.77
						0.118	50	351.06	24.20	53.41
				2	4.29	0.047	20	140.42	90.7	151.56
						0.083	35	245.74	51.93	89.50
						0.118	50	351.06	36.35	63.35
				3	5.2	0.047	20	140.42	121.25	194.72
						0.083	35	245.74	69.28	112.13
						0.118	50	351.06	48.50	80.04
0.073	0.002	0.004	18.8	0	1.94	0.027	20	102.26	72.96	93.18
						0.046	35	178.95	41.69	60.53
						0.066	50	255.64	29.18	45.53
				1	3.88	0.027	20	102.26	146.24	190.39
						0.046	35	178.95	83.57	109.81
						0.066	50	255.64	58.50	75.73
				2	5.82	0.027	20	102.26	219.53	266.11
						0.046	35	178.95	125.45	149.75
						0.066	50	255.64	87.81	112.08
				3	7.77	0.027	20	102.27	292.82	351.17
						0.046	35	178.95	167.32	201.57
						0.066	50	255.64	117.13	150.22
0.068	0.002	0.003	23.3	0	1.80	0.047	20	140.42	38.11	64.36
						0.083	35	245.74	21.78	44.24
						0.118	50	351.06	15.24	35.89
				1	3.74	0.047	20	140.42	79.33	97.25
						0.083	35	245.74	45.33	60.33
						0.118	50	351.06	31.73	45.80
				2	5.68	0.047	20	140.42	120.55	151.87
						0.083	35	245.74	68.89	95.09
						0.118	50	351.06	48.22	65.77

				3	7.63	0.047	20	140.42	161.78	191.11
						0.083	35	245.74	92.45	105.39
						0.118	50	351.06	64.71	80.62
0.073	0.002	0.003	25.0	0	1.92	0.047	20	140.42	40.77	86.31
						0.083	35	245.74	23.30	50.17
						0.118	50	351.06	16.31	39.54
				1	3.87	0.047	20	140.42	82.00	138.25
						0.083	35	245.74	46.85	84.17
						0.118	50	351.06	32.80	62.00
				2	5.81	0.047	20	140.42	123.22	183.14
						0.083	35	245.74	70.41	123.18
						0.118	50	351.06	49.29	68.71
				3	7.75	0.047	20	140.42	164.44	254.62
						0.083	35	245.74	93.97	151.98
						0.118	50	351.06	65.78	112.49

Table 6.2. Average RT values for all the different geometries of each HCR. The HCRs are ordered to match the increasing λ of their CFIR counterparts. The RT was calculated by using NaCl as a tracer element by measuring the increase and decrease of conductivity (0 to 50% and 100% to 50%) at the end of the reactor.

Coil Dia. (m)	External Tube Dia. (m)	Internal Tube Dia. (m)	λ (-)	Length (-)	Flow Velocity (m/s)	Flow Velocity (mL/min)	N_{Re} (-)	Theoretical Average RT (s)	Experimental Average RT (s)
0.5	0.002	0.004	125.5	1.43	0.027	20	102.26	54.01	83.54
					0.046	35	178.95	30.86	41.99
					0.066	50	255.64	21.60	34.61
				2.87	0.027	20	102.26	108.01	127.68
					0.046	35	178.95	61.72	80.80
					0.066	50	255.64	43.21	52.51
				4.30	0.027	20	102.26	162.02	182.35
					0.046	35	178.95	92.58	121.29
					0.066	50	255.64	64.81	83.09
				5.73	0.027	20	102.26	216.03	306.47
					0.046	35	178.95	123.44	175.92
					0.066	50	255.64	86.41	117.88
0.5	0.002	0.004	125.5	1.81	0.027	20	102.26	68.22	67.62
					0.046	35	178.95	38.98	42.029
					0.066	50	255.64	27.29	34.82
				3.75	0.027	20	102.26	141.51	163.72
					0.046	35	178.95	80.86	91.23
					0.066	50	255.64	56.60	68.59
				5.70	0.027	20	102.26	214.79	236.21
					0.046	35	178.95	122.74	141.13
					0.066	50	255.64	85.92	98.57
				7.64	0.027	20	102.26	288.08	299.25
					0.046	35	178.95	164.62	170.14
					0.066	50	255.64	115.23	118.59

0.5	0.002	0.003	167.3	1.42	0.047	20	140.42	30.11	72.35
					0.083	35	245.74	17.21	46.36
					0.118	50	351.06	12.04	32.86
				2.85	0.047	20	140.42	60.76	113.58
					0.083	35	245.74	34.72	65.35
					0.118	50	351.06	24.30	49.04
				4.29	0.047	20	140.42	91.14	161.16
					0.083	35	245.74	52.08	104.03
					0.118	50	351.06	36.45	78.44
				5.72	0.047	20	140.42	121.52	205.71
					0.083	35	245.74	69.44	106.82
					0.118	50	351.06	48.61	81.68
0.5	0.002	0.004	125.5	1.94	0.027	20	102.26	72.96	102.88
					0.046	35	178.95	41.69	58.28
					0.066	50	255.64	29.18	43.86
				3.88	0.027	20	102.26	146.24	180.62
					0.046	35	178.95	83.57	99.96
					0.066	50	255.64	58.50	74.18
				5.82	0.027	20	102.26	219.53	286.70
					0.046	35	178.95	125.45	158.31
					0.066	50	255.64	87.81	102.46
				7.77	0.027	20	102.26	292.82	331.42
					0.046	35	178.95	167.32	220.06
					0.066	50	255.64	117.13	155.64
0.5	0.002	0.003	167.3333	1.80	0.047	20	140.42	38.11	106.16
					0.083	35	245.74	21.78	63.86
					0.118	50	351.06	15.24	40.89
				3.74	0.047	20	140.42	79.33	112.08
					0.083	35	245.74	45.33	62.07

					0.118	50	351.06	31.73	44.32
				5.68	0.047	20	140.42	120.55	160.66
					0.083	35	245.74	68.89	88.85
					0.118	50	351.06	48.22	60.89
				7.63	0.047	20	140.42	161.78	180.01
					0.083	35	245.74	92.45	109.09
					0.118	50	351.06	64.71	83.06
0.5	0.002	0.003	167.3	1.92	0.047	20	140.42	40.77	81.84
					0.083	35	245.74	23.30	44.10
					0.118	50	351.06	16.31	31.79
				3.87	0.047	20	140.42	82.00	115.00
					0.083	35	245.74	46.85	69.73
					0.118	50	351.06	32.80	51.50
				5.81	0.047	20	140.42	123.22	158.27
					0.083	35	245.74	70.41	96.50
					0.118	50	351.06	49.29	68.95
				7.75	0.047	20	140.42	164.44	220.55
					0.083	35	245.74	93.97	127.28
					0.118	50	351.06	65.78	91.05

Table 6.3. Average RT values for all the different lengths of the SMR. The RT was calculated by using NaCl as a tracer element by measuring the increase and decrease of conductivity (0 to 50% and 100% to 50%) at the end of the reactor.

Internal Tube Dia.	No. of Elements	Length	Flow Velocity	Flow Velocity	N_{Re}	Theoretical Average Residence Time	Experimental Average Residence Time
(m)	(-)	(m)	(m/s)	(mL/min)	(-)	(s)	(s)
0.01	12	0.3	0.001	20	10.58	28.26	88.50
			0.002	35	18.52	16.15	55.20
			0.003	50	26.46	11.30	35.96
	24	0.6	0.001	20	10.58	56.52	177.10
			0.002	35	18.52	32.30	95.14
			0.003	50	26.46	22.61	84.29
	36	0.9	0.001	20	10.58	84.78	235.28
			0.002	35	18.52	48.45	133.70
			0.003	50	26.46	33.91	92.28
	48	1.2	0.001	20	10.58	113.04	317.81
			0.002	35	18.52	64.59	185.63
			0.003	50	26.46	45.22	120.03

6.4.2 Relative Width

The R_w is a parameter that measures how close the equipment under certain operational conditions approaches plug ideal plug flow conditions. The R_w was calculated for all of the RTDs with Equation 51. A R_w comparison among all the reactor geometries is presented in Figure 6.9 to 6.15. Table 6.4, 6.5 and 6.6 shows all the relevant data for this section for all of the geometries.

At a fixed length or inversion, the rise of N_{Re} had a negative effect on the R_w as the increased N_{Re} enhances axial dispersion in the flow path. As the number of inversions/length was increased, the difference between R_w among N_{Re} was gradually disappearing. This suggested that the R_w would eventually plateau disregarding the N_{Re} or number of inversions without altering the flow pattern, pitch, number of turns and dimensions of the coil and the coiled tube. After reaching this point, the mixing pattern and effectiveness would not improve. At short lengths, the R_w seemed to be highly dependent on the N_{Re}. Though, this dependency significantly decreased as the length/residence time increased.

The CFIRs had a significantly narrower flow pattern than the HCRs disregarding length or geometry, with some exceptions attributed to outliers or limited data available. However, the difference between R_w between the CFIRs and HCRs became less apparent as number of inversions (length in terms of HCRs) increased. The overall disparity between both types of reactors was more pronounced with the lower λ, being 12.5%, 12.6%, 13%, 6.3%, 8.5% and 5.3% for the λ of 13.8, 17.5, 18.3, 18.8, 23.3 and 25, respectively. This difference in R_w, and ultimately in reduced axial dispersion, was attributed to the secondary flow, also known as Dean vortices, caused by the centrifugal forces at the radius of the coiled tube. Each inversion added to the reactor narrowed the signal curve as each of them caused the inversion of the vortex rotation of the centrifugal forces at a 90° angle, which is always perpendicular to the coil axis (Rojahn et al. 2018; Rossi et al. 2017). Although the HCRs had no inversions, the R_w improved because of the presence of Dean vortices formed by coiling the tube with a resultant 0.5 m coil diameter due to space constraints in the laboratory. The HCRs benefitted from the centrifugal forces formed by the coil. However, the magnitude and the lack of inversions caused a wider signal for almost all of the experiments. Also, it

has been recorded that the oscillatory and antiphase pulsations caused by the peristaltic pumps can be used to partially enhance mixing, affecting the results for both reactor types (R. A. Truesdell et al. 2003; Richard A. Truesdell et al. 2005)

At fixed N_{Re}, the smaller λ showed higher R_w values than the coils with larger λ, with an overall R_w difference value of 16%. At fixed lengths and number of inversions, the magnitude of N_{Pe} or dispersion number increases with decreasing λ. It is more significant as N_{Re} increases (L. Sharma, Nigam, and Roy 2017). However, the R_w is unable to describe or represent the magnitude of the centrifugal force inside the coiled tubes as it is only a ratio between the first data point where the signal increases and the last data point in time where the normalized time reaches 1.

As seen in the other reactors, the SMR had a decreasing trend in R_w as the N_{Re} increased, mitigated as the length of the reactor increased. The R_w of SMR was on average 3% and 19% times lower than the CFIR with the highest and lowest λ, respectively. These lower values can be attributed to a large tube diameter (1.0 cm), causing a greater axial velocity profile even with the elements inside of it.

According to the R_w average values for all the geometries, the CFIRs with the highest λ benefit more from the addition of inversions and extra length with an overall increase of 44% for the λ 25 and 18% for the λ 13.8. The CFIRs with the lower λ had the best values overall but worst improvement on R_w. This confirms the importance of the inherent design and the presence of stronger centrifugal forces in reactors with reduced λ. The HCRs showed an overall R_w increase of 43% and 60% for the equivalent reactors with 4 and 3 mm of internal coil tube diameter, respectively. The SMRs presented an overall increase of 54%. The HCRs and SMRs benefited more from the extended length as their initial cross-sectional mixing is subpar due to the reduced initial secondary flow.

The R_w value does not take into account the actual distribution of the concentration of the tracer molecule, making them inconclusive for the purpose of the project. This value was used as supporting data for the characterization of the reactors, the significant quantification on the axial dispersion in all the geometries is further discussed in Section 6.4.5.

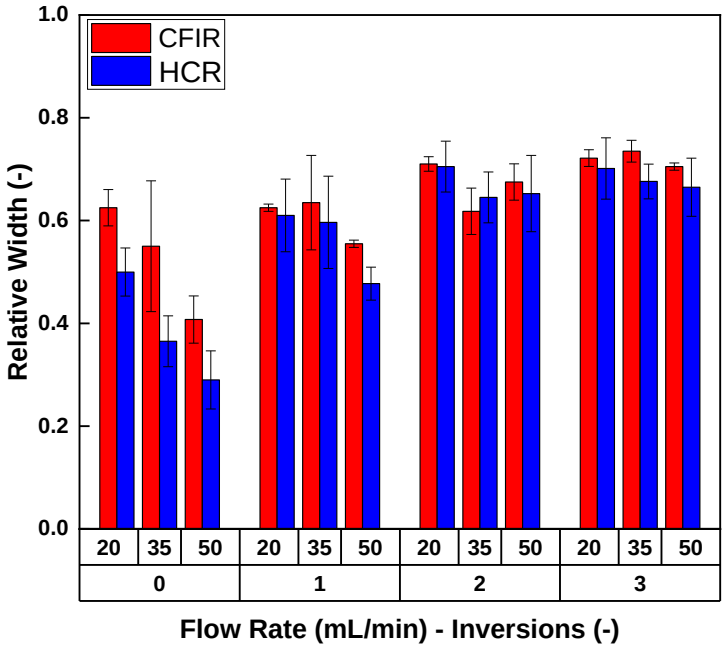

Figure 6.9. R_w values obtained from the RTD experiments for a CFIR (red) with an internal coiled tube diameter of 3 mm, a base coil of 52 mm and a λ of 18.3, and a HCR (blue) with an internal coiled tube diameter of 3 mm, a base coil of 0.5 m and a λ of 167.3. The RTD was calculated by using NaCl as a tracer element by measuring the increase and decrease of conductivity (0 to 50% and 100% to 50%) at the end of the reactor. The Rw value was calculated by dividing the normalised tracer concentration value at θ = 0.995 by θ = 0.005. The error bars represent the standard deviation of the samples (n=3).

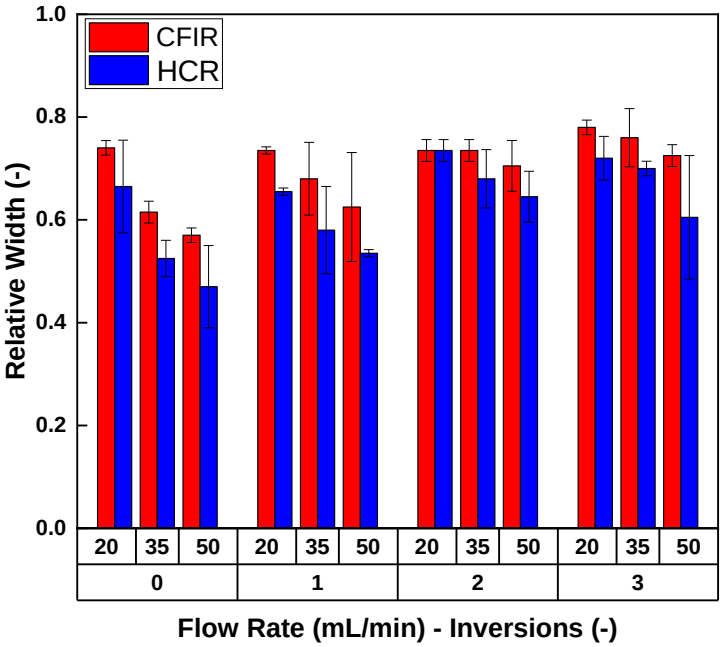

Figure 6.10. Rw values obtained from the RTD experiments for a CFIR (red) with an internal coiled tube diameter of 4 mm, a base coil of 52 mm and a λ of 13.8, and a HCR (blue) with an internal coiled tube diameter of 4 mm, a base coil of 0.5 m and a λ of 125.5. The RTD was calculated by using NaCl as a tracer element by measuring the increase and decrease of conductivity (0 to 50% and 100% to 50%) at the end of the reactor. The Rw value was calculated by dividing the normalised tracer concentration value at θ = 0.995 by θ = 0.005. The error bars represent the standard deviation of the samples (n=3).

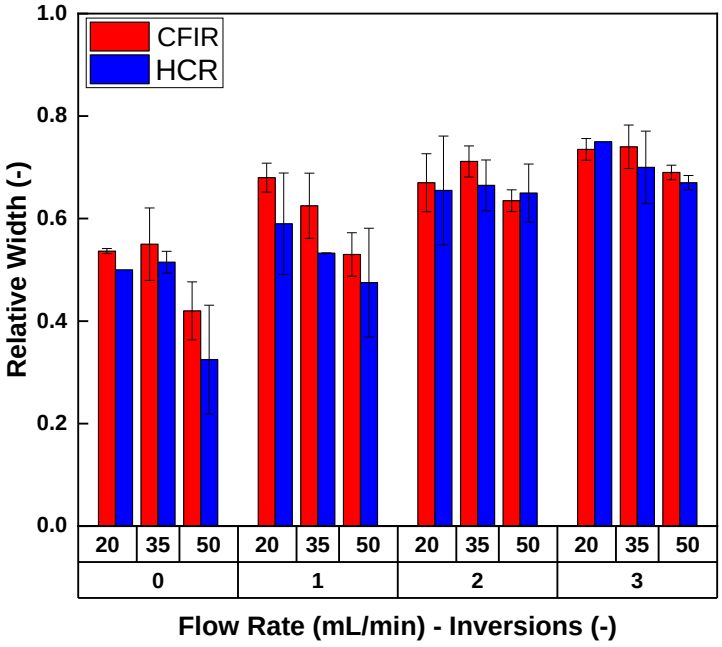

Figure 6.11. Rw values obtained from the RTD experiments for a CFIR (red) with an internal coiled tube diameter of 3 mm, a base coil of 67 mm and a λ of 23.3, and a HCR (blue) with an internal coiled tube diameter of 3 mm, a base coil of 0.5 m and a λ of 167.3. The RTD was calculated by using NaCl as a tracer element by measuring the increase and decrease of conductivity (0 to 50% and 100% to 50%) at the end of the reactor. The Rw value was calculated by dividing the normalised tracer concentration value at θ = 0.995 by θ = 0.005. The error bars represent the standard deviation of the samples (n=3).

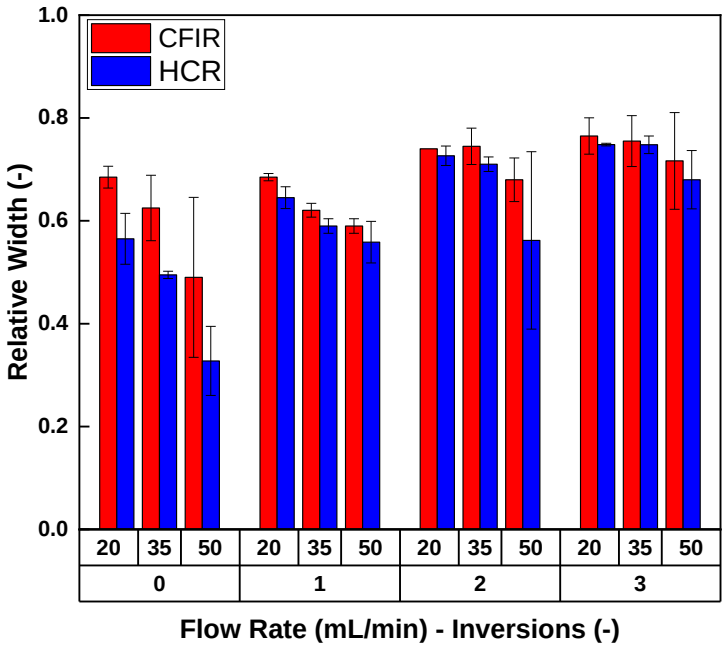

Figure 6.12. Rw values obtained from the RTD experiments for a CFIR (red) with an internal coiled tube diameter of 4 mm, a base coil of 67 mm and a λ of 17.5, and a HCR (blue) with an internal coiled tube diameter of 4 mm, a base coil of 0.5 m and a λ of 125.5. The RTD was calculated by using NaCl as a tracer element by measuring the increase and decrease of conductivity (0 to 50% and 100% to 50%) at the end of the reactor. The Rw value was calculated by dividing the normalised tracer concentration value at θ = 0.995 by θ = 0.005. The error bars represent the standard deviation of the samples (n=3).

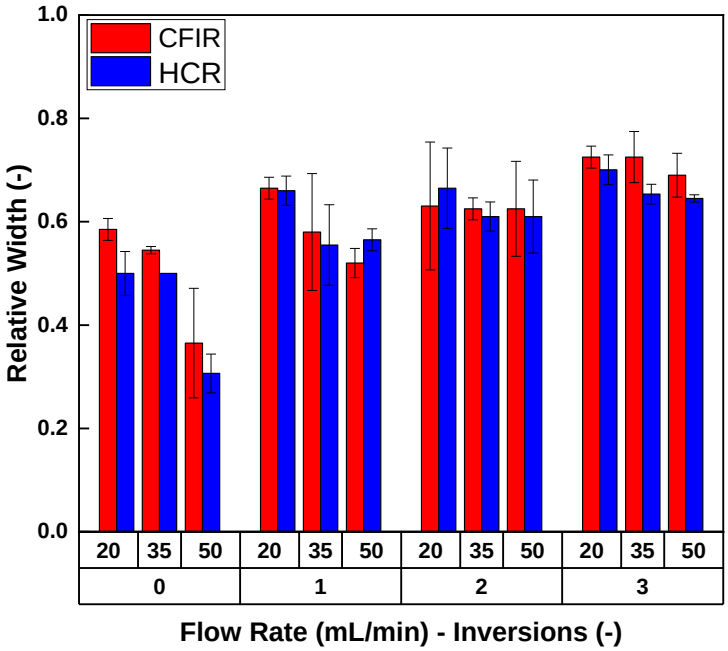

Figure 6.13. Rw values obtained from the RTD experiments for a CFIR (red) with an internal coiled tube diameter of 3 mm, a base coil of 72 mm and a λ of 25, and a HCR (blue) with an internal coiled tube diameter of 3 mm, a base coil of 0.5 m and a λ of 167.3. The RTD was calculated by using NaCl as a tracer element by measuring the increase and decrease of conductivity (0 to 50% and 100% to 50%) at the end of the reactor. The Rw value was calculated by dividing the normalised tracer concentration value at θ = 0.995 by θ = 0.005. The error bars represent the standard deviation of the samples (n=3).

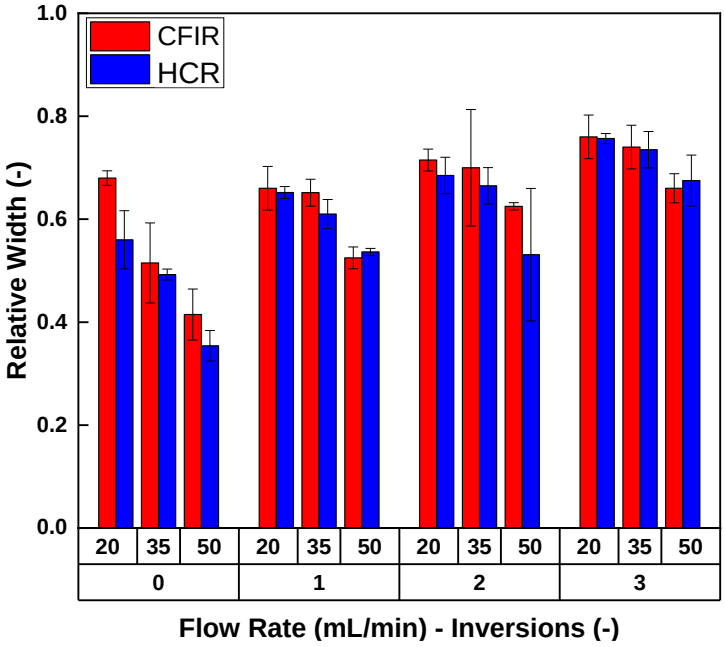

Figure 6.14. Rw values obtained from the RTD experiments for a CFIR (red) with an internal coiled tube diameter of 4 mm, a base coil of 72 mm and a λ of 18.8, and a HCR (blue) with an internal coiled tube diameter of 4 mm, a base coil of 0.5 m and a λ of 125.5. The RTD was calculated by using NaCl as a tracer element by measuring the increase and decrease of conductivity (0 to 50% and 100% to 50%) at the end of the reactor. The Rw value was calculated by dividing the normalised tracer concentration value at θ = 0.995 by θ = 0.005. The error bars represent the standard deviation of the samples (n=3).

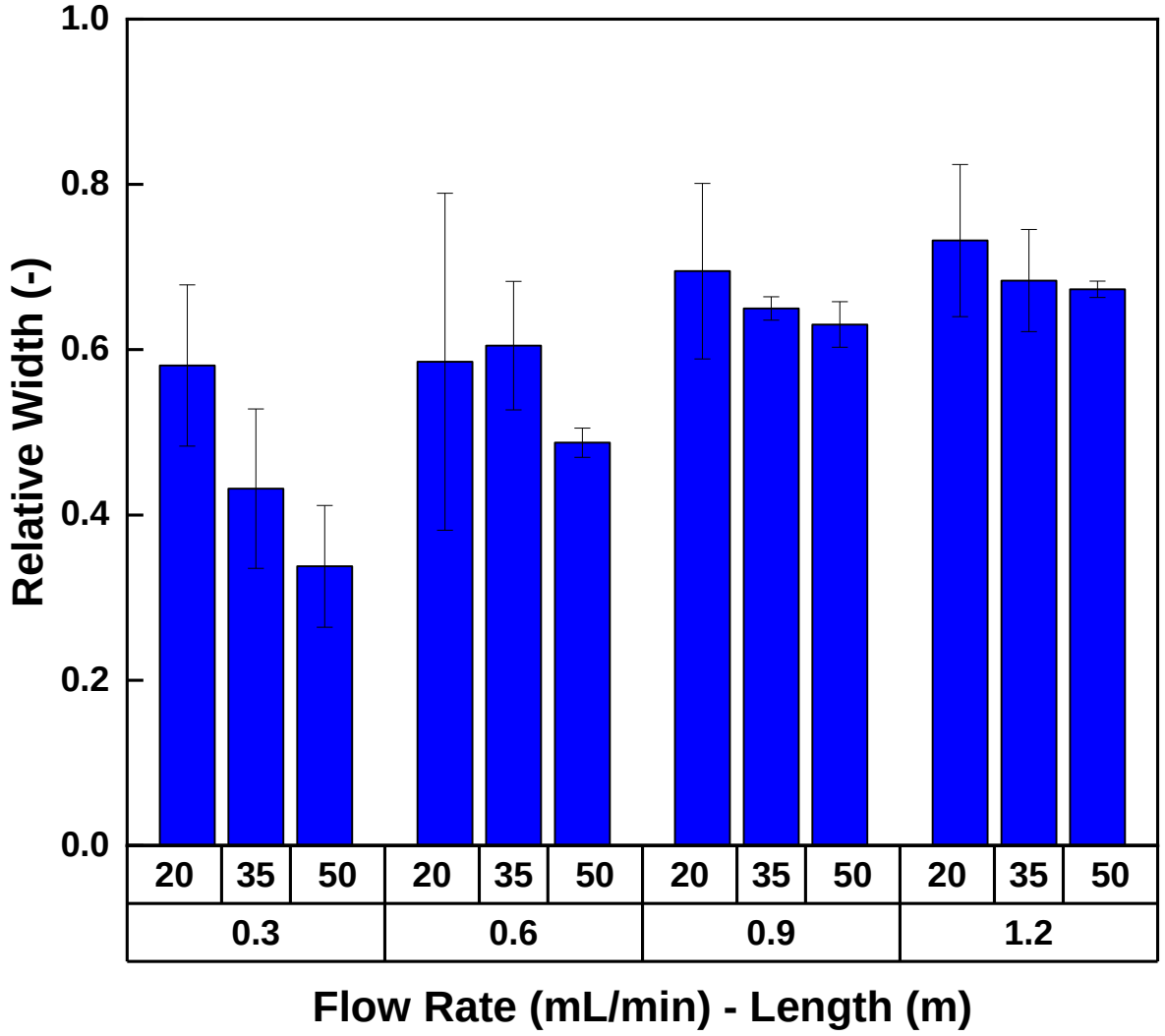

Figure 6.15. Rw values obtained from the RTD experiments for a SMR with a module length of 30 cm, an internal tube diameter or 1 cm and 12 elements. The RTD was calculated by using NaCl as a tracer element by measuring the increase and decrease of conductivity (0 to 50% and 100% to 50%) at the end of the reactor. The Rw value was calculated by dividing the normalised tracer concentration value at θ = 0.995 by θ = 0.005. The error bars represent the standard deviation of the samples (n=3).

Table 6.4. R_w values for all the different geometries of each CFIR. The data is ordered by rising λ value. The RT was calculated by using NaCl as a tracer element by measuring the increase and decrease of conductivity (0 to 50% and 100% to 50%) at the end of the reactor. The Rw value was calculated by dividing the normalised tracer concentration value at θ = 0.995 by θ = 0.005.

Coil Dia. (m)	External Tube Dia. (m)	Internal Tube Dia. (m)	λ (-)	No. of Inversions (-)	No. of Turns (-)	Length (m)	Flow Velocity (m/s)	Flow Velocity (mL/min)	N_{Re} (-)	R_w (-)
0.053	0.002	0.004	13.8	0	8	1.43	0.027	20	102.26	0.74
							0.046	35	178.95	0.62
							0.066	50	255.64	0.57
				1	16	2.87	0.027	20	102.26	0.74
							0.046	35	178.95	0.68
							0.066	50	255.64	0.63
				2	24	4.30	0.027	20	102.26	0.74
							0.046	35	178.95	0.74
							0.066	50	255.64	0.71
				3	32	5.73	0.027	20	102.26	0.78
							0.046	35	178.95	0.76
							0.066	50	255.64	0.73
0.068	0.002	0.004	17.5	0	8	1.81	0.027	20	102.26	0.69
							0.046	35	178.95	0.63
							0.066	50	255.64	0.49
				1	16	3.75	0.027	20	102.26	0.69
							0.046	35	178.95	0.62
							0.066	50	255.64	0.59
				2	24	5.70	0.027	20	102.26	0.74
							0.046	35	178.95	0.75
							0.066	50	255.64	0.68
				3	32	7.64	0.027	20	102.26	0.77
							0.046	35	178.95	0.76
							0.066	50	255.64	0.72

0.053	0.002	0.003	18.3	0	8	1.42	0.047	20	140.42	0.63
							0.083	35	245.74	0.55
							0.118	50	351.06	0.41
				1	16	2.85	0.047	20	140.42	0.63
							0.083	35	245.74	0.64
							0.118	50	351.06	0.56
				2	24	4.29	0.047	20	140.42	0.71
							0.083	35	245.74	0.62
							0.118	50	351.06	0.68
				3	32	5.72	0.047	20	140.42	0.72
							0.083	35	245.74	0.74
							0.118	50	351.06	0.71
0.073	0.002	0.004	18.8	0	8	1.94	0.027	20	102.26	0.68
							0.046	35	178.95	0.52
							0.066	50	255.64	0.42
				1	16	3.88	0.027	20	102.26	0.66
							0.046	35	178.95	0.65
							0.066	50	255.64	0.53
				2	24	5.82	0.027	20	102.26	0.72
							0.046	35	178.95	0.70
							0.066	50	255.64	0.63
				3	32	7.77	0.027	20	102.26	0.76
							0.046	35	178.95	0.74
							0.066	50	255.64	0.66
0.068	0.002	0.003	23.3	0	8	1.80	0.047	20	140.42	0.54
							0.083	35	245.74	0.55
							0.118	50	351.06	0.42
				1	16	3.74	0.047	20	140.42	0.68
							0.083	35	245.74	0.63

							0.118	50	351.06	0.53
				2	24	5.68	0.047	20	140.42	0.67
							0.083	35	245.74	0.71
							0.118	50	351.06	0.64
				3	32	7.63	0.047	20	140.42	0.74
							0.083	35	245.74	0.74
							0.118	50	351.06	0.69
0.073	0.002	0.003	25	0	8	1.92	0.047	20	140.42	0.59
							0.083	35	245.74	0.55
							0.118	50	351.06	0.37
				1	16	3.87	0.047	20	140.42	0.67
							0.083	35	245.74	0.58
							0.118	50	351.06	0.52
				2	24	5.81	0.047	20	140.42	0.63
							0.083	35	245.74	0.63
							0.118	50	351.06	0.63
				3	32	7.755	0.047	20	140.42	0.73
							0.083	35	245.74	0.73
							0.118	50	351.06	0.69

Table 6.5. R_w values for all the different geometries of each HCR. The data is ordered by the rising λ value of their CFIR counterparts. The RT was calculated by using NaCl as a tracer element by measuring the increase and decrease of conductivity (0 to 50% and 100% to 50%) at the end of the reactor. The Rw value was calculated by dividing the normalised tracer concentration value at θ = 0.995 by θ = 0.005.

Coil Dia. (m)	External Tube Dia. (m)	Internal Tube Dia. (m)	λ (-)	Length (m)	Flow Velocity (m/s)	Flow Velocity (mL/min)	N_{Re} (-)	R_w (-)
0.5	0.002	0.004	125.5	1.43	0.027	20	102.26	0.67
					0.046	35	178.95	0.53
					0.066	50	255.64	0.47
				2.87	0.027	20	102.26	0.66
					0.046	35	178.95	0.58
					0.066	50	255.64	0.54
				4.30	0.027	20	102.26	0.74
					0.046	35	178.95	0.68
					0.066	50	255.64	0.65
				5.73	0.027	20	102.26	0.72
					0.046	35	178.95	0.70
					0.066	50	255.64	0.61
0.5	0.002	0.004	125.5	1.81	0.027	20	102.26	0.57
					0.046	35	178.95	0.50
					0.066	50	255.64	0.33
				3.75	0.027	20	102.26	0.65
					0.046	35	178.95	0.59
					0.066	50	255.64	0.56
				5.70	0.027	20	102.26	0.73
					0.046	35	178.95	0.71
					0.066	50	255.64	0.56
				7.64	0.027	20	102.26	0.75
					0.046	35	178.95	0.75
					0.066	50	255.64	0.68

0.5	0.002	0.003	167.3	1.42	0.047	20	140.42	0.50
					0.083	35	245.74	0.37
					0.118	50	351.06	0.29
				2.85	0.047	20	140.42	0.61
					0.083	35	245.74	0.60
					0.118	50	351.06	0.48
				4.29	0.047	20	140.42	0.71
					0.083	35	245.74	0.65
					0.118	50	351.06	0.65
				5.72	0.047	20	140.42	0.70
					0.083	35	245.74	0.68
					0.118	50	351.06	0.665
0.5	0.002	0.004	125.5	1.935226	0.027	20	102.26	0.56
					0.046	35	178.95	0.49
					0.066	50	255.64	0.35
				3.88	0.027	20	102.26	0.65
					0.046	35	178.95	0.61
					0.066	50	255.64	0.54
				5.82	0.027	20	102.26	0.69
					0.046	35	178.95	0.67
					0.066	50	255.64	0.53
				7.77	0.027	20	102.26	0.76
					0.046	35	178.95	0.74
					0.066	50	255.64	0.68
0.5	0.002	0.003	167.3	1.80	0.047	20	140.42	0.50
					0.083	35	245.74	0.52
					0.118	50	351.06	0.32
				3.74	0.047	20	140.42	0.59
					0.083	35	245.74	0.53

					0.118	50	351.06	0.48
				5.68	0.047	20	140.42	0.65
					0.083	35	245.74	0.67
					0.118	50	351.06	0.65
				7.63	0.047	20	140.42	0.75
					0.083	35	245.74	0.70
					0.120	50	351.06	0.67
0.5	0.002	0.003	167.3	1.92	0.047	20	140.42	0.50
					0.083	35	245.74	0.50
					0.120	50	351.06	0.31
				3.87	0.047	20	140.42	0.66
					0.083	35	245.74	0.56
					0.180	50	351.06	0.57
				5.81	0.047	20	140.42	0.67
					0.083	35	245.74	0.61
					0.120	50	351.06	0.61
				7.75	0.047	20	140.42	0.70
					0.083	35	245.74	0.65
					0.120	50	351.07	0.65

Table 6.6. R_w values for all the different geometries of each SMR. The data is ordered by total length value. The RT was calculated by using NaCl as a tracer element by measuring the increase and decrease of conductivity (0 to 50% and 100% to 50%) at the end of the reactor. The Rw value was calculated by dividing the normalised tracer concentration value at θ = 0.995 by θ = 0.005.

Internal Tube Dia. (m)	No. of Elements (-)	Length (m)	Flow Velocity (m/s)	Flow Rate (mL/min)	N_{Re} (-)	R_w (-)
0.01	12	0.03	0.001	20	10.58	0.58
			0.002	35	18.52	0.43
			0.003	50	26.46	0.34
	24	0.06	0.001	20	10.58	0.59
			0.002	35	18.52	0.61
			0.003	50	26.46	0.49
	36	0.09	0.001	20	10.58	0.70
			0.002	35	18.52	0.65
			0.003	50	26.46	0.63
	48	0.12	0.001	20	10.58	0.73
			0.002	35	18.52	0.68
			0.003	50	26.46	0.67

6.4.3 Step Response Curves

The RTD curve (also known as F-curve) is a response function to the step input tracer experiment. The ideal theoretical RTD is a Dirac delta function with a value equal to the theoretical residence time of the geometry. The deviation from this ideal plug flow represents the axial dispersion in the dimensions and geometry of the system (Soni et al. 2019). Figure 6.16 to 6.21 represent the F-curves obtained in CFIR and HCR at N_{Re} of 100, 180 and 250; whilst for the SMR at N_{Re} of 10, 18 and 26. The difference in N_{Re} was due to the internal tube diameter. It was decided to keep these values as it would not be feasible to run the CFIRs and HCRs at that equivalent flow rate using the actual CCTC tube diameter scale. On the other hand, running the SMR in equivalent flow rates would require an enormous amount of chromatography resin and buffer. Also, it was decided that the experimental conditions for the proof of concept should be as close as possible to the actual manufacturing parameters in a CCTC system of this scale.

For the lowest values of N_{Re} narrower F-curves were observed across all inversions for CFIR and lengths for HCR and SMR. As the number of inversions and lengths increased for all geometries, the higher N_{Re} curves became comparable to the lowest ones. This was due to the increased inversions of the cross-sectional mixing caused by the centrifugal force caused by the coiling of the tube for CFIRs and SRs and the elements inside the SMRs. Similar trends were measured over the entire range of inversions and lengths. Comparable observations were reported for lower values of N_{Re} (< 200) (Saxena and Nigam 1984; L. Sharma, Nigam, and Roy 2017). The CFIR with 0 inversions is narrower compared to the HCR with equivalent length, demonstrating the effectiveness of a reduced λ; i. e. a λ 18.8 (CFIR) compared to λ 125.5 (HCR). When the length of the HCR was long enough the F-curve narrowness and distribution came closer to the CFIR. The SMR lagged behind in terms of narrowness compared to the CFIR but has similar distribution to the HCR in all three N_{Re} at their longest version (Figure 6.20 and 6.21). All the other geometries showed similar trends as the examples mentioned beforehand. Also, the F-curves agreed with the R_w results presented in Section 6.4.2.

The F-curves provide a visual evidence of the reduction of axial dispersion inside the different reactors but do not quantify the axial dispersion. In order to quantify and possible rank the geometries in terms of axial dispersion terms, an ADM was employed in Section 6.4.4.

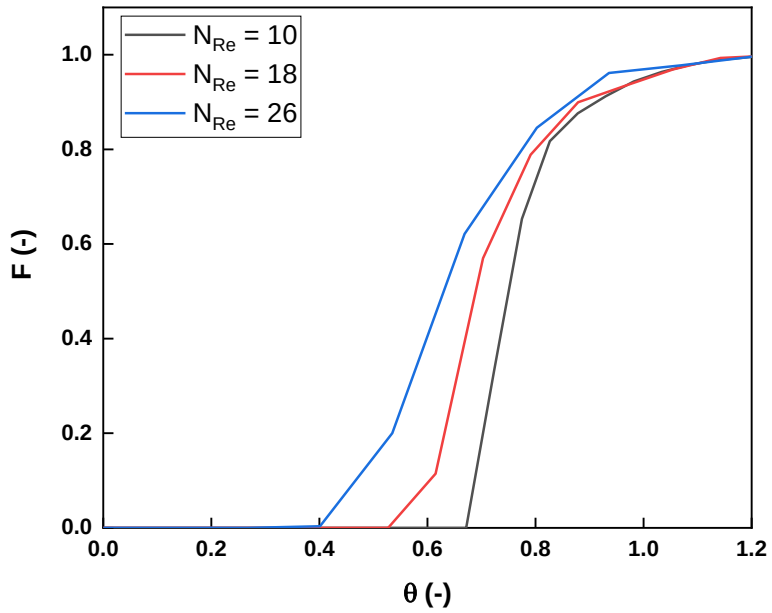

Figure 6.16. F-curve for SMR with a total length of 30 cm, internal tube diameter of 1 cm and 12 elements at a N_{Re} = 10 (black), 18 (red) and 26 (blue). F-curve was calculated by using NaCl as a tracer element by measuring the increase and decrease of conductivity (0 to 50% and 100% to 50%) at the end of the reactor.

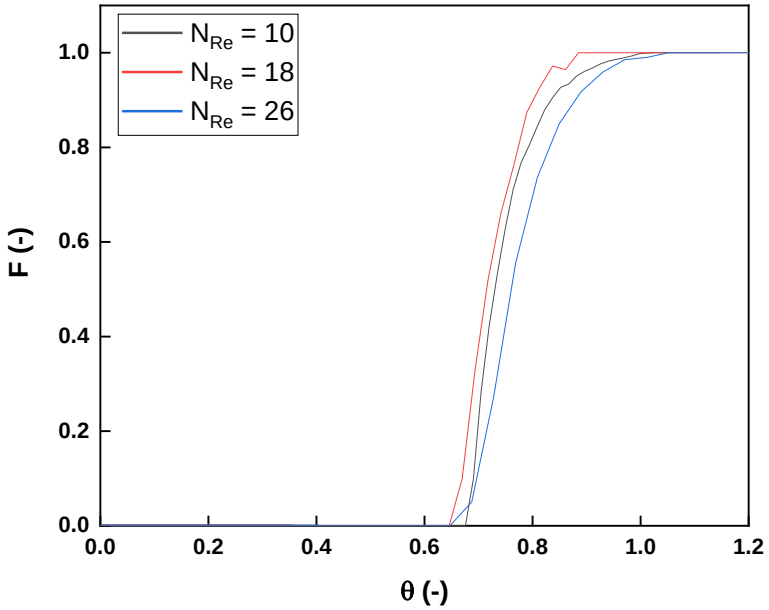

Figure 6.17. F-curve for SMR with a total length of 1.2 m, internal tube diameter of 1 cm and 48 elements at a N_{Re} = 10 (black), 18 (red) and 26 (blue). F-curve was calculated by using NaCl as a tracer element by measuring the increase and decrease of conductivity (0 to 50% and 100% to 50%) at the end of the reactor.

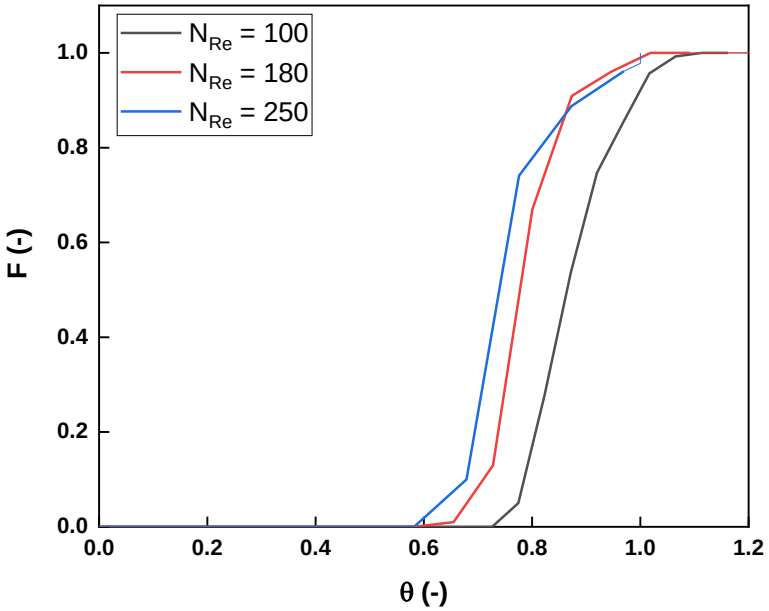

Figure 6.18. F-curve for CFIR with an internal coiled tube diameter of 4 cm, a coil base of 72 mm, 0 inversions and a λ of 18.8 at a N_{Re} = 100 (black), 180 (red) and 250 (blue). F-curve was calculated by using NaCl as a tracer element by measuring the increase and decrease of conductivity (0 to 50% and 100% to 50%) at the end of the reactor.

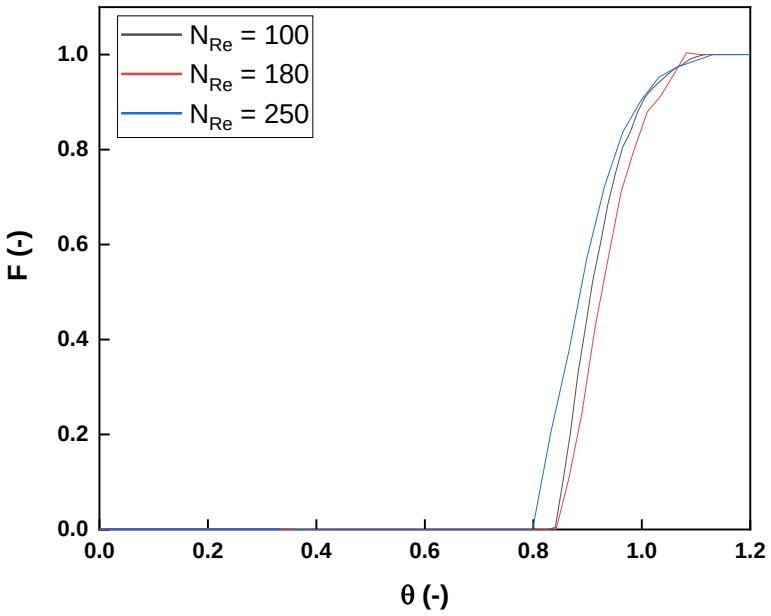

Figure 6.19. F-curve for CFIR with an internal coiled tube diameter of 4.0 cm, a coil base of 72.0 mm, 3 inversions and a λ of 18.8 at a N_{Re} = 100.0 (black), 180.0 (red) and 250.0 (blue). F-curve was calculated by using NaCl as a tracer element by measuring the increase and decrease of conductivity (0.0 to 50.0% and 100.0% to 50.0%) at the end of the reactor.

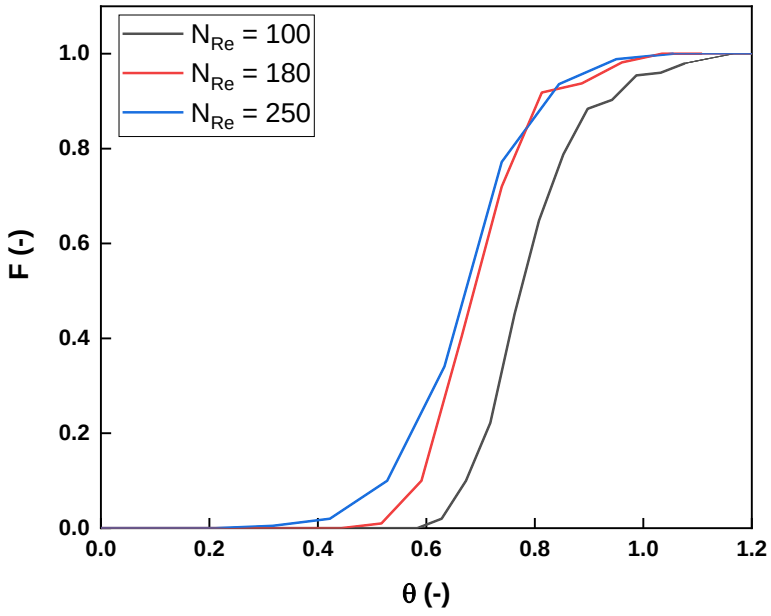

Figure 6.20. F-curve for HCR with total length of 1.9 m, an internal coiled tube diameter of 4 cm, a coil base of 0.5 m and a λ of 125.5 at a N_{Re} = 100 (black), 180 (red) and 250 (blue). F-curve was calculated by using NaCl as a tracer element by measuring the increase and decrease of conductivity (0 to 50% and 100% to 50%) at the end of the reactor.

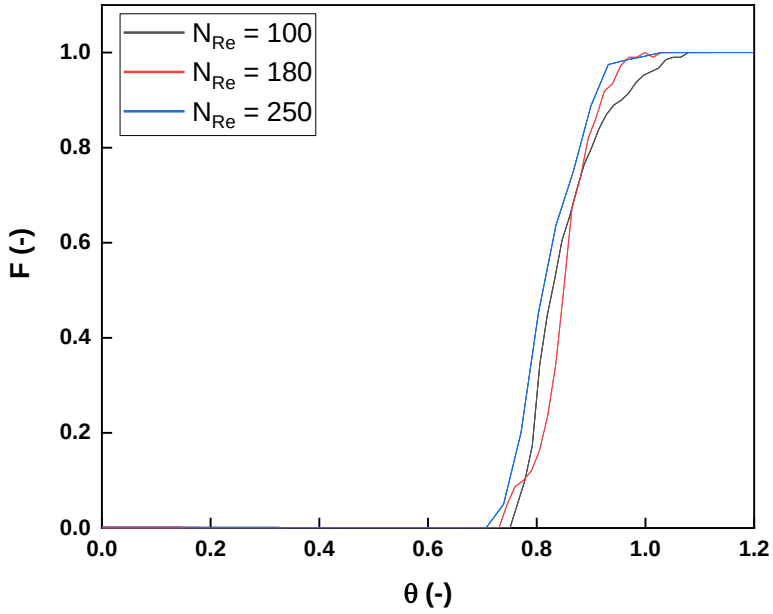

Figure 6.21. F-curve for HCR with a total length of 7.8 m, an internal coiled tube diameter of 4 cm, a coil base of 0.5 m and a λ of 125.5 at a N_{Re} = 100 (black), 180 (red) and 250 (blue). F-curve was calculated by using NaCl as a tracer element by measuring the increase and decrease of conductivity (0 to 50% and 100% to 50%) at the end of the reactor.

6.4.4 Axial Dispersion in Coiled Flow Inverter Reactor, Helical Coil Reactor and Static Mixer Reactor

This section focuses on using the ADM developed by Taylor and Aris to the data obtained from the different reactors in order to compare them (Rossi et al. 2017; Aris 1999). The ADM was fitted into E(θ) curves obtained from the RTD analysis (Section 6.3.3) using Equations 55 or 56. The ADM was expected to fit the E(θ)-curve as these curves are narrow enough to follow near-Gaussian distributions, disregarding the geometry. The fit was optimized by using Equation 61 by minimizing the residuals between the experimental and modelled data. Figures 6.23 to 6.28 are representative examples that display the $E(\theta)_{Exp}$ values obtained from the RTD data and the $E(\theta)_{ADM}$ calculated from the ADM. Table 6.7, 6.8 and 6.9 show the resulting parameters such as the N_{Pe} (calculated from Equation 53). The N_{Pe}, also known as Dispersion number or Bodenstein number, represents the ratio between convection and diffusion forces in a convection-diffusion transport system.

An acceptable agreement can be seen between the $E(\theta)_{Exp}$ values and the $E(\theta)_{ADM}$ data from all of the figures. The average residual error for all the reactor types was approximately $1.0X10^{-5}$, disregarding the N_{Re}. The model data had to be truncated after the dimensionless average RT (θ) reached 1, as the model is based on a Gaussian distribution which means that only one side of the "bell" shape of the curve was used for our purpose. This good prediction of the experimental data with the ADM in CFIRs, HCRs and SMRs suggested the existence of a secondary flow or enhanced cross-sectional mixing compared to the corresponding flow in a straight tube. The ADM has proven to provide a good approximation even at small discontinuities in the flow pattern at the 90° inversions. These discontinuities have practically no relevance on the model as the CFIRs act as short plug flow vessels in series bringing the overall flow pattern closer to plug flow ($R_w = 1$). A similar agreement was found for the rest of the RTD for all the other reactors (L. Sharma, Nigam, and Roy 2017).

Once the dispersion values were correctly established using the ADM, the applicability of such values was checked using a flow regime map (Ananthakrishnan, Gill, and Barduhn 1965; Rossi et al. 2017). As the N_{Re} is under the laminar region, the ADM only holds under certain conditions determined by the N_{Pe} and the relationship between the length and diameter of the tube in use (L/d_t). This model has been previously proved to work not only on straight tubes but also on CFIRs (Rossi et al. 2017). Figure 6.22 overlays some points representing the different CFIRs used throughout the experiment on a standard flow regime map for the applicability of the ADM. All points were selected from CFIRs operating at 50 mL/min as this condition yields the highest N_{Re}. None of the data falls under the pure convective regime or intermediate regime, validating our dispersion values. It can be observed that the CFIRs with 3 inversions are positioned at the top in terms of N_{Pe} (raised cross-sectional mixing due to inversions, geometry and length) and L/d_t (constant diameter over a larger length). A preliminary analysis shows that the CFRIs with the lowest λ rank on top for the geometries without inversions but rank last when 3 number of inversions are used. This was due to the overall length of the reactors which was shorter for the CFIRs with λ of 13.8 and 18.3. The extra length gives longer RT for the centrifugal forces to act upon and reduce the axial dispersion after every turn. The applicability for the rest of the reactors and parameters was also assessed giving positive results. The applicability was also corroborated using Equations 57 and 58.

The N_{Pe} was further used to quantitatively define the axial dispersion inside each of the geometries to determine the effects of length/inversion number, λ and type of reactor in Sections 6.4.5. Then, the data was used to determine if there is a relation between the degree of dispersion/cross-sectional mixing to the binding rate of BSA to the chromatography resin Macro-Prep High Q in each of the reactors.

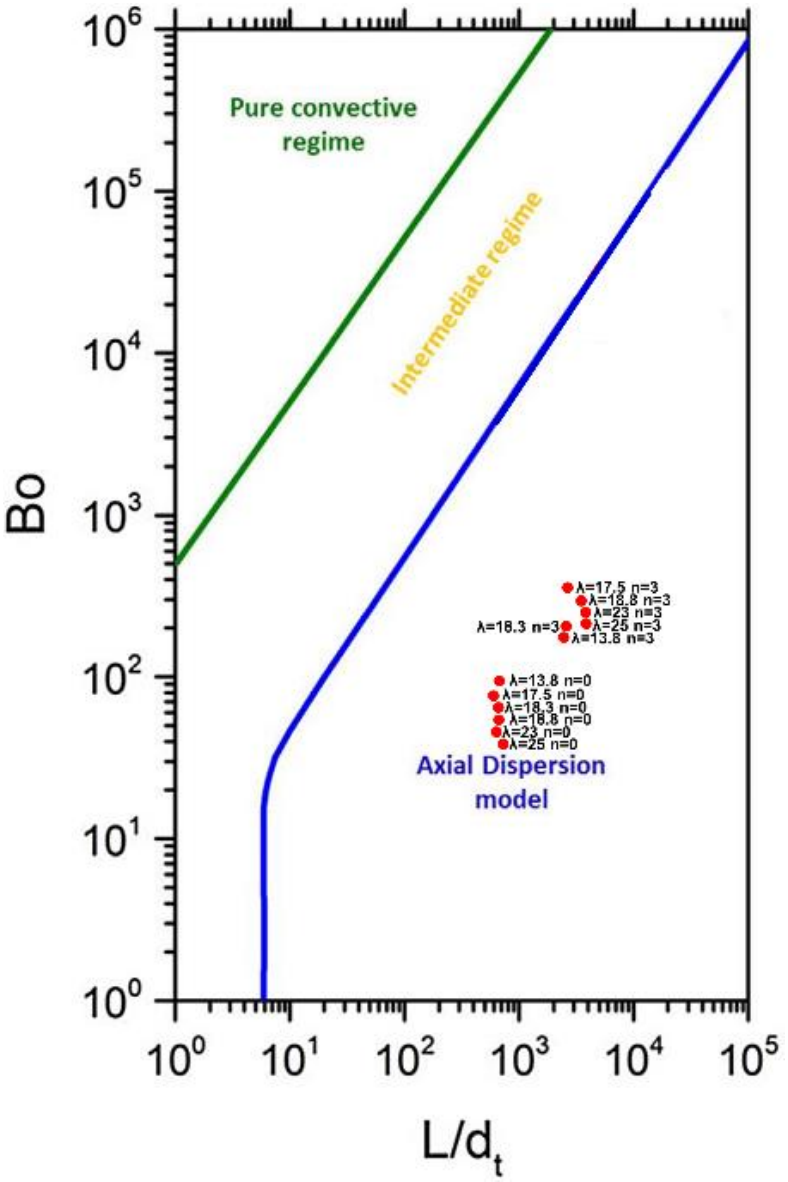

Figure 6.22. Map reporting which model to adopt for straight pipes. The operational points for all λ for CFIR can be found on the map knowing the aspect ratio of the coiled tube and of the Bodenstein number (NPe). Figure adapted from Rossi et al, 2017 from the data of Ananthakrishnan, Gill and Barduhn, 1965.

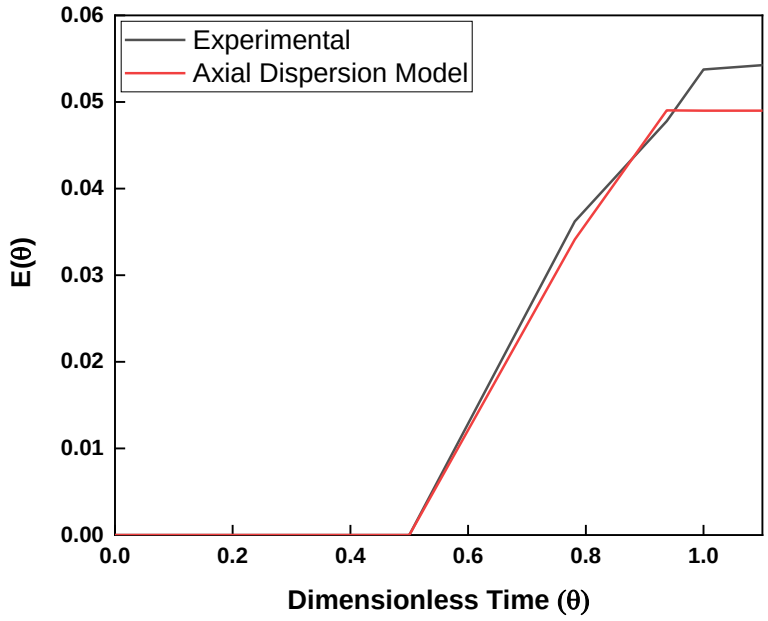

Figure 6.23. Comparison of results with experimental and calculated E-curves for SMR with a total length of 30 cm, internal tube diameter of 1 cm and 12 elements at a N_{Re} = 26. The experimental values (black) were fitted with theoretical values (red) obtained from the ADM.

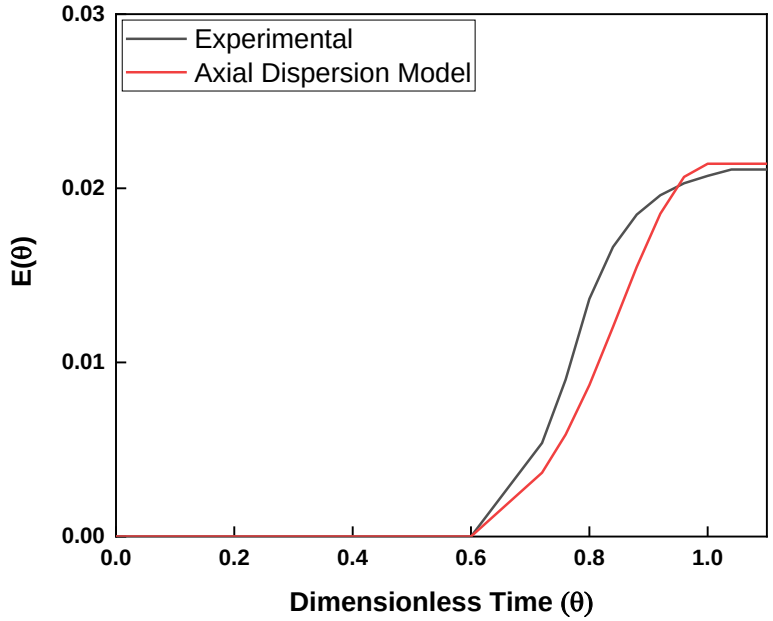

Figure 6.24. Comparison of results with experimental and calculated E-curves for SMR with a total length of 1.2 m, internal tube diameter of 1 cm and 48 elements at a N_{Re} = 26. The experimental values (black) were fitted with theoretical values (red) obtained from the ADM.

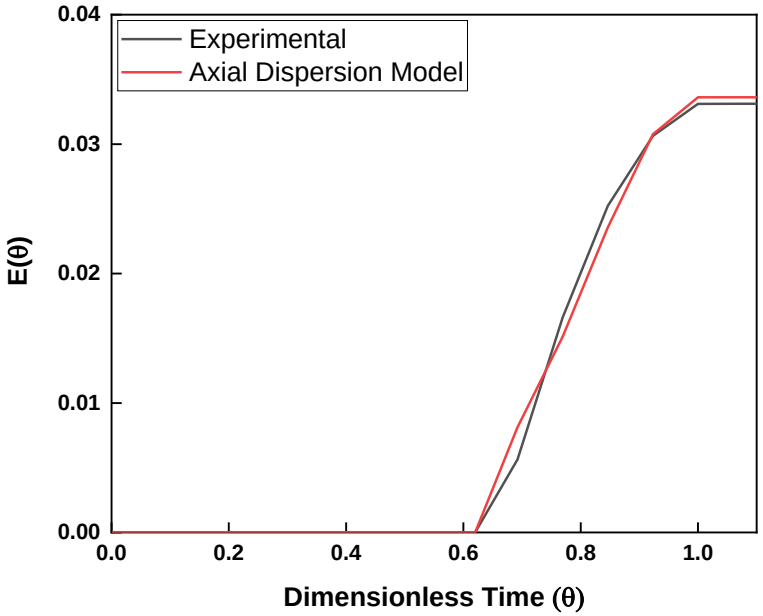

Figure 6.25. Comparison of results with experimental and calculated E-curves for CFIR with 0 inversions, an internal tube diameter of 4 mm and λ of 18.8 at a N_{Re} = 250. The experimental values (black) were fitted with theoretical values (red) obtained from the ADM.

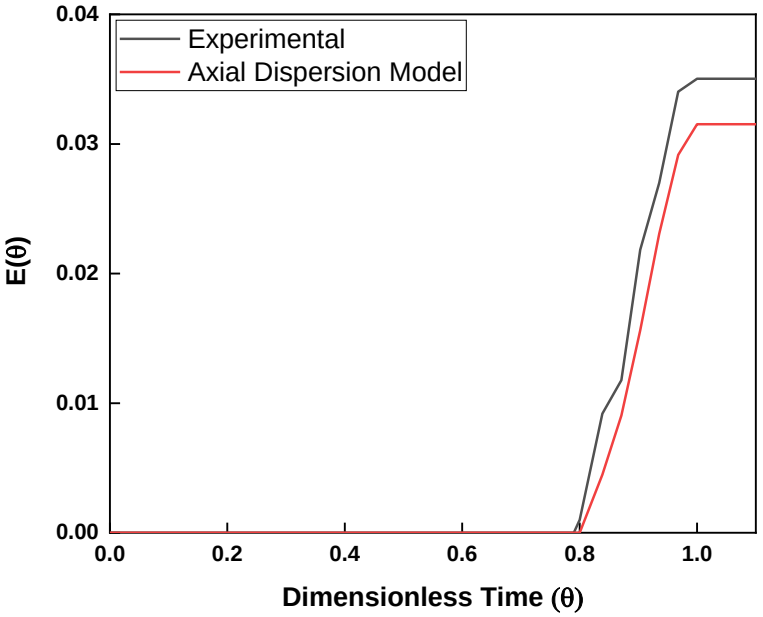

Figure 6.26. Comparison of results with experimental and calculated E-curves for CFIR with 3 inversions, an internal tube diameter of 4 mm and λ of 18.8 at a NRe = 250. The experimental values (black) were fitted with theoretical values (red) obtained from the ADM.

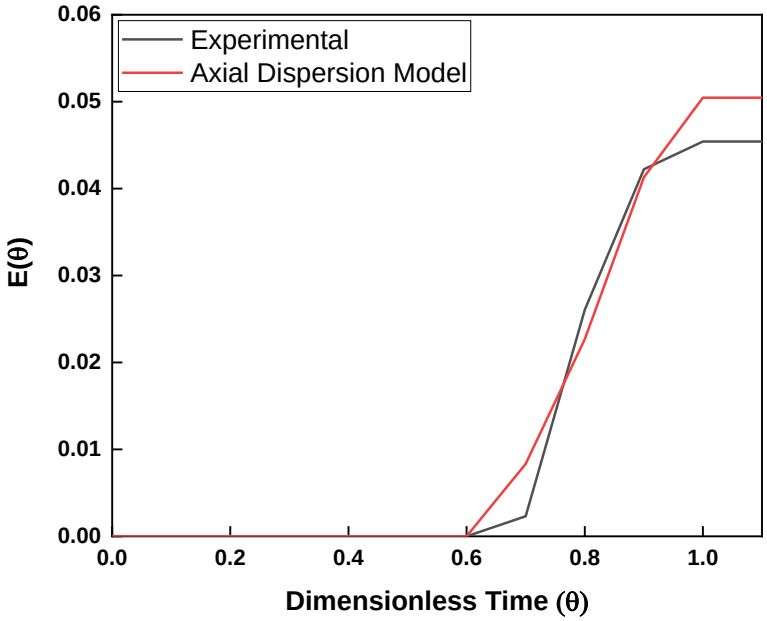

Figure 6.27. Comparison of results with experimental and calculated E-curves for CFIR with a total length of 1.9 m, an internal tube diameter of 4 mm and λ of 125.5 at a N_{Re} = 250. The experimental values (black) were fitted with theoretical values (red) obtained from the ADM.

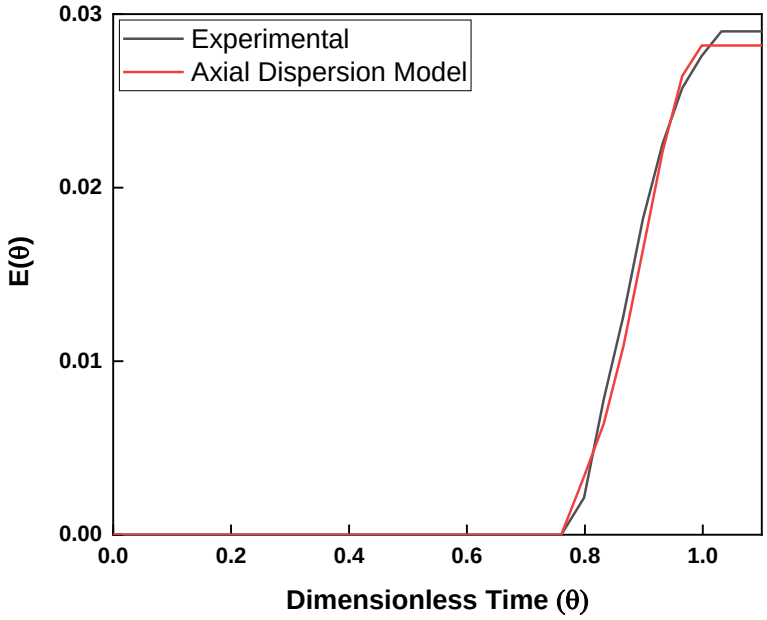

Figure 6.28. Comparison of results with experimental and calculated E-curves for CFIR with a total length of 7.8 m, an internal tube diameter of 4 mm and λ of 125.5 at a N_{Re} = 250. The experimental values (black) were fitted with theoretical values (red) obtained from the ADM.

Table 6.7. Axial dispersion related values for all the different geometries of each CFIR. The data is ordered by rising λ value. The dispersion values were calculated by fitting the ADM on the F-curves obtained from previous RTD results. The RTD was calculated by using NaCl as a tracer element by measuring the increase and decrease of conductivity (0 to 50% and 100% to 50%) at the end of the reactor.

Coil Dia.	External Tube Dia.	Internal Tube Dia.	λ	No. of Inversions	No. of Turns	Length	Flow Velocity	Flow Rate	N_{Re}	Dean Number	N_{Pe}	D/UL
(m)	(m)	(m)	(-)	(-)	(-)	(m)	(m/s)	(mL/min)	(-)	(-)	(-)	(-)
0.053	0.002	0.004	13.75	0	8	1.43	0.027	20	102.26	27.58	73.55	0.014
							0.046	35	178.95	48.26	74.21	0.013
							0.066	50	255.64	68.94	86.16	0.012
				1	16	2.87	0.027	20	102.26	27.58	84.30	0.012
							0.046	35	178.95	48.26	88.86	0.011
							0.066	50	255.64	68.94	91.88	0.011
				2	24	4.30	0.027	20	102.26	27.58	109.55	0.009
							0.046	35	178.95	48.26	114.22	0.009
							0.066	50	255.64	68.94	144.14	0.007
				3	32	5.73	0.027	20	102.26	27.58	118.27	0.008
							0.046	35	178.95	48.26	134.88	0.007
							0.066	50	255.64	68.94	158.58	0.006
0.068	0.002	0.004	17.5	0	8	1.81	0.027	20	102.26	24.44	56.55	0.018
							0.046	35	178.95	42.78	72.32	0.013
							0.066	50	255.64	61.11	77.55	0.013
				1	16	3.75	0.027	20	102.26	24.44	83.88	0.012
							0.046	35	178.95	42.78	96.55	0.010
							0.066	50	255.64	61.11	102.00	0.010
				2	24	5.70	0.027	20	102.26	24.44	90.57	0.011
							0.046	35	178.95	42.78	95.67	0.010
							0.066	50	255.64	61.11	128.41	0.008
				3	32	7.64	0.027	20	102.26	24.44	126.98	0.008
							0.046	35	178.95	42.78	137.88	0.007
							0.066	50	255.64	61.11	178.55	0.006
0.053	0.002	0.003	18.33333	0	8	1.42	0.047	20	140.42	32.80	56.07	0.018
							0.083	35	245.74	57.39	57.14	0.018

							0.118	50	351.06	81.99	63.22	0.016
				1	16	2.85	0.047	20	140.42	32.80	67.22	0.015
							0.083	35	245.74	57.39	77.55	0.013
							0.118	50	351.06	81.99	81.88	0.012
				2	24	4.29	0.047	20	140.42	32.80	88.00	0.011
							0.083	35	245.74	57.39	92.81	0.011
							0.118	50	351.06	81.99	123.74	0.008
				3	32	5.72	0.047	20	140.42	32.80	120.14	0.008
							0.083	35	245.74	57.39	136.55	0.007
							0.118	50	351.06	81.99	165.22	0.006
0.073	0.002	0.004	18.75	0	8	1.94	0.027	20	102.26	23.62	42.14	0.024
							0.046	35	178.95	41.33	45.88	0.022
							0.066	50	255.64	59.04	62.14	0.016
				1	16	3.88	0.027	20	102.26	23.62	77.53	0.013
							0.046	35	178.95	41.33	80.12	0.012
							0.066	50	255.64	59.04	86.01	0.012
				2	24	5.82	0.027	20	102.26	23.62	105.53	0.009
							0.046	35	178.95	41.33	111.81	0.009
							0.066	50	255.64	59.04	120.10	0.008
				3	32	7.77	0.027	20	102.26	23.66	123.23	0.008
							0.046	35	178.95	41.33	137.72	0.007
							0.066	50	255.64	59.04	174.54	0.006
0.068	0.002	0.003	23.33333	0	8	1.80	0.047	20	140.42	29.07	42.38	0.024
							0.083	35	245.74	50.87	37.41	0.027
							0.118	50	351.06	72.68	51.47	0.019
				1	16	3.74	0.047	20	140.42	29.07	59.91	0.017
							0.083	35	245.74	50.87	63.813	0.016
							0.118	50	351.06	72.68	80.51	0.012
				2	24	5.68	0.047	20	140.42	29.07	94.87	0.011
							0.083	35	245.74	50.87	101.42	0.010
							0.118	50	351.06	72.68	108.84	0.009

				3	32	7.63	0.047	20	140.42	29.07	109.98	0.010
							0.083	35	245.74	50.87	128.55	0.008
							0.118	50	351.056	72.68	168.75	0.006
0.073	0.002	0.003	25	0	8	1.92	0.047	20	140.42	28.08	33.41	0.030
							0.083	35	245.74	49.15	33.58	0.030
							0.118	50	351.06	70.21	43.86	0.023
				1	16	3.87	0.047	20	140.42	28.08	49.86	0.020
							0.083	35	245.74	49.15	53.88	0.019
							0.118	50	351.07	70.21	71.88	0.014
				2	24	5.81	0.047	20	140.42	28.08	83.96	0.012
							0.083	35	245.74	49.15	90.32	0.011
							0.118	50	351.06	70.21	99.32	0.010
				3	32	7.75	0.047	20	140.42	28.08	106.88	0.009
							0.083	35	245.74	49.15	118.55	0.008
							0.118	50	351.06	70.21	147.65	0.007

Table 6.8. Axial dispersion related values for all the different geometries of each HCR. The data is ordered by the rising λ value of their CFIR counterparts. The dispersion values were calculated by fitting the ADM on the F-curves obtained from previous RTD results. The RTD was calculated by using NaCl as a tracer element by measuring the increase and decrease of conductivity (0 to 50% and 100% to 50%) at the end of the reactor.

Coil Dia. (m)	External Tube Dia. (m)	Internal Tube Dia. (m)	λ (-)	Length (m)	Flow Velocity (m/s)	Flow Rate (mL/min)	N_{Re} (-)	Dean Number (-)	N_{Pe} (-)	D/UL (-)
0.5	0.002	0.004	125.5	1.4	0.026	20	102.26	9.13	25.64	0.110
					0.046	35	178.95	15.97	30.07	0.063
					0.066	50	255.64	22.82	42.07	0.044
				2.87	0.027	20	102.26	9.13	32.05	0.110
					0.046	35	178.95	15.97	44.52	0.063
					0.066	50	255.64	22.82	59.17	0.044
				4.30	0.027	20	102.26	9.13	39.65	0.110
					0.046	35	178.95	15.97	55.12	0.063
					0.066	50	255.64	22.82	79.41	0.044
				5.73	0.027	20	102.26	9.13	71.07	0.110
					0.046	35	178.95	15.97	78.17	0.063
					0.066	50	255.64	22.82	93.05	0.044
0.5	0.002	0.004	125.5	1.81	0.027	20	102.26	9.13	36.41	0.110
					0.046	35	178.95	15.97	39.43	0.063
					0.066	50	255.64	22.82	41.41	0.044
				3.75	0.027	20	102.26	9.13	38.74	0.110
					0.046	35	178.95	15.97	48.83	0.063
					0.066	50	255.64	22.82	57.41	0.043
				5.70	0.027	20	102.26	9.13	73.07	0.110
					0.046	35	178.95	15.97	90.07	0.063
					0.066	50	255.64	22.82	92.12	0.044
				7.64	0.027	20	102.26	9.13	111.74	0.110
					0.046	35	178.95	15.97	113.41	0.063
					0.066	50	255.64	22.82	132.74	0.044
0.5	0.002	0.003	167.3	1.42	0.047	20	140.42	10.86	21.33	0.092
					0.083	35	245.74	19.00	26.38	0.053

					0.118	50	351.06	27.14	33.85	0.037
				2.85	0.047	20	140.42	10.86	30.89	0.092
					0.083	35	245.74	19.00	38.82	0.053
					0.118	50	351.06	27.14	39.91	0.037
				4.29	0.047	20	140.42	10.86	55.17	0.092
					0.083	35	245.74	19.00	59.39	0.053
					0.118	50	351.06	27.14	71.30	0.037
				5.72	0.047	20	140.42	10.86	59.17	0.091
					0.083	35	245.74	19.00	77.44	0.053
					0.118	50	351.06	27.14	98.11	0.037
0.5	0.002	0.004	125.5	1.94	0.027	20	102.26	9.13	25.00	0.110
					0.046	35	178.95	15.97	45.41	0.063
					0.066	50	255.64	22.82	49.12	0.044
				3.88	0.027	20	102.26	9.13	56.17	0.101
					0.046	35	178.95	15.97	60.55	0.063
					0.066	50	255.64	22.82	62.88	0.044
				5.82	0.027	20	102.26	9.13	71.05	0.110
					0.046	35	178.95	15.97	85.67	0.063
					0.066	50	255.64	22.82	93.33	0.044
				7.77	0.027	20	102.26	9.13	110.33	0.110
					0.046	35	178.95	15.97	112.69	0.063
					0.066	50	255.64	22.82	135.12	0.044
0.5	0.002	0.003	167.3	1.80	0.047	20	140.42	10.86	23.48	0.092
					0.083	35	245.74	19.00	32.39	0.053
					0.118	50	351.06	27.14	31.43	0.037
				3.74	0.047	20	140.42	10.86	40.17	0.092
					0.083	35	245.74	19.00	52.22	0.053
					0.118	50	351.06	27.14	62.78	0.037
				5.68	0.047	20	140.42	10.86	53.55	0.092
					0.083	35	245.74	19.00	85.15	0.053
					0.118	50	351.06	27.14	98.80	0.037

				7.63	0.047	20	140.42	10.86	90.82	0.092
					0.083	35	245.74	19.00	123.14	0.053
					0.118	50	351.06	27.14	122.20	0.037
0.5	0.002	0.003	167.3	1.92	0.047	20	140.42	10.86	38.72	0.092
					0.083	35	245.74	19.00	25.00	0.053
					0.118	50	351.06	27.14	35.81	0.037
				3.87	0.047	20	140.42	10.86	45.53	0.092
					0.083	35	245.74	19.00	58.13	0.053
					0.118	50	351.06	27.14	74.46	0.037
				5.81	0.047	20	140.42	10.86	73.22	0.092
					0.083	35	245.73	19.00	83.53	0.053
					0.118	50	351.07	27.14	96.48	0.037
				7.75	0.047	20	140.42	10.86	104.53	0.092
					0.083	35	245.74	19.00	114.87	0.053
					0.118	50	351.06	27.14	134.55	0.037

Table 6.9. Axial dispersion related values for all the different geometries of each SMR. The data is ordered length. The dispersion values were calculated by fitting the ADM on the F-curves obtained from previous RTD results. The RTD was calculated by using NaCl as a tracer element by measuring the increase and decrease of conductivity (0 to 50% and 100% to 50%) at the end of the reactor.

Internal Tube Dia. (m)	No. of Elements (-)	Length (m)	Flow Velocity (m/s)	Flow Rate (mL/min)	N_{Re} (-)	N_{Pe} (-)	D/UL (-)
0.01	12	0.03	0.001	20	10.58	17.41	0.057
			0.002	35	18.52	24.45	0.041
			0.003	50	26.46	22.49	0.044
	24	0.06	0.001	20	10.58	29.49	0.034
			0.002	35	18.52	39.07	0.026
			0.003	50	26.46	29.85	0.033
	36	0.09	0.001	20	10.58	58.45	0.017
			0.002	35	18.52	68.04	0.015
			0.003	50	26.46	65.65	0.015
	48	0.12	0.001	20	10.58	102.41	0.010
			0.002	35	18.52	77.92	0.013
			0.003	50	26.46	83.32	0.012

6.4.5 Dispersion in Reactors

In the following sections, the effect of different design and operational parameters (λ, n and N_{Re}) on the cross-sectional mixing performances of CFIRs, SRs and SMRs is discussed thoroughly.

6.4.5.1 Curvature Ratio Effect

The effect of λ was explored by comparing the 6 different CFIRs and 2 HCRs with different λ. As mentioned before, the effect of the reduction λ on HCRs and CFIRs has a positive effect on the cross-sectional mixing on the radius of curvature (λ has an inverse effect on centrifugal force inside the tube). The flow rate was used was 20, 35 and 50 mg/mL, these flow rates are translated to 3 different N_{Re} for each internal coil tube diameter (100, 180 and 250 for 4 mm and 140, 250 and 350 for 3 mm). Figures 6.29 to 6.32 shows the relation between the N_{Pe} and N_{Re} over different λ at established inversions, while Figure 6.33 shows the relation between the N_{Pe} and length for all different N_{Re}.

For fixed flow inversion, there was an inverse relationship between λ and N_{Pe}. These results agreed with the broad conclusion that a reduction in the λ brings an increase of cross-sectional mixing due to increased centrifugal forces (L. Sharma, Nigam, and Roy 2017). The CFIRs with λ of 13.8 and 18.3 performed worse in comparison to the other CFIRs as the number of inversions are raised. These was due to the length of the CFIRs as the number of inversions increased, the longer the residence time the higher the N_{Pe}. However, the difference was still visible among the CFIRs with comparable length (Figure 6.33).

The difference in internal coiled tube diameter (3 and 4 mm) in CFIRs had no major effect on the N_{Pe}. It has been reported that an increase in tube diameter contributes to the axial dispersion if all parameters are kept similar or constant. However, the effects are not considered significant and were not clearly visible from these studies (Klutz et al. 2015). Also, the reduction in λ might have somewhat mitigated that negative effect.

For fixed flow inversion, the magnitude of N_{Pe} increases with decreasing λ, which becomes more significant with as N_{Re} increases. This happens because the secondary flows are less dominant and capable of influencing the cross-mixing effect, while they become more influential at higher N_{Re}. In other words, the magnitude of N_{Pe} increases significantly with increasing N_{Re} for a given configuration of λ, length, turns and inversions. This trend agreed with the data reported for other HCRs at N_{Re} ranging in the laminar and turbulent flow region (Kumar, Aggarwal, and Nigam 2006; L. Sharma, Nigam, and Roy 2017)

The N_{Pe} values for all equivalent HCRs were collected and contrasted according to the internal coiled tube diameter and their respective N_{Re}. The λ are 125.5 and 167.3 for the internal tube diameter of 4 and 3 mm. The difference on λ had no relevant effect on the N_{Pe}. The magnitude in N_{Re} and length of the SR had the most significant effect on the N_{Pe}, this dependence seemed to be linear. The λ, even if it is larger than 100, does have an impact on the reduction of the axial dispersion. It has been reported that it is required to have a De > 3 to have a significant cross-mixing improvement in the flow path (Klutz et al. 2015). The De for this HCRs has an approximate minimum and maximum value of 10 and 25. The magnitude of the De does not necessarily mean a superior axial dispersion reduction. The N_{Re} magnitude for equivalent lengths in the CFIRs was significantly lower but this point is further discussed in Section 6.4.5.2.

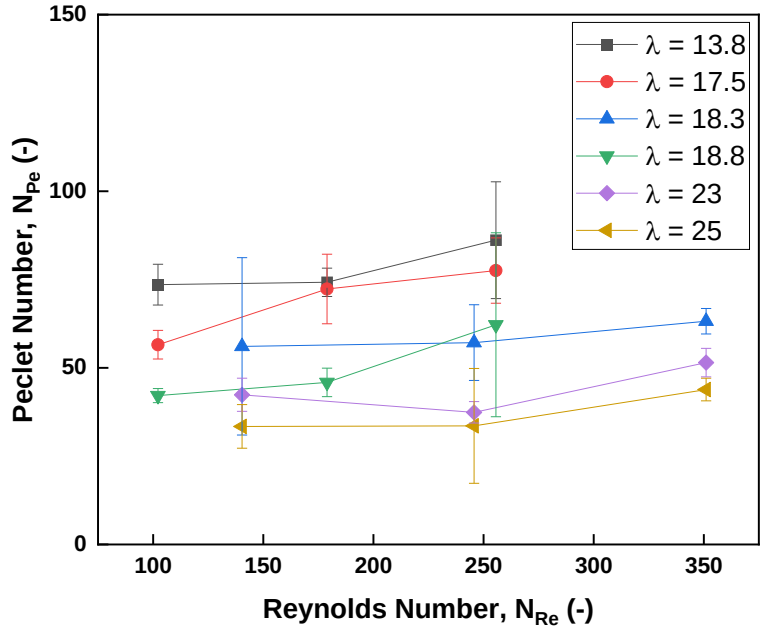

Figure 6.29. Effect of λ on N_{Pe} on different N_{Re} for CFIR with an internal coiled tube diameter of 3 mm (λ of 18.3, 23.3, 25) and 4 mm (λ of 13.8, 17.5 and 18.8) and 0 inversions. N_{Pe} were derived from the fitting of the ADM to the RTD experiments result values. The error bars represent the standard deviation of the samples (n=3).

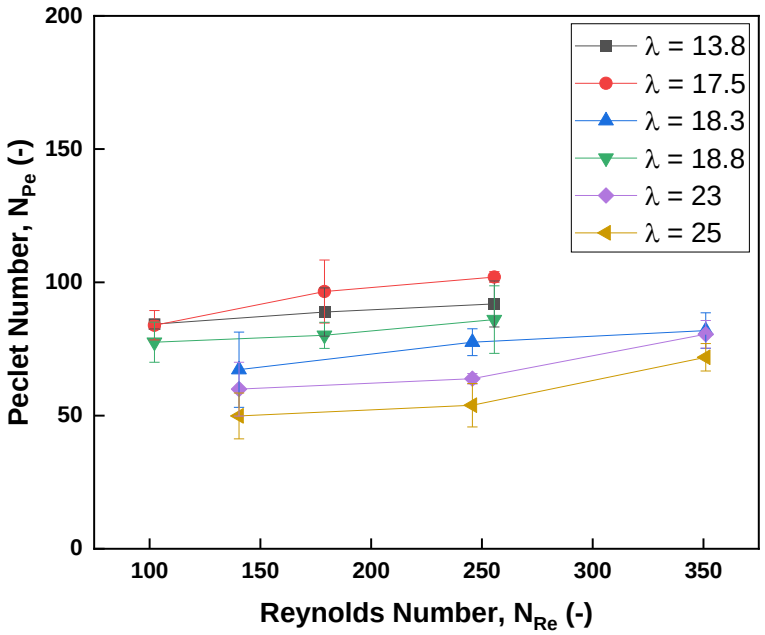

Figure 6.30. Effect of λ on N_{Pe} on different N_{Re} for CFIR with an internal coiled tube diameter of 3 mm (λ of 18.3, 23.3, 25) and 4 mm (λ of 13.8, 17.5 and 18.8) and 1 inversion. N_{Pe} were derived from the fitting of the ADM to the RTD experiments result values. The error bars represent the standard deviation of the samples (n=3).

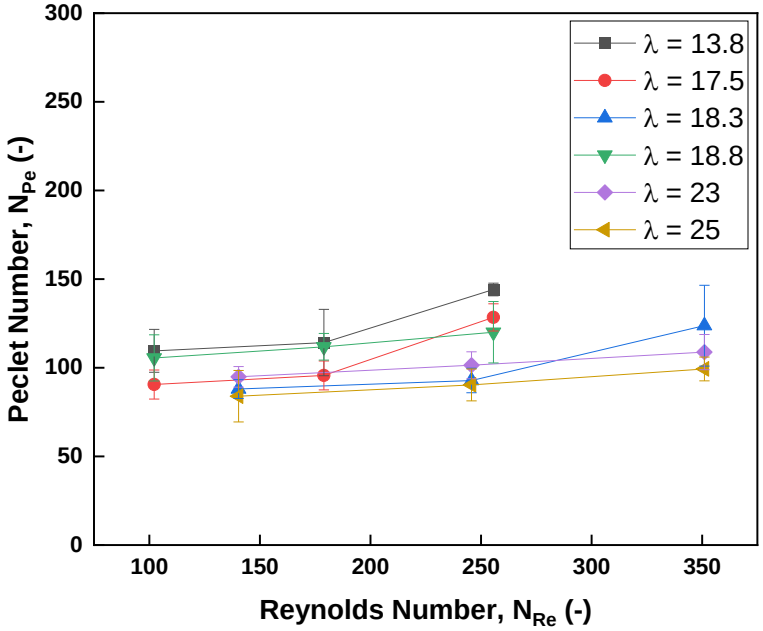

Figure 6.31. Effect of λ in N_{Pe} on different N_{Re} for CFIR with an internal coiled tube diameter of 3 mm (λ of 18.3, 23.3, 25.0) and 4 mm (λ of 13.8, 17.5 and 18.8) and 2 inversions. N_{Pe} were derived from the fitting of the ADM to the RTD experiments result values. The error bars represent the standard deviation of the samples (n=3).

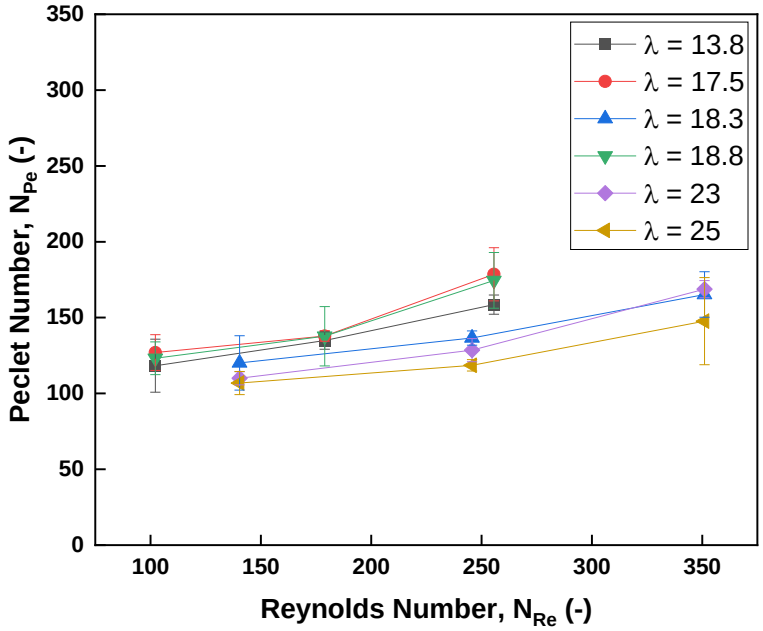

Figure 6.32. Effect of λ on N_{Pe} on different N_{Re} for CFIR with an internal coiled tube diameter of 3 mm (λ of 18.3, 23.3, 25) and 4 mm (λ of 13.8, 17.5 and 18.8) and 3 inversions. N_{Pe} were derived from the fitting of the ADM to the RTD experiments result values. The error bars represent the standard deviation of the samples (n=3).

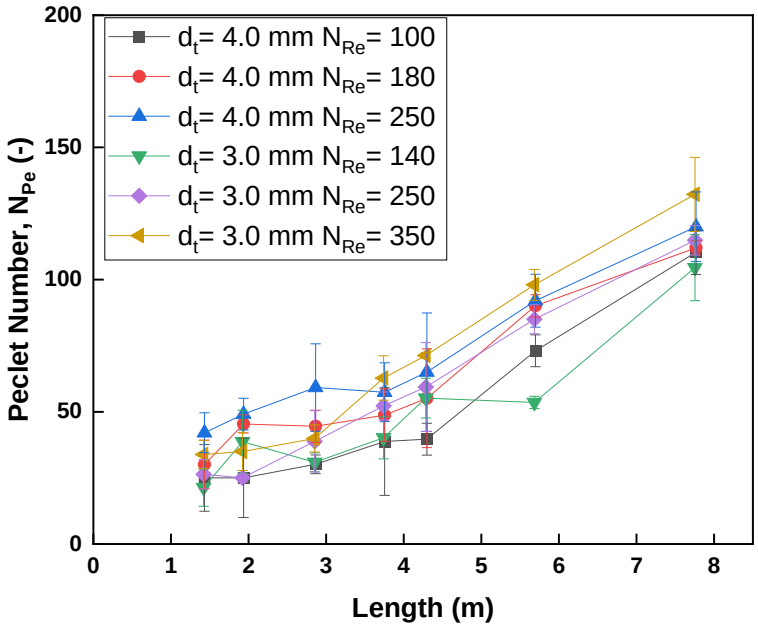

Figure 6.33. Effect of λ and N_{Re} on N_{Pe} at different lengths for HCR with an internal coiled tube diameter of 3 mm (λ of 167.3) and 4 mm (λ of 125.5). N_{Pe} were derived from the fitting of the ADM to the RTD experiments result values. The error bars represent the standard deviation of the samples (n=3).

6.4.5.2 Number of Inversions Effect

The CFIR design offers successive 90° bends to straight helical coils causing a shift in the stream line involved in the Dean vortices in order to reduce axial dispersion (Saxena and Nigam 1984; L. Sharma, Nigam, and Roy 2017). Figure 6.34 to 6.39 show the variation of N_{Pe} recorded after each inversion for each CFIR at 3 different N_{Re} for each internal coiled tube diameter (flow rates of 20, 30 and 50 mL/min). The inclusion of an inversion to the λ also meant the inclusion of 8 more turns, increasing the overall length of the reactor. The difference in length (as mentioned before) is mainly a factor at the higher number of inversions for the λ of 13.8 and 18.3. In this case the inversion and added length had a positive impact on the cross-sectional mixing.

For all N_{Re}, there was a sharp trend of the N_{Pe} to increasing as the CFIR increased in number of inversions. The magnitude of the N_{Pe} increase was significantly higher as the N_{Re} and the λ increased; i.e. CFIR with λ of 13.8 and a N_{Re} of 100 has an overall increase of 61% after 3 inversions while the CFIR with λ 18.8 and N_{Re} 100 has 192.3% after 3 inversions. As seen in the previous results sections in this chapter, the reduced

λ and the rise in N_{Re} have a positive effect on the N_{Pe}. This parameter represents the correlation between the convective and diffusive transport phenomena. The convective transport phenomena depend on the magnitude of the secondary flow in the liquid. As the Dean vortices mature and dominate the flow profile, the axial dispersion is reduced. At low mean flow rate (velocity), the effect of secondary flow is not strong enough. However, with an increasing flow rate (velocity), it induces a stronger cross-sectional mixing. This trend has been observed in the past with similar N_{Re}, the inclusion of inversions into the flow path causes a better mixing overall. All the CFIR data falls under the linear variation of N_{Pe} with N_{Re}. This linear variation stops at around N_{Re} = 2,000 (end of laminar flow), as the effective strength of secondary flow is successfully enhancing the radial mixing in the laminar flow. Beyond this point, the axial dispersion caused by the elevated N_{Re} offsets the benefits of the Dean vortices and the magnitude increase of N_{Pe} gets significantly reduced. This second behaviour could not be explored as the flow rates needed to achieve N_{Re} of up to 8,000 would require copious amounts of material, more specialised sensory devices and was out of scope (L. Sharma, Nigam, and Roy 2017).

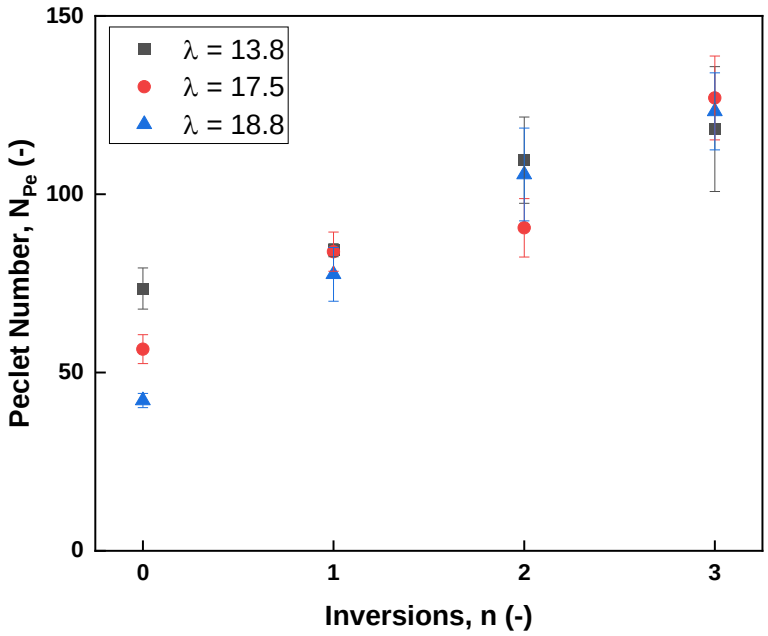

Figure 6.34. Effect of inversions on N_{Pe} for CFIR with an internal coiled tube diameter of 4 mm, with λ of 13.8 (black), 17.5 (red) and 18.8 (blue), and N_{Re} of 100. The N_{Pe} values were derived from the fitting of the ADM to the RTD experiments result values. The error bars represent the standard deviation of the samples (n=3).

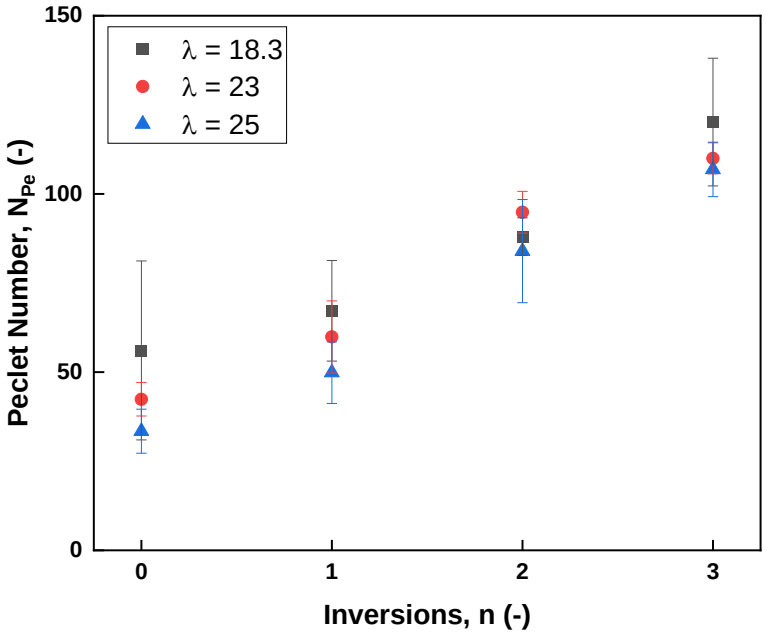

Figure 6.35. Effect of inversions on N_{Pe} for CFIR with an internal coiled tube diameter of 4 mm, with λ of 18.3 (black), 23.3 (red) and 25 (blue), and N_{Re} of 140. The N_{Pe} values were derived from the fitting of the ADM to the RTD experiments result values. The error bars represent the standard deviation of the samples (n=3).

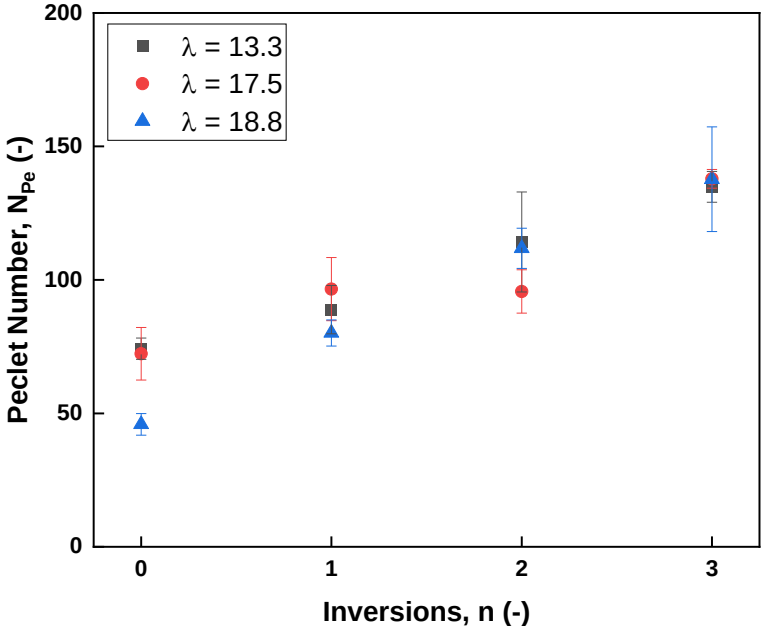

Figure 6.36. Effect of inversions on N_{Pe} for CFIR with an internal coiled tube diameter of 4 mm, with λ of 13.8 (black), 17.5 (red) and 18.8 (blue), and N_{Re} of 180. The N_{Pe} values were derived from the fitting of the ADM to the RTD experiments result values.

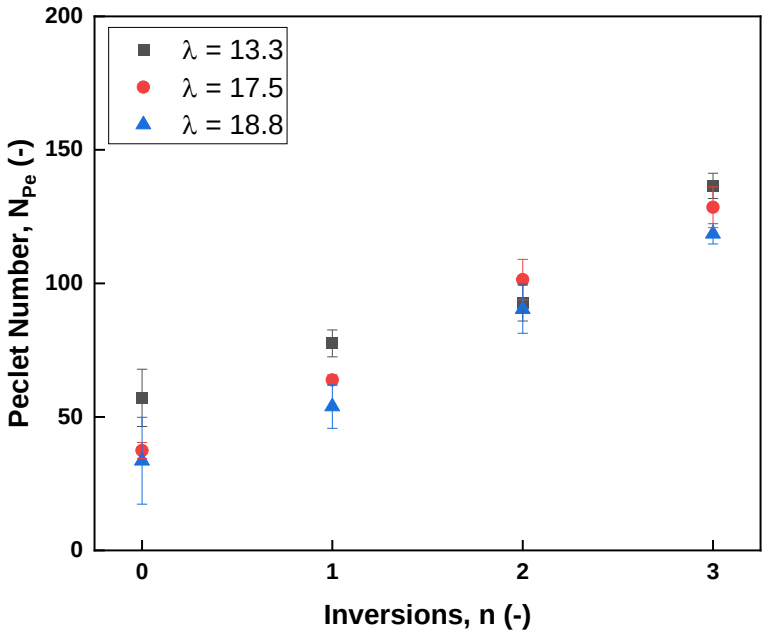

Figure 6.37. Effect of inversions on N_{Pe} for CFIR with an internal coiled tube diameter of 4 mm, with λ of 18.3 (black), 23.3 (red) and 25 (blue), and N_{Re} of 245. The N_{Pe} values were derived from the fitting of the ADM to the RTD experiments result values. The error bars represent the standard deviation of the samples (n=3).

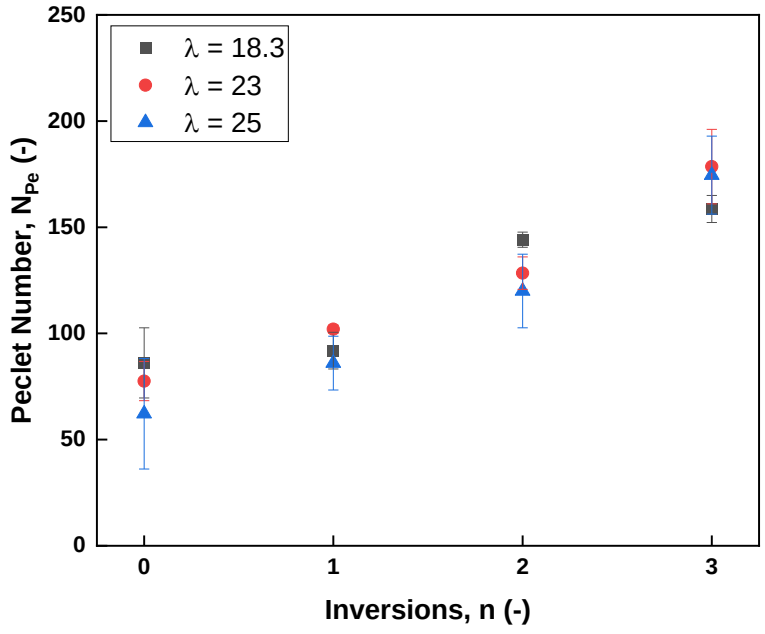

Figure 6.38. Effect of inversions on N_{Pe} for CFIR with an internal coiled tube diameter of 4 mm, with λ of 13.8 (black), 17.5 (red) and 18.8 (blue), and N_{Re} of 255. The N_{Pe} values were derived from the fitting of the ADM to the RTD experiments result values. The error bars represent the standard deviation of the samples (n=3).

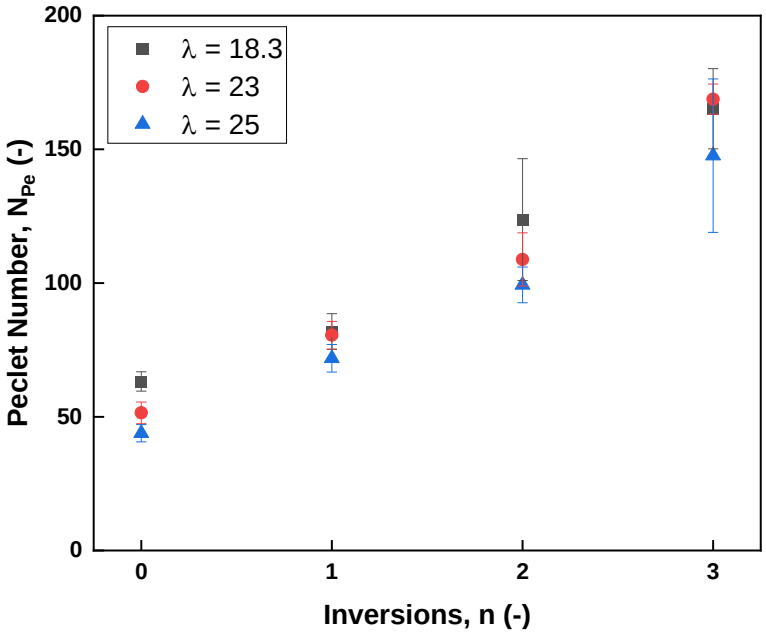

Figure 6.39. Effect of inversions on N_{Pe} for CFIR with an internal coiled tube diameter of 4 mm, with λ of 18.3 (black), 23.3 (red) and 25 (blue), and N_{Re} of 350. The N_{Pe} values were derived from the fitting of the ADM to the RTD experiments result values. The error bars represent the standard deviation of the samples (n=3).

6.4.5.3 Type of Reactor Effect

HCRs have been explored for mixing due to the combined contribution of secondary flow and Dean vortices. The introduction of a 90° flow inversion, causing a rotation of these Dean vortices by 90°, provides discrete planes of mixing because of the interchange of velocities of different ages due to the shift of centrifugal force. The mixing induced in a CFIR is more than of a straight HCR with the same length of coiled tube (Soni et al. 2019; Saxena and Nigam 1984). The N_{Pe} of CFIRs was compared with HCRs counterparts, matching the CFIRs in length and internal coiled tube diameter. Figures 6.40 to 6.45 show the relationship of N_{Pe} to the coiled tube length for comparison between CFIRs and HCRs with fixed λ.

From all CFIRs and HCRs, as the length and N_{Re} were raised, the N_{Pe} increased as well. It can clearly be seen how the lengths or RT of the reactor affects the cross-sectional mixing in a positive manner in both geometries. As seen in Section 6.4.4, the centrifugal force acting upon the fluid increases the development of secondary flows.

According to all the figures, it is clear how the CFIR are the better option at reducing the axial dispersion but the magnitude varies among the λ. The CFIRs are most effective when the λ is minimised as their secondary flow patterns are more dominant at lower N_{Re} and lengths. Though, as the λ is increased, the effectiveness of the CFIR geometry starts to plateau to the point where the HCR showed to be somewhat competitive at higher N_{Re} and lengths. This can be seen with CFIR with a λ 13.8 at N_{Re} of 250 that is on average 80% more effective than its HCR counterpart, whilst CFIR with a λ 25 at N_{Re} of 250 is on average 8.6% more effective. Related to this, the CFIRs with increased λ have a steeper slope compared to the ones with reduced λ. This is also explained by the fact that CFIR with reduced λ benefit from the geometry design since the very beginning of the flow path, while the reactors with increased λ mostly relied on the prolonged flow to achieve a substantial improvement (similar to the HCR behaviour).

Figure 6.46 and 6.47 displayed the results concerning the SMRs in terms of length and N_{Re}. At fixed N_{Re}, the N_{Pe} increased, as what it seems, an exponential trend as more static mixer modules were connected to increase its length, each module added 12 elements. The increase was measured to be of 446.6%, 483.1% and 547.8% for N_{Re} of 10, 18 and 26, respectively. The exponential behaviour seemed to be steeper than any other reactor, probably caused by the physical elements passively creating disturbances on the liquid flow. In fixed SMRs lengths, it seems that the increase of N_{Re} under the same length is not as impactful as the length increase. The increase of N_{Re} with fixed length was recorded to be 44.9% for 0.3 m and 71.7% for 1.2 m. It seemed that increasing the length of the SMR had a more significant impact on N_{Pe} than increasing the N_{Re}. According to these results, the best route to create a more efficient SMR is to increase the length before increasing the liquid velocity. For both comparisons, the N_{Pe} magnitude was not comparable to the CFIRs or HCRs, due to the lower N_{Re} used due to the limitation of resources and footprint in the working space. Even though the operational conditions for SMRs are not homologous to the ones used for CFIR/HCR, some conclusions can be drawn from the data presented here.

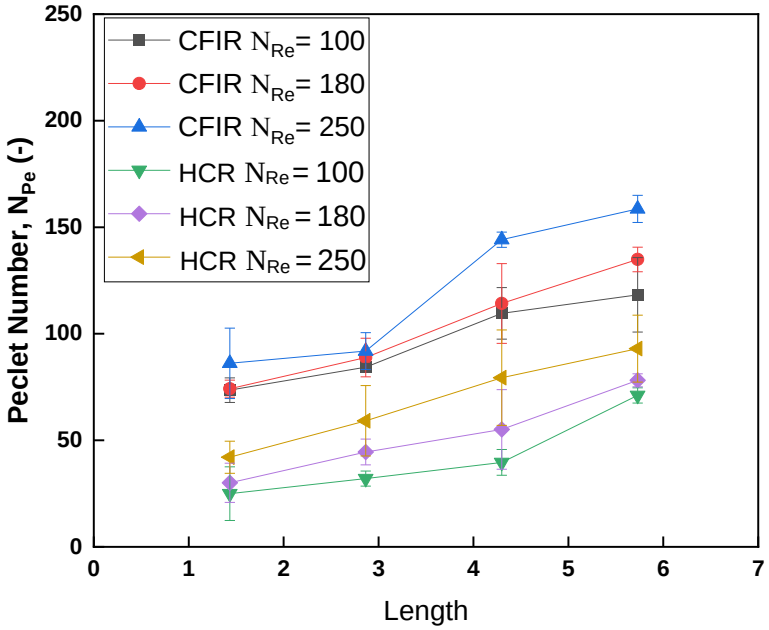

Figure 6.40. Effect of type of reactor on N_{Pe} with a λ of 13.8 (CFIR) or 125.5 (HCR) and an internal coiled tube diameter of 4 mm at different N_{Re}. Each point for the CFIRs represent an added inversion (from 0 to 3), while for the HCR it only represents added overall length. The N_{Pe} values were derived from the fitting of the ADM to the RTD experiments result values. The error bars represent the standard deviation of the samples (n=3).

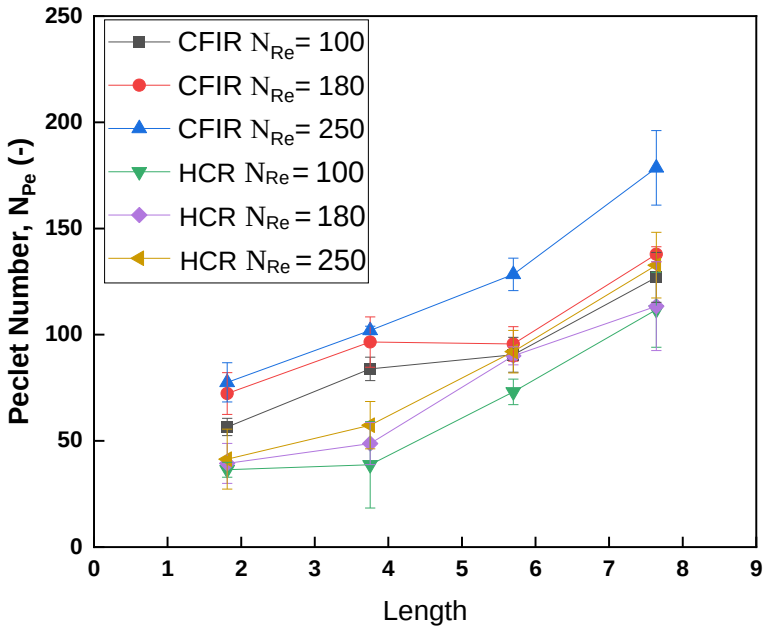

Figure 6.41. Effect of type of reactor on N_{Pe} with a λ of 17.5 (CFIR) or 125.5 (HCR) and an internal coiled tube diameter of 4 mm at different N_{Re}. Each point for the CFIRs represent an added inversion (from 0 to 3), while for the HCR it only represents added overall length. The N_{Pe} values were derived from the fitting of the ADM to the RTD experiments result values. The error bars represent the standard deviation of the samples (n=3).

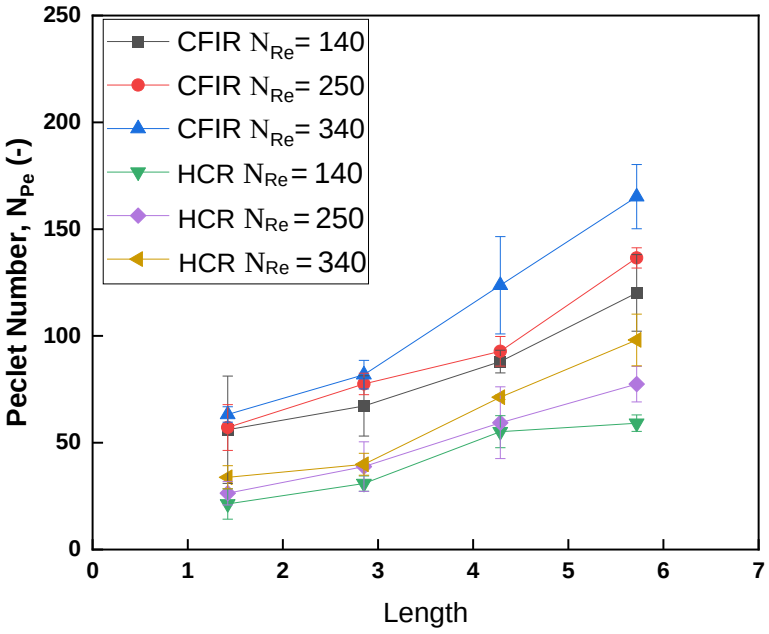

Figure 6.42. Effect of type of reactor on N_{Pe} with a λ of 18.3 (CFIR) or 167.3 (HCR) and an internal coiled tube diameter of 3 mm on at different N_{Re}. Each point for the CFIRs represent an added inversion (from 0 to 3), while for the HCR it only represents added overall length. The N_{Pe} values were derived from the fitting of the ADM to the RTD experiments result values. The error bars represent the standard deviation of the samples (n=3).

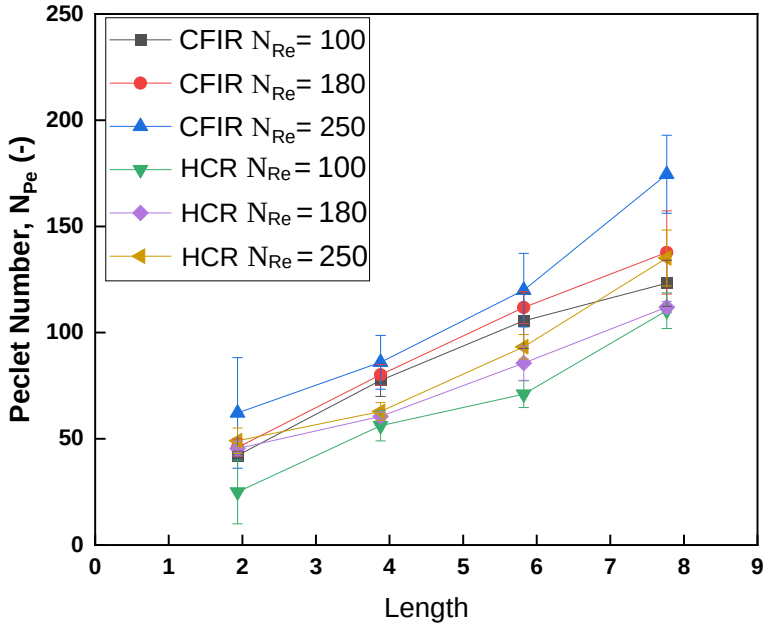

Figure 6.43. Effect of type of reactor on N_{Pe} with a λ of 18.8 (CFIR) or 125.5 (HCR) and an internal coiled tube diameter of 4 mm at different N_{Re}. Each point for the CFIRs represent an added inversion (from 0 to 3), while for the HCR it only represents added overall length. The N_{Pe} values were derived from the fitting of the ADM to the RTD experiments result values. The error bars represent the standard deviation of the samples (n=3).

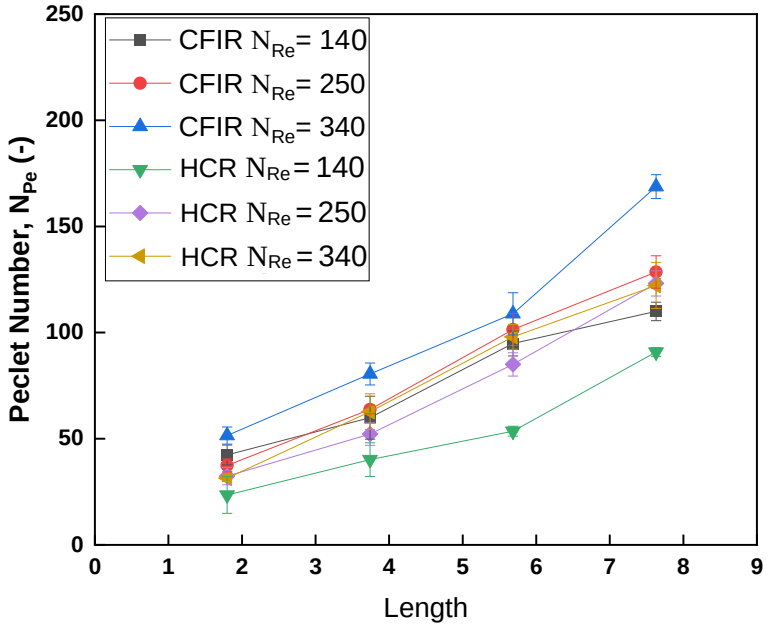

Figure 6.44. Effect of type of reactor on N_{Pe} with a λ of 23.3 (CFIR) or 167.3 (HCR) and an internal coiled tube diameter of 3 mm at different N_{Re}. Each point for the CFIRs represent an added inversion (from 0 to 3), while for the HCR it only represents added overall length. The N_{Pe} values were derived from the fitting of the ADM to the RTD experiments result values. The error bars represent the standard deviation of the samples (n=3).

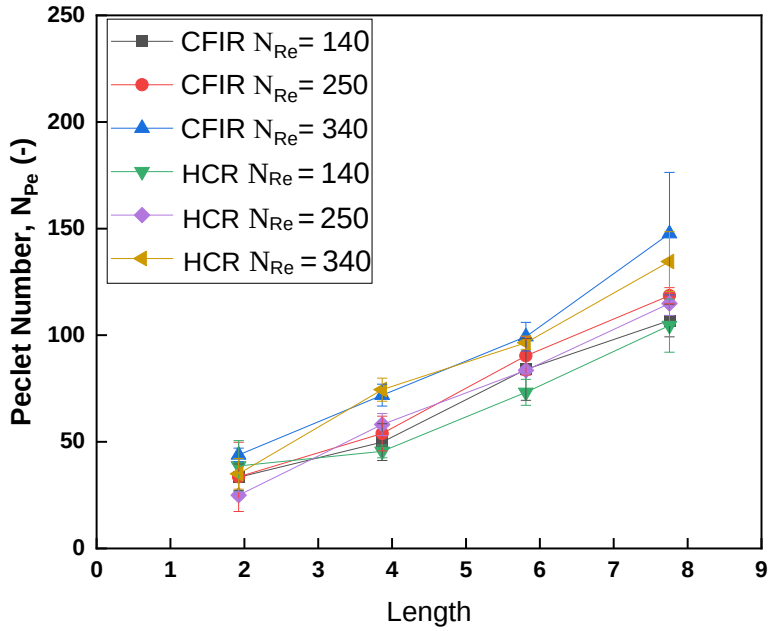

Figure 6.45. Effect of type of reactor on N_{Pe} with a λ of 25 (CFIR) or 167.3 (HCR) and an internal coiled tube diameter of 3 mm at different N_{Re}. Each point for the CFIRs represent an added inversion (from 0 to 3), while for the HCR it only represents added overall length. The N_{Pe} values were derived from the fitting of the ADM to the RTD experiments result values. The error bars represent the standard deviation of the samples (n=3).

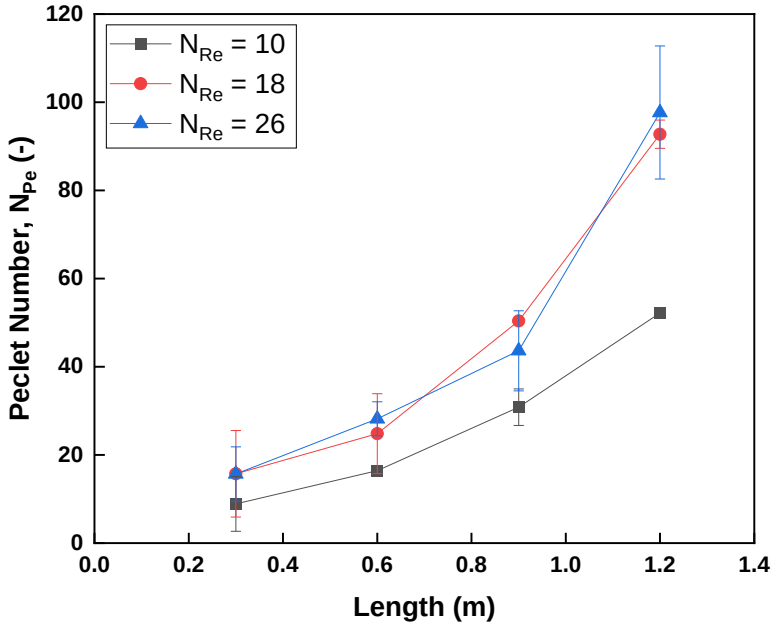

Figure 6.46. Effect of length on N_{Pe} in 3 different N_{Re} operational conditions with SMRs of 0.3 to 1.2 m in length, each 0.3 m module had 12 elements. The N_{Pe} values were derived from the fitting of the ADM to the RTD experiments result values. The error bars represent the standard deviation of the samples (n=3).

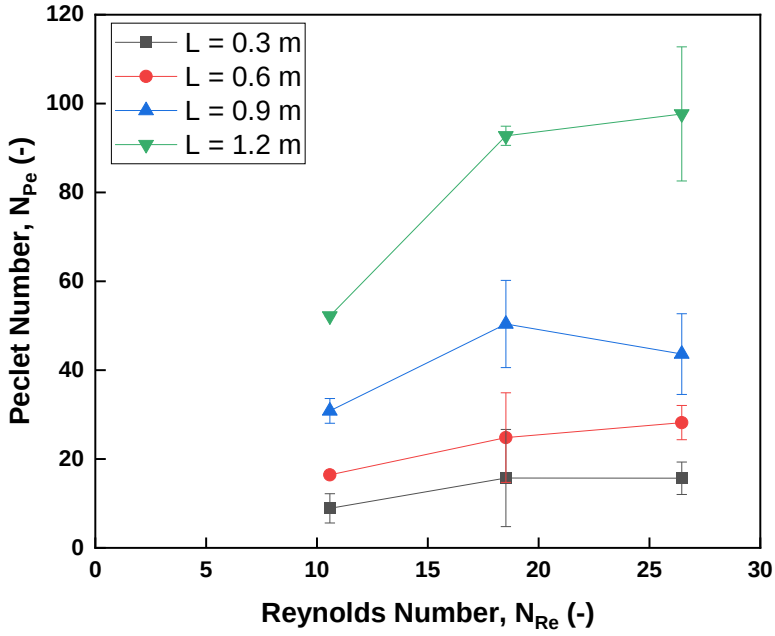

Figure 6.47. Effect of N_{Re} on N_{Pe} with SMRs of 0.3 to 1.2 m in length, each 0.3 m module had 12 elements. The N_{Pe} values were derived from the fitting of the ADM to the RTD experiments result values. The error bars represent the standard deviation of the samples (n=3).

6.4.6 Batch Binding Capacity in Reactors

In the following sections, the BBC in each type of reactor (CFIR, HCR and SMR) versus the length, the RT and the N_{Pe} is thoroughly discussed. The comparison between the ideal theoretical BBC values versus the experimental values is also presented at the end of this section. The BBC was obtained using the methodology explained in Section 2.19.

6.4.6.1 Batch Binding Capacity Vs Length

As seen in Section 6.4.5, increased length has a positive effect on the reduction of the axial dispersion. Figures 6.48 to 6.53 display the comparison between the normalised BBC against the length of each CFIR and HCR according to their N_{Re} (100, 180 and 250 for 4 mm and 140, 250 and 350 for 3 mm). Figure 6.54 shows such relationship with SMR in N_{Re} of 10, 18 and 26. Each one of the N_{Re} levels represent a flow rate of 20, 35 and 50 mL/min. Figure 6.55 shows the contrast in length efficiency between the CFIRs with the lowest and highest λ (13.8 and 25), the equivalent HCRs and the SMRs.

For all N_{Re}, the CFIRs with the lowest λ showed the highest BBC values; while the HCRs showed a relative similarity in BBC as they shared the same λ of 125.5 and 167.3 with their only difference being the length between each other. This can be clearly seen in Figure 6.48 and 6.51, all three HCRs show the same trend and magnitude. It can be deduced that the BBC was positively affected by the length and the effect is enhanced by the inclusion of inversions and reduced λ. This agreed with the results found in Section 6.4.5 as for increased lengths/inversions a better mixing in the flow path which at the same time propitiates the contact between the chromatography resin and the target molecule in the mobile phase.

Almost all CFIRs in every length and N_{Re} were superior by having an approximate difference of BBC of 20% to 70% between the CFIRs and their equivalents. The overall lowest difference in BBC between CFIRs and HCRs was found in λ of 23.3 and 25. This trend could be correlated to the dispersion number (Section 6.4.5) as the reactors with the highest N_{Pe} performed better in terms of BBC. This suggested that as the N_{Re} and length increased, the effectiveness in terms of BBC of the CFIRs becomes less apparent. The appropriate cross sectional mixing can only assure the bead is in

contact with the BSA. However, the adsorption and saturation of the chromatography media happens mainly in two ways of interaction: the external mass transfer between the surface and the protein, and the diffusion of the molecules into the pores of the bead. At the entrance of the reactor, the external mass transfer is the main way of interaction that acts at an accelerated rate as it depends on the contact between the resin and the BSA, propitiated by an effective cross-sectional mixing. After traveling through the reactor, the diffusion is the main way of interaction as the external ligands have already been saturated. The interaction dependent on diffusion happens at a constant rate, independent of effective mixing outside the resin bead. For this reason, the enhanced mixing of the CFIR starts to become not as impactful for the adsorption of the protein inside the resin bead at extended lengths (also translated into RT). Appropriate mixing is always required as the molecules always need to be in contact with the resin bead in order to start to diffuse into the bead, but this last part almost solely depends on the diffusion and adsorption rate.

Figure 6.54 shows the BBC against length inside SMRs at three different flow rates. The N_{Re} with the lowest value (10) showed a steeper curve during the first 0 to 0.6 m compared to the other two (18 and 26). Nevertheless, all the BBC for all N_{Re} converged at θ_{BBC}=0.9 at 0.9 m with an error of less than 5%. All of the N_{Re} reached an absorption of 1 after 1.2 m. SMRs with the lowest N_{Re} and lengths outperformed the other flow velocities as these operational parameters reduced the axial dispersion by providing enough RT for a better adsorption. The mid- and higher N_{Re} would require a longer length to fully develop an effective cross mixing and enough RT for the BSA to interact with the resin bead. After 0.9 m, it seemed that the higher N_{Re} conditions developed reach an optimum point between cross-mixing and length/RT in order to achieve comparable results. Another factor that can contribute with the higher BBC values at shorter lengths would be the settling of the resin inside the SMR. The resin beads had the tendency to settle around the elements of the SMR at lower flow velocities, giving each individual bead a longer RT than the one that can be measured.

Disregarding N_{Re}, Figure 6.55 shows the normalised BBC values of the SMR, CFIR with λ values of 13.8 and 25 and its HCR equivalents. At first glance, the BBC measured from the SMR at any of the lengths eclipsed the results from all the other reactors. The SMR achieves a BBC of 1 at only 15% and 20% of the total length of the other reactors. CFIRs achieve high efficiency rates after a certain number of turns

and lengths; inherently making the CFIR a worse option in terms of raw length. However, this length does not take into account the compactness of the reactors, which might even give CFIRs an advantage if optimised correctly by having a shorter coil or asymmetrical coil (Soni et al. 2019). It can also be noted that the reactor with λ 25 is barely reaches a BBC of 0.7 even being 2 m longer than the one with λ 13.8. The CFIR with better axial dispersion reduction achieved a higher BBC as it helps achieve a faster saturation of the bead by propitiating an early contact between the matrix and the BSA.

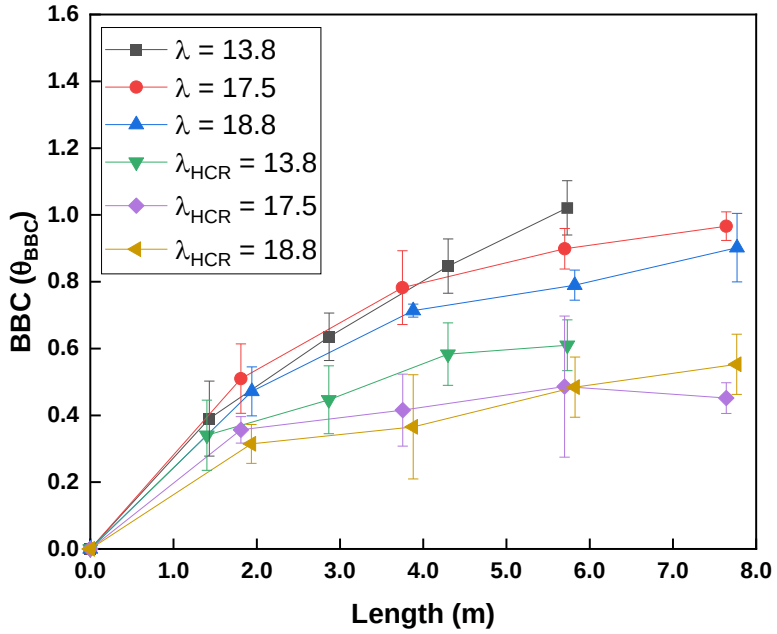

Figure 6.48. Effect of length on BBC on different CFIRs and its length HCR equivalents with an internal coiled tube diameter of 4 mm (λ of 13.8. 17.5 and 18.8 for CFIR and 125.5 for HCR) and a N_{Re} of 100 (flow rate of 20 mL/min). For CFIRs, each point in the graph represents an inversion in the reactor (0 to 3). The slurry concentration used was 10% (v/v). A final concentration of 2 mg/mL of BSA was used for all the geometries. The BBC was normalised appropriately using the results shown in Chapter 3. The error bars represent the standard deviation of the samples (n=3).

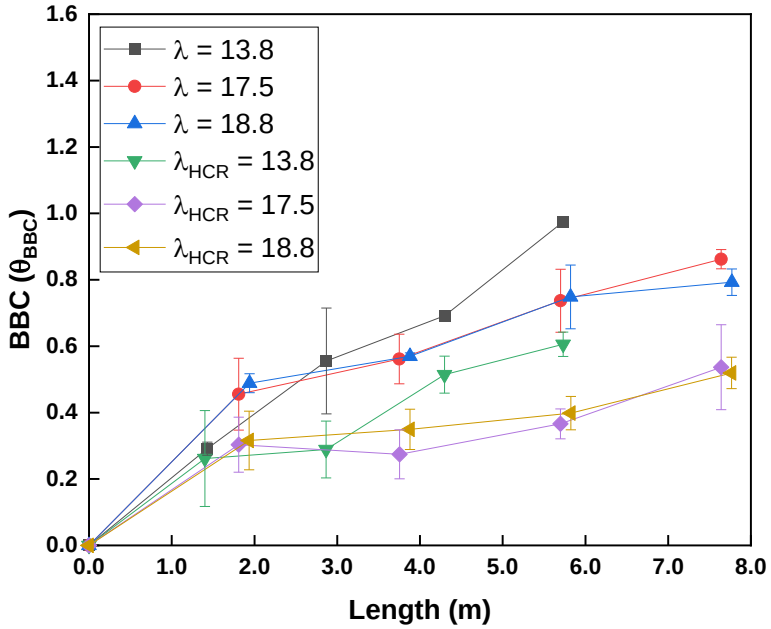

Figure 6.49. Effect of length on BBC on different CFIRs and its length HCR equivalents with an internal coiled tube diameter of 4 mm (λ of 13.8. 17.5 and 18.8 for CFIR and 125.5 for HCR) and a N_{Re} of 180. For CFIRs, each point in the graph represents an inversion in the reactor (0 to 3). The slurry concentration used was 10% (v/v). A final concentration of 2 mg/mL of BSA was used for all the geometries. The BBC was normalised appropriately using the results shown in Chapter 3. The error bars represent the standard deviation of the samples (n=3).

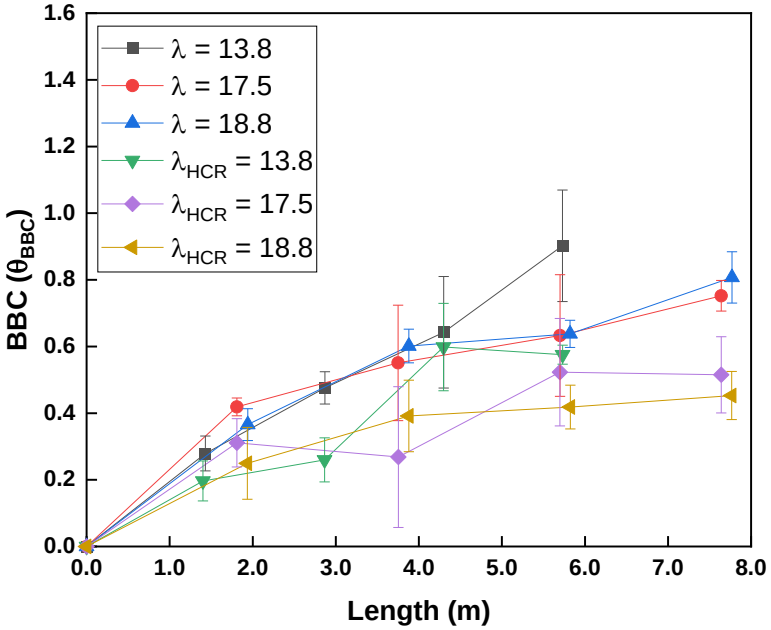

Figure 6.50. Effect of length on BBC on different CFIRs and its length HCR equivalents with an internal coiled tube diameter of 4 mm (λ of 13.8. 17.5 and 18.8 for CFIR and 125.5 for HCR) and a N_{Re} of 250. For CFIRs, each point in the graph represents an inversion in the reactor (0 to 3). The slurry concentration used was 10% (v/v). A final concentration of 2 mg/mL of BSA was used for all the geometries. The BBC was normalised appropriately using the results shown in Chapter 3. The error bars represent the standard deviation of the samples (n=3).

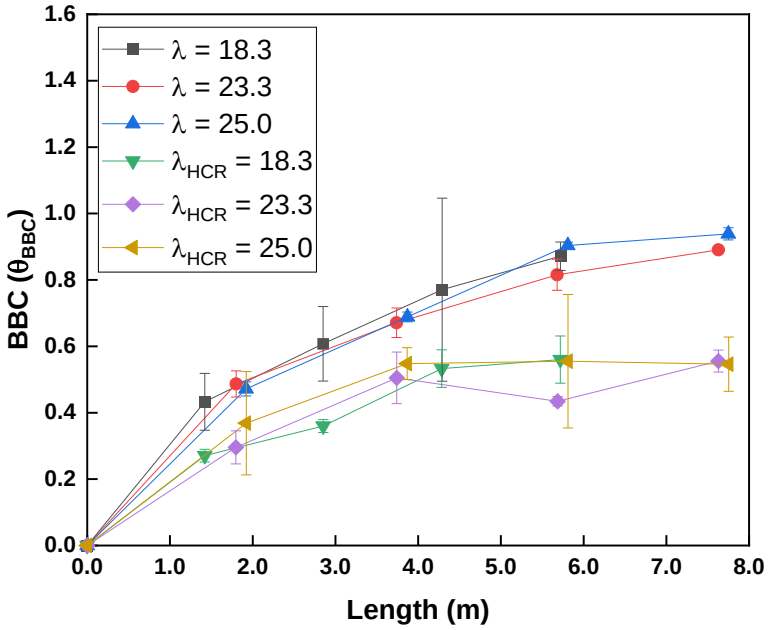

Figure 6.51. Effect of length on BBC on different CFIRs and its length HCR equivalents with an internal coiled tube diameter of 3 mm (λ of 18.3. 23.3 and 25 for CFIR and 167.3 for HCR) and a N_{Re} of 140. For CFIRs, each point in the graph represents an inversion in the reactor (0 to 3). The slurry concentration used was 10% (v/v). A final concentration of 2 mg/mL of BSA was used for all the geometries. The BBC was normalised appropriately using the results shown in Chapter 3. The error bars represent the standard deviation of the samples (n=3).

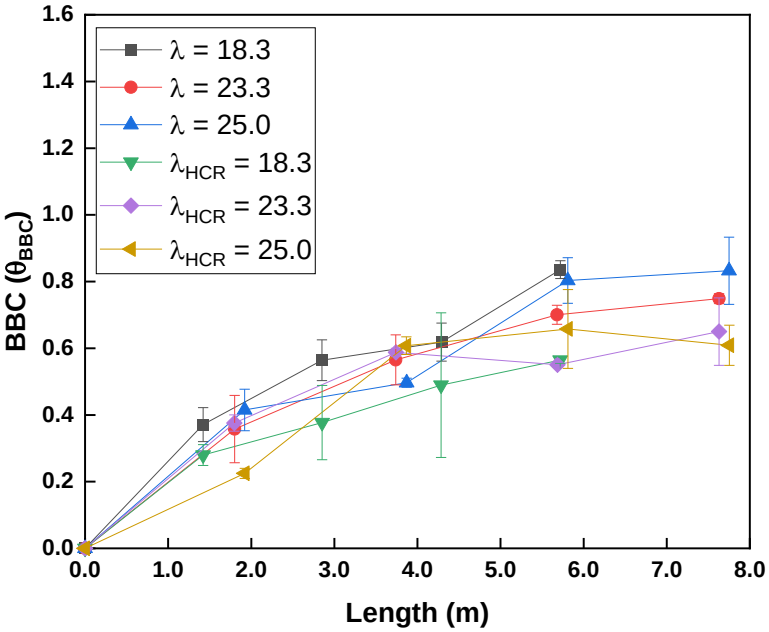

Figure 6.52. Effect of length on BBC on different CFIRs and its length HCR equivalents with an internal coiled tube diameter of 3 mm (λ of 18.3. 23.3 and 25 for CFIR and 167.3 for HCR) and a N_{Re} of 250. For CFIRs, each point in the graph represents an inversion in the reactor (0 to 3). The slurry concentration used was 10% (v/v). A final concentration of 2 mg/mL of BSA was used for all the geometries. The BBC was normalised appropriately using the results shown in Chapter 3. The error bars represent the standard deviation of the samples (n=3).

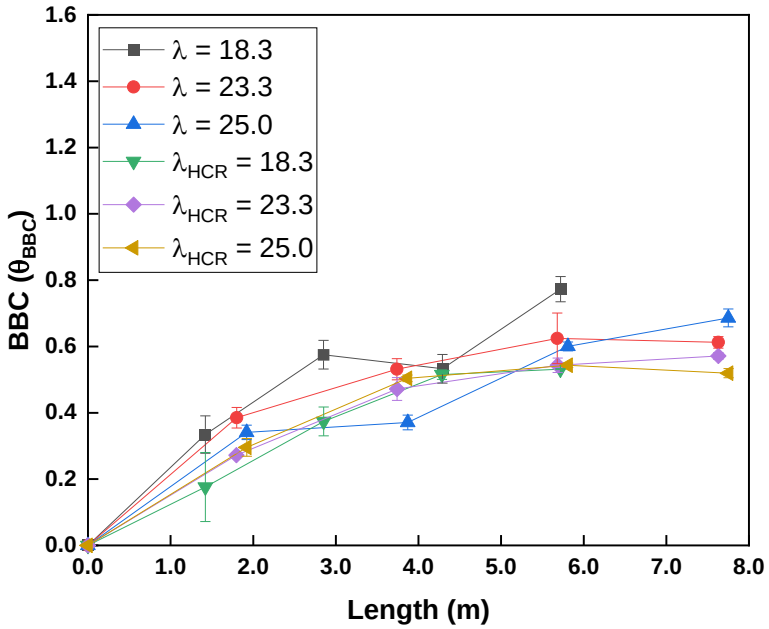

Figure 6.53. Effect of length on BBC on different CFIRs and its length HCR equivalents with an internal coiled tube diameter of 3 mm (λ of 18.3. 23.3 and 25 for CFIR and 167.3 for HCR) and a N_{Re} of 350. For CFIRs, each point in the graph represents an inversion in the reactor (0 to 3). The slurry concentration used was 10% (v/v). A final concentration of 2.0 mg/mL of BSA was used for all the geometries. The BBC was normalised appropriately using the results shown in Chapter 3. The error bars represent the standard deviation of the samples (n=3).

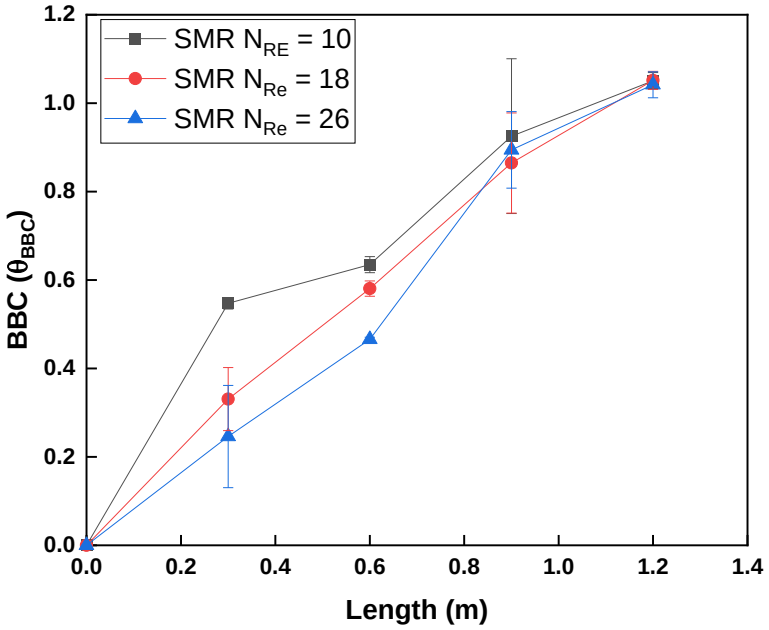

Figure 6.54. Effect of length on BBC on different N_{Re} operational conditions in a SMR. Each static mixer module (0.3 m) had 12 elements and an internal diameter of 1 cm. The slurry concentration used was 10% (v/v). A final concentration of 2 mg/mL of BSA was used for all the geometries. The BBC was normalised appropriately using the results shown in Chapter 3. The error bars represent the standard deviation of the samples (n=3).

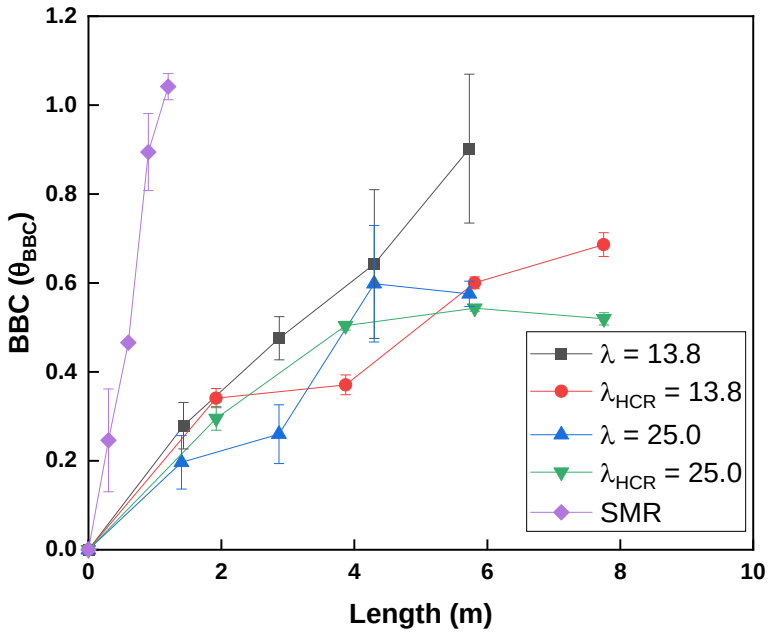

Figure 6.55. Effect of length on BBC on different CFIRs and its length HCR equivalents with an internal coiled tube diameter of 3 mm (λ of 18.3. 23.3 and 25 for CFIR and 167.3 for HCR) and a N_{Re} of 350. For CFIRs, each point in the graph represents an inversion in the reactor (0 to 3). The slurry concentration used was 10% (v/v). A final concentration of 2 mg/mL of BSA was used for all the geometries. The BBC was normalised appropriately using the results shown in Chapter 3. The error bars represent the standard deviation of the samples (n=3).

6.4.6.2 Batch Binding Capacity Vs Residence Time

In any chromatographic unit operation, the RT is a crucial aspect in achieving the maximum binding capacity. As seen in section 6.4.6.1, the length of the reactor has significant implications on the resultant BBC by reducing the axial dispersion (better mixing) but also by increasing the overall RT of the target molecule and resin beads. Figures 6.56 to 6.61 show the comparison between the normalised BBC against the RT of each CFIR and HCR according to their N_{Re} (100, 180 and 250 for 4 mm and 140, 250 and 350 for 3 mm). Figure 6.62 shows such relationship with SMR in N_{Re} of 10, 18 and 26. Each one of the N_{Re} levels represent a flow rate of 20, 35 and 50 mL/min. Figure 6.63 shows the contrast in length efficiency between the CFIRs with the lowest and highest λ (13.8 and 25), the equivalent HCRs and the SMRs.

All reactors showed a typical BBC curve trend as seen in Section 3.4.4 The curve became steeper as the N_{Re} decreased, indicating that the RT was not sufficient to have a full adsorption of the BSA on the bead surface. However, this was expected as

the system is being operated in a continuous mode and an optimisation of CFIR in CCTC was out of scope for this project.

As expected, a RT increase brought an increase in BBC for all reactor geometries. For all N_{Re} parameters, the CFIRs performed significantly better than any of their equivalent HCRs. As seen in the previous section, the efficiency decreased as the λ increased, suggesting that extending the length/RT is not enough if there is not enough contact with the BSA in the mobile phase. The BBC registered for CFIR with λ 13.8 was 81.1%, 86.7% and 66.4% higher than their HCR counterparts at their highest RT at all N_{Re}, respectively. Whilst the CFIR with λ 25 was 48.9%, 14.5% and 6.9% higher than its counterpart. The increase of N_{Re} has a negative impact on the BBC due to the reduction of RT inside the flow path. Nonetheless, this reduction is accentuated for the least efficient reactors as the resin bead is not able to be in contact with the BSA due to unfavourable mixing and shorter time in the reactor. This information can be correlated with the data gathered in Section 6.4.5 and agrees with the discussion presented in section 6.4.6.1.

Figure 6.62 shows the BBC against RT inside SMRs at three different flow rates. All N_{Re} seemed to have similar trend for the $t < 100$ s, following a standard BBC curve. Afterwards, the N_{Re} at 26 showed the steepest trend by reaching a BBC of 1 at $t > 120$ s, whilst the N_{Re} at 10 achieved a BBC of 1 at $t < 300$ s. This suggested that the SMR at all N_{Re} levels provided enough mixing for an adsorption dominated by mass transfer but when reaching to a diffusion dominated adsorption, it is significantly benefitted by the better cross-sectional mixing (Section 6.4.5). This better mixing operational conditions probably created a steeper BSA gradient around each individual bead, accelerating the diffusion. It was stated that the resin beads tend to sediment around the elements at slower operational conditions. Nonetheless, it is thought that this apparent increment in the individual RT was not as impactful as the bead is not getting the necessary contact with the BSA in the mobile phase to achieve a faster saturation. In the end, all operating conditions achieve a complete saturation but the operational condition running at 50 mL/min was vastly superior by being 265% faster than the one running at 20 mL/min.

Disregarding N_{Re}, Figure 6.63 shows the normalised BBC values of the SMR, CFIR with λ values of 13.8 and 25 and its HCR equivalents. The SMR stands as the superior

reactor by a difference of 3% to the CFIR λ 13.8, if taking into account BBC/RT as a value for comparison. While, the CFIR λ 25 has a difference of 36.1% compared to the SMR. The HCRs equivalent to λ 13.8 and 25 had the lowest efficiency of approximately 50% compared to the SMR. This meant that an optimised CFIR can surpass the efficiency registered for CFIR λ 13.8 and reach the one obtained by the SMR in the highest flow rate (50 mL/min). On top of that, this set of experiments did not take into account the travel time from one mixing module to the next one, only increasing the RT and therefore, the BBC at the end of the binding step.

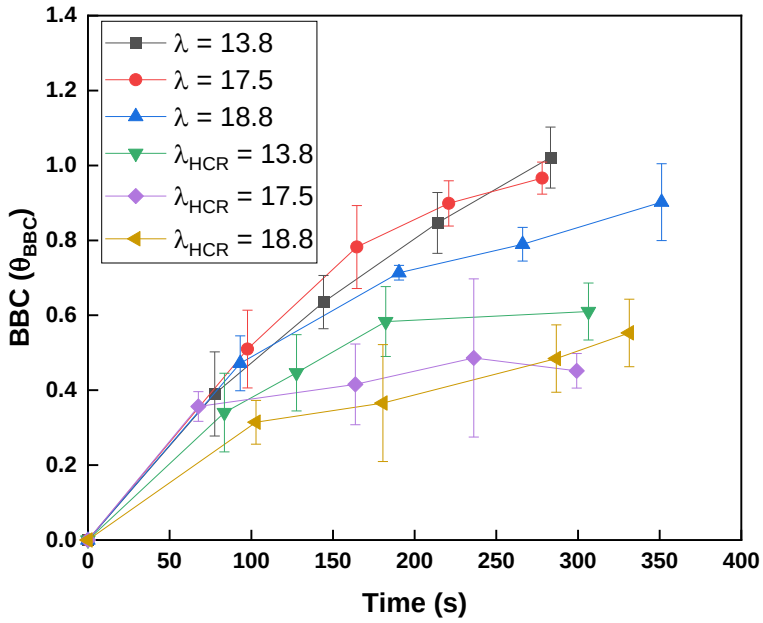

Figure 6.56. Effect of RT on BBC on different CFIRs and its length HCR equivalents with an internal coiled tube diameter of 4 mm (λ of 13.8. 17.5 and 18.8 for CFIR and 125.5 for HCR) and a N_{Re} of 100 (flow rate of 20 mL/min). For CFIRs, each point in the graph represents an inversion in the reactor (0 to 3). The slurry concentration used was 10% (v/v). A final concentration of 2.0 mg/mL of BSA was used for all the geometries. The BBC was normalised appropriately using the results shown in Chapter 3. The error bars represent the standard deviation of the samples (n=3).

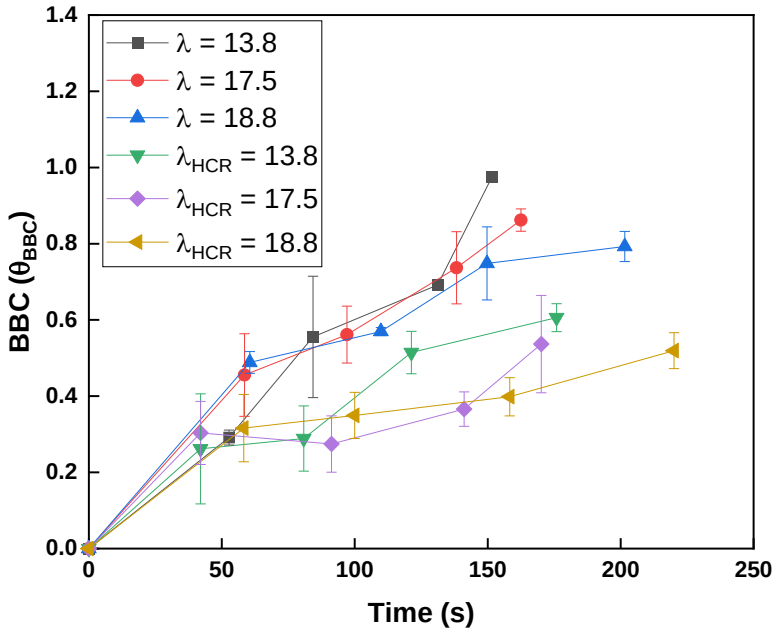

Figure 6.57. Effect of RT on BBC on different CFIRs and its length HCR equivalents with an internal coiled tube diameter of 4 mm (λ of 13.8. 17.5 and 18.8 for CFIR and 125.5 for HCR) and a N_{Re} of 180. For CFIRs, each point in the graph represents an inversion in the reactor (0 to 3). The slurry concentration used was 10% (v/v). A final concentration of 2 mg/mL of BSA was used for all the geometries. The BBC was normalised appropriately using the results shown in Chapter 3. The error bars represent the standard deviation of the samples (n=3).

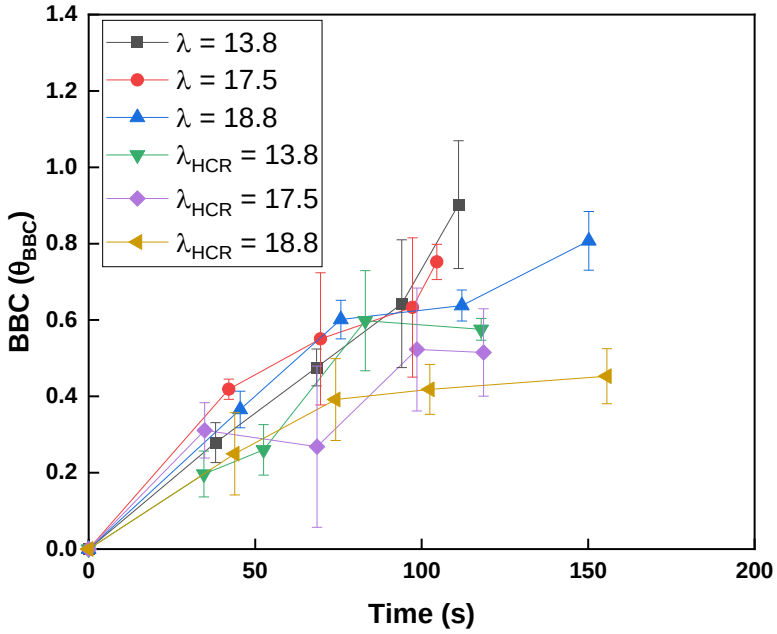

Figure 6.58. Effect of RT on BBC on different CFIRs and its length HCR equivalents with an internal coiled tube diameter of 4 mm (λ of 13.8. 17.5 and 18.8 for CFIR and 125.5 for HCR) and a N_{Re} of 250. For CFIRs, each point in the graph represents an inversion in the reactor (0 to 3). The slurry concentration used was 10% (v/v). A final concentration of 2 mg/mL of BSA was used for all the geometries. The BBC was normalised appropriately using the results shown in Chapter 3. The error bars represent the standard deviation of the samples (n=3).

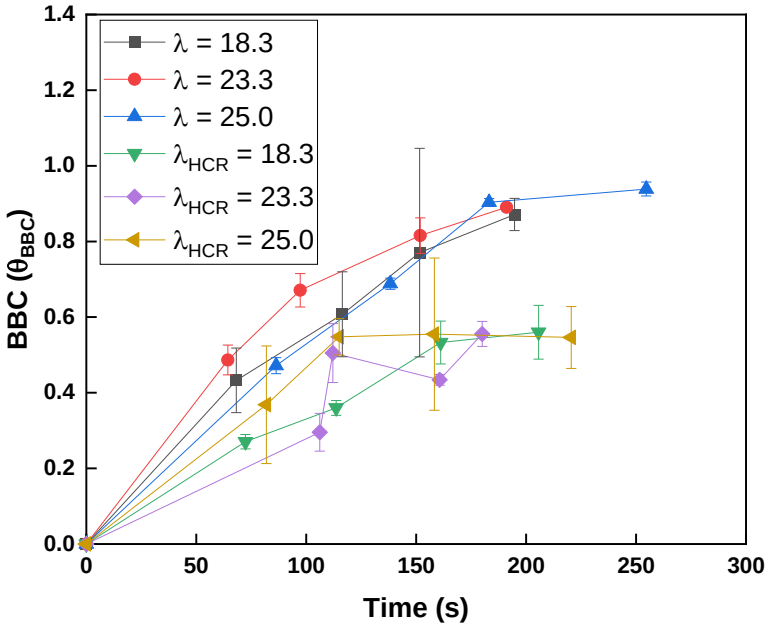

Figure 6.59. Effect of RT on BBC on different CFIRs and its length HCR equivalents with an internal coiled tube diameter of 3 mm (λ of 18.3. 23.3 and 25 for CFIR and 167.3 for HCR) and a N_{Re} of 140. For CFIRs, each point in the graph represents an inversion in the reactor (0 to 3). The slurry concentration used was 10% (v/v). A final concentration of 2 mg/mL of BSA was used for all the geometries. The BBC was normalised appropriately using the results shown in Chapter 3. The error bars represent the standard deviation of the samples (n=3).

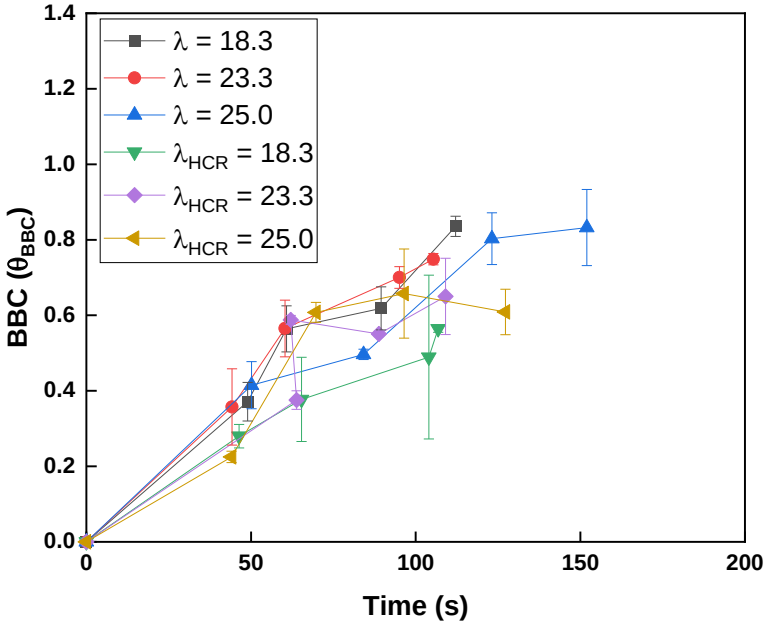

Figure 6.60. Effect of RT on BBC on different CFIRs and its length HCR equivalents with an internal coiled tube diameter of 3 mm (λ of 18.3. 23.3 and 25 for CFIR and 167.3 for HCR) and a N_{Re} of 250. For CFIRs, each point in the graph represents an inversion in the reactor (0 to 3). The slurry concentration used was 10% (v/v). A final concentration of 2 mg/mL of BSA was used for all the geometries. The BBC was normalised appropriately using the results shown in Chapter 3. The error bars represent the standard deviation of the samples (n=3).

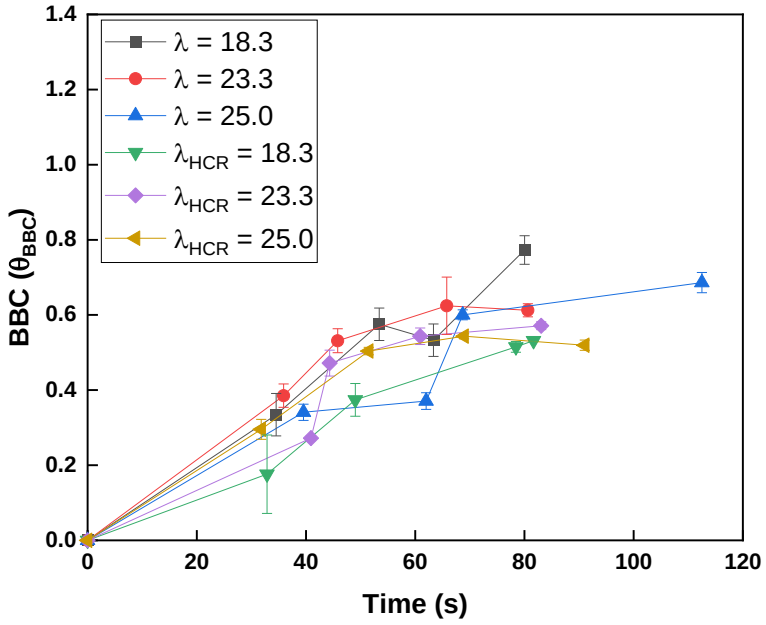

Figure 6.61. Effect of RT on BBC on different CFIRs and its length HCR equivalents with an internal coiled tube diameter of 3 mm (λ of 18.3. 23.3 and 25 for CFIR and 167.3 for HCR) and a NRe of 350. For CFIRs, each point in the graph represents an inversion in the reactor (0 to 3). The slurry concentration used was 10% (v/v). A final concentration of 2 mg/mL of BSA was used for all the geometries. The BBC was normalised appropriately using the results shown in Chapter 3. The error bars represent the standard deviation of the samples (n=3).

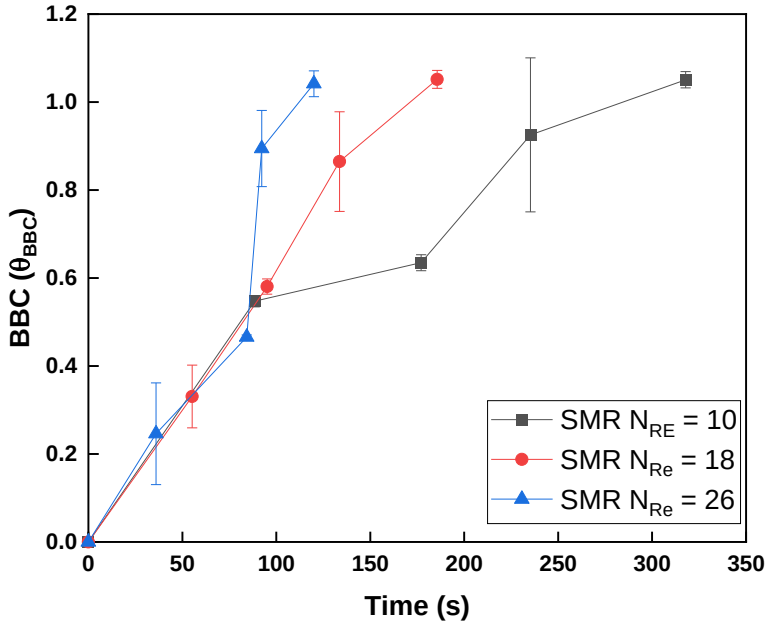

Figure 6.62. Effect of RT on BBC on different NRe operational conditions in a SMR. Each static mixer module (0.3 m) had 12 elements and an internal diameter of 1 cm. The slurry concentration used was 10% (v/v). A final concentration of 2 mg/mL of BSA was used for all the geometries. The BBC was normalised appropriately using the results shown in Chapter 3. The error bars represent the standard deviation of the samples (n=3).

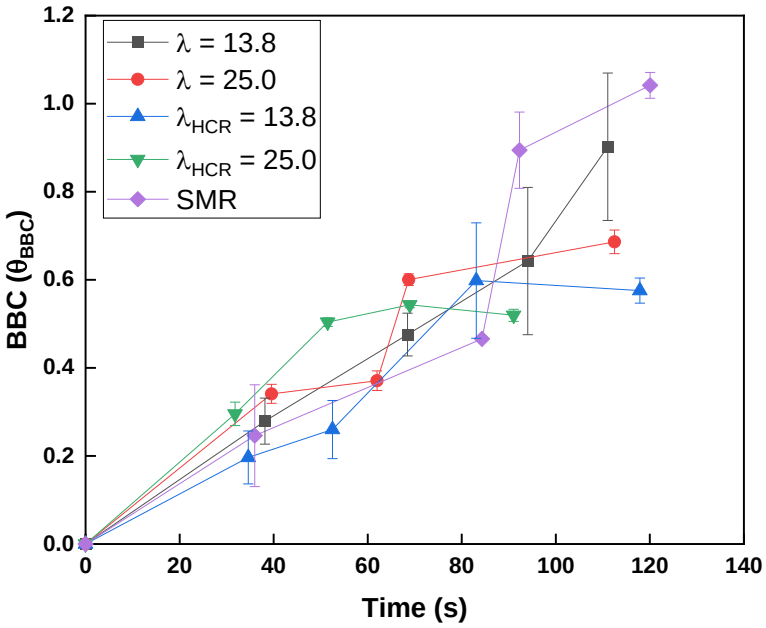

Figure 6.63. Effect of RT on BBC on different CFIRs and its length HCR equivalents with an internal coiled tube diameter of 3 mm (λ of 18.3. 23.3 and 25 for CFIR and 167.3 for HCR) and a N_{Re} of 350. For CFIRs, each point in the graph represents an inversion in the reactor (0 to 3). The slurry concentration used was 10% (v/v). A final concentration of 2 mg/mL of BSA was used for all the geometries. The BBC was normalised appropriately using the results shown in Chapter 3. The error bars represent the standard deviation of the samples (n=3).

6.4.6.3 Batch Binding Capacity Vs Dispersion Number

As discussed in previous sections, BBC in CCTC relies thoroughly on a compact and efficient mixing module which provides enough cross-sectional mixing in the flow under a certain minimum RT. As seen in Section 6.4.6.1 and 6.4.6.2, the reactors which performed better were the ones that favoured the reduction of the axial dispersion. Figures 6.64 to 6.69 display a direct comparison between the BBC and the N_{Pe} among different CFIRs and HCRs according to their N_{Re} (100, 180 and 250 for 4 mm and 140, 250 and 350 for 3 mm). Figure 6.70 shows such a relationship within different lengths and N_{Re} (10, 18 and 26) of the SMR. Each of the N_{Re} for all reactors represent a flow rate of 20, 35 and 50 mL/min. Finally, Figure 6.71 presents the contrast between BBC and N_{Pe} between the CFIRs with the lowest and highest λ (13.8 and 25), and their equivalent HCRs and the SMRs.

For all N_{Re}, the BBC for all reactors showed a subtle curved trend as the N_{Pe} was increasing. There is a positive direct correlation between a higher N_{Pe} (cross-sectional

mixing) and the BBC. As seen in Sections 6.4.6.1 and 6.4.6.2, the lower λ performed better compared to the higher λ and their HCRs counterparts. The higher the λ, the lower the magnitude for BBC and N_{Pe}. This contrast can be easily seen in Figure 6.64 as all the BBC and N_{Pe} CFIR values easily outclassed their HCR counterparts by presenting values 48% and 78% times higher in average for all points, respectively; while in Figure 6.69, the BBC and N_{Pe} CFIR values barely outclassed the HCRs by 7.9% and 8.6% times higher in average for all points, respectively.

As expected, the increase of N_{Re} had a negative impact on the BBC for all λ. The higher flow velocities favoured the cross-sectional mixing. However, this also meant that the resin slurry was spending less time in contact with the BSA. The N_{Re}, N_{Pe} and RT are all related, as the change of any one of them brings an increase/reduction of the other two. According to the results, the RT alone does not determine a full saturation of the chromatography media, a minimum amount of contact time and mixing should be given by the reactor to achieve the expected BBC. It seemed that in CCTC, the cross-sectional mixing is as significant as the RT during the binding step. It is also worth noticing that even when CFIRs achieved similar levels of magnitude of N_{Pe} after their fourth inversion the final BBC was significantly different among them. This could possibly be attributed to the unique design, involving the λ and the length between inversions. CFIRs with reduced λ would have the cross-sectional mixing advantage at the entrance of the flow path, enhancing the contact time and mass transfer between the BSA and the chromatography resin. CFIRs with increased λ eventually caught up in terms of N_{Pe} after a longer RT and reactor length. However, the initial contact time and interaction between the BSA and the resin beads at entrance of the flow path would be subpar causing a longer lag period between the mass transfer and diffusion way of molecule/matrix interaction. This can be seen with CFIRs λ 23.3 and 25 showed a difference of 7% between themselves but a difference of 31% and 47% against CFIR λ 13.8 in terms of BBC, respectively.

Figure 6.70 displays the BBC recorded for 4 different lengths of a SMR at 3 different flow rates. All N_{Re} seemed to have a similar curve as the N_{Pe} increased, with N_{Re} 10 being the steepest. N_{Re} 10 seems to be the best operational parameter of the three as it achieved a full adsorption at a lower N_{Pe}; though, in this case the combination of a higher RT and minimum efficient cross-sectional mixing were the main factors for these values. This operational parameter was recorded to be the least efficient in SMR

by taking into account the RT as all other parameters also reached full adsorption in lower RT. N_{Re} 18 and 26 had a difference of < 1% and < 5% on BBC and N_{Pe}, respectively, for the last two lengths. This suggested that a larger jump over N_{Re} is needed to have a significant impact on N_{Pe}, as the cross-sectional mixing mainly depends on the force with which the liquid is impacting on the elements inside the static mixer. However, these results are inconclusive with the amount of data collected from this experiment. It can be stated that a flow rate of 50 mL/min has a similar axial dispersion as 35 mL/min, making the higher flow rate a better operational parameter (also seen in Section 6.4.6.1 and 6.4.6.2).

Disregarding N_{Re}, Figure 7.71 shows the normalised BBC values of the SMR, CFIR with λ values of 13.8 and 25 and its HCR equivalents. The SMR stands superior by achieving a full adsorption at a N_{Pe} 76% and 68.9% times lower than the value calculated for the CFIR λ 13.8 and 25, respectively, which did not achieve a full adsorption on average. The N_{Pe} of the CFIR λ 13.8 was only 7% times higher than the CFIR λ 25, the BBC value was 13.5% higher possibly explained by the initial cross-sectional mixing advantage provided by the reduced λ. The HCR equivalent to λ 13.8 and 25 presented the worst conditions of all groups with N_{Pe} values 4.5% and 51.1% above the ones calculated for SMR but recorded BBC values 73.7% and 92.6% lower. The superiority of the SMR in the highest N_{Re} in terms of BBC vs N_{Pe} was expected as the SMR has been engineered and optimised with the only purpose of providing the highest level of mixing at relatively low operational conditions. It seemed that the physical inclusion of elements in the flow path has a higher advantage than relying on centrifugal forces. On top of that, it was observed that the physical elements blocking the elements allowed the resin beads to have a more uniform distribution around the cross-sectional plan and even were points were small amounts of resin would briefly slow down or settle (specially at the lowest N_{Re}). On the other hand, the CFIRs in this project were designed and built with the idea of proving the concept for these mixing modules as a viable option under CCTC operational conditions and dimensions. The optimisation in terms of conditions and dimensions of the CFIRs was out of scope. Nonetheless, the exploration of all these parameters offers a starting point and opens the window for even other mixing techniques.

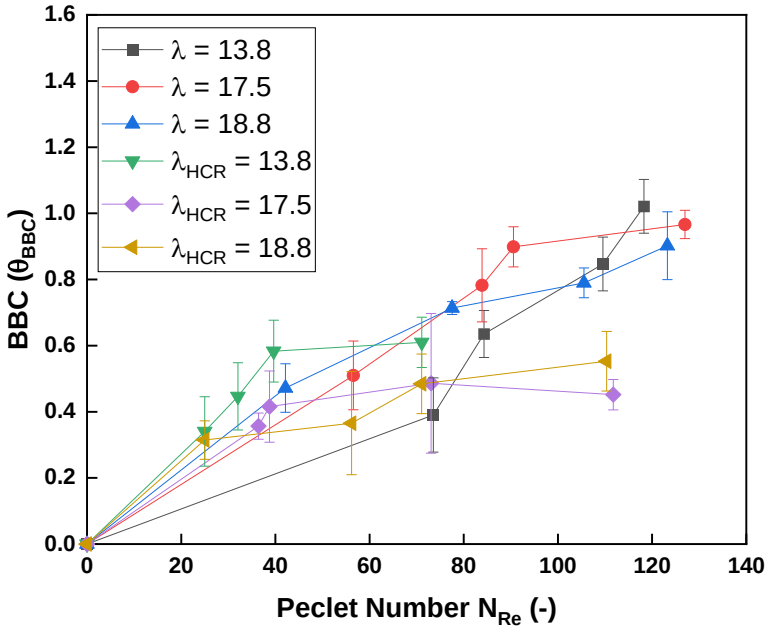

Figure 6.64. Effect of N_{Pe} on BBC on different CFIRs and its length HCR equivalents with an internal coiled tube diameter of 4 mm (λ of 13.8. 17.5 and 18.8 for CFIR and 125.5 for HCR) and a N_{Re} of 100 (flow rate of 20 mL/min). For CFIRs, each point in the graph represents an inversion in the reactor (0 to 3). The slurry concentration used was 10% (v/v). A final concentration of 2 mg/mL of BSA was used for all the geometries. The BBC was normalised appropriately using the results shown in Chapter 3. The error bars represent the standard deviation of the samples (n=3).

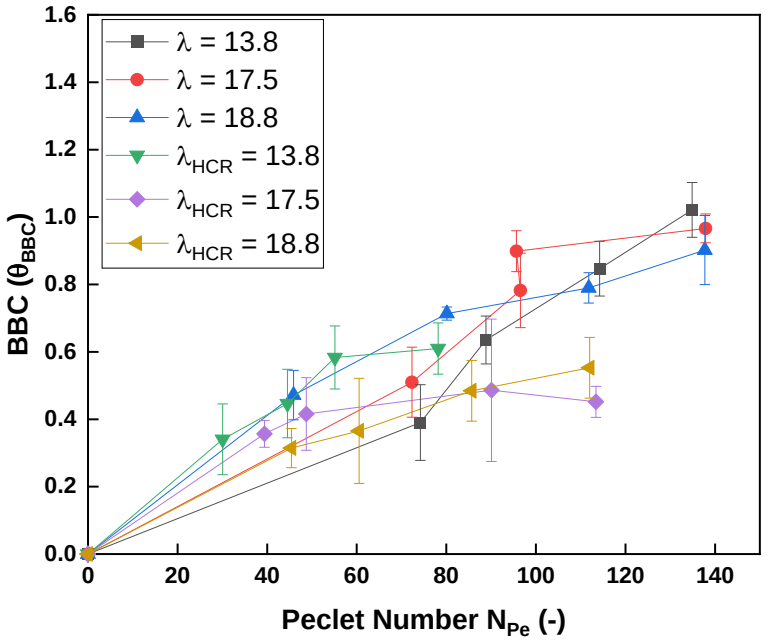

Figure 6.65. Effect of N_{Pe} on BBC on different CFIRs and its length HCR equivalents with an internal coiled tube diameter of 4 mm (λ of 13.8. 17.5 and 18.8 for CFIR and 125.5 for HCR) and a N_{Re} of 180. For CFIRs, each point in the graph represents an inversion in the reactor (0 to 3). The slurry concentration used was 10% (v/v). A final concentration of 2 mg/mL of BSA was used for all the geometries. The BBC was normalised appropriately using the results shown in Chapter 3. The error bars represent the standard deviation of the samples (n=3).

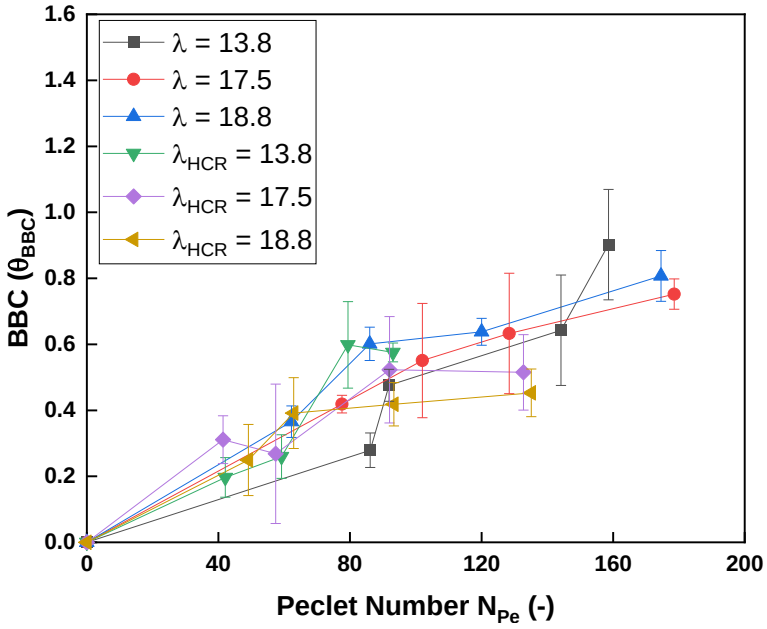

Figure 6.66. Effect of N_{Pe} on BBC on different CFIRs and its length HCR equivalents with an internal coiled tube diameter of 4 mm (λ of 13.8. 17.5 and 18.8 for CFIR and 125.5 for HCR) and a N_{Re} of 250. For CFIRs, each point in the graph represents an inversion in the reactor (0 to 3). The slurry concentration used was 10% (v/v). A final concentration of 2 mg/mL of BSA was used for all the geometries. The BBC was normalised appropriately using the results shown in Chapter 3. The error bars represent the standard deviation of the samples (n=3).

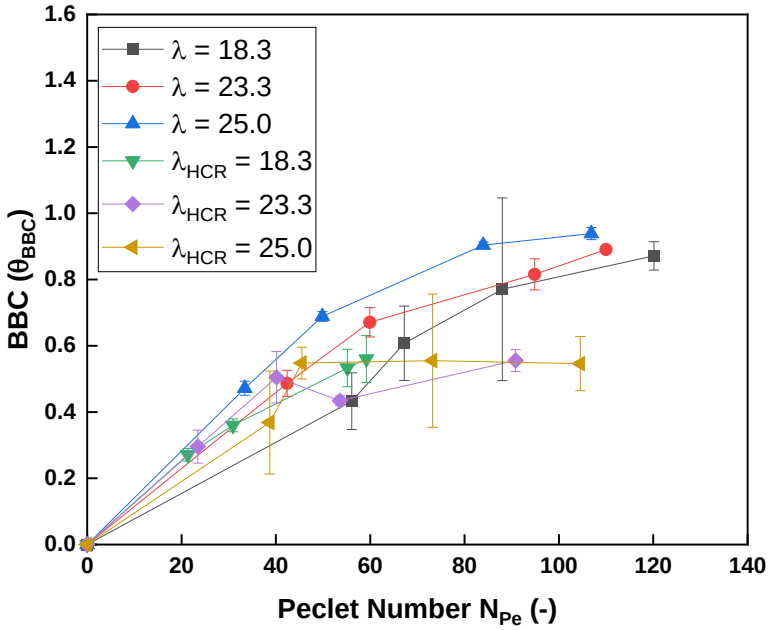

Figure 6.67. Effect of N_{Pe} on BBC on different CFIRs and its length HCR equivalents with an internal coiled tube diameter of 3 mm (λ of 18.3. 23.3 and 25 for CFIR and 167.3 for HCR) and a N_{Re} of 140. For CFIRs, each point in the graph represents an inversion in the reactor (0 to 3). The slurry concentration used was 10% (v/v). A final concentration of 2 mg/mL of BSA was used for all the geometries. The BBC was normalised appropriately using the results shown in Chapter 3. The error bars represent the standard deviation of the samples (n=3).

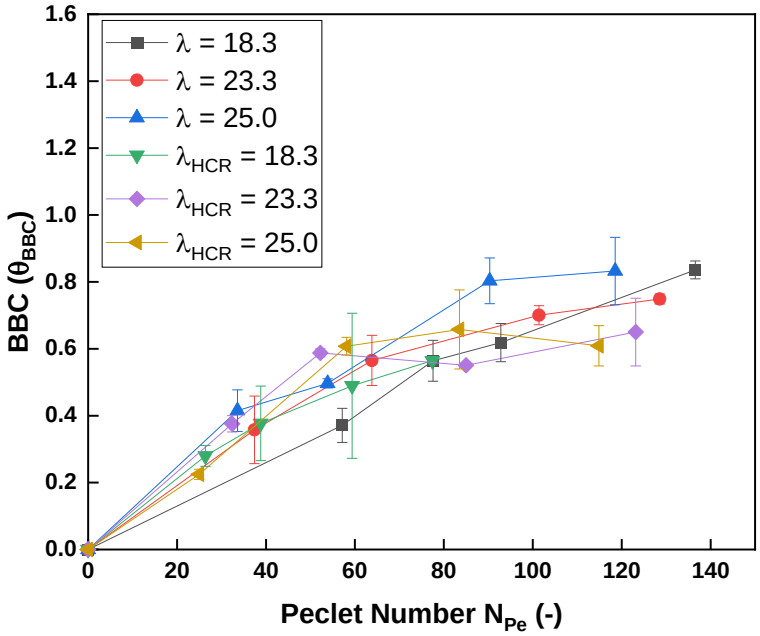

Figure 6.68 Effect of N_{Pe} on BBC on different CFIRs and its length HCR equivalents with an internal coiled tube diameter of 3.0 mm (λ of 18.3. 23.3 and 25 for CFIR and 167.3 for HCR) and a N_{Re} of 250. For CFIRs, each point in the graph represents an inversion in the reactor (0 to 3). The slurry concentration used was 10% (v/v). A final concentration of 2 mg/mL of BSA was used for all the geometries. The BBC was normalised appropriately using the results shown in Chapter 3. The error bars represent the standard deviation of the samples (n=3).

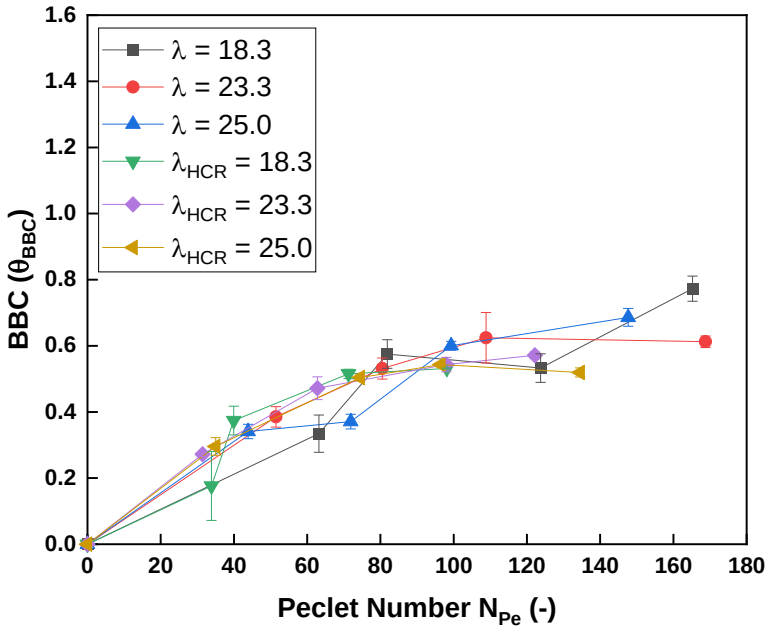

Figure 6.69. Effect of N_{Pe} on BBC on different CFIRs and its length HCR equivalents with an internal coiled tube diameter of 3 mm (λ of 18.3. 23.3 and 25.0 for CFIR and 167.3 for HCR) and a N_{Re} of 350. For CFIRs, each point in the graph represents an inversion in the reactor (0 to 3). The slurry concentration used was 10% (v/v). A final concentration of 2 mg/mL of BSA was used for all the geometries. The BBC was normalised appropriately using the results shown in Chapter 3. The error bars represent the standard deviation of the samples (n=3).

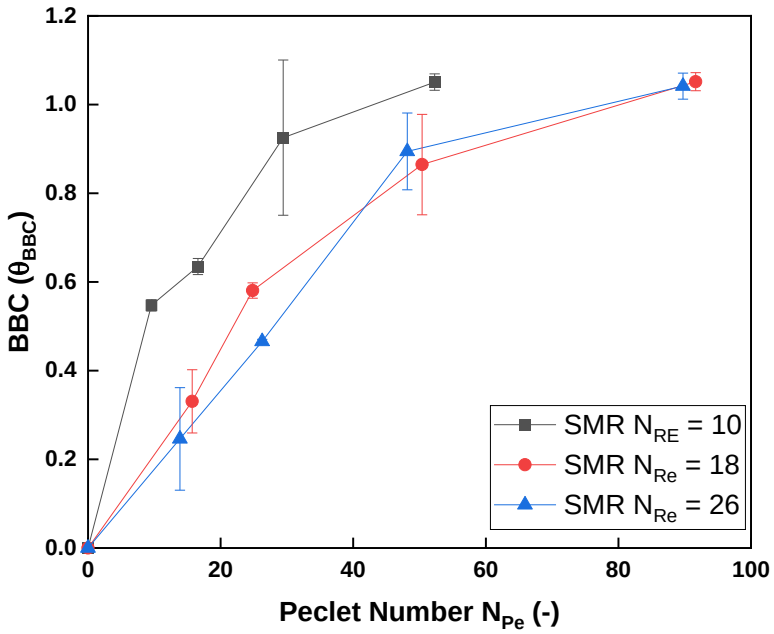

Figure 6.70. Effect of N_{Pe} on BBC on different NRe operational conditions in a SMR. Each static mixer module (0.3 m) had 12 elements and an internal diameter of 1 cm. The slurry concentration used was 10% (v/v). A final concentration of 2 mg/mL of BSA was used for all the geometries. The BBC was normalised appropriately using the results shown in Chapter 3. The error bars represent the standard deviation of the samples (n=3).

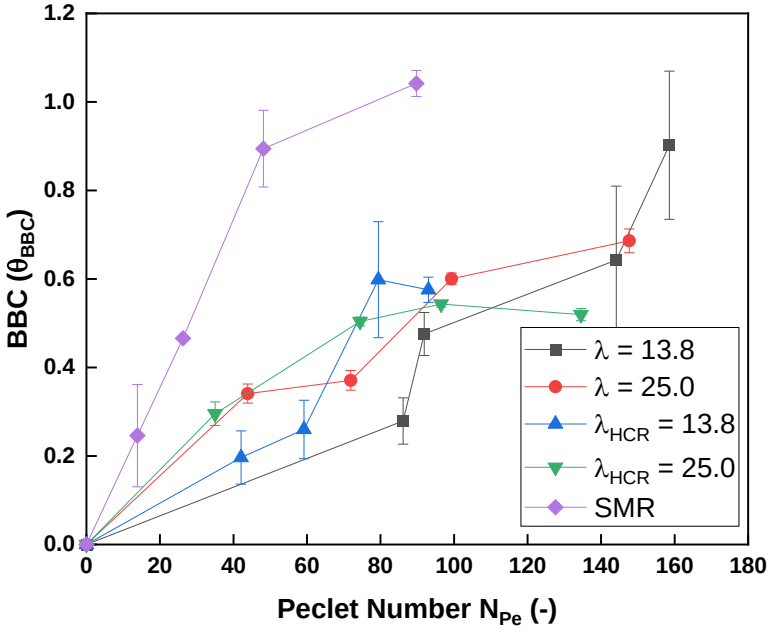

Figure 6.71. Effect of N_{Pe} on BBC on different CFIRs and its length HCR equivalents with an internal coiled tube diameter of 3 mm (λ of 18.3. 23.3 and 25 for CFIR and 167.3 for HCR) and a N_{Re} of 350. For CFIRs, each point in the graph represents an inversion in the reactor (0 to 3). The slurry concentration used was 10% (v/v). A final concentration of 2 mg/mL of BSA was used for all the geometries. The BBC was normalised appropriately using the results shown in Chapter 3. The error bars represent the standard deviation of the samples (n=3).

6.4.6.4 Batch Binding Capacity Model on Reactors

It is important to put all the BBC values for the reactors into perspective in relation to an ideal BBC absorbance curve. The contrast would bring a palpable sense of efficiency and how comparable the current reactors are to a theoretically ideal reactor. Previous sections in this chapter have already discussed the performance of the CFIRs during the batch adsorption of BSA and compared them to equivalent HCRs and current SMRs used for CCTC. Nonetheless, the values have not been compared to an adsorption in ideal conditions. Fortunately, the BBC adsorption model used for RT characterisation in mixing modules (Section 3.4.4) can be modified to achieve this purpose. Figure 6.72, 6.73 and 6.74 display the BBC over RT model at three different flow rates and at the conditions described in Section 6.3.4, in addition with the BBC values from CFIRs with a λ 13.8 and 25.0, equivalent HCRs for such λ and SMR.

It is noticeable from all three figures that not a single reactor had similar BBC values compared to the theoretical ones. However, the experimental BBC values showed a similar trend in the shape of the BBC curve. The curve was more noticeable at the lowest flow rate (20 mL/min), while it was more linear-like at the highest flow rate (50 mL/min). This was expected as the flow rate or N_{Re} increased, the RT inside the reactors decreased; i.e. the BBC signal for the first point for all reactors decreased from 0.35 to 0.22 (0.12 difference) for the lowest and highest flow rate, respectively. Even though the cross-sectional mixing increased with higher flow rates, it is not enough to mitigate the lack of overall contact time between the resin media and the BSA in the solution. Also, decreasing the RT (increasing the flow rate) reduces the window to fully develop an effective and matured cross-sectional mixed flow. As time passes, the average difference in BBC signal for the last point for all reactors turned out to be 0.69 and 0.62 (0.07 difference) at full length. Even though each reactor performed widely differently, the reduction in the difference accounts for the aforementioned claims regarding the need of enough RT or reactor length to achieve a fully matured flow.

As seen in the previous sections, the SMR reigns as the most productive reactor as it reaches full adsorption on all N_{Re}. CFIR λ 13.8 comes in close in all instances, followed by CFIR λ 25, as expected. CFIR λ 13.8 reached full adsorption for the first two N_{Re}

but was 10% lower than the highest one. However, this still made this reactor as an attractive alternative as the resin BBC capacity is never fully used during standard manufacturing campaigns. CFIR λ 25 was not competitive at a flow rate of 50 mL/min (usual CCTC flow rates) achieving a BBC under 0.7. HCRs could not compete against the others by merely reaching a BBC of 0.6 in all $N_{Re,}$ where most of the others had values above 0.9. This evidenced the initial lack of mixing and contact between the resin slurry and the BSA solution. This initial mixing starts with a reduced λ, which is further enhanced by the inclusion of inversions and high N_{Re}.

The model and the experimental data had a palpable contrast in the efficiency for each reactor as a whole. The efficiency of the reactor is a trade-off between the N_{Re} or RT and the BBC of the chromatography media. Unlike all other column-based chromatography techniques, overall BBC in CCTC also relies on the mixing inside the flow path. Figure 6.72, 6.73 and 6.74 had shown the importance of the operational conditions (flow rate), RT and the inherent design of the reactor. These results agreed with the findings discussed previously in this section. All remaining reactors BBC results were between CFIR λ 13.8 and CFIR λ 25, the efficiency of them decreased as the λ increased.

The BBC model can be used for comparison for the optimisation of the CFIR as a viable mixing module for CCTC, by modifying the dimensions of the coil and coiled tube. The optimisation would vary from a reduction in λ with a custom symmetrical or asymmetrical coil and coiled tube, adding inversions, number of turns and modify the operational parameters. However, this last one is also tied and would directly affect the performance of the solid/liquid module (hollow fibre) operational parameters. These sets of results could be marked as a stepping stone for the creation of a predictive BBC model in CFIRs and SMRs specifically tailored for chromatography adsorption.

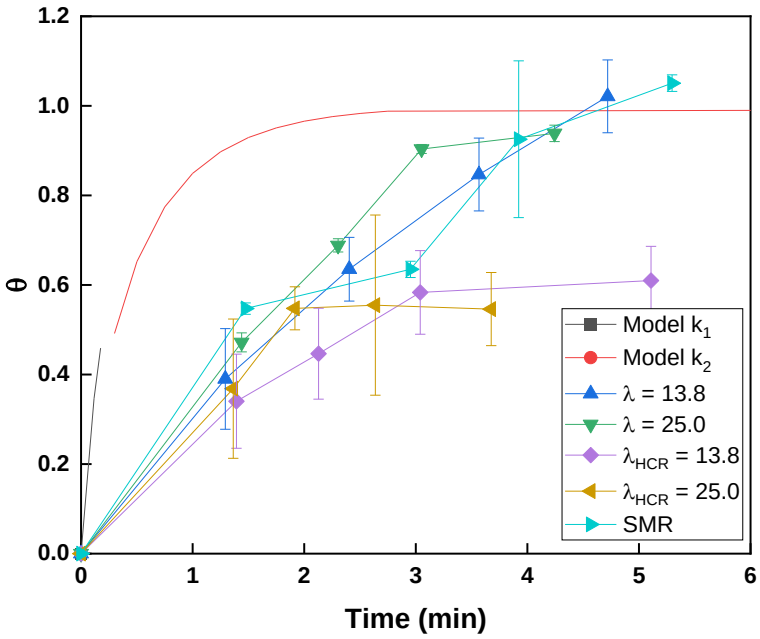

Figure 6.72. Comparison of BBC model and BBC values calculated from CFIRs, HCR. and SMRs against time. The constant models were fixed at k_1 = 1.3 and k_2 = 2. The N_{Re} was set to be 100 and 140 for reactors with coiled tube internal diameter of 4 and 3 mm, respectively. The CFIRs had a λ of 13.8 and 25 with a coiled tube internal diameter of 4 mm and 3 mm, respectively. The HCRs had a λ of 125.5 and 167.3 with a coiled tube internal diameter of 4 and 3 mm, respectively. The HCRs were equivalent in length and coiled tube internal diameter to their equivalent CFIRs. The error bars represent the standard deviation of the samples (n=3).

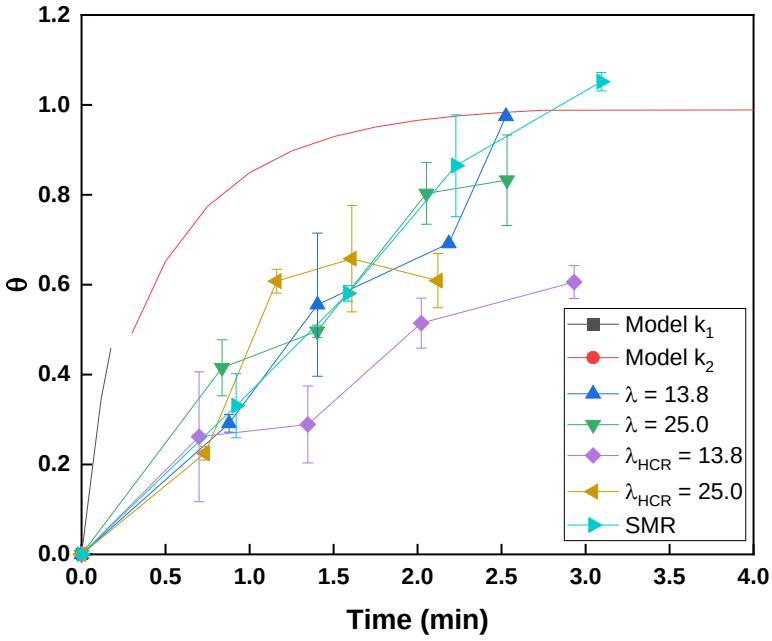

Figure 6.73. Comparison of BBC model and BBC values calculated from CFIRs, HCR. and SMRs against time. The constant models were fixed at k_1 = 1.3 and k_2 = 2. The N_{Re} was set to be 180 and 250 for reactors with coiled tube internal diameter of 4 and 3 mm, respectively. The CFIRs had a λ of 13.8 and 25 with a coiled tube internal diameter of 4 mm and 3 mm, respectively. The HCRs had a λ of 125.5 and 167.3 with a coiled tube internal diameter of 4 and 3 mm, respectively. The HCRs were equivalent in length and coiled tube internal diameter to their equivalent CFIRs. The error bars represent the standard deviation of the samples (n=3).

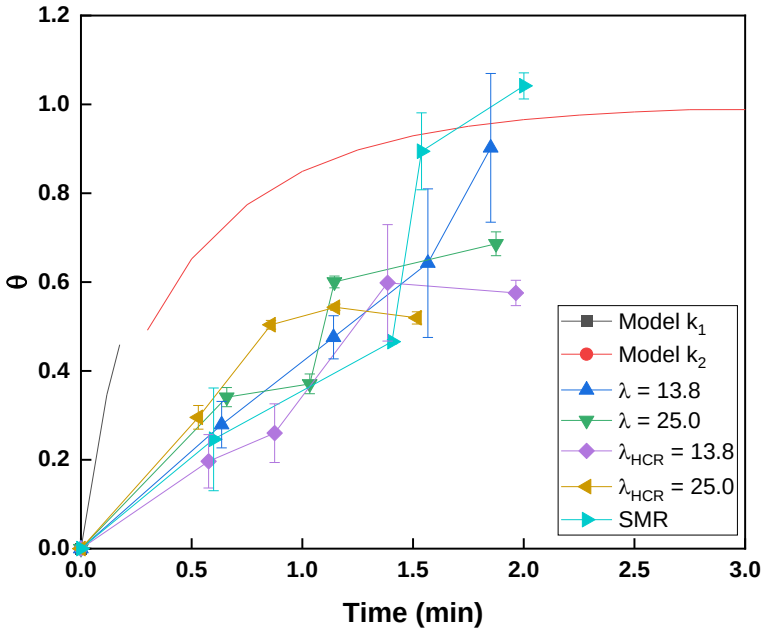

Figure 6.74. Comparison of BBC model and BBC values calculated from CFIRs, HCR. and SMRs against time. The constant models were fixed at k_1 = 1.3 and k_2 = 2. The N_{Re} was set to be 250 and 350 for reactors with coiled tube internal diameter of 4 and 3 mm, respectively. The CFIRs had a λ of 13.8 and 25 with a coiled tube internal diameter of 4 mm and 3 mm, respectively. The HCRs had a λ of 125.5 and 167.3 with a coiled tube internal diameter of 4 and 3 mm, respectively. The HCRs were equivalent in length and coiled tube internal diameter to their equivalent CFIRs. The error bars represent the standard deviation of the samples (n=3).

6.4.7 Footprint and Costs Implications

In addition to all the performance analysis, the footprint and costs have been estimated reactor type used in this project. The cost and foot print calculations were done with a CCTC system with an approximate hold up volume of 1 L and a resin slurry concentration of 5 % (v/v). Table 6.10 and 6.11 show the cost and footprint related values for each of the CFIRs and SMRs. The HCR was not taken into account as it was never taken as a realistic option to replace the static mixer modules, additionally the diameter was arbitrarily chosen due to work space limitations. However, the cost for the HCR would only imply the cost of the tubing. CFIRs and SMRs are either used in both vertical and horizontal positions, it all depends on the space available or the equipment itself. Even though a vertical position for the SMR is the ideal position in this case as gravity would help to extend the RT as the resin beads tend to settle if the N_{Re} is not high enough, the footprint was also calculated in a horizontal and a vertical position. The costs do not include any operational costs as the resources (resin slurry

and buffer consumption) would be identical as the flow rate is kept the same for both types of reactors.

CFIRs and SMRs costs behave differently due to their components. The CFIR main cost is the coiled tube as the cost is proportional to the length of the reactor. The coil is the cheapest part to produce and it is functional for up to 3 inversions and any coiled tube length. The coiled tube had a price of $3.5 and $5 for 3 and 4 mm diameters, while the coil ended with a final price per piece of $1.5 for the smallest reactor and $3.6 for the largest one. Table 6.10 shows a variable Cost x Footprint to easily visualise the ranking among the CFIRs for these terms. For this reason, CFIR λ 18.3 was the cheapest ($21.9 with 3 inversions), while CFIR λ 18.8 was the most expensive ($42.4 with 3 inversions). Disregarding its lowest λ, The CFIR λ 13.8 seemed to be in the middle of the costs among all reactors due to its smaller frame but larger coiled tube diameter.

On the other hand, the SMR is a modular product, which means that the addition of reactor length would be translated into the addition of a whole static mixer module. The SMR used for this project had a total length of 30 cm with an internal coiled diameter of 1 cm with a price of $131 per piece. A total length of 1.2 m was required for the rig of the 2-stage CCTC system, translated into 4 static mixers modules of such dimensions. For the calculations, a static mixer of 70 cm in length with a total price of $209 per piece (2 modules in total) was considered to make the SMR more realistic and competitive compared to the CFIRs.

CFIRs cost does not operate in their entirety as a modular cost. The CFIR had a base price (coil) plus the variable cost (coiled tube). The coil cost becomes less significant as the length of the tube increases, especially for the coils with 50 mm in diameter. The cost percentage for the coil varies from 20% to 6%, 26% to 7% and, 31% to 10% for reactors with 0 to 3 inversions using 50 mm, 63 mm and 75 mm coil diameters, respectively. This is expected as the larger the coil, the higher its impact in the overall costs. The main source of costs is the coiled tube, which varies as the number of turns, length and inversions are added to the design. At their longest length, an approximate of 90% to 95% is solely accounted to the coiled tube. Just like the coil, the larger the diameter or bore of the coiled tube, the higher the cost. In reality, it is common to maximise the use of the CFIR by using all the sides of the coil frame, making CFIR

costs be modular in fashion. However, the coil frame can be reused as it is never in contact with any buffer or substance, further reducing its material costs if it is planned to be used in a single-use fashion. The set up and preparation is simple and can be done in parallel to avoid idle times. The coil can also be used with several different coiled tube diameters with different lengths, pitches, turns and inversions if needed. This allows to really cater the needs of each manufacturing process with the optimal minimum RT and length. This makes the CFIR an extremely flexible choice over other alternatives in terms of cost for process optimisation and experimentation. The footprint greatly varies on the orientation, from 0.044 to 0.016 m^2 for horizontal and vertical position, respectively. The overall difference is approximately 310%. The vertical position has the advantage for being the most compact option; however, the orientation is also dependant on the use. Larger CFIRs would benefit for being horizontal and stacking them vertically as vertical footprint is usually not a problem; whilst smaller CFIRs would be positioned vertically and stacked horizontally (and vertically, if needed). For the scale of the current CCTC system design, a vertical orientation with a horizontal and vertical stack would probably be the ideal rig. The rig would have 2 stacked CFIRs at the bottom in vertical position with another two equal stacks above each other. The total footprint would be 0.025, 0.035 and 0.039 m^2 for the smaller to the largest coil. This design would match the height of the hollow fibre modules and at a reasonable height for manipulation.

On the other hand, SMRs operate in a modular cost fashion. The total cost of the static mixer is solely the static mixer itself. The modification of the RT/length will forcefully require the subtraction or addition of a static mixer module, which might not be available while performing performance/optimisation experiments. The SMR used in this project was made up, at its longest, of 4 static mixers (total price of $524); however, a reduction in static mixers (2 static mixers for a total price of $418) can be used to reduce costs. This modularity is not a complete disadvantage. The module comes already assembled from the manufacturer, the operator would only be required to connect the static mixers into the system. However, this modularity makes the static mixer a less attractive option as not a single part can be recycled for single-use systems, making it more expensive in the long run. As CFIRs, the footprint varies for both positions, from 0.036 m^2 for 4 horizontal 30 cm static mixers to 0.001 m^2 for 4 vertical static mixers. The overall difference is about 5010%. For this reason, the

optimal position for the static mixers is vertical with a footprint of 0.001 m^2 for all static mixers in one vertical stack (4 modules of 30 cm or 2 modules of 70 cm in length) or 0.002 m^2 for two separate vertical stacks (current rig used by Chromatan).

All CFIRs with 3 inversions were between a cost range of $21 up to $42, while the SMRs with a length of 1.2 and 1.4 m were calculated to be $524 and $418. The cost difference among the two reactors is significant for experimentation and manufacturing processes. A regular CCTC process is usually made up from 6 different chromatography steps (it may vary depending on the type of protein-ligand interaction), which is converted into approximately 6 CFIR λ 13.8 or 6 sets of 4 static mixers 30.0 cm in length (alternatively, 6 sets of 2 static mixers 70 cm in length). This is translated into $180.5 ($30.1 per reactor) for the CFIR, $3,144 for the 30 cm static mixer and $2,508 for the 70 cm static mixer. The number might vary as the number of stages and steps might increase the total number and an extra set of mixing modules are required as an “after binder” is commonly used after the binding step. There is a 13X and 17X fold decrease in costs if the static mixers are replaced by CFIRs. The difference between both type of reactors would not significantly change if a CFIR with a different λ was selected for the analysis. The CFIR λ 13.8 proved to be the most plausible candidate for further optimisation and implementation in terms of BBC.

The scale-up of the CCTC system is straight forwards in terms of resources and costs (Dutta et al. 2017). The scaling is directly related to the increase in capacity of the system capacity is increased; i.e. scaling the resin slurry volume from a 1 L system to a 20 L system is just a matter of increasing the former resin slurry volume by 20. This principle also applies to the average hollow fibre membrane area and buffer usage. The buffer tanks would have to be replaced by an online buffer mixing machine to keep footprint to a minimum and some of the streams would have to be recirculated (wash effluent to the binding stage dilution stream and the equilibration into the strip stage). In the case of the mixing modules, the modules would have to be redesigned and scaled up keeping the same RT while maintaining a similar flow pattern (N_{Re}) at a reasonable flow rate. The dimensions of the mixing modules will depend on the flow velocities chosen for a given flux in the chosen membrane areas.

Table 6.10. Cost and footprint values for all the CFIRs at any given length.

λ	Coil Dia.	Coil Side	Internal Coiled Tube Dia.	Horizontal Footprint	Vertical Footprint	Inversion	Length	Cost
(-)	(m)	(m)	(m)	(m^2)	(m^2)	(-)	(m)	(£)
13.8	0.053	0.203	0.004	0.041	0.012	0	1.43	8.62
						1	2.87	15.80
						2	4.30	22.94
						3	5.73	30.08
17.5	0.068	0.2275	0.004	0.052	0.017	0	1.81	9.03
						1	3.75	18.72
						2	5.70	28.45
						3	7.64	38.13
18.3	0.053	0.202	0.003	0.041	0.012	0	1.42	6.54
						1	2.85	11.64
						2	4.29	16.77
						3	5.72	21.87
18.8	0.073	0.2456	0.004	0.061	0.020	0	1.94	13.30
						1	3.88	22.99
						2	5.82	32.67
						3	7.77	42.40
23.3	0.068	0.2265	0.003	0.051	0.017	0	1.80	8.67
						1	3.74	15.58
						2	5.68	22.50
						3	7.63	29.45
25	0.073	0.2466	0.003	0.060	0.020	0	1.92	10.47
						1	3.87	17.42
						2	5.81	24.33
						3	7.75	31.24

Table 6.11. Cost and footprint values for the SMR at any given length for 30 cm and 70 cm static mixer modules. The 70 cm SMR was not used in any of the experiments, it is only for contrast.

Internal Dia. (m)	External Dia. (m)	Elements (-)	Length (m)	Horizontal Footprint (m^2)	Vertical Footprint (m^2)	Cost (£)
0.01	0.03	12	0.3	0.009	0.001	131
			0.6	0.018		262
			0.9	0.027		786
			1.2	0.036		524
0.01	0.03	12	0.7	0.018	0.001	209
			1.4	0.036		418

6.4.8 Reactor Characterisation Summary

The use of CFIRs as mixing modules for manufacturing processes precipitation or viral inactivation is not a new concept (Kateja *et al.*, 2016; David *et al.*, 2019). However, its use for chromatography separations had never been explored before as packed-bed chromatography is the standard. Chapter 6 focused on proving the concept of CFIR as a viable mixing module for the current CCTC system design. In order to be considered a viable CFIR, the reactor is required to provide the highest BBC. The BBC is the variable that is dependent on all the variables explored in this chapter, and ultimately, the decisive factor on whether a reactor is discarded or not. Table 6.12 shows the normalised BBC by the length, RT, N_{Pe}, vertical position footprint, horizontal position footprint and cost for the comparison among all the CFIRs and SMRs. The comparison only takes into account CFIRs and SMRs that were operated at a flow rate of 50 mL/min, as it is the most realistic parameter for operating a CCTC system. This section summarises the findings from Sections 6.4.6 and 6.4.7 in order to quantitatively rank the best reactors that could be taken forward for redesign and optimisation for future work. The reactors are ranked corresponding to their performance on each category; dark green being the best parameter to dark red being the worst one. There is not a standard CFIR used in the biomanufacturing environment. All values were taken as they were recorded and no normalisation was done to avoid any confusion between all CFIRs. All CFIRs were ranked according to their raw values for each category.

CFIR λ 13.8 showed to be the best option for most of the parameters that were explored. It was the best reactor in terms of BBC over length, N_{Pe} and, vertical and horizontal orientation footprint; while being second in time and cost. On the other hand, CFIR λ 23.3 and 25 showed to be worst reactor design by being the last or second to last in every parameter, with an exception in time and cost. It makes sense for CFIR λ 13.8 to be the best reactor design as its inherent reduced λ propitiates the creation of a stronger centrifugal force in the flow path; whilst the largest λ definitely showed an improved performance from HCRs but not as substantial as all the others due to their lower cross-sectional mixing. Even though CFIR λ 23.3 and 25 had a longer length, the BBC was not comparable or equal to the one measured for CFIR λ 13.8. The second best performing reactor was CFIR λ 18.3 due to the dimensions of its coil (the

same as CFIR λ 13.8) and smaller coiled tube (cheaper cost). This reactor was the second best for length and, vertical and horizontal orientation footprint; whereas, it ranked first in time and cost. The overall CFIR based on the normalisation of BBC over each of the parameters agrees with the theory observations and results found in the aforementioned sections.

SMR had its best performance at a length of 0.9 m for all considered parameters with the exception of horizontal orientation footprint. This is due to the fact that the increased magnitude of the parameters involving a fourth static mixer outweighs the benefit of a BBC increase of 10%. The third static mixer would be considered as trade-off between productivity and yield. Nevertheless, in this instance the addition of a fourth static mixer ensures a total adsorption and allows a more relaxed window of operation. On top of that, the price and extra RT of a fourth static mixer would be probably justified by the sale price of the therapeutic molecule.

The SMR with a length of 1.2 m proved to be best reactor in terms of BCC over length, N_{Pe} and, vertical and horizontal orientation foot print and only second and last in terms of time and cost, respectively. The SMR had the overall edge over the others as it achieved full adsorption while the closest BBC was CFIR λ 13.8 with 0.9. CFIRs cannot compete in terms of length with the static mixers, as having an extended piece of coiled tubing is integral to its performance and design. Even though the SMR ranked higher in terms of RT, the difference was only 6%. The CFIRs showed a higher magnitude in terms of N_{Pe} but the SMR managed to achieve BBC values equal or higher while operating at lower N_{Pe}, probably due to the inclusion of physical elements causing disruption in the flow path. The SMR has a slimmer design in either position, making it numerically a better option in either orientation. If the length is too long, its arrangement cannot be vertically stacked in a vertical orientation for pragmatic or overhead reasons. Also, stacking it vertically in horizontal orientation is not ideal as a portion of the resin beads might settle at the bottom of the tube. This positions the CFIRs and SMRs in relative equal terms for practical footprint terms. Finally, the SMRs are 13x to 17x times more expensive than the CFIRs. This is the most attractive feature for the CFIRs, it reaches high BBC values (even before optimisation) for just a fraction of the price. The CCTC system is meant to be operated via single use modules, making the CFIR the best option in terms of costs and simplicity.

In summary, commercially available SMRs used for this project are better fitted to provide a full BSA adsorption under average CCTC flow operational conditions. However, CFIRs λ 13.8 proved to be a viable candidate for further study and optimisation for the replacement of static mixers as the mixing modules for the current CCTC system design. The main feature of CFIRs is their simplicity, versatility to be stacked disregarding their orientation and lower cost. CFIRs could possible outshine SMRs as the BBC difference between the best ranking CFIR and the SMR was only of 10% and chromatography processes never operate at full BBC or DBC capacity.

Table 6.12. Comparison summary for all CFIRs operated at a flow rate of 50 mL/min. The BBC values have been normalised in respect to the length, RT, N_{Pe}, horizontal orientation footprint, vertical orientation footprint and cost values, respectively. The BBC performance values for each section for each of the 3 inversion CFIRs are colour coded to show their rank among that specific value among only all the CFIRs. The colours start from dark green being the best value to red being the worst value; passing through light green, yellow and orange in that order.

λ	Coil Dia.	Coiled Tube Dia.	Horizontal Footprint	Vertical Footprint	Inversion	BBC	BBC/Length	BBC/Time	BBC/N_{Pe}	BBC/H.Footprint	BBC/V.Footprint	BCC/Cost
(-)	(m)	(m)	(m^2)	(m^2)	(-)	(-)	(m^{-1})	(s^{-1})	(-)	(m^{-2})	(m^{-2})	(£$^{-1}$)
13.8	0.053	0.004	0.041	0.012	0	0.28	0.19	0.007	0.003	6.77	22.53	0.032
					1	0.48	0.17	0.007	0.005	11.55	38.42	0.030
					2	0.64	0.15	0.007	0.004	15.60	51.90	0.028
					3	0.90	0.16	0.008	0.006	21.89	72.86	0.030
17.5	0.068	0.004	0.052	0.017	0	0.42	0.23	0.010	0.005	8.09	24.23	0.046
					1	0.55	0.15	0.008	0.005	10.64	31.85	0.029
					2	0.63	0.11	0.007	0.005	12.23	36.60	0.022
					3	0.75	0.10	0.007	0.004	14.53	43.51	0.020
18.3	0.053	0.003	0.041	0.012	0	0.33	0.24	0.010	0.005	8.20	27.60	0.051
					1	0.58	0.20	0.011	0.007	14.10	47.46	0.049
					2	0.53	0.12	0.008	0.004	13.06	43.96	0.032
					3	0.77	0.14	0.010	0.005	18.94	63.76	0.035
18.8	0.073	0.004	0.061	0.020	0	0.37	0.19	0.008	0.006	6.01	18.31	0.027
					1	0.60	0.16	0.008	0.007	9.89	30.11	0.026
					2	0.64	0.11	0.006	0.005	10.49	31.94	0.020
					3	0.81	0.10	0.005	0.005	13.27	40.41	0.019
23.3	0.068	0.003	0.051	0.017	0	0.39	0.21	0.011	0.007	7.51	22.68	0.044
					1	0.53	0.14	0.012	0.007	10.36	31.28	0.034
					2	0.62	0.11	0.009	0.006	12.17	36.76	0.028
					3	0.61	0.08	0.008	0.004	11.94	36.05	0.021
25	0.073	0.003	0.060	0.020	0	0.34	0.18	0.009	0.008	5.65	17.36	0.033
					1	0.37	0.10	0.006	0.005	6.15	18.88	0.021
					2	0.60	0.10	0.009	0.006	9.95	30.55	0.025
					3	0.69	0.09	0.006	0.005	11.37	34.92	0.022

Table 6.13. Comparison summary for all SMRs operated at a flow rate of 50 mL/min. The BBC values have been normalised in respect to the length, RT, N_{Pe}, horizontal orientation footprint, vertical orientation footprint and cost values, respectively. The BBC performance values for each of the SMRs are colour coded to show their rank among that specific value among the set of SMRs. The colours start from dark green being the best value to red being the worst value; passing through light green, yellow and orange, in that order.

Internal Dia.	Elements	Horizontal Footprint	Vertical Footprint	Length	BBC	BBC/Length	BCC/Time	BCC/NPe	BBC/H.Foot print	BBC/V.Foot print	BCC/Cost
(m)	(-)	(m^2)	(m^2)	(m)	(-)	(m^{-1})	(s^{-1})	(-)	(m^{-2})	(m^{-2})	(£$^{-1}$)
0.01	12	0.009	0.001	0.3	0.25	0.82	0.007	0.018	27.34	348.15	0.002
		0.018		0.6	0.47	0.78	0.006	0.018	25.88	658.99	0.002
		0.027		0.9	0.89	0.99	0.010	0.019	33.13	1265.35	0.002
		0.036		1.2	1.04	0.87	0.009	0.012	28.94	1473.70	0.002

6.5 Conclusion

The proof of concept for CFIR as a viable replacement for the SMR in the current CCTC design proof of concept was explored throughout this chapter. CFIRs are currently a trending technology for an inexpensive and simple way of not only mixing but increasing productivity; i.e. mAb/protein precipitation, protein refolding biodiesel production (Kateja et al. 2016a; Kurt et al. 2017; A. K. Sharma et al. 2016; López-Guajardo et al. 2017). CFIRs had never been used for any chromatography purposes in the past for CCTC or any type. This was the first approach of integrating this technology into chromatography.

In order to study its effectiveness, three different types of reactors were used: CFIR, HCR and SMR. Each CFIR had its counterpart reactor as a HCR; while the SMR had no direct counterpart with any of them due to flow velocity and residence time limitations. The experiments were set to explore 6 different λ (13.8, 17.5, 18.3, 18.8, 23.3 and 25) at 3 different flow rates (20, 35 and 50 mL/min).

In order to determine the RTD for each of the reactors, NaCl was pumped as a tracer molecule and the conductivity recorded at the end of the flow path until it plateaued. The average residence time was 30% times higher than the theoretical one for both CFIRs and HCRs over all λ; whilst, SMRs was 88% times higher. This indicates that the secondary flow inside CFIRs and HCRs (no matter of magnitude) were able to hold the tracer molecule for longer into a more narrowed RTD. This trend has also been reported in literature (David *et al.*, 2019). SMRs had a longer average RT due to their larger diameter (1 cm) and number of elements inside its tubes, causing the distribution to be wider. No significant pressure drop was observed during normal operation.

The R_w value of all reactors was calculated from the RTD curves. The rise of N_{Re} had a negative effect on the R_w, as the increased N_{Re} enhances axial dispersion in the flow path. However, as the number of inversions/length was increased, the difference between R_w both N_{Re} extremes was gradually reduced, suggesting that the cross-sectional mixing effects caused by the secondary flow partially offsets the axial dispersion increase by the higher N_{Re}. The R_w significantly improved in the CFIRs compared to the HCRs as the λ decreased, with an average difference of 12.5% and

5.3% for λ 13.8 and 25, respectively. This is due to the decrease in λ, as it meant a higher centrifugal forces in the flow path. The SMR had the same trend in terms of N_{Re} and R_w but showed lower values due to the large diameter (decreased N_{Re}) which would cause a higher axial velocity profile.

The ADM was used to obtain a quantitative value for the reduction of axial dispersion, which would be represented by the N_{Pe}. The estimation of the N_{Pe} was done by fitting the ADM into the experimental data. The applicability of the ADM for all reactors was confirmed using a regime map and defined equations. The N_{Pe} was estimated with an average residual error of $1.0X10^{-5}$. For CFIRs, there was an inverse relationship between λ and N_{Pe}; in other words, the reduction in λ brings an increase of cross-sectional mixing due to increased centrifugal forces. This magnitude increase of N_{Pe} became more significant as N_{Re} increases. These phenomena happened because the secondary flow patterns are less dominant at lower N_{Re} and less capable of influencing the cross-mixing effect. The number of inversions had a positive impact on the reduction of axial dispersion. The magnitude of N_{Pe} increase was more pronounced with higher λ with increases from 170% for the lowest λ and 250% for the highest ones.

For HCRs, the difference of λ (167.3 for 3 mm and 125.5 for 4 mm) of N_{Pe} was not significant. Even though the λ is > 120 for both HCRs, the N_{Pe} seemed mainly positively affected as the length of the reactor increased. The HCRs had a similar increasing linear trend for N_{Pe} as N_{Re} and length was added to the reactor but at a smaller magnitude; even becoming fairly comparable at higher CFIR λ (only 50% different for λ 13.8 and 6% for λ 25).

The effects of λ, number of inversions and type of reactor were explored. The CFIRs with the lowest λ and increased number of inversions had the upper hand in terms of cross-sectional mixing, even at shorter lengths. This made CFIR λ 13.8 the best reactor in terms of mixing and length (N_{Pe} > 150) while CFIR λ 23.3 and 25 were the worst in terms of axial dispersion reduction and length (N_{Pe}). The length of the reactors played a role on this axial dispersion reduction. However, the initial advantage due to the innate design of the lower λ made it impossible to close the gap between them. The SMR at maximum length (1.2 m) showed an axial dispersion reduction 60% lower than the best performing CFIR (λ 13.8). HCRs at their longest length were approximately 25% below against CFIRs.

Afterwards, all the aforementioned reactors were used for BBC studies with BSA as the molecule of interest and Macro-Prep High Q as the chromatography media. The BBC experiments were performed at three different flow rates: 20, 30 and 50 ml/min. A comparison between all the reactors was made using the previously mentioned characterization parameters to normalize the calculated BBC for each reactor. CFIR λ 13.8 showed to be the best design as it ranked first on total BBC relative to its length, N_{Pe} and, horizontal and vertical orientation footprint; while, second in RT and cost. The 3 inversion CFIR λ 13.8 was the only reactor to achieve a total 0.9 BBC at 50 mL/min, whilst 3 inversion CFIR λ 25 only achieved a 0.69 BBC. All the other reactors approximately ranked in decreasing order as the λ increased with some fluctuations with the reactors with close λ values. CFIR λ 18.3 outclassed CFIR λ 13.8 in RT and cost as it is the smallest reactor made from the shortest coiled tube but its BBC was of 0.77. The SMR at its longest length (1.2 m) managed to beat all the CFIRs and HCRs in terms of BBC, length, N_{Pe} and, vertical and horizontal orientation footprint; second on RT and last on costs. The SMR at length 0.9 m and 1.2 m achieved a total BBC of 0.9 and 1.0, making it the best option in terms of adsorption alone but the worst for costs. The required SMR for a single step for a 2-stage CCTC at this scale costs £524, while a 3 inversion CFIR costs on average £32.2.

According to all the results, the SMR is the best reactor in terms of productivity and performance with CFIR λ 13.8 being the second best reactor and CFIR λ 23.3 and 25 being the worst designs (not including any HCR, which would rank last). Although, CFIR λ 13.8 could be regarded as the best option as it showed great potential achieving an adsorption of at least 90% at a comparable RT (110 s) in a non-optimized CFIR design at a significant reduced cost. CFIRs were 13X to 17X cheaper than the SMRs for a 2-stage CCTC system. SMR suffer from lack of flexibility due to their modular nature and the dependency for the manufacturer to provide a specialized static mixer for each manufacturing process.

There is no doubt that SMR is the currently the optimum choice in terms of BBC for the current CCTC system design, however CFIRs are definitely a real alternative. The overall BBC value can be improved with a better design and it is known that chromatography systems always operate under the maximum capacity of the resin. The inclusion of CFIRs would simplify the design by replacing the mixing module with a simple peristaltic tube that is already used for all the other connections and the

solid/liquid separation module. CFIRs would reduce the overall operational costs by more than 10 fold, if optimized and implemented correctly. Also, these type of reactors introduce a higher degree of flexibility to the overall design, as they can be manipulated, connected, lengthened, shortened and replaced with ease.

In conclusion, CFIRs have been shown to be very versatile in all sorts of unit operations. This can be also said for continuous non-column chromatography as it has been proven to be viable alternative with high potential if further investigated down the line. This replacement would certainly make the CCTC technique even more attractive in terms of costs and innovation by implementing a relevant and popular mixing technique.

Chapter 7: Conclusion/Discussion

7.1 Aim and Objectives Review

This thesis presented a method to characterise and build a 2-stage CCTC system in order to understand and simplify the current mixing module design (in turn the overall design) and asses the structural and performance changes of agarose- and synthetic-based chromatography resins exposed to this bioprocessing conditions. This chapter reviews each results chapter in order to assess their original goals and objectives.

The objectives of the first results chapter involved characterising the chromatography resin (Macro-Prep High Q and Q Sepharose FF), mixing (static mixer) and solid/liquid separation (hollow fibre) modules for the exploration of the operational process parameters that would be further be used for a 2-stage CCTC system. The resin was characterised by a series of BBC and DBC studies to establish residence times and maximum binding capacities. The mixing module was characterised with BBC studies. The operational parameters for the hollow fibre were explored by critical flux experiments to establish stable flow rates. All the parameters were set; however, the physical properties of the resins (lifetime and physical structure) were seemingly affected by the testing.

The objective of the second results chapter was to quantify mechanical differences between agarose- (Q Sepharose FF and Q Sepharose HP) and methacrylate- (Macro-Prep High Q) based chromatography media after being exposed to different mechanical strains caused by the CCTC system components following the PSD results from the previous chapter. To fulfil this, the performance of these resins were investigated using DBC studies. The structural properties were qualitatively and quantitatively analysed by using SEM and ImageJ software. In terms of shear stress, none of the systems produced a high enough shear to damage the surface of the resin in a significant way. The results showed that the CCTC system component that had the most and least impact on performance and structural properties (PSD, average pore size, average porosity and average pore count) were the magnetic stirrer mixer and the hollow fibre module, respectively. The peristaltic pump had no significant effects on the rigid resin but affected the shape of the agarose-based one. It was also observed that Macro-Prep High was more robust in terms of shear forces but it was extremely brittle to grinding forces caused by the magnetic stirrer mixer. On the other

hand, Q Sepharose FF and Q Sepharose HP were flexible enough to withstand fragmentation, but not rigid enough to maintain a consistent spherical shape and even surface texture.

The objectives of the third results chapter involved the testing and assessment of the custom 2-stage CCTC rig by separation BSA, as the product, and myoglobin, as the contaminant. All the knowledge and experience acquired in previous chapters led to the successful operation of the system and, in the end, a high quality purification. Secondly, a salt step-gradient separation of ovalbumin into its major components was also performed to explore the possibility of purifying at least two components with closely related elution behaviours. The ovalbumin separation demonstrated the limitation of the CCTC technique to separate closely elution molecules due to the online mixing nature of the system, making traditional packed bed chromatography a better option for these challenging separations. The results in this chapter showed the potential in terms of resin volume, lack of bed packing, resin usage, time and product production, even with a non-optimised CCTC rig. However, the draw backs of the system were also shown, such as high buffer usage, inability to pause or stop without needing to re-start the run, preparation of resin slurry (settling by gravity or centrifuge), hollow fibre fouling, dilution of product, complicated sampling for resin slurry, lack of specialised equipment or chromatography resin and limited experience of the technique due to non-accessibility in the market current market.

Finally, the objective of the final results chapter involved the proof of concept of CFIR as a replacement for static mixers as mixing modules for chromatography resin for the CCTC technique. The average residence time and cross-sectional mixing was defined for all CFIRs, HCRs, and SMRs. The results for this section have shown that a higher N_{Re}, a smaller λ and an increased number of inversions (length for HCR and SMR) yield a reduction in axial dispersion. Subsequently, the reactors were used for binding BSA to Macro-Prep High Q in order to relate cross-sectional mixing with BBC for all reactors. The BBC showed that the smaller the λ and the length/inversions added the reactor, the higher BBC will turn out to be. This agreed with the aforementioned axial dispersion reduction characterisation results. The results reported that the SMR ranked as the best reactor in terms of BBC relative to length, axial dispersion reduction and foot print, and second in RT and last in costs. CFIR λ 13.8 showed to be a great competitor by being the second best choice for length, axial dispersion reduction and

foot print; whilst being the second choice for RT and cost. After analysing the qualitative and quantitative aspects of both reactors, it was concluded that the CFIR is a viable option as a mixing module for protein adsorption for chromatography resin in a CCTC system. The advantages of the CFIR could definitely outperform the use of SMRs in a technique like this with further study and characterisation.

7.2 Overall Conclusions

The overall aim of this research was to understand and simplify the current CCTC design, this understanding involved the exploration of the effects on structure and performance the current CCTC system had in agarose- and synthetic-based chromatography resins. A sequential approach was done in order to accomplish this aim by the characterization of each system module, chromatography resin under different system modules to establish any significant lifetime impact. Then, the testing of the CCTC was done by doing a straight-forward separation (BSA and myoglobin) and a challenging separation (major ovalbumin variants with closely related elution behaviour). Finally, a simplification of the current design was explored by looking at CFIRs as viable mixing modules in the current CCTC design. This work has highlighted and addressed some of the challenges and effects that revolve around the recovery of biopharmaceuticals, as well as the resin materials, using the emergent CCTC technique and has built and simplified the design of the very same technique.

The biopharmaceutical market has been proven to be one of the most profitable businesses in most recent history with no sign of stopping at any given moment (MordorIntelligence 2018; Ho and Gibaldi 2013). USP productivity can be increased without significantly affecting the COGs in most of the cases as the fermentation vessel and materials do not require to crucially change. However, DSP costs increase as the target product titre increases as the process step is tied to a capacity or limitation on volume/time/target molecule binding. This increase on cost can bring product loses or unproductive purification steps that would require a redesign or replacement. A DSP bottleneck was imminent due to this product intensification. However, it is something that has been addressed by looking for solutions to each of the process unit operations in the biopharmaceutical manufacturing line. Most of the

production lines depend on chromatography as the purification workhorse and main unit operation to ensure the highest degree of quality and purity. However, the intensification of USP manufacturing processes and over reliability on traditional chromatography have pressured the discovery of new operational parameters and alternatives to reduce costs while maintaining the same level of quality. Nowadays, scientists and companies all over the world are trying to find alternatives such as modifying operational parameters, better chromatography resins (DBC, narrower and narrower PSD, highly resistant to chemicals and low pressure drop), different valve connections (scale up/out), multiple inter-connected columns (semi-continuous processes) and new chromatography formats. As seen in Chapter 1, there is concrete evidence suggesting that shifting chromatography into a semi-continuous, resin efficient and smaller unit operation would definitely reduce the COGs and increase the productivities. A relatively new alternative known CCTC, a non-column chromatography technique, was developed to fulfil this market need and provide a viable alternative solution. Even though the system is currently unavailable to purchase in the biopharmaceutical market, there is strong evidence suggesting that CCTC is a better technology for COGs (resin utilisation and resin volume), footprint (smaller equipment and concentrated buffer stocks) and straight forward scale up (increase mixer length and membrane area for hollow fibre). As one of the first viable chromatography unit operations that does not use a column for its operation, CCTC has certainly made an impact on how to approach chromatography as a whole.

The use of mixing (static mixer) and solid/liquid separation (hollow fibre) modules brought a new dimension of operational parameters for chromatography separations. Operational processing variables, such as binding capacity, residence time, resin slurry concentration, TMP profiles and flow velocities (flow rate or N_{Re}); were mainly investigated through adsorption/desorption (DBC and BBC) and critical flux experiments. Adsorption studies performed in small scale (50 to 100 mL beakers) or large scale (0.3 to 1.2 m SMR) showed that the BBC in Macro-Prep High Q (agarose-based resin with 50 µm diameter) and Q Sepharose FF (methacrylate-based resin with 90 µm diameter) were of approximately 18 mg/mL after 120 s and 25 mg/mL after 200 s, respectively. In general terms, a decrease in residence time is directly related to the reduction of bead diameter and, in this case, a lower BBC. The mixing module was chosen to be a set of 4 static mixers (2 per stage) with a 1 cm diameter and 30 cm

length, resulting in a residence time of approximately 120 s. Critical flux studies in a hollow fibre module of modified polyethersulfone membrane with a pore size of 0.65 μm, a tube length of 45 cm and a total membrane of 175 cm^2 gave a critical flux of 55 LMH for Macro-Prep High Q and 76.4 LMH for Q Sepharose FF. This was translated to a total flow rate of 51 mL/min (resin slurry feed flow rate of 13 mL/min and a permeate flow rate of 38 mL/min). The chromatography resin slurry at 40% (v/v) with the smaller size seemed to partially foul the hollow fibre at reduced fluxes; while the larger media completely clogged the hollow fibre. For this reason, a resin slurry of 20% (v/v) was used to avoid any fouling. These simple studies for the chromatography resin, static mixers and hollow fibres allowed the rapid evaluation of operational process variables. However, the protein kinetics studies required high amounts of resin, protein and buffer material. Currently there is not an existing method, technique or equipment to be able to measure the free protein in the resin slurry.

The used chromatography resin showed a reduced particle size signalling that something in the CCTC system was structurally damaging the bead and possibly hindering the performance in the long run. The CCTC rig and some of its components were used to observe the lifetime of both type of resins under continuous conditions for shorter (4 h) and longer (36 h) period of times. The different equipment configurations used were: CCTC system coupled with a magnetic stirrer or overhead impeller mixer in the resin reservoir, a peristaltic pump with a magnetic stirrer or overhead impeller mixer in the resin reservoir and the magnetic stirrer or overhead impeller mixer in the resin reservoir. In addition to these methods, the USD rotary disc device was used to show the effect of high shear (equivalent to a low-shear large-scale centrifuge) on the resin media. All these experiments were subjected to PSD analysis, DBC experiments and SEM imaging followed by a qualitative and quantitative analysis done in ImageJ.

The performance results suggest that resin exposed to the CCTC system, any of its configurations and USD rotary disc device did not show a significant deviation from its original DBC even after 36 h of use, a deviation approximately of less than 5%. The rigid resin media (Macro-Prep High Q) was reduced to 60% from its original size by the magnetic stirrer mixer due to its brittle nature, while the flexible resin media was merely reduced 6%. However, the flexible media was more susceptible to deformation due to the tube compression in the peristaltic pump. The surface of both types of media

is affected directly depending on the type of mixer that was being used. The magnetic stirrer mixer reduced the surface pores in Macro-Prep High Q (0.04 to 0.023 μm) due to the outer layer being eroded, exposing inner structures. On the other hand, an increase of pores was seen in Q Sepharose HP (0.01 to 0.7 μm) caused by the constant wear and tear of the surface. The overhead impeller had an opposite effect on Macro-Prep High Q (0.04 to 0.5 μm) due to the erosion but still not fragmentation of the surface, while Q Sepharose (0.01 to 0.02 μm) had a milder increase due to the gentler deformation of the surface. The PSD variation effects (due to fragmentation and chipping) on the resin are not attributed to the shear the beads are experiencing as the high shear resin samples did not show any significant deviation from the control. We cannot attribute to any of the PSD changes to the shear stress as the high shear conditions used in both bead materials were 30,000X and 14,000X higher than the one experienced inside a static mixer and 20X to 96X to the one experienced inside the resin reservoir mixer. The beads exposed to that high shear did not showed significant variation on their PSD. There were some fines detected by the Matersizer 3000 in the agarose-based media samples, also seen in a lesser proportion in the methacrylate-based one, that can be attributed to the analysis approximation used by the equipment and also by the transparent nature of the chromatography media. Some mitigation was achieved but not completely. The conjunction of all these results suggested that the hollow fibre modules in operation have no significant effect on the media. The peristaltic pump has no significant effect on rigid resin while it only causes deformation in flexible resins. The overhead impeller mixer offers the least structural and surface damage. In contrast, the magnetic stirrer mixer showed no reason to be ever be used for operation at any scale or even BBC studies (as it was previously reported). These experiments showed the possible effects of the CCTC system on the chromatography resin on two common types of chromatography resin under.

After ensuring the operational parameters and the possible effects of the system on the chromatography media, only then the custom CCTC rig was used first for the separation of the binary mixture of BSA and myoglobin using 20% (v/v) Macro-Prep High Q as the chromatography media. The separation was done in a 2-stage CCTC batch fashion, this means that the resin slurry was recovered after each step and used for the next step in the same 2-stage CCTC rig. The BSA yield and purity after all the steps were 99.1% and 99.6%, respectively. The system remained stable throughout

all the steps while operating at an approximate flux of 70 LMH and a TMP between 15 and 40 kPa. The overall productivity for this separation was deemed to be 22.3 g of BSA per L of resin per h, with potential to be at least doubled by shortening residence times of wash, elution and strip steps; as well as the use of a different resin with a higher slurry concentration. Nearly non-detectable levels of BSA were present after the binding stage, meaning the SMR provided enough residence time for the complete absorption. The bind step and 2 wash steps were enough to remove the majority of the contaminant. All these values were congruent with theoretical calculations and similar to previously reported values in literature (Napadensky *et al.*, 2013b; Amit K. Dutta *et al.*, 2016).

In order to get an idea of the technique limitations, the same CCTC rig was used to separate ovalbumin variants with closely related elution points in 2 salt-gradient elution steps using 20% (v/v) Q Sepharose FF as the chromatography media to exploit its increased BBC. The separation intended to separate the first and second variants (7% and 12% elution gradient). After the separation was performed, it was concluded that the CCTC system struggles to separate molecules with such close elution points. The product permeates on both elution steps and practically had all major variants. This behaviour can be majorly attributed to the in-line mixing between the elution buffer and the resin slurry, creating micro-environments at the entrance of the static mixer. Even though the separation of the first and second ovalbumin could not be achieved, the experiment was taken as evidence as to why the creators of the CCTC technique mainly focused on separations based on affinity interactions.

These two separations clearly showed the advantages and draw backs CCTC has against standard column base techniques. The main advantages were the lack of column packing, complete resin utilisation at all times, truly continuous mode, low operating pressure independent of resin bead size, single use technology (cheaper technology) and easy operation. On the other hand, the draw-backs were resin slurry concentration preparation (long settling times if not centrifuged), impossibility to pause or stop the run forcing a whole re-start, flow rate limitations by TMP/Flux, resin deformation or attrition, lack of UV-absorbance sensors for resin slurry, settlement of resin in the flow path and substantial volume of buffer usage. The system has the potential to be the best chromatography technique option for a continuous affinity

separation. However, the technology and its sensors/controllers have not yet been developed completely to satisfy the specific needs of a flowing resin slurry.

The proof of concept for CFIR as a viable replacement for the current CCTC design was fully explored using three types of reactors: CFIRs (λ 13.8, 17.5, 18.3, 18.8, 23.3 and 25), HCRs (125.5 and 167.3) and SMRs (1 cm internal diameter). The reactors were characterized in terms of average RTD and axial dispersion reduction (N_{Pe}) via an ADM. The average RT was in average 30% higher than the theoretical on for both CFIRs and HCRs. No measurable pressure drops were detected while operating all the reactors, as seen in Chapter 1. The plug flow pattern or R_w was also calculated from the RTD. The CFIRs had a smaller R_w by 13% to 5% compared to their HCR counterparts. It was seen that the larger the λ, the smaller the R_w. SMRs showed a lower R_w, due to its increased axial velocity profile caused by a larger diameter. The ADM was used to calculate the axial dispersion reduction or N_{Pe} from the normalized RTD curves (F-curves). According to the N_{Pe} values, CFIRs with smaller λ had a higher axial dispersion reduction; however, the CFIRs with higher λ had the highest improvement (250% increase in magnitude) compared to the smaller ones (170% increase in magnitude). HCRs at their longest length performed worse, 50% lower in smaller λ and only 6% for larger λ. In general terms, the cross-mixing inside the reactors was enhanced by length/RT, λ and N_{Re}. These factors contribute on the creation of a matured flow powered by the centrifugal force exerted by the curvature of the coiled tube and enhanced by the 90° inversion. SMRs showed N_{Pe} values approximately 60% lower compared to the best performing CFIR. Nonetheless, this can be due to the larger diameter (lower N_{Re}) and scale of the module.

The reactors were used to calculate the BBC experiments using BSA as the molecule of interest and Macro-prep High Q as the chromatography media. SMR length 1.2 m and CFIR λ 13.8 were the only reactor capable of achieving BBCs above 90% under standard CCTC operation conditions (flow rate 50 mL/min). CFIR λ 23.3 and 25 could only achieve BBCs of 65%. This trend confirmed that CFIRs with smaller λ performed better due to their enhanced initial axial dispersion reduction, propitiating the mass transfer between the mobile phase into the resin bead. This is crucial as the ligands on the most external surface of the bead have to be saturated in order to allow the BSA to diffuse into the bead. Additionally, at this point the mixing inside the reactor needs to be efficient but it is not crucial. The SMR might have performed better due to

the elements inside its flow path, creating disruptions and settlement of the resin (caused by obstruction and gravity) which would increase the overall RT for each resin bead.

According to all the results, SMR is the best reactor in terms of productivity and performance with CFIR λ 13.8 being the second best reactor whilst CFIR λ 23.3 and 25 were the worst designs (only above the HCRs). Nevertheless, it can be argued that CFIR λ is pragmatically the best reactor, even above the SMR. CFIR λ 13.8 achieved an adsorption of at least 90% at an approximate comparable time (RT of 110 s) at significant cheaper cost. CFIRs, in general, were 13x or 17x cheaper than the SMRs for a 2-stage CCTC system. In a single use environment, the coil in any CFIR can be reused as it has never been in contact with any feed, buffer or waste; while the static mixer has to be disposed for every subsequent use. In terms of resources, such as buffer or resin usage, there is no competition as they would be operated at the same resin slurries, flow rates and feed concentrations. On top of that, CFIRs outclass the SMR in terms of flexibility due to their adaptable coiled tube length (adaptable RT) and simplistic design. Realistically the SMRs and CFIRs would occupy a similar footprint in an AKTA-like machine due to the stackable nature of the CFIRs.

The aforementioned results confirmed that CFIRs are viable options for the replacement of static mixers as mixing modules. This adds one more unit operation in which CFIRs can be used effectively to reduce processing costs and simplify the process design. Further research of CFIRs in chromatography is worth looking into as the biopharmaceutical market is heading into a continuous processing type of manufacturing, making the CCTC a better and more attractive option as time goes on.

This study has highlighted the advantages and draw backs of the CCTC technique through the characterization of the system itself and the chromatography resin and presented CFIRs as a viable alternative for the mixing module design. The continuous exploration of the current CCTC technique and dedicated components such as chromatography resins, component modules and process control equipment will make this chromatography method a strong competitor against column-based techniques.

Chapter 8: Future Work

8.1 General Observations

Due to its reliability and vast experience, chromatography has been regarded as the workhorse and go to option for the purification of biopharmaceutical products, with 500 tons of products, such as mAbs, enzymes and other therapeutic molecules, being produced per year (Hagel, Jagschies and Sofer, 2008). Chromatography is the most expensive part of the mAb DSP manufacturing train by accumulating around approximately 60% of all the costs due to its expensive chromatography media. Even though this cost has been decreasing over time since the introduction of expensive chromatography resins (i.e. Protein A), it is undeniable that the reduction in COGs from this material has been a high priority in the DSP environment. (Anurag S. Rathore et al. 2015; Crommelin, Sindelar, and Meibohm 2016; Hernandez 2015). Ignoring the economic aspects of chromatography, the focus on USP optimization for increased product titres in the recent years has put a burden on DSP, especially on chromatography as a unit operation. The current DSP in those manufacturing facilities is incapable of handling these increased product titres with the current purification platforms and operational parameters, bringing imminent product losses and impending validation procedures for the increased load. This statement does not imply that the current processes are unable to cope with the titre but the purification with the current technologies would imply a significant sacrifice on productivity, footprint or COGs in order to do so in the same manufacturing line (Hentschel 2013). As seen in Chapter 1, the implementation of new technologies chromatographic technologies into the DSP unit operations can substantially improve the productivity and reduce the COGs and equipment footprint for a more cost-effective process.

Nevertheless, biopharmaceutical companies have started to look for more cost-effective options in order to enhance or replace traditional chromatography processes to avoid product loss and push process intensification in all operational units to keep up with other industry trends (Godawat et al. 2012; Warikoo et al. 2012). This has led to the emergence of new chromatography techniques that are able to cope with high amounts of product material under shorter cycle times and less resources, such as SMB, CAC, PCC, among others (Zydney 2016). However, these techniques employ the same mode of operation, a traditional packed-bed, and only change the number of columns, the feeding/valve system or geometry of the column.

Chromatography has been undoubtedly improved and has even mimicked a trendy semi-continuous unit operation. Nonetheless, it has not solved some of the most recurring problems in chromatography, like column packing, non-continuous product stream, high pressures, incomplete resin usage at all times (long processing times or cycles as consequence), high resin volume and complicated valve-switch systems. CCTC was introduced as a creative and straightforward solution for binary separations, focused on affinity chromatography separations, under traditional packed-bed chromatography techniques.

Due to the relatively recent introduction to the biopharmaceutical environment of CCTC, there is a need to identify its maximum potential and limitations to ease and accelerate its introduction into the biopharmaceutical manufacturing market as a viable option that could drastically reduce costs for the producer and consumer. A sequential and logical approach was taken in this project in order to achieve a better understanding of the emergent CCTC technique; still, a further investigation on current concerns and a new variety of approaches are yet to be explored. Improvements to the chromatography media (material and particle size) as well as CCTC design and process conditions optimizations, such as mixing equipment (mixing modules or resin reservoir modules), scale (mixing module and hollow fibre dimensions) and flow rate (flux/TMP values), can be used as stepping stones for the extension of resin lifetime and the stability of the system.

The creators of the CCTC technique and Purolite Corporation have already collaborated and reported in conjunction the production of a Protein A prototype chromatography resin known as prototype Praesto D5980. The Praesto D5980 is an agarose-based resin with a bead diameter of approximate 25 μm with a BBC of 66 g of mAb/mL of resin due to its specially designed low cross-linking density (3.5%), providing greater access to the ligand sites. The simple change of a specialised CCTC resin provided a 4X reduction in resin volume and nearly a 3X increase in productivity, translating to 140 g of mAb/mL of resin per hour (almost 10X higher than conventional column-based chromatography) (Fedorenko et al. 2020). Instead of finding alternatives for the mixing modules, as presented in Chapter 6, the creator of the CCTC technique, Oleg Shinkazh, has already explored an alternative for the solid/liquid separation module based on a 3-D printed spiral separator. The replacement of the hollow fibre for a 3-D printed spiral separator would bring massive

improvements to the operational space as the stability of the hollow fibre controlled by the flux/TMP parameters is no longer a problem. The system inlets and outlets, stages and steps would remain relatively unchanged. However, the name of the system would change to Continuous Counter-current Spiral Chromatography (CCSC), as the tangential flow aspect is being replaced. The alternative has just recently been patented and no articles have been published at the moment (Shinkazh and Fedorenko 2020).

Replacing or changing modules or aspects of the module is not the only approach that can be taken to raise awareness and confidence levels about the potential of the system and optimization of its design. There has been an effort to couple the CCTC system into a continuous manufacturing line. The CCTC system was successfully used to purify mAb from CCF from a perfusion bioreactor (Phase I). The 21 h continuous operation gave as a result a mAb yield of 92% and a HCP and DNA removal of 4.9 and 4.7 logs, respectively (Soltani et al. 2018).The system has presented an attractive continuous cost-effective mAb purification platform that can only be improved by further exploration. PendoTECH has also contributed by creating an in-line turbidity monitoring sensor for process streams. The PendoTECH turbidity flow cell is able to monitor the exact resin slurry concentration at the inlet and outlet stream to calculate cycle time, theoretical yields and steady-state operation (Fedorenko et al. 2018). Even though the sensor does not improve the productivity of the CCTC technique, it increases its reliability and footing to be an attractive use for mAb purification.

The research and improvements on CCTC are on a steadily growing and as any emergent technology, the inability to commercially acquire the system has slowed down its introduction to the research and industrial environment. This window of opportunity is left open for researches to explore and expand the knowledge on the CCTC technique as a whole process, batch step or isolated modules.

The following sections briefly describe several potential routes that can be taken in order to enhance the results presented in this thesis and contribute on building a substantial understanding of the CCTC technique, system and design. These concepts were considered taking into account the research plans that Chromatan has expressed currently involving the CCTC technique in general.

8.2 Scale-down System for Continuous Counter-current Tangential Chromatography Technique for High-throughput Technique and Modelling

All the experiments in Chapter 3, 5 and 6, involving BSA, myoglobin, ovalbumin and buffer reactants, showed the significant amount of material needed for a single batch 2-stage CCTC system run. In order to reduce resources, a high-throughput technique involving a scale-down version of a CCTC system can be assembled with CFIRs or SMRs and shorter hollow fibres (smaller membrane areas). Not only this will reduce the costs but it will increase the amount of data that can be obtained in a single run. The overall time of a specific process will be decreased albeit not drastically, as the average residence time for the protein adsorption and desorption will have to remain constant no matter the scale. It will be easier to modify this scale-down model with CFIRs rather than SMRs for its flexibility and adaptability. The adaptability of the CFIRs could be used to characterized protein adsorption/desorption kinetics at different RT, resin materials and resin sizes with ease. This scale-down CCTC system can be used to obtain the necessary data under different operational parameters, chromatography resins, mixing modules and hollow fibre materials and pore sizes, and be able to develop a model that could predict the concentration of any product or contaminant particle in any of the inlets, outlets and intermediate streams. On top of that, operational parameters such as flow velocities, pH, salt gradients and loading concentrations could be manipulated while the system is running. This can fit into a DoE approach.

8.3 Coiled Flow Inverter Reactor Design and Footprint Optimisation for Process Intensification

Chapter 6 showed that CFIRs have the potential to be used as a mixing device for resin slurries in CCTC systems. Using on these results as a foundation, the concept

of using CFIRs for chromatography techniques can be expanded by optimizing the coil tube and coiled tube ratio (λ) and their diameters to avoid any resin settling and maximize cross-sectional mixing. The versatility of CFIRs means that they can be easily adapted by shortening or lengthening the reactor (increasing/decreasing the diameters, pitch, coil, inversion and/or length) depending on the adsorption/desorption kinetics of the chromatography resin. The same flexibility allows the reactors to be designed as an asymmetrical or symmetrical reactor in order to fit certain footprint limitations. Ultimately, the CFIRs could be produced as CFIR cassettes ready to be connected to the CCTC system. CFIRs can also be used for the high-throughput scale-down experiments, as the SMR length is impossible to be modified unless extra modules were purchased beforehand. Also, CFIRs offer a better option as single-use technologies are becoming a staple in the biopharmaceutical market, making CFIRs a more sensible option in environmental and economic terms. The CFIR optimization has the potential to reduce significantly the footprint and costs for each reactor, as well as to expand the uses of CFIR in the biopharmaceutical industry. Further studies can be done in isolation and with less resources by not requiring a complete CCTC rig in order to make a substantial finding in the area.

8.4 Hollow Fibre Membrane Design, Material and Membrane Effects

While research continues in this area from the research group at Chromatan with the 3-D spiral separator, it should be noted that there is not any intention of deceasing the research on hollow fibre as the solid/liquid separation module. The information on the resin slurry inside the hollow fibre is limited. It is suspected that not only the membrane but also the tube design affects the performance of the hollow fibre i.e. as results show, the resin slurry inlet and outlet diameters might have a direct impact on the critical flux and stability of the system. A different manufacturing design or arrangement of the hollow fibres (straight or crossed) would probably bring positive impact on the stability of the system. Also, a further optimization on operational parameters can be done by modifying the material and pores of the membranes for each chromatography step as pertinent. The purpose of each chromatography step is vastly different compared to

each other, dependent on an IEC or AC, which will modify the buffer choice for each of them. The membrane can be specially chosen to react to the step conditions (temperature, ionic strength and pH) increase product/waste material retrieval.

8.5 Variety of Chromatography Media and Resin Aging Analytical Techniques

While efforts from Purolite Corporation have already created a prototype for a chromatography resin for CCTC, it should be acknowledged that commercially available resins might be able to be used without any complication or jeopardize the quality of the product. The chromatography resins commercially available that extends from a wide range of media materials to different ligand types could be tested in a CCTC system. For example, hydrophobic interaction chromatography (HIC) can benefit from the short-adsorption time that happens between loading and elution steps, as it has been reported an unfolding of proteins upon adsorption has been reported. CCTC could potentially mitigate such effects and increase the efficacy and yield of such proteins (Jungbauer, Machold, and Hahn 2005). The employment of commercially available resins can cement the current viability of the CCTC technique as this variable would not be an obstacle at the moment of investing research resources on emergent technologies. In some instances, the use of an already commercially available chromatography media would be more cost-effective than using a CCTC tailored resin. The CCTC technique was created with an AC mode in mind. Nonetheless, only experimenting and using different chromatography media and operation parameters, as seen in Chapter 5 with the separation of ovalbumin variants in two closely related elution steps, will discover the true potential or niche biopharmaceutical manufacturing platform.

Several analytical strategies have been presented for the assessment of the macro- and micro-structural state of the resin beads. However, there is no standard testing for performance, such as BBC and overall lifetime of commercially available and CCTC tailored resins. Establishing matured standard studies and its pertinent analytical techniques would not only help this technique but the whole chromatography scene

as chromatography resins would be pushed to their limits and improved for further product iterations with Quality by Design (QbD) properties in mind.

8.6 Process Controllers and In-line Sensors for UV-absorbance

Due to its relative recent creation and unique operational mode for a chromatography technique, very few dedicated CCTC process controllers and in-line sensors are available to ease the research or operation. The introduction of resin beads in the flow path has staggered the in-line sample measurement. Currently, is possible to pair a UV-absorbance detector on the product/contaminant permeate streams; however, the retentate stream (resin slurry with free and absorbed product material and contaminants) is unable to be measured directly. A tool that could potentially addressed this limitation would be a scale-down Tangential Flow Filtration (TFF) incorporated into the retentate stream. This tool can be used for resin slurry or any other large particles that would block or distort the UV-absorption signal. On top of that, the membrane in the miniature TFF modules could be tailored for the targeted molecules. This would allow the measurement of the time cycle and performance of the whole system and detect the site of any potential issue. As described in Chapter 5, the complete stop of a CCTC run would result on product loss and unclean resin. In the case of an early sign of a membrane fouling, a process controller that could potentially calculate in real time the flow ratios between permeate and retentate for each step would be mitigate this system draw-back. This tool would decrease the overall performance but would avoid complete product loss and give the operators time to choose a route of action. These analytic and processing tools would certainly aid the CCTC system to be regarded as a viable chromatography option.

References

Aldington, Suzanne, and Julian Bonnerjea. 2007. “Scale-up of Monoclonal Antibody Purification Processes.” *Journal of Chromatography B: Analytical Technologies in the Biomedical and Life Sciences*. https://doi.org/10.1016/j.jchromb.2006.11.032.

Ananthakrishnan, V., W. N. Gill, and Allen J. Barduhn. 1965. “Laminar Dispersion in Capillaries: Part I. Mathematical Analysis.” *AIChE Journal*. https://doi.org/10.1002/aic.690110620.

Anderson, Neal G. 2001. “Practical Use of Continuous Processing in Developing and Scaling up Laboratory Processes.” *Organic Process Research and Development*. https://doi.org/10.1021/op0100605.

Anderson, T. H., and D. E. Brune. 1982. “Continuous Production of Microalgae Using a Scouring Film Reactor.” *Aquacultural Engineering*. https://doi.org/10.1016/0144-8609(82)90028-0.

Aniceto, José P.S., and Carlos M. Silva. 2014. “Simulated Moving Bed Strategies and Designs: From Established Systems to the Latest Developments.” *Separation and Purification Reviews*. https://doi.org/10.1080/15422119.2013.851087.

Aoyagi, Kazuko. 2001. *Molecular Biology Problem Solver: A Laboratory Guide*. *Molecular Biology*. https://doi.org/10.1002/0471223905.ch11.

Aris, R. 1999. “A. On the Dispersion of a Solute in a Fluid Flowing through a Tube.” In *Process Systems Engineering*. https://doi.org/10.1016/S1874-5970(99)80009-5.

Arnold, Lindsay. 2018. “Challenges & Results: Moving to Multicolumn Chromatography.” *Pharmaceutical Engineering*, 2018. https://ispe.org/pharmaceutical-engineering/may-june-2018/challenges-results-moving-multicolumn-chromatography.

Bacchin, P., P. Aimar, and R. W. Field. 2006. “Critical and Sustainable Fluxes: Theory, Experiments and Applications.” *Journal of Membrane Science*. https://doi.org/10.1016/j.memsci.2006.04.014.

Bahadir, Ozlem. 2013. “Ion-Exchange Chromatography and Its Applications.” In

Column Chromatography. https://doi.org/10.5772/55744.

Bangrak, Phoowit, Savitree Limtong, and Muenduen Phisalaphong. 2011. “Continuous Ethanol Production Using Immobilized Yeast Cells Entrapped in Loofareinforced Alginate Carriers.” *Brazilian Journal of Microbiology* 42 (2): 676–84. https://doi.org/10.1590/S1517-838220110002000032.

Belfort, Georges, Robert H. Davis, and Andrew L. Zydney. 1994. “The Behavior of Suspensions and Macromolecular Solutions in Crossflow Microfiltration.” *Journal of Membrane Science*. https://doi.org/10.1016/0376-7388(94)00119-7.

Bender, Richard H. 1996. “Benchmark Costs for Pharmaceutical Facilities.” *Pharmaceutical Engineering*.

Beneš, Milan J., Daniel Horák, and Frantisek Svec. 2005. “Methacrylate-Based Chromatographic Media.” *Journal of Separation Science*. https://doi.org/10.1002/jssc.200500186.

Bertsch, Arnaud, Stephan Heimgartner, Peter Cousseau, and Philippe Renaud. 2001. “Static Micromixers Based on Large-Scale Industrial Mixer Geometry.” *Lab on a Chip*. https://doi.org/10.1039/b103848f.

Biosciences, A. 2001. “Use of Sodium Hydroxide for Cleaning and Sanitizing Chromatography Media and Systems.” *Process Chromatogr*, no. 4: 1–6. http://scholar.google.com/scholar?hl=en&btnG=Search&q=intitle:Use+of+sodium+hydroxide+for+cleaning+and+sanitizing+chromatography+media+and+systems#0.

Boschetti, E. 1994. “Advanced Sorbents for Preparative Protein Separation Purposes.” *Journal of Chromatography A*. https://doi.org/10.1016/0021-9673(94)80017-0.

Challener, Cynthia A. 2018. “Making the Move to Continuous Chromatography.” *BioPharm International*.

Chatel, Alex, Peter Kumpalume, and Mike Hoare. 2014. “Ultra Scale-down Characterization of the Impact of Conditioning Methods for Harvested Cell Broths on Clarification by Continuous Centrifugation-Recovery of Domain Antibodies from Rec E. Coli.” *Biotechnology and Bioengineering* 111 (5): 913–24.

https://doi.org/10.1002/bit.25164.

Chen, Jim C., Qilin Li, and Menachem Elimelech. 2004. “In Situ Monitoring Techniques for Concentration Polarization and Fouling Phenomena in Membrane Filtration.” *Advances in Colloid and Interface Science*. https://doi.org/10.1016/j.cis.2003.10.018.

Chris Wayne. 2019. “Theoretical Analysis and Experimental Investigation of Simulated Moving Bed Chromatography for the Purification of Protein Mixtures.” University College London.

Crommelin, Daan J.A., Robert D. Sindelar, and Bernd Meibohm. 2016. *Pharmaceutical Biotechnology: Fundamentals and Applications, Third Edition*. *Pharmaceutical Biotechnology: Fundamentals and Applications, Third Edition*.

David, Laura, Benjamin Maiser, Martin Lobedann, Peter Schwan, Michael Lasse, Horst Ruppach, and Gerhard Schembecker. 2019. “Virus Study for Continuous Low PH Viral Inactivation inside a Coiled Flow Inverter.” *Biotechnology and Bioengineering*. https://doi.org/10.1002/bit.26872.

Dowding, Peter J., and Brian Vincent. 2000. “Suspension Polymerisation to Form Polymer Beads.” *Colloids and Surfaces A: Physicochemical and Engineering Aspects*. https://doi.org/10.1016/S0927-7757(99)00375-1.

Downstream Column. 2020. “When to Choose Agarose or Methacrylic Polymer Resins,” 2020.

Dutta, Amit K., Dmitriy Fedorenko, Jasmine Tan, Joseph A. Costanzo, David S. Kahn, Andrew L. Zydney, and Oleg Shinkazh. 2017. “Continuous Countercurrent Tangential Chromatography for Mixed Mode Post-Capture Operations in Monoclonal Antibody Purification.” *Journal of Chromatography A*. https://doi.org/10.1016/j.chroma.2017.06.018.

Dutta, Amit K., Jasmine Tan, Boris Napadensky, Andrew L. Zydney, and Oleg Shinkazh. 2016a. “Performance Optimization of Continuous Countercurrent Tangential Chromatography for Antibody Capture.” *Biotechnology Progress*. https://doi.org/10.1002/btpr.2250.

Biotechnology Progress. 2016. “Performance Optimization of Continuous

Countercurrent Tangential Chromatography for Antibody Capture." *Biotechnology Progress*. https://doi.org/10.1002/btpr.2250.

Dutta, Amit K., Travis Tran, Boris Napadensky, Achyuta Teella, Gary Brookhart, Philip A. Ropp, Ada W. Zhang, Andrew D. Tustian, Andrew L. Zydney, and Oleg Shinkazh. 2015a. "Purification of Monoclonal Antibodies from Clarified Cell Culture Fluid Using Protein A Capture Continuous Countercurrent Tangential Chromatography." *Journal of Biotechnology*. https://doi.org/10.1016/j.jbiotec.2015.02.026.

Dutta, Amit K, Jasmine Tan, Boris Napadensky, and Andrew L Zydney. 2016. "Performance Optimization of Continuous Countercurrent Tangential Chromatography for Antibody Capture," no. 1. https://doi.org/10.1002/btpr.2250.

Dutta, Amit K, Travis Tran, Boris Napadensky, Achyuta Teella, Gary Brookhart, Philip A Ropp, Ada W Zhang, Andrew D Tustian, Andrew L Zydney, and Oleg Shinkazh. 2015b. "Purification of Monoclonal Antibodies from Clarified Cell Culture Fluid Chromatography." *Journal of Biotechnology*. https://doi.org/10.1016/j.jbiotec.2015.02.026.

Ecker, Dawn M., Susan Dana Jones, and Howard L. Levine. 2015. "The Therapeutic Monoclonal Antibody Market." *MAbs*. https://doi.org/10.4161/19420862.2015.989042.

Elwinger, Fredrik. 2017. "Characterizing Chromatography Media NMR-Based Approaches." KTH Royal Institute of Technology.

Ersson, Bo, Lars Rydén, and Jan Christer Janson. 2011. "Introduction to Protein Purification." *Protein Purification: Principles, High Resolution Methods, and Applications: Third Edition*, 2011. https://doi.org/10.1002/9780470939932.ch1.

Etzel, Mark R., and William T. Riordan. 2009. "Viral Clearance Using Monoliths." *Journal of Chromatography A*. https://doi.org/10.1016/j.chroma.2008.09.101.

Farid, Suzanne S. 2007. "Process Economics of Industrial Monoclonal Antibody Manufacture." *Journal of Chromatography B: Analytical Technologies in the Biomedical and Life Sciences*. https://doi.org/10.1016/j.jchromb.2006.07.037.

BioPharm International. 2009. "Economic Drivers and Trade-Offs in Antibody

Purification Processes.” *BioPharm International*.

Fedorenko, Dmitriy, Amit K. Dutta, Jasmine Tan, Jonathan Walko, Mark Brower, Nuno D.S. Pinto, Andrew L. Zydney, and Oleg Shinkazh. 2020. “Improved Protein A Resin for Antibody Capture in a Continuous Countercurrent Tangential Chromatography System.” *Biotechnology and Bioengineering*. https://doi.org/10.1002/bit.27232.

Fedorenko, Dmitriy, Jasmine Tan, Oleg Shinkazh, and Dennis Annarelli. 2018. “In-Line Turbidity Sensors for Monitoring Process Streams in Continuous Countercurrent Tangential Chromatography (CCTC).” *BioProcess International*, 2018.

Ferraris, Chiara F., Jeffrey W. Bullard, and Vincent Hackley. 2006. “Particle Size Distribution by LASER Diffraction Spectrometry: Application to Cementitious Powders.” In *AIChE Annual Meeting, Conference Proceedings*.

Gallagher, John. 1987. “Peter Mohr and Klaus Pommerening. Affinity Chromatography-Practical and Theoretical Aspects. Marcel Dekker, New York, 1986. $79.75, 312pp.” *Biomedical Chromatography*. https://doi.org/10.1002/bmc.1130020413.

Godawat, Rahul, Kevin Brower, Sujit Jain, Konstantin Konstantinov, Frank Riske, and Veena Warikoo. 2012. “Periodic Counter-Current Chromatography - Design and Operational Considerations for Integrated and Continuous Purification of Proteins.” *Biotechnology Journal*. https://doi.org/10.1002/biot.201200068.

Godawat, Rahul, Konstantin Konstantinov, Mahsa Rohani, and Veena Warikoo. 2015. “End-to-End Integrated Fully Continuous Production of Recombinant Monoclonal Antibodies.” *Journal of Biotechnology*. https://doi.org/10.1016/j.jbiotec.2015.06.393.

Gottschalk, Uwe. 2013. “Biomanufacturing: Time for Change?” *Pharmaceutical Bioprocessing*. https://doi.org/10.4155/pbp.13.2.

Gronemeyer, Petra, Reinhard Ditz, and Jochen Strube. 2014. “Trends in Upstream and Downstream Process Development for Antibody Manufacturing.” *Bioengineering*. https://doi.org/10.3390/bioengineering1040188.

Guélat, Bertrand, Guido Ströhlein, Marco Lattuada, Lydia Delegrange, Pascal Valax, and Massimo Morbidelli. 2012. “Simulation Model for Overloaded Monoclonal Antibody Variants Separations in Ion-Exchange Chromatography.” *Journal of Chromatography A*. https://doi.org/10.1016/j.chroma.2012.06.081.

Guo, Jing, and Giorgio Carta. 2015. “Unfolding and Aggregation of Monoclonal Antibodies on Cation Exchange Columns: Effects of Resin Type, Load Buffer, and Protein Stability.” *Journal of Chromatography A*. https://doi.org/10.1016/j.chroma.2015.02.047.

Gustavsson, Per Erik, and Per Olof Lars Son. 2003. “Chapter 6 Monolithic Polysaccharide Materials.” In *Journal of Chromatography Library*. https://doi.org/10.1016/S0301-4770(03)80022-2.

Hagel, Lars, Günter Jagschies, and Gail Sofer. 2008a. *Handbook of Process Chromatography*. *Handbook of Process Chromatography*.

Jagschies, Sofer and Lars Hagel. 2008. “Process-Design Concepts.” In *Handbook of Process Chromatography*. https://doi.org/10.1016/b978-012374023-6.50005-1.

Hahn, Tobias, Pascal Baumann, Thiemo Huuk, Vincent Heuveline, and Jürgen Hubbuch. 2016. “UV Absorption-Based Inverse Modeling of Protein Chromatography.” *Engineering in Life Sciences* 16 (2): 99–106. https://doi.org/10.1002/elsc.201400247.

Hammond, J B, and N J Kruger. 1988. “The Bradford Method for Protein Quantitation.” *Methods in Molecular Biology (Clifton, N.J.)* 3: 25–32. https://doi.org/10.1385/0-89603-126-8:25.

Hansen, Steen, Stig Pedersen-Bjergaard, and Knut Rasmussen. 2011. “Introduction to Pharmaceutical Analysis.” In *Introduction to Pharmaceutical Chemical Analysis*. https://doi.org/10.1002/9781119953647.ch1.

Hardin, Ann Marie, Chithkala Harinarayan, Gunnar Malmquist, Andreas Axén, and Robert van Reis. 2009. “Ion Exchange Chromatography of Monoclonal Antibodies: Effect of Resin Ligand Density on Dynamic Binding Capacity.” *Journal of Chromatography A* 1216 (20): 4366–71. https://doi.org/10.1016/j.chroma.2008.08.047.

Helmy, Iman M., and Adel M. Abdel Azim. 2012. “Efficacy of ImageJ in the Assessment of Apoptosis.” *Diagnostic Pathology*. https://doi.org/10.1186/1746-1596-7-15.

Hentschel, Norbert. 2013. “EMA Expert Workshop on Validation of Manufacturing for Biological Medicinal Products.” In *Traditional Validation - Downstream*, 1–16.

Hernandez, Randi. 2015. “Continuous Manufacturing: A Changing Processing Paradigm.” *BioPharm International*.

Ho, Rodney J.Y., and Milo Gibaldi. 2013. *Biotechnology and Biopharmaceuticals: Transforming Proteins and Genes into Drugs: Second Edition*. *Biotechnology and Biopharmaceuticals: Transforming Proteins and Genes into Drugs: Second Edition*. https://doi.org/10.1002/9781118660485.

Hober, Sophia, Karin Nord, and Martin Linhult. 2007. “Protein A Chromatography for Antibody Purification.” *Journal of Chromatography B: Analytical Technologies in the Biomedical and Life Sciences*. https://doi.org/10.1016/j.jchromb.2006.09.030.

Huang, Yadong, and Lennart Mucke. 2012. “Alzheimer Mechanisms and Therapeutic Strategies.” *Cell*. https://doi.org/10.1016/j.cell.2012.02.040.

Ioannidis, Nicolas. 2009. “Manufacturing of Agarose-Based Chromatographic Media with Controlled Pore and Particle Size.” *PhD Thesis*.

James, Sherry. 2016. “Monoclonal Antibodies (MAbs) Market Size Worth $138.6 Billion by 2024: Grand View Research, Inc.” *PRNewswire*, 2016.

Jensen, Ellen C. 2013. “Quantitative Analysis of Histological Staining and Fluorescence Using ImageJ.” *Anatomical Record*. https://doi.org/10.1002/ar.22641.

Jiang, Canping, Jing Liu, Michael Rubacha, and Abhinav A. Shukla. 2009. “A Mechanistic Study of Protein A Chromatography Resin Lifetime.” *Journal of Chromatography A* 1216 (31): 5849–55. https://doi.org/10.1016/j.chroma.2009.06.013.

Jungbauer, Alois. 1993. “Preparative Chromatography of Biomolecules.” *Journal of Chromatography A*. https://doi.org/10.1016/0021-9673(93)83082-4.

Jungbauer, Alois. 2005. “Chromatographic Media for Bioseparation.” *Journal of*

Chromatography A. https://doi.org/10.1016/j.chroma.2004.08.162.

Jungbauer, Alois. 2013. “Continuous Downstream Processing of Biopharmaceuticals.” *Trends in Biotechnology*. https://doi.org/10.1016/j.tibtech.2013.05.011.

Jungbauer, Alois, Christine Machold, and Rainer Hahn. 2005. “Hydrophobic Interaction Chromatography of Proteins: III. Unfolding of Proteins upon Adsorption.” *Journal of Chromatography A*. https://doi.org/10.1016/j.chroma.2005.04.002.

Kateja, Nikhil, Harshit Agarwal, Aditya Saraswat, Manish Bhat, and Anurag S. Rathore. 2016a. “Continuous Precipitation of Process Related Impurities from Clarified Cell Culture Supernatant Using a Novel Coiled Flow Inversion Reactor (CFIR).” *Biotechnology Journal*. https://doi.org/10.1002/biot.201600271.

Nikhil Kateja, Harshit Agarwal, Aditya Saraswat, Manish Bhat, Anurag S. Rathore. 2016. “Continuous Precipitation of Process Related Impurities from Clarified Cell Culture Supernatant Using a Novel Coiled Flow Inversion Reactor (CFIR).” *Biotechnology Journal*. https://doi.org/10.1002/biot.201600271.

Kaul, Rajni, and Bo Mattiasson. 1993. “Affinity Ultrafiltration for Protein Purification.” In *Molecular Interactions in Bioseparations*. https://doi.org/10.1007/978-1-4899-1872-7_32.

Kayser, Oliver, and Heribert Warzecha. 2012. *Pharmaceutical Biotechnology: Drug Discovery and Clinical Applications*. *Pharmaceutical Biotechnology: Drug Discovery and Clinical Applications*. https://doi.org/10.1002/9783527632909.

Keller, Karsten, Thomas Friedmann, and Arthur Boxman. 2001. “The Bioseparation Needs for Tomorrow.” *Trends in Biotechnology*. https://doi.org/10.1016/S0167-7799(01)01803-0.

Kelley, Brian. 2007. “Very Large Scale Monoclonal Antibody Purification: The Case for Conventional Unit Operations.” *Biotechnology Progress*. https://doi.org/10.1021/bp070117s.

Klutz, Stephan, Safa Kutup Kurt, Martin Lobedann, and Norbert Kockmann. 2015. “Narrow Residence Time Distribution in Tubular Reactor Concept for Reynolds Number Range of 10-100.” *Chemical Engineering Research and Design*.

https://doi.org/10.1016/j.cherd.2015.01.003.

Klutz, Stephan, Martin Lobedann, Christian Bramsiepe, and Gerhard Schembecker. 2016. “Continuous Viral Inactivation at Low PH Value in Antibody Manufacturing.” *Chemical Engineering and Processing: Process Intensification*. https://doi.org/10.1016/j.cep.2016.01.002.

Konstantinidis, Spyridon, Hai Yuan Goh, José M. Martin Bufájer, Paul de Galbert, Maria Parau, and Ajoy Velayudhan. 2018. “Flexible and Accessible Automated Operation of Miniature Chromatography Columns on a Liquid Handling Station.” *Biotechnology Journal*. https://doi.org/10.1002/biot.201700390.

Krohn, Brian J., Clayton V. McNeff, Bingwen Yan, and Daniel Nowlan. 2011. “Production of Algae-Based Biodiesel Using the Continuous Catalytic Mcgyan® Process.” *Bioresource Technology*. https://doi.org/10.1016/j.biortech.2010.05.035.

Kumar, Vimal, Mohit Aggarwal, and K. D.P. Nigam. 2006. “Mixing in Curved Tubes.” *Chemical Engineering Science*. https://doi.org/10.1016/j.ces.2006.04.040.

Kumar, Vimal, Monisha Mridha, A. K. Gupta, and K. D.P. Nigam. 2007. “Coiled Flow Inverter as a Heat Exchanger.” *Chemical Engineering Science*. https://doi.org/10.1016/j.ces.2007.01.032.

Kurt, Safa Kutup, Mohd Akhtar, Krishna D.P. Nigam, and Norbert Kockmann. 2017. “Continuous Reactive Precipitation in a Coiled Flow Inverter: Inert Particle Tracking, Modular Design, and Production of Uniform CaCO3 Particles.” *Industrial and Engineering Chemistry Research* 56 (39): 11320–35. https://doi.org/10.1021/acs.iecr.7b02240.

Langer, Eric. 2014. “Continuous Bioprocessing and Perfusion: Wider Adoption Coming as Bioprocessing Matures.” *BioProcessing Journal*. https://doi.org/10.12665/j131.langer.

Leonard, M. 1997. “New Packing Materials for Protein Chromatography.” *Journal of Chromatography B: Biomedical Applications*. https://doi.org/10.1016/S0378-4347(97)00160-6.

Lerche, K. H., and K. H. Richter. 1995. “Physical Methods of Chemistry.” *Zeitschrift*

Für Physikalische Chemie. https://doi.org/10.1524/zpch.1995.189.part_1.146.

Levenspiel, Octave. 1999. “Chemical Reaction Engineering.” *Industrial and Engineering Chemistry Research*. https://doi.org/10.1021/ie990488g.

Lewis-Sandy, D. 2001. “Optimizing Consumables Reuse for Therapeutic Protein Production.” In *Proceedings of IBC’s 4th International Conference on Production and Economics of Biopharmaceuticals*. San Diego, CA.

Li, Feng, Brian Lee, Joe Zhou, Tim Tressel, and Xiaoming Yang. 2006. “Current Therapeutic Antibody Production and Process Optimization.” *BioProcessing Journal*. https://doi.org/10.12665/j54.lizhou.

Li, Qiang, Gareth J. Mannall, Shaukat Ali, and Mike Hoare. 2013. “An Ultra Scale-down Approach to Study the Interaction of Fermentation, Homogenization, and Centrifugation for Antibody Fragment Recovery from Rec E. Coli.” *Biotechnology and Bioengineering*. https://doi.org/10.1002/bit.24891.

Longer, Eric. 2010. “Downstream Processing: Promising Technologies Are on the Horizon: The New Technologies Being Developed to Improve Downstream Systems Go beyond Traditional Chromatography.” *BioPharm International*.

López-Guajardo, Enrique, Enrique Ortiz-Nadal, Alejandro Montesinos-Castellanos, and Krishna D.P. Nigam. 2017. “Coiled Flow Inverter as a Novel Alternative for the Intensification of a Liquid-Liquid Reaction.” *Chemical Engineering Science*. https://doi.org/10.1016/j.ces.2017.01.016.

Lupis, Claude, and Eric Langer. 2015. “12th Annual Report and Survey of Biopharmaceutical Manufacturing Capacity and Production, April 2015.” *Pharmaceutical Manufacturing*.

Mahajan, Ekta, Anupa George, and Bradley Wolk. 2012. “Improving Affinity Chromatography Resin Efficiency Using Semi-Continuous Chromatography.” *Journal of Chromatography A*. https://doi.org/10.1016/j.chroma.2011.12.106.

Malvern Instruments Limited. 2015. *A Basic Guide to Particle Characterization*. https://www.cif.iastate.edu/sites/default/files/uploads/Other_Inst/Particle Size/Particle Characterization Guide.pdf.

Mascia, Salvatore, Patrick L. Heider, Haitao Zhang, Richard Lakerveld, Brahim

Benyahia, Paul I. Barton, Richard D. Braatz, et al. 2013. “End-to-End Continuous Manufacturing of Pharmaceuticals: Integrated Synthesis, Purification, and Final Dosage Formation.” *Angewandte Chemie - International Edition* 52 (47): 12359–63. https://doi.org/10.1002/anie.201305429.

Mathys, Peter, Robert Schaetti, and Zdravko Mandic. 2004. Static mixer. US7316503B2, issued 2004.

Mauryn C. Nweke. 2017. “Chromatography Resin Characterisation to Analyse Lifetime and Performance During Biopharmaceutical Manufacture.” University College London.

McGlaughlin, Molly S. 2012. “An Emerging Answer to the Downstream Bottleneck.” *BioProcess International*.

Mollan, Matthew J., and Mayur Lodaya. 2004. “Continuous Processing in Pharmaceutical Manufacturing: Where We Have Been and Where We Are Going.” *American Pharmaceutical Review*.

Mollerup, Jørgen M. 2008. “A Review of the Thermodynamics of Protein Association to Ligands, Protein Adsorption, and Adsorption Isotherms.” *Chemical Engineering and Technology*. https://doi.org/10.1002/ceat.200800082.

MordorIntelligence. 2018. “Biopharmaceuticals Market - GROWTH, TRENDS, AND FORECAST (2019 - 2024).” MordorIntelligence. 2018.

Mridha, Monisha, and K. D P Nigam. 2008. “Coiled Flow Inverter as an Inline Mixer.” *Chemical Engineering Science*. https://doi.org/10.1016/j.ces.2007.10.028.

Mu, Y., A. Lyddiatt, and A. W. Pacek. 2005. “Manufacture by Water/Oil Emulsification of Porous Agarose Beads: Effect of Processing Conditions on Mean Particle Size, Size Distribution and Mechanical Properties.” *Chemical Engineering and Processing: Process Intensification*. https://doi.org/10.1016/j.cep.2005.03.005.

Müller-Späth, T., G. Ströhlein, L. Aumann, H. Kornmann, P. Valax, L. Delegrange, E. Charbaut, et al. 2011. “Model Simulation and Experimental Verification of a Cation-Exchange IgG Capture Step in Batch and Continuous Chromatography.” *Journal of Chromatography A*. https://doi.org/10.1016/j.chroma.2011.05.103.

Napadensky, Boris, Oleg Shinkazh, Achyuta Teella, and Andrew L. Zydney. 2013a.

"Continuous Countercurrent Tangential Chromatography for Monoclonal Antibody Purification." *Separation Science and Technology (Philadelphia)*. https://doi.org/10.1080/01496395.2013.767837.

Nweke, Mauryn C., R. Graham McCartney, and Daniel G. Bracewell. 2017. "Mechanical Characterisation of Agarose-Based Chromatography Resins for Biopharmaceutical Manufacture." *Journal of Chromatography A*. https://doi.org/10.1016/j.chroma.2017.11.038.

Nweke, Mauryn C., Anurag S. Rathore, and Daniel G. Bracewell. 2018. "Lifetime and Aging of Chromatography Resins during Biopharmaceutical Manufacture." *Trends in Biotechnology*. https://doi.org/10.1016/j.tibtech.2018.01.001.

Nweke, Mauryn C., Mark Turmaine, R. Graham McCartney, and Daniel G. Bracewell. 2017. "Drying Techniques for the Visualisation of Agarose-Based Chromatography Media by Scanning Electron Microscopy." *Biotechnology Journal*. https://doi.org/10.1002/biot.201600583.

Pacis, Efren, Marcella Yu, Jennifer Autsen, Robert Bayer, and Feng Li. 2011. "Effects of Cell Culture Conditions on Antibody N-Linked Glycosylation-What Affects High Mannose 5 Glycoform." *Biotechnology and Bioengineering*. https://doi.org/10.1002/bit.23200.

Pakiman, N., N. H. Isa, M. A. Abol Hassan, J. K. Walter, and N. Abdullah. 2012. "Comparison of Binding Capacity and Affinity of Monoclonal Antibody towards Different Affinity Resins Using High-Throughput Chromatography Method." *Journal of Applied Sciences* 12 (11): 1136–41. https://doi.org/10.3923/jas.2012.1136.114.

Paul, Edward L., Victor A. Atiemo-Obeng, and Suzanne M. Kresta. 2004. "Handbook of Industrial Mixing: Science and Practice - Wiley Online Library." John Wiley & Sons. 2004.

Petrides, Demetri, Doug Carmichael, Charles Siletti, and Alexandros Koulouris. 2014. "Biopharmaceutical Process Optimization with Simulation and Scheduling Tools." *Bioengineering*. https://doi.org/10.3390/bioengineering1040154.

Poole, Colin F. 1995. "Fundamentals of Preparative and Nonlinear Chromatography."

Analytica Chimica Acta. https://doi.org/10.1016/0003-2670(95)90109-4.

Przybycien, Todd M., Narahari S. Pujar, and Landon M. Steele. 2004. “Alternative Bioseparation Operations: Life beyond Packed-Bed Chromatography.” *Current Opinion in Biotechnology*. https://doi.org/10.1016/j.copbio.2004.08.008.

Pungor, Erno, Noubar B. Afeyan, Neal F. Gordon, and Charles L. Cooney. 1987. “Continuous Affinity-Recycle Extraction: A Novel Protein Separation Technique.” *Bio/Technology*. https://doi.org/10.1038/nbt0687-604.

Purolite Life Sciences. 2021. “What Is Agarose?,” 2021. https://www.purolite.com/life-sciences-blog/why-agarose-in-chromatography.

Qiu, Zheyan, Lina Zhao, and Laurence Weatherley. 2010. “Process Intensification Technologies in Continuous Biodiesel Production.” *Chemical Engineering and Processing: Process Intensification*. https://doi.org/10.1016/j.cep.2010.03.005.

Rabe, Michael, Dorinel Verdes, and Stefan Seeger. 2011. “Understanding Protein Adsorption Phenomena at Solid Surfaces.” *Advances in Colloid and Interface Science*. https://doi.org/10.1016/j.cis.2010.12.007.

Rajendran, Arvind, Galatea Paredes, and Marco Mazzotti. 2009. “Simulated Moving Bed Chromatography for the Separation of Enantiomers.” *Journal of Chromatography A*. https://doi.org/10.1016/j.chroma.2008.10.075.

Rathore, A. S. 2015. “Continuous Processing for Production of Biotech Therapeutics.” *PDA Journal of Pharmaceutical Science and Technology*. https://doi.org/10.5731/pdajpst.2015.01072.

Rathore, Anurag, and Vijesh Kumar. 2017. “Mechanistic Modeling of Preparative Ion-Exchange Chromatography.” *BioPharm International*.

Rathore, Anurag S., Harshit Agarwal, Abhishek Kumar Sharma, Mili Pathak, and S. Muthukumar. 2015. “Continuous Processing for Production of Biopharmaceuticals.” *Preparative Biochemistry and Biotechnology*. https://doi.org/10.1080/10826068.2014.985834.

Rathore, Anurag S., Peter Latham, Howard Levine, John Curling, and Oliver Kaltenbrunner. 2004. “Costing Issues in the Production of Biopharmaceuticals.” *BioPharm International*.

Renaud, P C, and R F Probstein. 1991. “Physicochemical and Hydrodynamic Effects on Colloidal Fouling Reduction in Reverse Osmosis.” *Report*.

Rojahn, Patrick, Volker Hessel, Krishna D.P. Nigam, and Frank Schael. 2018. “Applicability of the Axial Dispersion Model to Coiled Flow Inverters Containing Single Liquid Phase and Segmented Liquid-Liquid Flows.” *Chemical Engineering Science*. https://doi.org/10.1016/j.ces.2018.02.031.

Rossi, Damiano, Luigi Gargiulo, Gleb Valitov, Asterios Gavriilidis, and Luca Mazzei. 2017. “Experimental Characterization of Axial Dispersion in Coiled Flow Inverters.” *Chemical Engineering Research and Design*. https://doi.org/10.1016/j.cherd.2017.02.011.

Saxena, A. K., and K. D.P. Nigam. 1984. “Coiled Configuration for Flow Inversion and Its Effect on Residence Time Distribution.” *AIChE Journal*. https://doi.org/10.1002/aic.690300303.

Schaschke, Carl. 2014. *A Dictionary of Chemical Engineering*. *A Dictionary of Chemical Engineering*. https://doi.org/10.1093/acref/9780199651450.001.0001.

Schneider, Caroline A., Wayne S. Rasband, and Kevin W. Eliceiri. 2012. “NIH Image to ImageJ: 25 Years of Image Analysis.” *Nature Methods*. https://doi.org/10.1038/nmeth.2089.

Separation Science. 2021. “Comparing Silica and Agarose Resins for Analysis of Proteins with SEC,” 2021.

Sharma, Abhishek Kumar, Harshit Agarwal, Mili Pathak, Krishna D.P. Nigam, and Anurag S. Rathore. 2016. “Continuous Refolding of a Biotech Therapeutic in a Novel Coiled Flow Inverter Reactor.” *Chemical Engineering Science*. https://doi.org/10.1016/j.ces.2015.10.009.

Sharma, Loveleen, K. D.P. Nigam, and Shantanu Roy. 2017. “Single Phase Mixing in Coiled Tubes and Coiled Flow Inverters in Different Flow Regimes.” *Chemical Engineering Science*. https://doi.org/10.1016/j.ces.2016.11.034.

Shinkazh, Oleg, and Dmitriy Fedorenko. 2020. Continuous Countercurrent Spiral Chromatography, issued 2020.

Shinkazh, Oleg, Dharmesh Kanani, Morgan Barth, Matthew Long, Daniar Hussain,

and Andrew L. Zydney. 2011. “Countercurrent Tangential Chromatography for Large-Scale Protein Purification.” *Biotechnology and Bioengineering*. https://doi.org/10.1002/bit.22960.

Shukla, Abhinav A, Brian Hubbard, Tim Tressel, Sam Guhan, and Duncan Low. 2007. “Downstream Processing of Monoclonal Antibodies — Application of Platform Approaches &” 848: 28–39. https://doi.org/10.1016/j.jchromb.2006.09.026.

Soltani, Soroosh, Amit K Dutta, Dmitriy Fedorenko, Jasmine Tan, John Chorazyczewski, Andrew L Zydney, and Oleg Shinkazh. 2018. “Integrated Continuous and Single-Use (ICS) Bio-Production Platform.” *BioProcess International*, 3–6.

Sommerfeld, Sven, and Jochen Strube. 2005. “Challenges in Biotechnology Production - Generic Processes and Process Optimization for Monoclonal Antibodies.” *Chemical Engineering and Processing: Process Intensification*. https://doi.org/10.1016/j.cep.2005.03.006.

Soni, Surbhi, Loveleen Sharma, Priya Meena, Shantanu Roy, and K. D.P. Nigam. 2019. “Compact Coiled Flow Inverter for Process Intensification.” *Chemical Engineering Science*. https://doi.org/10.1016/j.ces.2018.09.008.

Stone, Melani C., and Giorgio Carta. 2007. “Protein Adsorption and Transport in Agarose and Dextran-Grafted Agarose Media for Ion Exchange Chromatography.” *Journal of Chromatography A*. https://doi.org/10.1016/j.chroma.2007.02.041.

Storti, F., and F. Balsamo. 2010. “Particle Size Distributions by Laser Diffraction: Sensitivity of Granular Matter Strength to Analytical Operating Procedures.” *Solid Earth*. https://doi.org/10.5194/se-1-25-2010.

Straathof, A. J.J. 2011. “The Proportion of Downstream Costs in Fermentative Production Processes.” In *Comprehensive Biotechnology, Second Edition*. https://doi.org/10.1016/B978-0-08-088504-9.00492-X.

Strube, Jochen, Florian Grote, Jan Pablo Josch, and Reinhard Ditz. 2011. “Process Development and Design of Downstream Processes.” *Chemie-Ingenieur-Technik*. https://doi.org/10.1002/cite.201100017.

Suda, Eric J., Kristin E. Thomas, Timothy M. Pabst, Paul Mensah, Natraj Ramasubramanyan, Mark E. Gustafson, and Alan K. Hunter. 2009. “Comparison of Agarose and Dextran-Grafted Agarose Strong Ion Exchangers for the Separation of Protein Aggregates.” *Journal of Chromatography A*. https://doi.org/10.1016/j.chroma.2009.05.021.

Teipel, U. 2002. “Problems in Characterizing Transparent Particles by Laser Light Diffraction Spectrometry.” *Chemical Engineering and Technology*. https://doi.org/10.1002/1521-4125(200201)25:1<13::AID-CEAT13>3.0.CO;2-A.

Tran, Miller, Christina Van, Daniel J. Barrera, Pär L. Pettersson, Carlos D. Peinado, Jack Bui, and Stephen P. Mayfield. 2013. “Production of Unique Immunotoxin Cancer Therapeutics in Algal Chloroplasts.” *Proceedings of the National Academy of Sciences of the United States of America*. https://doi.org/10.1073/pnas.1214638110.

Truesdell, R. A., P. V. Vorobieff, L. A. Sklar, and A. A. Mammoli. 2003. “Mixing of a Continuous Flow of Two Fluids Due to Unsteady Flow.” *Physical Review E - Statistical Physics, Plasmas, Fluids, and Related Interdisciplinary Topics*. https://doi.org/10.1103/PhysRevE.67.066304.

Truesdell, Richard A., J. W. Bartsch, T. Buranda, L. A. Sklar, and A. A. Mammoli. 2005. “Direct Measurement of Mixing Quality in a Pulsatile Flow Micromixer.” *Experiments in Fluids*. https://doi.org/10.1007/s00348-005-0015-7.

Unrean, Pornkamol, and Friedrich Srienc. 2010. “Continuous Production of Ethanol from Hexoses and Pentoses Using Immobilized Mixed Cultures of Escherichia Coli Strains.” *Journal of Biotechnology*. https://doi.org/10.1016/j.jbiotec.2010.08.002.

Vaňková, Katarína, Zdenka Onderková, Monika Antošová, and Milan Polakovič. 2008. “Design and Economics of Industrial Production of Fructooligosaccharides.” *Chemical Papers*. https://doi.org/10.2478/s11696-008-0034-y.

Vogel, Jens H., Huong Nguyen, Markus Pritschet, Richard Van Wegen, and Konstantin Konstantinov. 2002. “Continuous Annular Chromatography: General Characterization and Application for the Isolation of Recombinant Protein Drugs.” *Biotechnology and Bioengineering*. https://doi.org/10.1002/bit.10411.

Voulgaris, Ioannis, Alex Chatel, Mike Hoare, Gary Finka, and Mark Uden. 2016. “Evaluation of Options for Harvest of a Recombinant E. Coli Fermentation Producing a Domain Antibody Using Ultra Scale-down Techniques and Pilot-Scale Verification.” *Biotechnology Progress*. https://doi.org/10.1002/btpr.2220.

Walthe, Jason, Rahul Godawat, Chris Hwang, Yuki Abe, Andrew Sinclair, Konstantin Konstantinov, Mahsa Rohani, et al. 2015. “FDA Perspective on Continuous Manufacturing.” *Journal of Biotechnology*. https://doi.org/10.1038/nrd3746.

Wang, Dong Mei, Gang Hao, Qing Hong Shi, and Yan Sun. 2007. “Fabrication and Characterization of Superporous Cellulose Bead for High-Speed Protein Chromatography.” *Journal of Chromatography A* 1146 (1): 32–40. https://doi.org/10.1016/j.chroma.2007.01.089.

Warikoo, Veena, Rahul Godawat, Kevin Brower, Sujit Jain, Daniel Cummings, Elizabeth Simons, Timothy Johnson, et al. 2012. “Integrated Continuous Production of Recombinant Therapeutic Proteins” 109 (12): 3018–29. https://doi.org/10.1002/bit.24584.

Warner, Tim N., and Sam Nochumson. 2003. “Rethinking the Economics of Chromatography: New Technologies and Hidden Costs.” *BioPharm International*.

Weaver, Justin, Scott M. Husson, Louise Murphy, and S. Ranil Wickramasinghe. 2013. “Anion Exchange Membrane Adsorbers for Flow-through Polishing Steps: Part II. Virus, Host Cell Protein, DNA Clearance, and Antibody Recovery.” *Biotechnology and Bioengineering*. https://doi.org/10.1002/bit.24724.

Werner, Rolf G. 2004. “Economic Aspects of Commercial Manufacture of Biopharmaceuticals.” In *Journal of Biotechnology*. https://doi.org/10.1016/j.jbiotec.2004.04.036.

William, Lynn. 1951. Bead polymerization of methyl methacrylate. US2701245A, issued 1951.

Wu, Yige, Dicky Abraham, and Giorgio Carta. 2015. “Particle Size Effects on Protein and Virus-like Particle Adsorption on Perfusion Chromatography Media.” *Journal of Chromatography A* 1375: 92–100. https://doi.org/10.1016/j.chroma.2014.11.083.

Yang, Ou, Maen Qadan, and Marianthi Ierapetritou. 2019. “Economic Analysis of Batch and Continuous Biopharmaceutical Antibody Production: A Review.” *Journal of Pharmaceutical Innovation*. https://doi.org/10.1007/s12247-018-09370-4.

Zhang, Hu, Simyee Kong, Andrew Booth, Rihab Boushaba, M. Susana Levy, and Michael Hoare. 2007. “Prediction of Shear Damage of Plasmid DNA in Pump and Centrifuge Operations Using an Ultra Scale-down Device.” *Biotechnology Progress*. https://doi.org/10.1021/bp070066z.

Zhou, Joe X., and Tim Tressel. 2006. “Basic Concepts in Q Membrane Chromatography for Large-Scale Antibody Production.” *Biotechnology Progress*. https://doi.org/10.1021/bp050425v.

Zhou, Qing Zhu, Lian Yan Wang, Guang Hui Ma, and Zhi Guo Su. 2008. “Multi-Stage Premix Membrane Emulsification for Preparation of Agarose Microbeads with Uniform Size.” *Journal of Membrane Science*. https://doi.org/10.1016/j.memsci.2008.05.025.

Zydney, Andrew L. 2016. “Continuous Downstream Processing for High Value Biological Products : A Review” 113 (3): 465–75. https://doi.org/10.1002/bit.25695.